Initial Data for the Two-Body Problem of General Relativity

by

Gregory B. Cook

A dissertation submitted to the faculty of The University of North Carolina at Chapel Hill in partial fulfillment of the requirements for the degree of Doctor of Philosophy in the Department of Physics and Astronomy.

Chapel Hill

1990

Approved by:

_____

Advisor

_____

Reader

_____

Reader

_____

Reader

_____

Reader

© 1990
Gregory B. Cook
ALL RIGHTS RESERVED

GREGORY B. COOK: Initial Data for the Two-Body Problem of General Relativity (Under the direction of James W. York, Jr.)

ABSTRACT

The numerical study of Einstein's equations is of considerable interest for both astrophysical and purely theoretical reasons as it provides the only known avenue for the study of strong field, highly relativistic gravitational interactions. Of particular interest is the geometrodynamic two-body problem since the collision of two black holes is believed to be a strong source of gravitational radiation. Before studying the dynamics of such collisions, one must first obtain complete initial-data sets which represent two black holes in some initial configuration including non-vanishing linear and angular momenta for each hole. A formalism for constructing such initial-data sets is reviewed. Based on this formalism, computational techniques are developed which allow for the complete specification of initial data describing both one and two black holes with individually specifiable linear and angular momenta. In the case of two black holes, the initial data is constructed in two separate, base coordinate systems. Bispherical coordinates are used to construct very accurate initial-data sets. Čadež coordinates are also used because this coordinate system is most appropriate for future work on the evolution of the initial data. A method for locating apparent horizons in the initial-data sets is developed by posing the apparent-horizon equation as a boundary-value problem. This method is applied to the single-hole, initial-data sets leading to a new understanding of the physical content of these initial hypersurfaces. The physical content of the two-hole, initial-data sets is also explored.

To my wife, Tonya,
and my parents,
for their love,
support, and
understanding.

"If I have seen further it is by
standing on the shoulders of giants"

Sir Isaac Newton

Acknowledgements

I gratefully acknowledge the assistance and encouragement I have received from my family, friends, colleagues, and instructors. I am most especially thankful to my advisor, James W. York, Jr., for his support, inspiration, and for many invaluable discussions. I have also benefitted greatly from my interactions with Bernard Whiting, Charles Evans, Steve Christensen, Tsvi Piran, and Steve Detweiler. In particular, I wish to thank Bernard Whiting for his seemingly endless patience and enthusiasm.

I am grateful for the support I have received from the Department of Physics and Astronomy at The University of North Carolina at Chapel Hill. Much of the computational work contained in this dissertation has been performed on the Convex supercomputer run by the Academic Computing Services at UNC–Chapel Hill and on the Cray Y-MP supercomputer at the North Carolina Supercomputing Center. Financial support has been provided in part through National Science Foundation grants PHY-8407492, PHY-8908741, and PHY-9001645.

TABLE OF CONTENTS

Page

LIST OF TABLES viii

LIST OF FIGURES ix

NOTATION AND CONVENTIONS xi

Chapter

1. Introduction 1
2. The $(3+1)$ Decomposition 5
3. The Conformal and Transverse-Traceless Decompositions 16
4. The Conformal Imaging Approach 20
5. Solutions of the Momentum Constraint 32
6. Inversion-Symmetric Extrinsic Curvature for Two Black Holes 39
7. The Hamiltonian Constraint and Boundary Conditions 45
8. Numerical Solution of the Hamiltonian Constraint for a Single, Axisymmetric Black Hole 54
9. Axisymmetric Numerical Solutions of the Hamiltonian Constraint for Two Black Holes 64
10. The Hamiltonian Constraint for Two Black Holes Using Čadež Coordinates 76
11. Apparent Horizons on Inversion-Symmetric Initial-Data Sets 91
12. Apparent Horizons for a Single Black Hole with Linear or Angular Momentum 96
13. Inversion-Symmetric, Single-Hole Initial-Data Sets 105
14. Inversion-Symmetric, Two-Hole Initial-Data Sets 113
15. Conclusion 126

Appendix A: The Multigrid Algorithm 131

Appendix B: Numerical Solutions of the One-Hole Hamiltonian Constraint 136

Appendix C: Numerical Solutions of the Two-Hole Hamiltonian Constraint in Bispherical Coordinates 152

Appendix D: Numerical Solutions of the Two-Hole Hamiltonian Constraint in Čadež Coordinates 173

References 194

LIST OF TABLES

Table **Page**

8.1 Numerical solution of the model problem compared with the exact solution. 63

8.2 Energy and minimal surface mass for a single black hole with linear momentum. 63

8.3 Energy and minimal surface mass for a single black hole with angular momentum. 63

9.1 ADM energy of time-symmetric solutions of the Hamiltonian constraint at (80×80), (120×120), and (160×160) mesh resolutions, Richardson extrapolated and compared with the analytic solution for the ADM energy. β indicates the separation of the two holes. 73

9.2 Total energy and masses for two holes which are very far apart, the larger hole having linear momentum P. The Extrinsic Curvature obeys the isometry condition with the plus sign. $(\alpha = 20, \beta = 50)$ 73

9.3 Total energy and masses for two holes which are very far apart, the larger hole having linear momentum P. The Extrinsic Curvature obeys the isometry condition with the minus sign. $(\alpha = 20, \beta = 50)$ 74

9.4 Total energy and masses for two holes which are very far apart, the larger hole having angular momentum S. The Extrinsic Curvature obeys the isometry condition with the minus sign. $(\alpha = 20, \beta = 50)$ 74

12.1 Minimal-surface mass and apparent-horizon mass for a hole with linear momentum P generated from $\bar{A}^+_{ij}$. Also tabulated are the apparent-horizon amplitude $\mathcal{H}$ and its standard deviation σ 104

LIST OF FIGURES

Figure **Page**

4.1 Embedding diagram of time-symmetric, maximal slice of Schwarzschild geometry in isotropic coordinates. 23

4.2 Time-symmetric, maximal slice of Kruskal space-time, labeled in isotropic coordinates and showing "top" and "bottom" sheets in the two different universes. 24

4.3 Initial slice topologies for two black holes. a) Topology of an $N + 1$ sheeted manifold. b) Topology of a two-sheeted manifold. 25

8.1 Computational mesh and "virtual" boundary points. 59

9.1 Two-hole background space parameterization and solution domain. 64

10.1 Čadež coordinates near the two holes showing important coordinate lines and the *three* region nature of the coordinate system. 79

10.2 Eight-point differencing molecule used for singular point. 85

11.1 An apparent horizon S intersecting the initial-data surface Σ. n^μ is the timelike unit normal vector for the initial-data surface and s^μ is the *outward* pointing spacelike unit normal to the apparent horizon. 92

12.1 Apparent-horizon function $h(\theta)$ for a hole with linear momentum $P/a = 10$ generated by $\bar{A}^+_{ij}$. 104

13.1 Energy and velocity for a boosted black hole with linear momentum P generated from the extrinsic curvature $\bar{A}^+_{ij}$. 108

13.2 Energy and velocity for a boosted black hole with linear momentum P generated from the extrinsic curvature $\bar{A}^-_{ij}$. 108

13.3 Energy of a spinning black hole with angular momentum S. 109

13.4 The location of the top and bottom apparent horizons (for data sets generated from $\bar{A}^+_{ij}$) and the minimal surface in the conformal background space. Also plotted are the spatial projections of various "outgoing" null vectors with negative expansion. 110

13.5 The location of the apparent horizons (for data sets generated from $\bar{A}^+_{ij}$) and the minimal surface illustrated on an embedding diagram of the geometry. 111

14.1 (a) total energy, (b) separation, (c) maximum radiation energy, and (d) maximum radiation efficiency for two holes with linear momenta P aligned anti-parallel to each other and generated by an inversion-symmetric extrinsic curvature obeying the isometry condition with a plus sign. 116

14.2 (a) total energy, (b) separation, (c) maximum radiation energy, and (d) maximum radiation efficiency for two holes with linear momenta P aligned parallel to each other and generated by an inversion-symmetric extrinsic curvature obeying the isometry condition with a plus sign. 117

14.3 (a) total energy, (b) separation, (c) maximum radiation energy, and (d) maximum radiation efficiency for two holes with linear momenta P aligned anti-parallel to each other and generated by an inversion-symmetric extrinsic curvature obeying the isometry condition with a minus sign. 119

14.4 (a) total energy, (b) separation, (c) maximum radiation energy, and (d) maximum radiation efficiency for two holes with linear momenta P aligned parallel to each other and generated by an inversion-symmetric extrinsic curvature obeying the isometry condition with a minus sign. 120

14.5 (a) total energy, (b) separation, (c) maximum radiation energy, and (d) maximum radiation efficiency for two holes with angular momenta S aligned anti-parallel to each other and generated by an inversion-symmetric extrinsic curvature obeying the isometry condition with a minus sign. 122

14.6 (a) total energy, (b) separation, (c) maximum radiation energy, and (d) maximum radiation efficiency for two holes with angular momenta S aligned parallel to each other and generated by an inversion-symmetric extrinsic curvature obeying the isometry condition with a minus sign. 123

14.7 Comparison of the scaled total energy for two holes with angular momenta S aligned anti-parallel and parallel to each other showing the spin-spin interaction. 124

Notation and Conventions

This work conforms to the notation and conventions of Misner, Thorne, and Wheeler [1973] unless otherwise noted. The units used in this work are kept arbitrary throughout the development of the theoretical foundations by the use of the proportionality constant $\kappa = 8\pi G/c^4$ in Einstein's equations $G^{\mu\nu} = \kappa T^{\mu\nu}$ and in other dimensionfull quantities. In the numerical work, gravitational units ($G = c = 1$; $\kappa = 8\pi$) are used.

Lower case Greek indices take on the values 0,1,2,3. If the manifold is pseudo-Riemanian, then the "zero" index is associated with the timelike direction and the signature of the metric is $(-+++)$. In Chapter 2, Riemanian manifolds are considered in which the signature of the metric is $(++++)$.

Lower case Latin indices take on the values 1,2,3 and indicate that the tensor is purely spatial. The signature of the spatial metric is $(+++)$. In Chapter 3, spatial hypersurfaces of arbitrary dimension are considered. In this case, Latin indices take on the values 1,2,... and the signature of the spatial metric is $(++\ldots)$.

Partial derivatives are written either explicitly or with comma notation

$$\frac{\partial V^\mu}{\partial x^\nu} = \partial_\nu V^\mu \equiv V^\mu{}_{,\nu}.$$

General covariant derivatives are expressed by either ∇_ν or by semicolon notation

$$\nabla_\nu V^\mu \equiv V^\mu{}_{;\nu}.$$

The induced, spatial covariant derivative on a three-dimensional, spacelike hypersurface is expressed by D_i.

Beginning in Chapter 3, a background space is used which is conformally related to the physical space. Certain fields are used in both spaces by means of conformal transformations. Conformally transformed fields are expressed using the same symbol used for the field in the physical space with the addition of an overbar. For example, the physical metric is denoted by γ_{ij} and the conformal metric by $\bar{\gamma}_{ij}$. The spatial covariant derivative compatible with the conformal metric is denoted by $\bar{D}_i$. Also, the conformal Laplacian is denoted by $\overline{\nabla}^2 \equiv \bar{\gamma}^{ij}\bar{D}_i\bar{D}_j$.

Beginning in Chapter 4, spatial hypersurfaces which are constructed from manifolds containing multiple "throats" or "holes" are considered. To indicate that a certain quantity is associated with a specific hole, a lower case Greek index will be used. This is not a tensor index and its position (up or down) is not significant. Tensor indices on these fields will be denoted using lower case Latin indices since the fields are purely spatial.

Chapter 1: Introduction

The most widely accepted theory of the dynamics of classical gravitational interactions is the theory of general relativity.* Proposed in 1916 by Albert Einstein, it forever changed our understanding of what gravity is and how it shapes our universe. The Newtonian view of gravity held it as a force which acted through space and affected the course of matter through time. General relativity, on the other hand, intimately links gravity with space and time by considering our universe as a four-dimensional, pseudo-Riemannian manifold in which curvature in the space-time metric *is* the manifestation of gravity.

Any theory of gravity is meant to describe the basic attractive interaction between massive objects. The most fundamental dynamical interaction in any theory of gravity, then, is that between two massive bodies. The two-body problem, from the point of view of Newtonian gravity, is well understood. One can easily specify the masses, initial positions, and initial velocities of two point particles and determine the time development of this initial configuration. The Newtonian equations of motion for two massive point particles are exactly solvable. The analogous problem in general relativity is not well understood.

The two-body problem of general relativity has been studied through many approximations. The most familiar general relativistic solution to the two-body problem is the prediction of the precession of the perihelion of an orbit. This is one example of an approximate solution which can be obtained by assuming the gravitational field is weak. The general formalisms for obtaining such solutions are known as the post-Newtonian and the post-Minkowskian approximation methods. The collision of two Schwarzschild black holes has been studied, analytically, in the limit that one hole is much smaller than the other so that it can be treated as a perturbation. There are certainly other approximation methods for studying the two-body problem, but to date there are no known exact or approximate analytic solutions to the problem of the strong field, relativistic interaction of two massive bodies. Currently, the only known avenue for the investigation of these very interesting situations is through the use of numerical techniques.

---

* Here, the term classical gravitation is meant to imply that in any problem to which general relativity is applied; the length, energy, and time scales are in the classical and not in the quantum regime.

An important consequence of the theory of general relativity is the production and propagation of gravitational waves from dynamic gravitational configurations. Violent astrophysical events, such as binary coalescence, will most likely be the strongest emitters of gravitational radiation. It is believed that the detection and study of gravitational waves from these events will play an important role in the understanding of such astrophysical phenomena. Because of this, a vigorous experimental and theoretical investigation of methods for detecting gravitational waves is under way, stemming from the early 1960s. The latest generation of detectors, known as Laser Interferometer Gravity Wave Observatories (LIGOs), should be sensitive enough to have a high probability of detecting gravitational waves. As of this writing, the National Science Foundation has included funding for the LIGOs in the budget for fiscal year 1991, with an estimated four-year expenditure of $192 million.

The numerical study of Einstein's equations has been under exploration since the early 1960s (Hahn and Lindquist [1964]), and has been vigorously pursued since the mid 1970s. To quote Thorne [1987], "The effort may absorb almost as many person-years as the development of gravitational-wave detectors; but it will be well worthwhile: the payoffs will include the ability to compute in detail the waveforms from the strongest gravity-wave sources in the universe, such as the spiraling together and coalescence of two black holes—waveforms that will be crucial to the interpretation of gravity-wave observations and to their use in strong-field, highly dynamical tests of general relativity."

Considering the statements above, I feel that the study of the fully relativistic, strong-field, two-body problem is of prime concern to the fields of classical general relativity and relativistic astrophysics. There are essentially two avenues for pursuing this problem. The first involves a study of the collision of two compact material objects such as neutron stars. Efforts in this line have been made by Evans [1986b], [1987]. The second avenue involves the purely geometrodynamic collision of two black holes. In this case, one of the pioneering numerical relativistic calculations was undertaken by Smarr [1977] in exploring the head-on collision of two black holes. In the first case, matter is present in quantities sufficient to produce strong gravitational fields. The matter fields evolve in a tightly coupled manner with the gravitational field and, given the proper initial conditions, produce a collision. A numerical calculation of this kind involves solving the full Einstein field equations and the relativistic hydrodynamic equations on a simply connected topology. In the case of a purely geometrodynamic collision, only the Einstein field equations need to be solved since the space-time is considered to contain no matter. On the other hand, to support the strong gravitational fields, we must use non-trivial topologies. With this second approach, the interaction of black holes can be modeled and it is the interaction of two black holes which is the closest relativistic analog of the Newtonian two-body problem for point masses.

The aim of this dissertation is to advance the understanding of the relativistic two-body problem for black holes. A great deal of theoretical and computational work has already been done toward this goal. Misner [1963], Lindquist [1963], and Brill and Lindquist [1963] found a set of analytic solutions to the initial-value equations of general relativity which represented any number of black holes initially at rest in a vacuum. Hahn and Lindquist [1964] and Čadež [1971] made early attempts to evolve this initial data numerically but met with little success. Besides the computational resources available, the major hindrance in these early calculations stemmed from a poor formal understanding of both the initial-value problem and the dynamics and kinematics of the Einsteinian evolution equations. York [1971], [1972], [1973a], [1979], Ó Murchada and York [1973], [1974a], [1974b], [1974c] and Smarr and York [1978a], [1978b] made many advances in the theoretical understanding of these problems and Smarr *et al.* [1976] and Smarr [1977] performed the first successful numerical simulation of black hole collisions. Smarr's calculations started with Misner's initial data for two black holes initially at rest and followed the holes as they fell into a head-on collision while emitting gravitational radiation.

In order to simulate more realistic and interesting situations, it is necessary to specify initial conditions which represent black holes with non-zero linear and angular momenta. York [1979], Bowen [1979b], and Bowen and York [1980] developed a formalism for specifying the initial data for a single black hole with non-zero linear and angular momenta. Many authors, (York and Piran [1982], Choptuik [1982], Rauber [1986], and Cook and York [1990]), have studied single-hole, axisymmetric initial-data sets using numerical methods based on this framework. The formalism employed for prescribing the initial data for a single hole was generalized to allow for multiple black holes by Kulkarni *et al.* [1983], York [1984], and Kulkarni [1984]. In principle, this method allows for the individual specification of linear and angular momenta for each hole permitting one, for example, to specify initial data for the spiralling coalescence of two black holes. Based on this formal approach, Bowen, Rauber, and York [1984] detailed an approach for specifying the initial data for two black holes with axisymmetric parallel spins. Rauber [1986] attempted to solve numerically for the data sets based on this approach but was unable to generate any complete solutions.

We call the collection of the formalisms and assumptions described in the papers listed above the *conformal imaging technique*. This approach is not unique and in fact Thornburg [1987] has found numerical solutions, based on an alternate set of assumptions, to the initial value equations for two black holes with axisymmetric linear and angular momenta. I feel, however, that the conformal imaging approach will be a more fruitful approach and proceed in this dissertation to describe and

examine solutions to the initial-value equations, based on the conformal imaging approach, which describe two black holes with axisymmetric linear and angular momenta.

In the chapters which follow, I begin by outlining the conformal imaging approach. This consists of the (3+1) decomposition of Einstein's equations, York's conformal decomposition of the constraint equations, and the choice of the topology of the initial-data slice along with the isometry condition imposed on this slice and its consequences for the initial-value equations. Next, I will discuss the analytic solutions to the momentum constraint equations for a single black hole, the formal extension to multiple black holes, and my algorithm for evaluating this formal solution. The following chapters will discuss the numerical techniques used, and the solutions found, for the case of a single black hole with linear or angular momentum and for two black holes with axisymmetric linear or angular momenta. One aspect of initial-data slices which has not been explored sufficiently is the existence and location of apparent horizons. I will proceed with a description of the consequences of the conformal imaging approach on the existence and location of these apparent horizons and detail their properties for the single black hole initial-data sets. Finally, I will conclude with some remarks on future work.

Chapter 2: The $(3+1)$ Decomposition

Einstein's equations in full covariant form are a set of coupled partial differential equations, the solution of which is a metric $g_{\mu\nu}$ that represents the full pseudo-Riemannian geometry of a space-time. This metric is not a dynamical object in that it does not change in time. On the contrary, the metric represents the geometry at all times just as the metric of a two-sphere represents the geometry of that two-sphere at all points on the sphere. In order for Einstein's equations to reveal their dynamical nature, we must break the full, four-dimensional covariance and exploit the special nature of time. One method of doing this is the (3+1) decomposition of Arnowitt, Deser, and Misner (ADM) [1962]. The idea behind the $(3+1)$ decomposition is to divide space-time into a sequence of "instants" of time. Each instant of time holds an "instantaneous state" of the gravitational field which dynamically evolves from instant to instant. Formally, the $(3+1)$ decomposition allows Einstein's equations to be posed as a Cauchy problem (*cf.* Choquet-Bruhat and York [1980]). In the remainder of this chapter, I will present the $(3+1)$ splitting of Einstein's equations based largely on York [1979], Bowen [1979b], and Evans [1984]. The Einstein equations will be split into constraint equations which are solved to give the initial data for a gravitational configuration on some initial slice, and evolution equations which describe the dynamics of general relativity and take the gravitational configuration from slice to slice.

Consider a 4-dimensional space with metric $g_{\mu\nu}$ having signature $(\epsilon+++)$, where $\epsilon = \pm$. (For generality, we consider both pseudo-Riemannian ($\epsilon = -$) and Riemannian ($\epsilon = +$) spaces. In this work, we will only be concerned with pseudo-Riemannian space-times, though it is useful to keep track of where the special nature of time affects the equations. Also, the generality is useful considering the importance of Euclidian methods in other areas of relativity.) The space is assumed to be globally hyperbolic ($\epsilon = -$ case) so that it can be foliated by a family of 3-dimensional hypersurfaces Σ that fills the space V. Let τ be a scalar function such that the level surfaces of τ are the hypersurfaces Σ. If the space can contain a foliation $\{\Sigma\}$, then the foliation can be described by a closed one-form $\underset{\sim}{\Omega} = \Omega_\mu \underset{\sim}{e}^\mu$ where

$$d\underset{\sim}{\Omega} = 0 \qquad \text{or} \qquad \nabla_{[\mu}\Omega_{\nu]} = 0 \tag{2.1}$$

and $\underset{\sim}{e}^{\mu}$ is a general basis of forms. Since Ω is closed, it must satisfy

$$\underset{\sim}{\Omega} = d\tau \qquad \text{or} \qquad \Omega_\mu = \nabla_\mu \tau. \tag{2.2}$$

The lapse function α defines the norm $\|\Omega\|$ by means of the space-time metric $g_{\mu\nu}$

$$\|\Omega\| = g^{\mu\nu}\Omega_\mu\Omega_\nu = g^{\mu\nu}\nabla_\mu\tau\nabla_\nu\tau = \epsilon\alpha^{-2}, \tag{2.3}$$

so the normalized one-form $\underset{\sim}{\omega}$ associated with $\{\Sigma\}$ is given by

$$\omega_\mu \equiv \alpha\Omega_\mu = \alpha\nabla_\mu\tau. \tag{2.4}$$

The minus sign for pseudo-Riemannian space-times and the strictly positive nature of α guarantee that the hypersurfaces defined by $\underset{\sim}{\omega}$ will be spacelike everywhere. The unit normal vector of a slice is given by

$$n^\nu = \epsilon g^{\mu\nu}\omega_\mu, \tag{2.5}$$

so that $n^\mu\omega_\mu = 1$ (and so that it is timelike $n_\mu n^\mu = -1$ for $\epsilon = -$).

The spatial metric $\gamma_{\mu\nu}$ induced by $g_{\mu\nu}$ onto a slice Σ is given by

$$\gamma_{\mu\nu} = g_{\mu\nu} - \epsilon n_\mu n_\nu = g_{\mu\nu} - \epsilon\omega_\mu\omega_\nu, \tag{2.6}$$

and the inverse spatial metric is given by

$$\gamma^{\mu\nu} = g^{\mu\alpha}g^{\nu\beta}\gamma_{\alpha\beta} = g^{\mu\nu} - \epsilon n^\mu n^\nu. \tag{2.7}$$

Each index on a tensor can be decomposed into two pieces, one which is purely spatial and lies entirely in the surface Σ and one which is entirely normal to the surface. The projection operator $\perp$, which projects free indices into the slice Σ, is defined as

$$\perp^\mu_\nu \equiv \gamma^\mu_\nu = \delta^\mu_\nu - \epsilon n^\mu n_\nu \qquad ; \qquad \perp^\mu_\nu n_\mu = 0. \tag{2.8}$$

Similarly, the projection operator N, which projects free indices normal to the slice, is defined as

$$N^\mu_\nu \equiv \epsilon n^\mu n_\nu = \delta^\mu_\nu - \perp^\mu_\nu \qquad ; \qquad N^\mu_\nu n_\mu = n_\nu. \tag{2.9}$$

Note that $\perp$ and N are idempotent projection operators since

$$\perp^\mu_\rho \perp^\rho_\nu = \perp^\mu_\nu \qquad \text{and} \qquad \perp^\mu_\mu = 3, \tag{2.10}$$

and

$$N^\mu_\rho N^\rho_\nu = N^\mu_\nu \qquad \text{and} \qquad N^\mu_\mu = 1. \tag{2.11}$$

Given the spatial metric on a hypersurface Σ, we can define a spatial covariant derivative D_μ which is compatible with the metric $\gamma_{\mu\nu}$ and which, acting upon spatial tensors, produces spatial tensors. This operator is defined by taking the full covariant derivative of a tensor and projecting all free indices into the hypersurface. Letting $\perp$ with no indices represent the product of n projection operators, one for each free index on the object upon which it is acting, then

$$\begin{aligned} D_\mu T^{\alpha\cdots\beta}{}_{\rho\cdots\sigma} &\equiv \perp \nabla_\mu T^{\alpha\cdots\beta}{}_{\rho\cdots\sigma} \\ &= \perp^\nu_\mu \perp^\alpha_\kappa \cdots \perp^\beta_\lambda \perp^\zeta_\rho \cdots \perp^\xi_\sigma \nabla_\nu T^{\kappa\cdots\lambda}{}_{\zeta\cdots\xi}. \end{aligned} \tag{2.12}$$

It is easily seen that the spatial covariant derivative is compatible with the spatial metric

$$D_\alpha \gamma_{\mu\nu} = \perp^\beta_\alpha \perp^\rho_\mu \perp^\sigma_\nu \nabla_\beta \left(g_{\rho\sigma} - \epsilon n_\rho n_\sigma\right) = 0. \tag{2.13}$$

The requirement that the spatial covariant derivative acts only on spatial tensors is required in order for Leibnitz's rule to hold.

$$\begin{aligned} D_\alpha \left(V^\mu W_\mu\right) &= \perp^\beta_\alpha \nabla_\beta \left(V^\mu W_\mu\right) \\ &= \perp^\beta_\alpha V^\mu \left(\perp^\rho_\mu + N^\rho_\mu\right) \nabla_\beta W_\rho + \perp^\beta_\alpha W_\mu \left(\perp^\mu_\rho + N^\mu_\rho\right) \nabla_\beta V^\rho \\ &= V^\mu D_\alpha W_\mu + W_\mu D_\alpha V^\mu + \perp^\beta_\alpha \left(V^\mu N^\rho_\mu \nabla_\beta W_\rho + W_\mu N^\mu_\rho \nabla_\beta V^\rho\right) \end{aligned} \tag{2.14}$$

which satisfies Leibnitz's rule only if V^μ and W_μ are purely spatial, i.e. $N^\rho_\mu V^\mu = 0$ and $N^\mu_\rho W_\mu = 0$.

A slice Σ has "intrinsic" curvature defined in the standard way by the commutation of covariant derivatives. If $N^\mu_\rho W_\mu = 0$, then

$$\left[D_\mu, D_\nu\right] W_\sigma = W_\rho \, {}^{(3)}R^\rho{}_{\sigma\nu\mu} \qquad \text{and} \qquad n_\rho \, {}^{(3)}R^\rho{}_{\sigma\nu\mu} = 0. \tag{2.15}$$

Here, ${}^{(3)}R^\rho{}_{\sigma\nu\mu}$ is the spatial Riemann tensor for the hypersurface Σ, as opposed to ${}^{(4)}R^\rho{}_{\sigma\nu\mu}$ which is the Riemann tensor for the full 4-dimensional space. Since Σ is an embedded hypersurface, the shape of the slice in the full space or the "extrinsic" curvature of the slice is also of interest. The extrinsic curvature of a hypersurface is related to the projection of the gradient of the surface normal vector field. This naturally consists of two parts: the symmetric part $\Theta_{\underline{\mu\nu}}$, known as the "strain", and the antisymmetric part $\omega_{\underset{\sim}{\mu\nu}}$, known as the "twist"

$$\Theta_{\underline{\mu\nu}} \equiv \perp \nabla_{(\mu} n_{\nu)} \qquad \text{and} \qquad \omega_{\underset{\sim}{\mu\nu}} \equiv \perp \nabla_{[\mu} n_{\nu]}. \tag{2.16}$$

Since the vector field n^μ is surface-forming by definition ($d\underset{\sim}{\Omega} = 0$), it is easy to show that

$$\omega \wedge d\omega = 0 \qquad \text{or} \qquad \omega_{[\mu} \nabla_\nu \omega_{\sigma]} = 0. \tag{2.17}$$

It follows immediately that $n_{[\mu}\nabla_\nu n_{\sigma]} = 0$. By contracting with n^μ and projecting the remaining free indices we find

$$\begin{aligned} \perp \left(n^\mu n_{[\mu}\nabla_\nu n_{\sigma]}\right) &= \frac{1}{3} \perp \left(-\nabla_{[\nu} n_{\sigma]} + \frac{1}{2} n^\mu \left(n_\sigma \nabla_{[\mu} n_{\nu]} - n_\nu \nabla_{[\mu} n_{\sigma]}\right)\right) \\ &= -\frac{1}{3} \perp \nabla_{[\nu} n_{\sigma]} = 0. \end{aligned} \tag{2.18}$$

And so the twist vanishes. The extrinsic curvature of the slice, $K_{\mu\nu}$, is defined as minus the strain

$$K_{\mu\nu} \equiv -\Theta_{\underline{\mu\nu}} = - \perp \nabla_{(\mu} n_{\nu)}. \tag{2.19}$$

Note that the choice of the minus sign is a convention. The extrinsic curvature can be expressed in a more convenient form by expanding the gradient of the unit normal

$$\begin{aligned} \nabla_\mu n_\nu = \delta^\alpha_\mu \delta^\beta_\nu \nabla_\alpha n_\beta &= \left(\perp^\alpha_\mu + \epsilon n^\alpha n_\mu\right) \left(\perp^\beta_\nu + \epsilon n^\beta n_\nu\right) \nabla_\alpha n_\beta \\ &= \perp \nabla_\mu n_\nu + \epsilon n_\mu \perp a_\nu \end{aligned} \tag{2.20}$$

where the acceleration of the unit normal, a_μ, has been used

$$a_\mu = n^\nu \nabla_\nu n_\mu. \tag{2.21}$$

Note that the acceleration is purely spatial since its contraction with the unit normal vanishes. This follows from the identity

$$\nabla_\mu \left(n_\nu n^\nu\right) = 2 n^\nu \nabla_\mu n_\nu = 0. \tag{2.22}$$

Since the acceleration is spatial, $\perp a^\mu = a^\mu$ and we find

$$\nabla_\mu n_\nu = -K_{\mu\nu} + \epsilon n_\mu a_\nu. \tag{2.23}$$

Since the extrinsic curvature is symmetric, we can express it as

$$K_{\mu\nu} = -\nabla_{(\mu} n_{\nu)} + \epsilon n_{(\mu} a_{\nu)} \tag{2.24}$$

from which it is easily seen that the extrinsic curvature is also purely spatial. From this and the definition of the Lie derivative, it follows that

$$\begin{aligned} K_{\mu\nu} &= \perp K_{\mu\nu} = \perp \left(-\nabla_{(\mu} n_{\nu)} + \epsilon n_{(\mu} a_{\nu)}\right) = - \perp \nabla_{(\mu} n_{\nu)} \\ &= -\frac{1}{2} \perp \pounds_{\mathbf{n}} g_{\mu\nu}. \end{aligned} \tag{2.25}$$

Alternatively, if we look at the Lie derivative of the spatial metric, we find

$$\begin{aligned} \pounds_{\mathbf{n}} \gamma_{\mu\nu} &= \pounds_{\mathbf{n}} \left(g_{\mu\nu} - \epsilon n_\mu n_\nu\right) \\ &= 2 \left(\nabla_{(\mu} n_{\nu)} - \epsilon n_{(\mu} a_{\nu)}\right) \\ &= -2 K_{\mu\nu}. \end{aligned} \tag{2.26}$$

Since the unit normal is a timelike vector, the Lie derivative, alone n^μ, of the spatial metric (and thus the extrinsic curvature) is related to the "velocity" of the spatial metric on the slice Σ.

Given a slice Σ in space-time, its complete geometry is described by its spatial metric and extrinsic curvature. Thus, the spatial metric and extrinsic curvature represent the "instantaneous state" of the gravitational field and are the dynamical quantities which will be followed to explore the evolution of a gravitational field. In order that a foliation of slices, $\{\Sigma\}$, can fit into the higher dimensional space, they must satisfy certain conditions known as the Gauss-Codazzi-Ricci conditions. These are obtained by taking all of the possible projections of the Riemann tensor of the full space. We can spatially project all of the indices of the Riemann tensor into the hypersurface, contract one index with the unit normal and spatially project the remaining three free indices, and finally we can contract two of the indices with unit normals and project the remaining two. All other combinations are identically zero by the symmetries of the Riemann tensor. To explore these, consider first

$$\begin{aligned} D_\mu D_\nu V_\rho =& \perp \nabla_\mu \left(\perp \nabla_\nu V_\rho \right) \\ =& \perp \nabla_\mu \nabla_\nu V_\rho + \perp \left(\nabla_\nu V_\sigma \right) \left(\nabla_\mu \perp^\sigma_\rho \right) + \perp \left(\nabla_\sigma V_\rho \right) \left(\nabla_\mu \perp^\sigma_\nu \right). \end{aligned} \tag{2.27}$$

If we now expand the gradient of the projection operator, we find

$$\nabla_\sigma \perp^\mu_\nu = \epsilon n_\nu K_\sigma{}^\mu - n_\nu n_\sigma a^\mu + \epsilon n^\mu K_{\sigma\nu} - n^\mu n_\sigma a_\nu. \tag{2.28}$$

Combining (2.27) and (2.28), we find

$$D_\mu D_\nu V_\rho = \perp \nabla_\mu \nabla_\nu V_\rho + \epsilon \perp K_{\mu\rho} K_\nu{}^\sigma V_\sigma + \epsilon \perp K_{\mu\nu} n^\sigma \nabla_\sigma V_\rho. \tag{2.29}$$

Then, using the definition of the Riemann tensor in terms of the commutation of covariant derivatives (2.15), we get

$$^{(3)}R_{\mu\nu\rho}{}^\sigma V_\sigma = \perp {}^{(4)}R_{\mu\nu\rho}{}^\sigma V_\sigma + \epsilon \perp K_{\mu\rho} K_\nu{}^\sigma V_\sigma - \epsilon \perp K_{\nu\rho} K_\mu{}^\sigma V_\sigma, \tag{2.30}$$

which gives us the form of the fully projected Riemann tensor known as Gauss' equation:

$$\perp {}^{(4)}R_{\mu\nu\rho\sigma} = {}^{(3)}R_{\mu\nu\rho\sigma} - \epsilon K_{\mu\rho} K_{\nu\sigma} + \epsilon K_{\mu\sigma} K_{\nu\rho}. \tag{2.31}$$

If we contract one index on the Riemann tensor with the unit normal and project the rest, we find

$$\perp {}^{(4)}R_{\mu\nu\rho}{}^\sigma n_\sigma = \perp \left(\nabla_\mu \nabla_\nu n_\rho - \nabla_\nu \nabla_\mu n_\rho \right). \tag{2.32}$$

To simplify this, consider one of the terms on the right-hand side.

$$\begin{aligned} \perp \nabla_\mu \nabla_\nu n_\rho =& \perp \nabla_\mu \left(-K_{\nu\rho} + \epsilon n_\nu a_\rho \right) = -D_\mu K_{\nu\rho} + \epsilon \perp \left(a_\rho \nabla_\mu n_\nu \right) \\ =& -D_\mu K_{\nu\rho} - \epsilon a_\rho K_{\mu\nu}. \end{aligned} \tag{2.33}$$

It follows, then, that the singly contracted, projected Riemann tensor gives

$$\perp {}^{(4)}R_{\mu\nu\rho}{}^{\sigma}n_{\sigma} = D_{\nu}K_{\mu\rho} - D_{\mu}K_{\nu\rho}, \tag{2.34}$$

which is known as Codazzi's equation.

Note that Gauss' and Codazzi's equations depend only on the spatial metric, extrinsic curvature, and their spatial derivatives. This implies that the Gauss-Codazzi equations represent integrability conditions which the spatial metric and extrinsic curvature must satisfy in order for any given slice to fit into the full space. These equations will be directly related to the constraints of general relativity. Finally, explicit calculation shows

$$\begin{aligned} \pounds_{\mathbf{n}}K_{\mu\nu} &= n^{\rho}\nabla_{\rho}K_{\mu\nu} + K_{\mu\rho}\nabla_{\nu}n^{\rho} + K_{\rho\nu}\nabla_{\mu}n^{\rho} \\ &= {}^{(4)}R_{\mu\rho\nu}{}^{\sigma}n^{\rho}n_{\sigma} - K_{\mu\rho}K_{\nu}{}^{\rho} + \epsilon K_{\mu\rho}n_{\nu}a^{\rho} - \nabla_{\mu}a_{\nu} + \epsilon a_{\mu}a_{\nu} + \epsilon n_{\mu}n^{\rho}\nabla_{\rho}a_{\nu}. \end{aligned} \tag{2.35}$$

Projecting this into the hypersurface yields

$$\perp {}^{(4)}R_{\mu\rho\nu}{}^{\sigma}n^{\rho}n_{\sigma} = \perp \pounds_{\mathbf{n}}K_{\mu\nu} + K_{\mu\rho}K_{\nu}{}^{\rho} - \epsilon a_{\mu}a_{\nu} + D_{\mu}a_{\nu}. \tag{2.36}$$

If we now consider

$$\begin{aligned} n^{\mu}\pounds_{\mathbf{n}}K_{\mu\nu} &= n^{\mu}n^{\rho}\nabla_{\rho}K_{\mu\nu} + n^{\mu}K_{\mu\rho}\nabla_{\nu}n^{\rho} + n^{\mu}K_{\rho\nu}\nabla_{\mu}n^{\rho} \\ &= -K_{\rho\nu}a^{\rho} + K_{\rho\nu}a^{\rho} = 0, \end{aligned} \tag{2.37}$$

we see that $\pounds_{\mathbf{n}}K_{\mu\nu}$ is purely spatial so we find that the twice contracted, projected Riemann tensor gives

$$\perp {}^{(4)}R_{\mu\rho\nu}{}^{\sigma}n^{\rho}n_{\sigma} = \pounds_{\mathbf{n}}\mathrm{K}_{\mu\nu} + K_{\mu\rho}K_{\nu}{}^{\rho} - \epsilon a_{\mu}a_{\nu} + D_{\mu}a_{\nu}, \tag{2.38}$$

which is known as Ricci's equation. Ricci's equation involves the Lie derivative along the normal vector field. This is, roughly speaking, a normal or time derivative. However, it should be noted that $\pounds_{\mathbf{n}}$ is not the natural time derivative orthogonal to the hypersurface. We want to take the Lie derivative along a vector field t^{μ} which is dual to the natural one-form associated with the hypersurface. The timelike vector field should satisfy

$$\Omega_{\mu}t^{\mu} = 1 \qquad \text{or} \qquad \langle \underset{\sim}{\Omega}, \overline{t} \rangle = 1. \tag{2.39}$$

From (2.4) and (2.5) we find that one such vector is

$$t^{\mu} = N^{\mu} \equiv \alpha n^{\mu}. \tag{2.40}$$

Of course, this is not a unique choice. We can add to N^μ any spatial vector, β^μ, since $\langle \underset{\sim}{\Omega}, \overline{\beta} \rangle = 0$. The freedom in the definition of the timelike vector stems from the general covariance of Einstein's equations. In general then, the timelike vector is defined as

$$t^\mu \equiv \alpha n^\mu + \beta^\mu, \tag{2.41}$$

and we find that

$$\begin{aligned} \pounds_{\mathbf{t}} K_{\mu\nu} &= \pounds_{\alpha \mathbf{n}} K_{\mu\nu} + \pounds_\beta K_{\mu\nu} \\ &= \alpha \pounds_{\mathbf{n}} K_{\mu\nu} + \pounds_\beta K_{\mu\nu}. \end{aligned} \tag{2.42}$$

As a final simplification of Ricci's equation, consider the acceleration a_μ,

$$\begin{aligned} a_\mu = n^\nu \nabla_\nu n_\mu &= 2 n^\nu \nabla_{[\nu} n_{\mu]} = \epsilon 2 n^\nu \nabla_{[\nu} \left(\alpha \Omega_{\mu]} \right) \\ &= \epsilon n^\nu \left(\Omega_\mu \nabla_\nu \alpha - \Omega_\nu \nabla_\mu \alpha \right) = -\epsilon \alpha^{-1} \left(\perp \nabla_\mu \alpha \right) \\ &= -\epsilon D_\mu \ln \alpha. \end{aligned} \tag{2.43}$$

Combining (2.38), (2.42), and (2.43) we find that Ricci's equation takes the form:

$$\perp {}^{(4)}R_{\mu\rho\nu}{}^\sigma n^\rho n_\sigma = \alpha^{-1} \pounds_{\mathbf{t}} K_{\mu\nu} + K_{\mu\rho} K_\nu{}^\rho - \epsilon \alpha^{-1} D_\mu D_\nu \alpha - \alpha^{-1} \pounds_\beta K_{\mu\nu}. \tag{2.44}$$

With the Gauss-Codazzi-Ricci equations, we can decompose the 4-dimensional Riemann tensor

$$\begin{aligned} {}^{(4)}R_{\mu\nu\rho\sigma} = &\perp {}^{(4)}R_{\mu\nu\rho\sigma} - \epsilon n_\mu \perp {}^{(4)}R_{\rho\sigma\nu\delta} n^\delta + \epsilon n_\nu \perp {}^{(4)}R_{\rho\sigma\mu\delta} n^\delta \\ &- \epsilon n_\rho \perp {}^{(4)}R_{\mu\nu\sigma\delta} n^\delta + \epsilon n_\sigma \perp {}^{(4)}R_{\mu\nu\rho\delta} n^\delta \\ &+ n_\mu n_\rho \perp {}^{(4)}R_{\nu\delta\sigma\gamma} n^\delta n^\gamma - n_\mu n_\sigma \perp {}^{(4)}R_{\nu\delta\rho\gamma} n^\delta n^\gamma \\ &+ n_\nu n_\sigma \perp {}^{(4)}R_{\mu\delta\rho\gamma} n^\delta n^\gamma - n_\nu n_\rho \perp {}^{(4)}R_{\mu\delta\sigma\gamma} n^\delta n^\gamma, \end{aligned} \tag{2.45}$$

into

$$\begin{aligned} {}^{(4)}R_{\mu\nu\rho\sigma} = &{}^{(3)}R_{\mu\nu\rho\sigma} - \epsilon K_{\mu\rho} K_{\nu\sigma} + \epsilon K_{\mu\sigma} K_{\nu\rho} \\ &+ \epsilon 2 n_\mu D_{[\rho} K_{\sigma]\nu} + \epsilon 2 n_\nu D_{[\sigma} K_{\rho]\mu} + \epsilon 2 n_\rho D_{[\mu} K_{\nu]\sigma} + \epsilon 2 n_\sigma D_{[\nu} K_{\mu]\rho} \\ &+ n_\mu n_\rho \left(\alpha^{-1} \pounds_{\mathbf{t}} K_{\nu\sigma} + K_{\nu\delta} K_\sigma{}^\delta - \epsilon \alpha^{-1} D_\nu D_\sigma \alpha - \alpha^{-1} \pounds_\beta K_{\nu\sigma} \right) \\ &- n_\nu n_\rho \left(\alpha^{-1} \pounds_{\mathbf{t}} K_{\mu\sigma} + K_{\mu\delta} K_\sigma{}^\delta - \epsilon \alpha^{-1} D_\mu D_\sigma \alpha - \alpha^{-1} \pounds_\beta K_{\mu\sigma} \right) \\ &+ n_\nu n_\sigma \left(\alpha^{-1} \pounds_{\mathbf{t}} K_{\mu\rho} + K_{\mu\delta} K_\rho{}^\delta - \epsilon \alpha^{-1} D_\mu D_\rho \alpha - \alpha^{-1} \pounds_\beta K_{\mu\rho} \right) \\ &- n_\mu n_\sigma \left(\alpha^{-1} \pounds_{\mathbf{t}} K_{\nu\rho} + K_{\nu\delta} K_\rho{}^\delta - \epsilon \alpha^{-1} D_\nu D_\rho \alpha - \alpha^{-1} \pounds_\beta K_{\nu\rho} \right). \end{aligned} \tag{2.46}$$

The Ricci tensor is defined by contracting the first and third indices on the Riemann tensor using the full metric. Since the spatial Riemann tensor is purely spatial, this is equivalent to contracting it with the spatial metric. This leads to

$$\begin{aligned} {}^{(4)}R_{\mu\nu} = &{}^{(3)}R_{\mu\nu} - \epsilon K K_{\mu\nu} + \epsilon 2 K_{\mu\rho} K_\nu{}^\rho + \epsilon \alpha^{-1} \pounds_{\mathbf{t}} K_{\mu\nu} - \alpha^{-1} D_\mu D_\nu \alpha \\ &- \epsilon \alpha^{-1} \pounds_\beta K_{\mu\nu} + \epsilon n_\mu \left(D_\nu K - D_\rho K_\nu{}^\rho \right) + \epsilon n_\nu \left(D_\mu K - D_\rho K_\mu{}^\rho \right) \\ &+ n_\mu n_\nu \left(\alpha^{-1} \pounds_{\mathbf{t}} K - K_\rho{}^\sigma K_\sigma{}^\rho - \epsilon \alpha^{-1} D^\rho D_\rho \alpha - \alpha^{-1} \pounds_\beta K \right), \end{aligned} \tag{2.47}$$

where the trace of the extrinsic curvature

$$K = g^{\mu\nu}K_{\mu\nu} = \gamma^{\mu\nu}K_{\mu\nu}. \tag{2.48}$$

has been used. Finally, the Ricci scalar is defined by tracing the Ricci tensor giving

$${}^{(4)}R = {}^{(3)}R - \epsilon K^2 - \epsilon K_\rho{}^\sigma K_\sigma{}^\rho + \epsilon 2\alpha^{-1}\pounds_{\mathbf{t}}K - 2\alpha^{-1}D^\rho D_\rho\alpha - \epsilon 2\alpha^{-1}\pounds_\beta K. \tag{2.49}$$

With these results, we can begin splitting Einstein's equations. In fully covariant form, Einstein's equations are written

$$G_{\mu\nu} = {}^{(4)}R_{\mu\nu} - \frac{1}{2}g_{\mu\nu}{}^{(4)}R = \kappa T_{\mu\nu}, \tag{2.50}$$

where $T_{\mu\nu}$ is the stress energy tensor of the sources and κ is the proportionality constant which, in gravitational units ($G = c = 1$), is $\kappa = 8\pi$. We can decompose the stress energy tensor as

$$T_{\mu\nu} = S_{\mu\nu} + 2n_{(\mu}j_{\nu)} + n_\mu n_\nu \rho, \tag{2.51}$$

where the spatial stress $S_{\mu\nu}$, momentum density j_μ, and energy density ρ are defined as

$$S_{\mu\nu} \equiv \perp T_{\mu\nu}, \tag{2.52}$$

$$j_\mu \equiv \epsilon \perp T_{\mu\nu}n^\nu, \tag{2.53}$$

and

$$\rho \equiv n^\mu n^\nu T_{\mu\nu}. \tag{2.54}$$

By tracing Einstein's equations and the decomposition of the stress energy tensor, we find that

$${}^{(4)}R = -\kappa T = -\kappa\left(S + \epsilon\rho\right), \tag{2.55}$$

where T is the trace of the stress energy tensor and S is the trace of the spatial stress tensor. Combining (2.50), (2.51), and (2.55) Einstein's equations take the form

$${}^{(4)}R_{\mu\nu} = \kappa\left(S_{\mu\nu} + 2n_{(\mu}j_{\nu)} - \frac{1}{2}\gamma_{\mu\nu}\left(S + \epsilon\rho\right) - \frac{1}{2}\epsilon n_\mu n_\nu\left(S - \epsilon\rho\right)\right). \tag{2.56}$$

The final step in splitting Einstein's equations is accomplished by taking all possible projections of (2.56). First, if we contract both indices with the unit normal, we find

$$\begin{aligned} {}^{(4)}R_{\mu\nu}n^\mu n^\nu &= \alpha^{-1}\pounds_{\mathbf{t}}K - K_\mu{}^\nu K_\nu{}^\mu - \epsilon\alpha^{-1}D^\mu D_\mu\alpha - \alpha^{-1}\pounds_\beta K \\ &= -\frac{\epsilon}{2}\left({}^{(3)}R - \epsilon K^2 + \epsilon K_\mu{}^\nu K_\nu{}^\mu + \kappa T\right) \\ &= -\frac{\epsilon\kappa}{2}\left(S - \epsilon\rho\right), \end{aligned} \tag{2.57}$$

where (2.49) and (2.55) have been used. Simplifying, this gives

$$ {}^{(3)}R - \epsilon K^2 + \epsilon K_\mu{}^\nu K_\nu{}^\mu = -\epsilon 2\kappa\rho. \tag{2.58} $$

By contracting one index with the unit normal and spatially projecting the other, we find

$$ \begin{aligned} \perp {}^{(4)}R_{\mu\nu} n^\nu &= D_\mu K - D_\nu K_\mu{}^\nu \\ &= \epsilon\kappa j_\mu, \end{aligned} \tag{2.59} $$

which can be expressed more conveniently as

$$ D_\nu \left(K^{\mu\nu} - \gamma^{\mu\nu} K \right) = -\epsilon\kappa j^\mu. \tag{2.60} $$

The final projection of the Einstein equation comes from spatially projecting both indices where we find

$$ \begin{aligned} \perp {}^{(4)}R_{\mu\nu} = {}^{(3)}R_{\mu\nu} &- \epsilon K K_{\mu\nu} + \epsilon 2 K_{\mu\rho} K_\nu{}^\rho + \epsilon\alpha^{-1} \pounds_{\mathbf{t}} K_{\mu\nu} \\ &- \alpha^{-1} D_\mu D_\nu \alpha - \epsilon\alpha^{-1} \pounds_\beta K_{\mu\nu} \\ = \kappa &\left(S_{\mu\nu} - \frac{1}{2}\gamma_{\mu\nu} \left(S + \epsilon\rho \right) \right), \end{aligned} \tag{2.61} $$

which can be rewritten as

$$ \begin{aligned} \pounds_{\mathbf{t}} K_{\mu\nu} = \epsilon D_\mu D_\nu \alpha &- \epsilon\alpha {}^{(3)}R_{\mu\nu} - 2\alpha K_{\mu\rho} K_\nu{}^\rho + \alpha K K_{\mu\nu} \\ &+ \pounds_\beta K_{\mu\nu} + \epsilon\alpha\kappa \left(S_{\mu\nu} - \frac{1}{2}\gamma_{\mu\nu} \left(S + \epsilon\rho \right) \right). \end{aligned} \tag{2.62} $$

Equations (2.58), (2.60), and (2.62) are the projections of Einstein's equations. Equations (2.58) and (2.60) contain no time derivatives and are, respectively, the Hamiltonian and momentum constraint equations. The spatial metric and extrinsic curvature must satisfy these equations on every slice in the foliation. Equation (2.62) describes the time evolution of the extrinsic curvature. Apparently missing from the decomposition of Einstein's equations is the equation describing the evolution of the spatial metric. This, however, is simply obtained from the definition of the extrinsic curvature (2.26), which gives us

$$ \pounds_{\mathbf{t}} \gamma_{\mu\nu} = -2\alpha K_{\mu\nu} + \pounds_\beta \gamma_{\mu\nu}. \tag{2.63} $$

To this point, the basis of vectors $\overline{e}_\mu$ and its dual basis, the basis of forms $\underset{\sim}{e}^\mu$ defined by

$$ \langle \underset{\sim}{e}^\mu, \overline{e}_\nu \rangle = \delta^\mu_\nu, \tag{2.64} $$

have been assumed to be completely general. To proceed, we will specialize the basis of vectors by splitting it into a purely spatial set of basis vectors plus a timelike basis vector which is orthogonal to the spatial basis. We choose the timelike basis vector to be the timelike vector t^μ:

$$ \overline{t} = t^\mu \overline{e}_\mu = \overline{e}_0. \tag{2.65} $$

The remaining three basis vectors are chosen to be purely spatial and must satisfy

$$\langle \underset{\sim}{\Omega}, \overline{e}_i \rangle = \Omega_\nu \langle \underset{\sim}{e}^\nu, \overline{e}_i \rangle = 0, \tag{2.66}$$

where $\{i = 1, 2, 3\}$ designates the three spatial basis vectors. The final demand is that the timelike basis vector must commute with the spatial basis vectors

$$\left[\overline{t}, \overline{e}_i\right] = \pounds_{\mathbf{t}} \overline{e}_i = 0. \tag{2.67}$$

If we now consider $\pounds_{\mathbf{t}} \langle \underset{\sim}{\Omega}, \overline{e}_i \rangle$ and use this last demand, we find

$$\begin{aligned} \pounds_{\mathbf{t}} \langle \underset{\sim}{\Omega}, \overline{e}_i \rangle &= \langle \pounds_{\mathbf{t}} \underset{\sim}{\Omega}, \overline{e}_i \rangle = (\pounds_{\mathbf{t}} \Omega_\nu) \langle \underset{\sim}{e}^\nu, \overline{e}_i \rangle \\ &= (t^\rho \nabla_\rho \Omega_\nu + \Omega_\rho \nabla_\nu t^\rho) \langle \underset{\sim}{e}^\nu, \overline{e}_i \rangle \\ &= 2 t^\rho \nabla_{[\rho} \Omega_{\nu]} \langle \underset{\sim}{e}^\nu, \overline{e}_i \rangle = 0, \end{aligned} \tag{2.68}$$

so the spatial basis vectors remain purely spatial as they are dragged along t^μ. Finally, because $\overline{e}_0$ is a coordinate basis vector (2.65) and since it commutes with the remaining basis vectors (2.67), we find that the effect of the Lie derivative along t^μ on *any* tensor is the action of partial differentiation,

$$\pounds_{\mathbf{t}} T^{\alpha \cdots \beta}{}_{\rho \cdots \sigma} = \partial_t T^{\alpha \cdots \beta}{}_{\rho \cdots \sigma}. \tag{2.69}$$

With this choice of the bases, we can examine the components of the important tensors. From (2.65) we find that the components of the timelike vector t^μ are

$$t^\mu = [\, 1 \quad 0 \quad 0 \quad 0 \,]. \tag{2.70}$$

Equation (2.66) requires

$$n_i = 0. \tag{2.71}$$

Since the contraction of n_μ with any contravariant index of a spatial tensor must vanish, this implies that any zeroth contravariant component of a spatial tensor must vanish. For example, the components of the shift vector must be

$$\beta^\mu = [\, 0 \quad \beta^i \,]. \tag{2.72}$$

Given the definition of the timelike vector (2.41), its components (2.70), and the components of the shift (2.72), we find that the components of the unit normal vector must be

$$n^\mu = [\, \alpha^{-1} \quad -\alpha^{-1} \beta^i \,]. \tag{2.73}$$

From (2.5) we have $n_\mu n^\mu = \epsilon$, combined with (2.71) and (2.73) these imply

$$n_\mu = [\,\epsilon\alpha \quad 0 \quad 0 \quad 0\,]. \tag{2.74}$$

Equation (2.71) also implies from the definition of the spatial metric (2.6) that the spatial components of the spatial metric are identically the spatial components of the full metric

$$\gamma_{ij} = g_{ij}. \tag{2.75}$$

Since any zeroth component of a contravariant tensor must vanish, we find that the components of the inverse spatial metric must be

$$\gamma^{\mu\nu} = \begin{bmatrix} 0 & 0 \\ 0 & \gamma^{ij} \end{bmatrix}, \tag{2.76}$$

and the components of the full inverse metric must be

$$g^{\mu\nu} = \begin{bmatrix} \epsilon\alpha^{-2} & -\epsilon\alpha^{-2}\beta^j \\ -\epsilon\alpha^{-2}\beta^i & \gamma^{ij} + \epsilon\alpha^{-2}\beta^i\beta^j \end{bmatrix}. \tag{2.77}$$

If we consider $\gamma^{\mu\rho}g_{\rho\nu} = (g^{\mu\rho} - \epsilon n^\mu n^\rho)g_{\rho\nu} = \delta^\mu_\nu - \epsilon n^\mu \delta^0_\nu$, use (2.75) and (2.76), and restrict to spatial indices, we find

$$\gamma^{ik}\gamma_{kj} = \delta^i_j. \tag{2.78}$$

This means that the spatial components of the metric and inverse metric are three-dimensional inverses and can be used to raise and lower spatial indices on spatial tensors. Using this property to define the spatial, covariant form of the shift vector, β_i, as

$$\beta_i = \gamma_{ij}\beta^j, \tag{2.79}$$

we find the components of the full metric to be

$$g_{\mu\nu} = \begin{bmatrix} \epsilon\alpha^2 + \beta_\ell\beta^\ell & \beta_j \\ \beta_i & \gamma_{ij} \end{bmatrix}, \tag{2.80}$$

and so the line element is

$$ds^2 = \gamma_{ij}\left(dx^i + \beta^i dt\right)\left(dx^j + \beta^j dt\right) + \epsilon\alpha^2 dt^2. \tag{2.81}$$

The entire content of the decomposed Einstein equations is now expressible as the spatial components of (2.58), (2.60), (2.62), and (2.63):

$$R - \epsilon K^2 + \epsilon K_{ij}K^{ij} = -\epsilon 2\kappa\rho, \tag{2.82}$$

$$D_j\left(K^{ij} - \gamma^{ij}K\right) = -\epsilon\kappa j^i, \tag{2.83}$$

$$\begin{aligned}\partial_t K_{ij} = \epsilon D_i D_j\alpha - \epsilon\alpha\left[R_{ij} + \epsilon 2K_{i\ell}K_j{}^\ell - \epsilon K K_{ij} - \kappa S_{ij} + \frac{1}{2}\kappa\gamma_{ij}\left(S + \epsilon\rho\right)\right], \\ + \beta^\ell D_\ell K_{ij} + K_{i\ell}D_j\beta^\ell + K_{\ell j}D_i\beta^\ell\end{aligned} \tag{2.84}$$

and

$$\partial_t\gamma_{ij} = -2\alpha K_{ij} + D_i\beta_j + D_j\beta_i, \tag{2.85}$$

where we have dropped the label on the Ricci tensor and Ricci scalar which distinguish them from their four-dimensional counterparts.

Chapter 3: The Conformal and Transverse-Traceless Decompositions

The Hamiltonian or scalar constraint equation, (2.82), and the momentum or vector constraint equation, (2.83), represent integrability conditions which the two fields γ_{ij} and K_{ij} and any matter fields must satisfy on a spacelike hypersurface Σ. These fields are the initial data which must be given to solve Einstein's equations as a Cauchy problem and, as a necessary condition, they must satisfy the constraints. Since Einstein's equations are dynamical, the constraints cannot restrict all of the components of the metric and extrinsic curvature. Since γ_{ij} and K_{ij} are symmetric, three-dimensional tensors, they each have six independent components. There are four constraint equations and so four of the 12 components are not independent. But which four? York has developed a method of breaking up the metric and extrinsic curvature into constrained and unconstrained pieces. This method involves the conformal decomposition of the initial data and relies on a certain decomposition of symmetric tensors (York [1972], [1973a], and [1979]).

For generality, I start by considering an n dimensional spacelike hypersurface Σ, and restrict n later to be three. To begin, we conformally relate the metric γ_{ij} to a conformal background metric $\bar{\gamma}_{ij}$ by

$$\gamma_{ij} \equiv \psi^{4/(n-2)}\bar{\gamma}_{ij} \qquad \text{and} \qquad \gamma^{ij} \equiv \psi^{-4/(n-2)}\bar{\gamma}^{ij}. \tag{3.1}$$

Here, to avoid confusion, I mark tensors in the conformal background space with an overbar. This relationship forces other relationships between certain quantities on the physical hypersurface and the background space. For example, from the definition of the connection,

$$\begin{aligned} \Gamma^{i}{}_{jk} &= \frac{1}{2}\gamma^{i\ell}\left(\gamma_{j\ell,k} + \gamma_{k\ell,j} - \gamma_{jk,\ell}\right) \\ &= \bar{\Gamma}^{i}{}_{jk} + \frac{2}{n-2}\psi^{-1}\left(\delta^{i}_{j}\overline{\nabla}_{k}\psi + \delta^{i}_{k}\overline{\nabla}_{j}\psi - \bar{\gamma}_{jk}\overline{\nabla}^{i}\psi\right), \end{aligned} \tag{3.2}$$

we define the change in the connection as

$$\delta\Gamma^{i}{}_{jk} \equiv \Gamma^{i}{}_{jk} - \bar{\Gamma}^{i}{}_{jk} = \frac{2}{n-2}\left(\delta^{i}_{j}\overline{\nabla}_{k}\ln\psi + \delta^{i}_{k}\overline{\nabla}_{j}\ln\psi - \bar{\gamma}_{jk}\bar{\gamma}^{i\ell}\overline{\nabla}_{\ell}\ln\psi\right), \tag{3.3}$$

where $\overline{\nabla}_{k}$ is the covariant derivative compatible with $\bar{\gamma}_{ij}$. If we consider the Riemann tensor

$$R_{ijk}{}^{\ell} = \Gamma^{\ell}{}_{ki,j} - \Gamma^{\ell}{}_{kj,i} + \Gamma^{m}{}_{ki}\Gamma^{\ell}{}_{mj} - \Gamma^{m}{}_{kj}\Gamma^{\ell}{}_{mi}, \tag{3.4}$$

we find

$$\delta R_{ijk}{}^{\ell} \equiv R_{ijk}{}^{\ell} - \bar{R}_{ijk}{}^{\ell} = \delta\Gamma^{\ell}{}_{ki,j} - \delta\Gamma^{\ell}{}_{kj,i} + \delta\Gamma^{m}{}_{ki}\delta\Gamma^{\ell}{}_{mj} - \delta\Gamma^{m}{}_{kj}\delta\Gamma^{\ell}{}_{mi}. \tag{3.5}$$

The change in the Ricci tensor is defined easily by

$$\begin{aligned}
\delta R_{ij} &\equiv R^{\ell}{}_{i\ell j} - \bar{R}^{\ell}{}_{i\ell j} = R_{i\ell j}{}^{\ell} - \bar{R}_{i\ell j}{}^{\ell} = \delta R_{i\ell j}{}^{\ell} \\
&= \delta\Gamma^{\ell}{}_{ij;\ell} - \delta\Gamma^{\ell}{}_{j\ell;i} + \delta\Gamma^{m}{}_{ji}\delta\Gamma^{\ell}{}_{\ell m} - \delta\Gamma^{m}{}_{\ell i}\delta\Gamma^{\ell}{}_{jm} \\
&= \frac{2}{n-2}\left[(2-n)\,\overline{\nabla}_i\overline{\nabla}_j \ln\psi - \bar{\gamma}_{ij}\bar{\gamma}^{\ell m}\overline{\nabla}_\ell\overline{\nabla}_m \ln\psi\right] \\
&\quad + \frac{4}{n-2}\left[\left(\overline{\nabla}_i \ln\psi\right)\overline{\nabla}_j \ln\psi - \bar{\gamma}_{ij}\bar{\gamma}^{\ell m}\left(\overline{\nabla}_\ell \ln\psi\right)\overline{\nabla}_m \ln\psi\right].
\end{aligned} \tag{3.6}$$

Finally, if we consider the effect on the Ricci scalar, we find

$$\begin{aligned}
R &= \gamma^{ij}R_{ij} = \psi^{-4/(n-2)}\bar{\gamma}^{ij}R_{ij} \\
&= \psi^{-4/(n-2)}\bar{R} - \frac{4\,(n-1)}{n-2}\psi^{-(n+2)/(n-2)}\overline{\nabla}^2\psi.
\end{aligned} \tag{3.7}$$

With these relations, we can consider a conformal decomposition of the constraint equations of Einstein's theory. Here, we will take $n = 3$ and the covariant derivative compatible with $\bar{\gamma}_{ij}$ is $\bar{D}_i$. We also specify conformal transformations for the extrinsic curvature, the energy density, and the momentum density. The trace and trace-free parts of the extrinsic curvature are considered separately so

$$K^{ij} = A^{ij} + \frac{1}{3}\gamma^{ij}K. \tag{3.8}$$

For now, we assign the following arbitrary weights to the conformal transformations. Values for these will be determined later:

$$A^{ij} \equiv \psi^{\alpha}\bar{A}^{ij} \qquad \text{or} \qquad A_{ij} = \psi^{\alpha+8}\bar{A}_{ij}, \tag{3.9}$$

$$K \equiv \psi^{\beta}\bar{K}, \tag{3.10}$$

$$\rho \equiv \psi^{\gamma}\bar{\rho}, \tag{3.11}$$

and

$$j^i \equiv \psi^{\delta}\bar{j}^i. \tag{3.12}$$

The Hamiltonian constraint, (2.82), becomes

$$8\overline{\nabla}^2\psi - \psi\bar{R} + \epsilon\frac{2}{3}\psi^{2\beta+5}\bar{K}^2 - \epsilon\psi^{2\alpha+13}\bar{A}_{ij}\bar{A}^{ij} = \epsilon 2\kappa\psi^{\gamma+5}\bar{\rho}. \tag{3.13}$$

The momentum constraint equation, (2.83), takes the form

$$D_j\left(A^{ij} - \frac{2}{3}\gamma^{ij}K\right) = -\epsilon\kappa j^i. \tag{3.14}$$

If we consider the first term on the left-hand side, we find that for any symmetric, traceless tensor A^{ij} which transforms as (3.9),

$$D_j A^{ij} = \psi^{-10} \bar{D}_j \left(\psi^{10+\alpha} \bar{A}^{ij} \right). \tag{3.15}$$

Thus, if we choose $\alpha = -10$, we see that

$$D_j A^{ij} = \psi^{-10} \bar{D}_j \bar{A}^{ij}, \tag{3.16}$$

and if $\bar{A}^{ij}$ is divergenceless, then A^{ij} will be as well. With (3.16), the momentum constraint becomes

$$\psi^{-10} \bar{D}_j \bar{A}^{ij} - \frac{2}{3} \psi^{\beta-4} \bar{\gamma}^{ij} \bar{D}_j \bar{K} - \frac{2}{3} \beta \psi^{\beta-5} \bar{K} \bar{\gamma}^{ij} \bar{D}_j \psi = -\epsilon \kappa \psi^{\delta} \bar{j}^i. \tag{3.17}$$

If we choose $\beta = 0$ so that the trace of the extrinsic curvature has no conformal scaling and choose $\delta = -10$, then the momentum constraint simplifies to

$$\bar{D}_j \bar{A}^{ij} - \frac{2}{3} \psi^6 \bar{\gamma}^{ij} \bar{D}_j K = -\epsilon \kappa \bar{j}^i. \tag{3.18}$$

The conformal relations of all quantities have now been defined except for those of ρ. At this point, the Hamiltonian constraint takes the form

$$8 \overline{\nabla}^2 \psi - \psi \bar{R} + \epsilon \frac{2}{3} \psi^5 K^2 - \epsilon \psi^{-7} \bar{A}_{ij} \bar{A}^{ij} = \epsilon 2 \kappa \psi^{\gamma+5} \bar{\rho}. \tag{3.19}$$

A simplifying choice for γ would be $\gamma = -5$. However, this choice does not lead to a well posed problem for the linearized Hamiltonian constraint on asymptotically flat hypersurfaces (*cf.* York [1979]). This would require $\gamma < -5$. A good choice for γ can be found by demanding that the dominance of energy condition be maintained locally. This requires that

$$\rho^2 - \gamma_{ij} j^i j^j = \psi^{-16} \left(\psi^{2\gamma+16} \bar{\rho}^2 - \bar{\gamma}_{ij} \bar{j}^i \bar{j}^j \right) \geq 0, \tag{3.20}$$

and we take $\gamma = -8$. The Hamiltonian constraint now takes the form

$$8 \overline{\nabla}^2 \psi - \psi \bar{R} + \epsilon \frac{2}{3} \psi^5 K^2 - \epsilon \psi^{-7} \bar{A}_{ij} \bar{A}^{ij} = \epsilon 2 \kappa \psi^{-3} \bar{\rho}. \tag{3.21}$$

The final step which may be taken in simplifying the constraints is to note that in the momentum constraint, $\bar{A}^{ij}$ only occurs in a divergence term so that the transverse part of $\bar{A}^{ij}$ is not restricted by the equations. Thus, we may split the tensor into its transverse and longitudinal parts. Recalling that $\bar{A}^{ij}$ is traceless, the longitudinal part of $\bar{A}^{ij}$ is defined as the symmetric, traceless gradient of a vector "potential" W^i:

$$\bar{A}^{ij}_{L} = \bar{D}^i W^j + \bar{D}^j W^i - \frac{2}{3} \bar{\gamma}^{ij} \bar{D}_k W^k \equiv (LW)^{ij}. \tag{3.22}$$

We then find

$$\bar{A}^{ij} = \bar{A}^{ij}_{TT} + (LW)^{ij}, \tag{3.23}$$

where $\bar{A}^{ij}_{TT}$ is the transverse traceless part of $\bar{A}^{ij}$ and satisfies

$$\bar{D}_j \bar{A}^{ij}_{TT} = 0. \tag{3.24}$$

The divergence of the traceless part of the extrinsic curvature then reduces to

$$\begin{aligned} \bar{D}_j \bar{A}^{ij} = \bar{D}_j (LW)^{ij} &= \bar{D}_j \bar{D}^j W^i + \frac{1}{3} \bar{D}^i \left(\bar{D}_j W^j \right) + \bar{R}_j{}^i W^j \\ &\equiv (\Delta_L W)^i, \end{aligned} \tag{3.25}$$

and the momentum constraint is

$$(\Delta_L W)^i - \frac{2}{3} \psi^6 \bar{\gamma}^{ij} \bar{D}_j K = -\epsilon \kappa \bar{\jmath}^i. \tag{3.26}$$

While the background field $\bar{A}^{ij}$ is naturally split into its transverse and longitudinal parts, it should be noted that the split in the physical field is not so distinct. Equation (3.16) guarantees that the transversality of $\bar{A}^{ij}_{TT}$ is preserved under the conformal transformation to the physical space. However, York [1973b] has shown that the "longitudinal" part of A^{ij}, given by

$$A^{ij}_L = \psi^{-10} (LW)^{ij}, \tag{3.27}$$

is not orthogonal to $\psi^{-10} \bar{A}^{ij}_{TT}$ (*cf.* Evans [1984]) and so $\bar{A}^{ij}_L$ is *not*, in general, purely longitudinal.

The constraint equations (3.21) and (3.26) determine the conformal factor ψ and the vector potential W^i. We are free to choose the remaining parts of the gravitational initial data in any way we like. Specifically, the conformal background metric $\bar{\gamma}_{ij}$, the trace of the extrinsic curvature K, and the transverse-traceless part of the background extrinsic curvature $\bar{A}^{ij}_{TT}$ are all freely specifiable fields, as are the background sources $\bar{\rho}$ and $\bar{\jmath}^i$. In fact, these *must* be specified before the constraint equations can be solved.

If we recall that γ_{ij} has six independent components and use the Hamiltonian constraint to fix the conformal factor ψ, then the background metric $\bar{\gamma}_{ij}$ must have five independent components. These are not, however, all dynamical degrees of freedom. We must remember that there is coordinate freedom within the hypersurface Σ and this eliminates three of the remaining five independent components from being dynamical degrees of freedom. This tells us that the equivalence class of conformal three-geometries represents the two freely specifiable, dynamical degrees of freedom of the metric γ_{ij}. Similarly, with the extrinsic curvature, the momentum constraint governs three of the six independent components of K^{ij}. Remaining are the transverse-traceless part, $\bar{A}^{ij}_{TT}$, with two degrees of freedom and the trace, K, with one. The trace of the extrinsic curvature is taken as a condition on the time coordinate and is not considered as a dynamical degree of freedom. Thus, the two freely specifiable, dynamical degrees of freedom of the extrinsic curvature are carried by its transverse-traceless parts.

Chapter 4: The Conformal Imaging Approach

The *conformal imaging approach* encompasses the $(3+1)$ and conformal decomposition techniques described in the previous chapters, along with a set of assumptions for choosing the freely specifiable data and the topology of the initial slice, taken in order to calculate initial-data sets which represent one or more black holes in an astrophysical setting. The $(3+1)$ decomposition of Einstein's equations and York's conformal decomposition of the constraints provide a foundation for specifying initial-data sets for a wide range of problems of astrophysical interest. If we restrict ourselves to considering only four-dimensional, pseudo-Riemannian space-times foliated by spacelike hypersurfaces, then the Hamiltonian and momentum constraints can be expressed respectively as:

$$8\overline{\nabla}^2\psi - \psi\bar{R} - \frac{2}{3}\psi^5 K^2 + \psi^{-7}\bar{A}_{ij}\bar{A}^{ij} = -2\kappa\psi^{-3}\bar{\rho}, \tag{4.1}$$

and

$$\bar{D}_j\bar{A}^{ij} - \frac{2}{3}\psi^6\bar{\gamma}^{ij}\bar{D}_j K = \kappa\bar{j}^i \tag{4.2a}$$

or

$$(\Delta_L W)^i - \frac{2}{3}\psi^6\bar{\gamma}^{ij}\bar{D}_j K = \kappa\bar{j}^i. \tag{4.2b}$$

Note that (4.2b) is the most restricted form of the momentum constraint, however, we will also have use for the form given in (4.2a).

In order to solve the constraints for ψ and W^i, we must *first* specify the unconstrained portions of the initial data. We must choose first the conformal *background* metric $\bar{\gamma}_{ij}$. Given this background metric, we must choose the transverse-traceless part of the *background* extrinsic curvature so as to satisfy (3.24). Next, we must choose the trace of the extrinsic curvature in the physical space. Finally, we must choose values for the *background* sources $\bar{\rho}$ and $\bar{j}^i$.

While these choices determine all of the freely specifiable fields present in an initial-data set, there is one other choice which must be made. This final choice is the prescription of the topology of the initial-data slice. Einstein's equations in no way determine the topology of the initial manifold. It can be chosen, for example, to be closed, if one is interested in cosmological models. Alternately, it can be chosen to be unbounded and, perhaps, asymptotically flat. In any case, the manifold

can be simply connected or multiply connected. These are just some of the possible choices and the physical consequences of these choices can be fully determined only after initial data has been constructed.

In order to represent astrophysical situations, the first assumption is that the initial slice is asymptotically flat. Since we want to investigate black holes, we choose that there be no matter sources, so

$$\bar{\rho} = 0 \tag{4.3}$$

and

$$\bar{j}^i = 0. \tag{4.4}$$

We also demand that the trace of the extrinsic curvature vanish on the initial slice, so

$$K = 0. \tag{4.5}$$

This condition implies that the hypersurface is maximally embedded in the full space-time (*cf.* York and Piran [1982]) and decouples the momentum constraint from the Hamiltonian constraint. The final assumptions on the data are that the hypersurface be conformally flat and that the transverse-traceless part of the background extrinsic curvature vanish. The first assumption means we choose the conformal background metric to be a flat metric

$$\bar{\gamma}_{ij} = f_{ij}. \tag{4.6}$$

The second assumption is

$$\bar{A}^{ij}_{TT} = 0, \tag{4.7}$$

and it should be noted here that assumption (4.7) will be relaxed when multiple black holes are considered. These last two choices affect the gravitational wave content of the initial-data slice. We recognize this from the fact that the conformal three-geometry and the transverse-traceless part of the extrinsic curvature represent the dynamical degrees of freedom of the gravitational field. In the case of a single Schwarzschild black hole, initial data can be chosen on an asymptotically and conformally flat, maximally embedded initial slice. In this case, the full extrinsic curvature vanishes and the initial slice contains no gravitational waves. However, in general, if the configuration is not static, there will be gravitational radiation present in initial slices constructed with (4.6) and (4.7). More will be said about this later.

Given these assumptions, the constraint equations now take the following form:

$$\overline{\nabla}^2 \psi = -\frac{1}{8}\psi^{-7}\bar{A}_{ij}\bar{A}^{ij}, \tag{4.8}$$

and

$$\bar{D}_j \bar{A}^{ij} = 0, \tag{4.9a}$$

or

$$(\Delta_L W)^i = 0. \tag{4.9b}$$

Note that the full trace-free background extrinsic curvature $\bar{A}_{ij}$ is used in (4.8) and (4.9a) instead of just the longitudinal part. This is a reflection of the earlier comment on relaxing condition (4.7).

The only assumptions left to be made are those which fix the topology of the initial slice. Assume first that the topology is taken to be a simply connected, Euclidean E^3 topology. Asymptotic flatness implies (York [1979]) that

$$\psi = 1 + \mathcal{O}(r^{-1}) \tag{4.10}$$

and

$$\bar{K}^i{}_j = \mathcal{O}(r^{-2}). \tag{4.11}$$

Since there are no sources to support a non-trivial solution, the only regular solution to Einstein's equations is empty, flat space, so there is no gravitational field. In order to represent black holes (and therefore strong gravitational fields) in vacuum, non-trivial topologies must be used. The simplest example of this comes from the Schwarzschild solution. If we choose a $t = constant$ slice of the Schwarzschild solution in isotropic coordinates, the metric and extrinsic curvature on the slice are

$$\gamma_{ij} = \left(1 + \frac{\kappa M}{16\pi r}\right)^4 f_{ij} \tag{4.12}$$

and

$$K_{ij} = 0. \tag{4.13}$$

This slice is asymptotically and conformally flat and maximally embedded in the full space-time. The conformal factor is

$$\psi = 1 + \frac{\kappa M}{16\pi r}, \tag{4.14}$$

and it is singular at $r = 0$. In order for the manifold to be regular, the origin is cut out and the manifold becomes "non-contractable".

It appears at first that this geometry simply represents a single asymptotically flat hypersurface with the origin removed. This situation would not represent a complete manifold. Consider, however, the line element of (4.12) using spherical coordinates,

$$ds^2 = \left(1 + \frac{\kappa M}{16\pi r}\right)^4 \left(dr^2 + r^2 d\Omega^2\right), \tag{4.15}$$

and then change to a new radial coordinate

$$r' = \left(\frac{\kappa M}{16\pi}\right)^2 \frac{1}{r}. \tag{4.16}$$

(Note that $r = r' = \kappa M/16\pi$ is a fixed point set in this transformation and coincides with the location of the Schwarzschild event horizon.) In terms of this new coordinate the line element becomes

$$ds^2 = \left(1 + \frac{\kappa M}{16\pi r'}\right)^4 \left(dr'^2 + r'^2 d\Omega^2\right), \tag{4.17}$$

which is identical to (4.15) except that it is in terms of the new radial coordinate r'. We see now that the initial slice is asymptotically flat as $r' \to \infty$ in just the same way that it is asymptotically flat as $r \to \infty$. $r' \to \infty$ is, of course, the same as $r \to 0$ and it can now be seen that the geometry of (4.12) is actually that of *two* asymptotically flat spaces joined at the spherical surface $r = r' = \kappa M/16\pi$ (see Figure 4.1), and this implies that the manifold is complete.

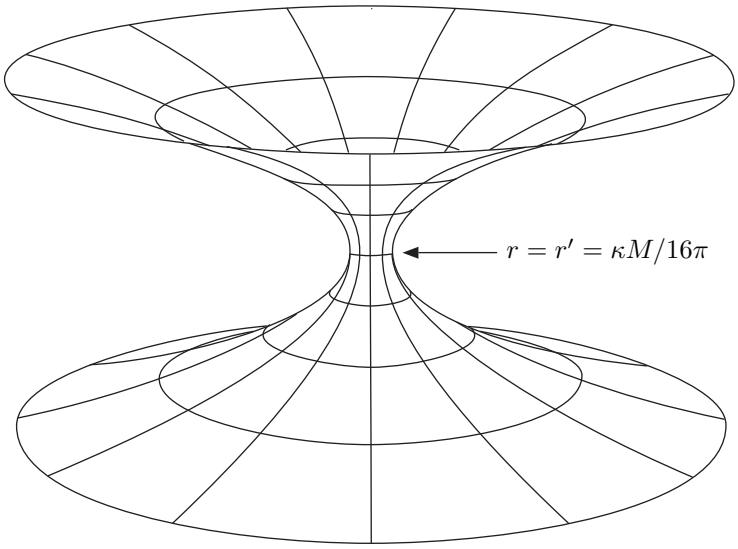


Figure 4.1: Embedding diagram of time-symmetric, maximal slice of Schwarzschild geometry in isotropic coordinates.

These two asymptotically flat spaces are often referred to as the "top" and "bottom" sheets of the manifold and the region connecting them is known as an Einstein-Rosen bridge (Einstein and Rosen [1935]). The region interior to the event horizon on the top sheet, $r < \kappa M/16\pi$, is not the interior of the black hole, but is an identical "second" or "alternate" universe. This can be seen most easily by plotting the initial slice in the familiar Kruskal coordinates (Figure 4.2).

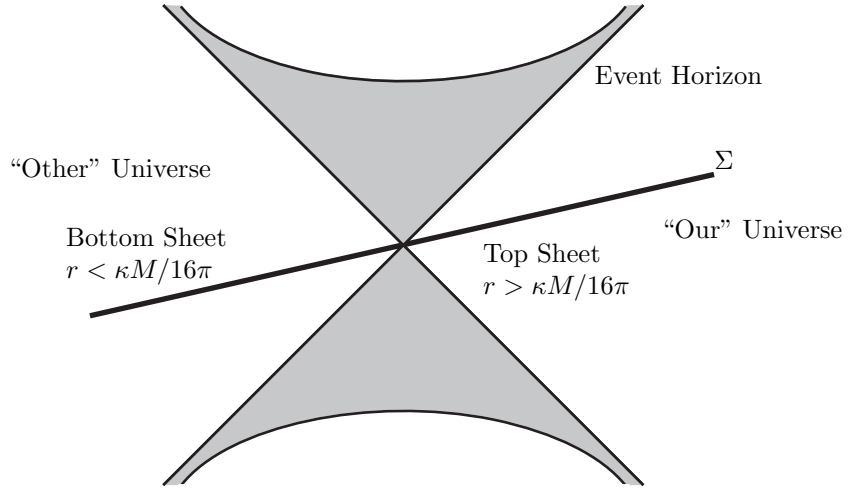


Figure 4.2: Time-symmetric, maximal slice of Kruskal space-time, labeled in isotropic coordinates and showing "top" and "bottom" sheets in the two different universes.

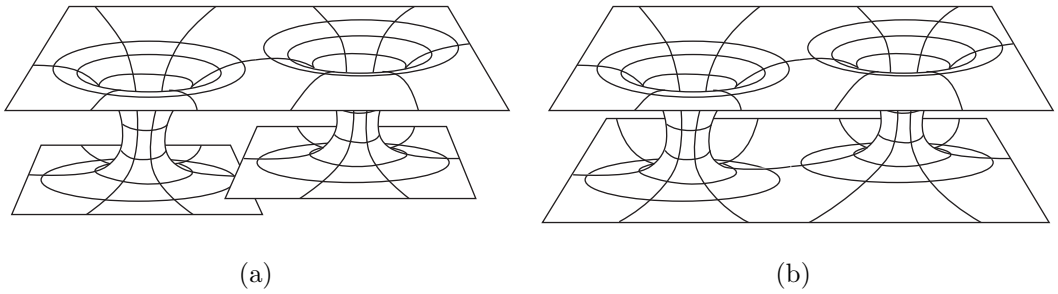
This example illustrates the main principle followed in constructing vacuum, black-hole initial-data sets: we use multiple asymptotically flat sheets connected by Einstein-Rosen bridges. In doing this, two criteria must be satisfied in the resulting initial-data sets. The first is regularity and the second is completeness of the manifold (*cf.* Brill and Lindquist [1963]).

If we want to represent more than one black hole on the initial slice, then there are essentially two avenues which can be taken in choosing the topology of the initial slice. Let us assume that there are to be N black holes in our "universe". One approach for modeling this is to allow each of the holes to connect to its own isolated, asymptotically flat universe through an Einstein-Rosen bridge. This produces an $N+1$ sheeted manifold (Figure 4.3a). The second approach is to allow all N holes to connect to the *same* alternate, asymptotically flat universe through N Einstein-Rosen bridges. This produces a multiply-connected, two-sheeted manifold (Figure 4.3b).

Analytic solutions to the initial-value equations on both topologies have been found which represent multiple black holes at a moment of time symmetry (Misner [1963], Lindquist [1963], and Brill and Lindquist [1963]). If all of the holes are momentarily at rest, then the extrinsic curvature vanishes everywhere on the initial slice and the Hamiltonian constraint (4.8) reduces to Laplace's equation. A solution representing N black holes is

$$\psi = 1 + \sum_{\alpha=1}^{N} \frac{\mu_\alpha}{|\mathbf{x} - \mathbf{C}_\alpha|}, \tag{4.18}$$

where μ_α are constants related to the masses of the holes and the points $\mathbf{C}_\alpha$ are the positions of the centers of the holes in the background space. The points $\mathbf{C}_\alpha$ are deleted from the manifold so that



(a) (b)

Figure 4.3: Initial slice topologies for two black holes.
a) Topology of an $N+1$ sheeted manifold.
b) Topology of a two-sheeted manifold.

it is regular, and if they are sufficiently far apart, then each corresponds to asymptotic infinity on a connecting sheet, as in Figure 4.3a, so the manifold is complete. In order to produce a two-sheeted solution, as in Figure 4.3b, Misner [1963] demanded that the top and bottom sheets be identical. Enforcing this required the addition of an infinite number of poles to (4.18) with the weights and locations of the poles determined by the method of spherical-inversion imaging from electrostatics. Misner showed that the infinite series converges to an analytic function and is a solution to Laplace's equation so long as the holes are not too close to each other.

In order to construct initial data which represents more physically interesting situations, it is necessary to consider cases which are not time-symmetric and, so, have non-vanishing extrinsic curvature. This requires solving both the Hamiltonian constraint (4.8) and the momentum constraint (4.9) on one of the two topologies discussed above. Analytically, the $N+1$ sheeted topology offers a simpler approach since solutions to the constraints naturally produce this topology with no additional effort. Construction of initial data on the two-sheeted manifold requires that the initial data satisfy an isometry condition which enforces Misner's requirement that the two sheets be identical. On the other hand, we note that in general the Hamiltonian constraint (4.8) is a quasi-linear, elliptic, differential equation and it will be necessary, in most cases, to solve it numerically. From this point of view, we find that constructing initial data on an $N+1$ sheeted topology will require numerical solutions on all $N+1$ asymptotically flat sheets. The two-sheeted topology requires solution on only one sheet since the other is identical. Thus, the two-sheeted manifold proves to be computationally more convenient.

Thornburg [1987] has argued for the use of $N+1$ sheeted manifolds by suggesting that the Hamiltonian constraint be solved only on the top sheet. He argues that the apparent horizons, which are present around the black holes, form a natural boundary for the region in which the

Hamiltonian constraint must be solved. Doing this, however, ignores the remainder of the initial-data slice. While information can never cross the apparent horizons into the top sheet during the time evolution, this does not preclude the existence of global structures which can be located only by knowing the initial data on the complete manifold as I will show later (*cf.* Cook and York [1990]).

The final assumption of the conformal imaging approach is to assume that the initial-data manifold has a two-sheeted topology and that the sheets are related by an isometry which requires the two sheets, and any fields on them, to be identical. The approach, for the case of a single hole, was detailed by Bowen [1979b] and Bowen and York [1980]. The extension for multiple holes was carried out by Kulkarni, Shepley, and York [1983]. In the remainder of this chapter, I will outline the approach, closely following Kulkarni *et al.* [1983].

Let M_N denote the two-sheeted manifold containing N Einstein-Rosen bridges, each representing a single black hole. To construct the manifold, take two identical, three-dimensional Euclidean spaces E^3 with N non-intersecting spheres, located at $\mathbf{C}_\alpha$ and with radii a_α ($\alpha = 1, \ldots, N$), removed. The two spaces will represent the top and bottom sheets of M_N and will be labeled, respectively, by Y and Z. If $\mathbf{p} = (p^1, p^2, p^3)$ represents a point in either sheet, then the sheets are defined by

$$Y = Z \equiv \left\{ \mathbf{p} \in E^3 : |\mathbf{p} - \mathbf{C}_\alpha| > a_\alpha, \alpha = 1, \ldots, N \right\}. \tag{4.19}$$

The collection of boundaries B is defined as

$$B \equiv \bigcup_{\alpha=1}^{N} B_\alpha \qquad \text{where} \qquad B_\alpha \equiv \left\{ \mathbf{p} \in E^3 : |\mathbf{p} - \mathbf{C}_\alpha| = a_\alpha \right\}. \tag{4.20}$$

Let the union of the top sheet and the boundary be $\bar{Y} \equiv Y \cup B$, and similarly $\bar{Z} \equiv Z \cup B$. The manifold M_N is now defined as $M_N \equiv \bar{Y} \cup \bar{Z}$, with the boundaries B_α (each representing a throat or bridge) identified. To put coordinates on the manifold, we define a collection of coordinate maps Ψ_α on M_N, each covering Y and Z through the α^{th} throat. Let $\mathbf{x}$ denote the range of points in E^3 covered by the maps and define

$$X \equiv \left\{ \mathbf{x} \in E^3 : |\mathbf{x} - \mathbf{C}_\alpha| > a_\alpha, \alpha = 1, \ldots, N \right\} \tag{4.21}$$

and

$$S_\alpha \equiv \left\{ \mathbf{x} \in E^3 : |\mathbf{x} - \mathbf{C}_\alpha| = a_\alpha \right\}. \tag{4.22}$$

We can now define the maps $\mathbf{J}_\alpha$ which identify the two sheets through each of the throats

$$\mathbf{J}_\alpha : E^3 - \{a_\alpha\} \to E^3 - \{a_\alpha\} \tag{4.23}$$

by

$$\mathbf{J}_\alpha(\mathbf{x}) \equiv \left(\frac{a_\alpha^2}{r_\alpha}\right)\mathbf{n}_\alpha + \mathbf{C}_\alpha, \tag{4.24}$$

where

$$r_\alpha = |\mathbf{x} - \mathbf{C}_\alpha| \tag{4.25}$$

and

$$\mathbf{n}_\alpha = \frac{(\mathbf{x} - \mathbf{C}_\alpha)}{r_\alpha}. \tag{4.26}$$

We now define the α^{th} image of X as

$$I_\alpha = \mathbf{J}_\alpha[\mathbf{X}], \tag{4.27}$$

and the α^{th} coordinate map as

$$\Psi_\alpha : (Y \cup B_\alpha \cup Z) \to (X \cup S_\alpha \cup I_\alpha), \tag{4.28}$$

where

$$\Psi_\alpha(\mathbf{p}) = \begin{cases} (p^1, p^2, p^3) \in (X \cup S_\alpha), & \text{if } \mathbf{p} \in (Y \cup B_\alpha) \\ \mathbf{J}_\alpha(p^1, p^2, p^3) \in I_\alpha, & \text{if } \mathbf{p} \in Z. \end{cases} \tag{4.29}$$

Note that $\mathbf{J}_\alpha^2$ is the identity operator since

$$\mathbf{J}_\alpha[\mathbf{J}_\alpha[X]] = X, \tag{4.30}$$

and so $\mathbf{J}_\alpha$ is its own inverse.

For the case of one hole, we recover exactly the manifold structure seen previously for the Schwarzschild black hole. In this case, one coordinate patch will smoothly cover the entire manifold. If we consider the two sheets separately, we have points on the top sheet labeled by (r, θ, ϕ), and on the bottom sheet by (r', θ', ϕ'). From (4.29), points on the top sheet will have coordinates (r, θ, ϕ), while a point on the bottom sheet will have coordinates $\mathbf{J}_1(r', \theta', \phi')$. In terms of spherical coordinates this yields

$$\left(r = \frac{a_1^2}{r'}, \theta = \theta', \phi = \phi'\right), \tag{4.31}$$

which is just the coordinate transformation (4.16) with $a_1 = \kappa M/16\pi$. So spherical coordinates with the origin removed correspond, in this case, to the single coordinate patch for a single Einstein-Rosen bridge topology, with the region interior to $r = \kappa M/16\pi$ being the bottom sheet.

In addition to having a two-sheeted manifold, it is required that any fields on the two sheets of the manifold must be identical. More precisely, we require that the isometry between the sheets be generated by the maps $\mathbf{J}_\alpha$ via the pull-back maps $\mathbf{J}_\alpha^*$. That is,

$$(\text{data at } \mathbf{x} \in X) = \pm \mathbf{J}_\alpha^* (\text{data at } \mathbf{J}_\alpha(\mathbf{x})). \tag{4.32}$$

The change of sign is allowed since the square of a map is the identity (4.30) and since it will give physically meaningful results. Since the second sheet is covered in its entirety by N different coordinate maps I_α (4.27), it is required for consistency that (4.32) be satisfied not for a single α but for *all* $\alpha = 1, \ldots, N$. This guarantees that fields on the bottom sheet will be identical to the fields on the top sheet no matter which coordinate map is used.

In the case of a scalar field Φ on the manifold, the isometry condition (4.32) requires

$$\Phi\left(\mathbf{x}\right) = \pm\Phi\left(\mathbf{J}_\alpha\left(\mathbf{x}\right)\right). \tag{4.33}$$

For a one-form ω_i, (4.32) requires

$$\omega_i\left(\mathbf{x}\right) = \pm(\mathbf{J}_\alpha)_i{}^j\omega_j\left(\mathbf{J}_\alpha\left(\mathbf{x}\right)\right), \tag{4.34}$$

where

$$(\mathbf{J}_\alpha)_i{}^j \equiv \frac{\partial(\mathbf{J}_\alpha)^j}{\partial x^i} \tag{4.35}$$

is the Jacobian of the map $\mathbf{J}_\alpha$. For a vector field V^i, (4.32) requires

$$V^i\left(\mathbf{x}\right) = \pm\left(\mathbf{J}_\alpha^{-1}\right)_j{}^i V^j\left(\mathbf{J}_\alpha\left(\mathbf{x}\right)\right), \tag{4.36}$$

where the inverse Jacobian, defined by

$$\left(\mathbf{J}_\alpha^{-1}\right)_k{}^i(\mathbf{J}_\alpha)_j{}^k = \delta^k_j, \tag{4.37}$$

is used. The extension to other tensor fields is obvious.

The two fields of importance for gravitational initial data are the metric and extrinsic curvature. These must satisfy

$$\gamma_{ij}\left(\mathbf{x}\right) = \pm(\mathbf{J}_\alpha)_i{}^k(\mathbf{J}_\alpha)_j{}^\ell\gamma_{k\ell}\left(\mathbf{J}_\alpha\left(\mathbf{x}\right)\right) \tag{4.38}$$

and

$$A_{ij}\left(\mathbf{x}\right) = \pm(\mathbf{J}_\alpha)_i{}^k(\mathbf{J}_\alpha)_j{}^\ell A_{k\ell}\left(\mathbf{J}_\alpha\left(\mathbf{x}\right)\right). \tag{4.39}$$

To explore the isometry conditions on the background fields, consider the form that the Jacobian (4.35) and the inverse Jacobian take in Cartesian coordinates:

$$(\mathbf{J}_\alpha)_i{}^j = \frac{a_\alpha^2}{r_\alpha^2}\left(\delta_i^j - 2n_\alpha^j n_i^\alpha\right) \tag{4.40a}$$

and

$$\left(\mathbf{J}_\alpha^{-1}\right)_i{}^j = \frac{r_\alpha^2}{a_\alpha^2}\left(\delta_i^j - 2n_\alpha^j n_i^\alpha\right). \tag{4.40b}$$

Using the conformal decomposition of the metric (3.1) and the assumption that the background metric is flat (4.6), the isometry condition on the metric becomes

$$\psi^4(\mathbf{x})\, f_{ij} = \pm(\mathbf{J}_\alpha)_i{}^k(\mathbf{J}_\alpha)_j{}^\ell \psi^4(\mathbf{J}_\alpha(\mathbf{x}))\, f_{k\ell}. \tag{4.41}$$

Using the explicit form of the Jacobian (4.40), this reduces to

$$\psi^4(\mathbf{x})\, f_{ij} = \pm\left(\frac{a_\alpha}{r_\alpha}\right)^4 \psi^4(\mathbf{J}_\alpha(\mathbf{x}))\, f_{ij}, \tag{4.42}$$

or more simply

$$\psi(\mathbf{x}) = \frac{a_\alpha}{r_\alpha}\psi(\mathbf{J}_\alpha(\mathbf{x})). \tag{4.43}$$

Note that the isometry condition with a minus sign is not allowed since this would imply the conformal factor vanishes on each throat which would make the metric singular. Now, if we consider the conformal transformation of the extrinsic curvature, we find from (3.9) and (4.39)

$$\begin{aligned}\psi^{-2}(\mathbf{x})\,\bar{A}_{ij}(\mathbf{x}) &= \pm(\mathbf{J}_\alpha)_i{}^k(\mathbf{J}_\alpha)_j{}^\ell \psi^{-2}(\mathbf{J}_\alpha(\mathbf{x}))\,\bar{A}_{k\ell}(\mathbf{J}_\alpha(\mathbf{x})) \\ &= \pm(\mathbf{J}_\alpha)_i{}^k(\mathbf{J}_\alpha)_j{}^\ell \left(\frac{a_\alpha}{r_\alpha}\right)^2 \psi^{-2}(\mathbf{x})\,\bar{A}_{k\ell}(\mathbf{J}_\alpha(\mathbf{x}))\end{aligned}, \tag{4.44}$$

or using (4.40),

$$\bar{A}_{ij}(\mathbf{x}) = \pm\left(\frac{a_\alpha}{r_\alpha}\right)^6 \left(\delta_i^k - 2n_\alpha^k n_i^\alpha\right)\left(\delta_j^\ell - 2n_\alpha^\ell n_j^\alpha\right)\bar{A}_{k\ell}(\mathbf{J}_\alpha(\mathbf{x})). \tag{4.45}$$

Equations (4.43) and (4.45) are conditions which solutions to the two constraint equations (4.8) and (4.9) must satisfy in order to represent inversion-symmetric initial data on a regular, complete, two-sheeted initial slice. Since the background fields on the two sheets of the manifold are related by (4.43) and (4.45), it is only necessary to solve the constraints on one sheet, provided these relations are compatible with the constraints. Assume that $\psi(\mathbf{x})$ and $\bar{A}_{ij}(x)$ are solutions of (4.8) and (4.9a) in the region $\bar{X}$ defined by

$$\bar{X} = X \bigcup_{\alpha=1}^{N} S_\alpha, \tag{4.46}$$

that is, the top sheet plus all of the throats. Now consider the coordinate patch Ψ_α and let $\tilde{\psi}(x)$ and $\tilde{A}_{ij}(x)$ be defined for $\mathbf{x}$ in the region I_α. They will take values via the two relations (4.43) and (4.45) for the α^{th} hole:

$$\tilde{\psi}(\mathbf{x}) = \frac{a_\alpha}{r_\alpha}\psi(\mathbf{J}_\alpha(\mathbf{x})) \tag{4.47}$$

$$\tilde{A}_{ij}(\mathbf{x}) = \pm\left(\frac{a_\alpha}{r_\alpha}\right)^6 \left(\delta_i^k - 2n_\alpha^k n_i^\alpha\right)\left(\delta_j^\ell - 2n_\alpha^\ell n_j^\alpha\right)\bar{A}_{k\ell}(\mathbf{J}_\alpha(\mathbf{x})) \tag{4.48}$$

To simplify notation, let $\mathbf{x}' \equiv \mathbf{J}_\alpha(\mathbf{x})$. From (4.30), this gives

$$\mathbf{x} = \mathbf{J}_\alpha(\mathbf{x}'). \tag{4.49}$$

Using the following definitions,

$$r'_\alpha \equiv |\mathbf{x}' - \mathbf{C}_\alpha| \qquad \text{and} \qquad \mathbf{n}'_\alpha \equiv \frac{(\mathbf{x}' - \mathbf{C}_\alpha)}{r'_\alpha}, \tag{4.50}$$

one finds:

$$r_\alpha = r_\alpha\left(\mathbf{J}_\alpha\left(\mathbf{x}'\right)\right) = \frac{a_\alpha^2}{r'_\alpha} \tag{4.51}$$

and

$$\mathbf{n}_\alpha = \mathbf{n}_\alpha\left(\mathbf{J}_\alpha\left(\mathbf{x}'\right)\right) = \mathbf{n}'_\alpha. \tag{4.52}$$

The data on the bottom sheet can now be written as

$$\tilde{\psi}\left(\mathbf{x}\right) = \frac{r'_\alpha}{a_\alpha}\psi\left(\mathbf{x}'\right) \tag{4.53}$$

and

$$\tilde{A}_{ij}\left(\mathbf{x}\right) = \pm\left(\frac{r'_\alpha}{a_\alpha}\right)^6 \left(\delta_i^k - 2n'^k_\alpha n'^\alpha_i\right)\left(\delta_j^\ell - 2n'^\ell_\alpha n'^\alpha_j\right)\bar{A}_{k\ell}\left(\mathbf{x}'\right). \tag{4.54}$$

Checking to see if the extrinsic curvature on the bottom sheet satisfies the momentum constraint, we find

$$\begin{aligned}\bar{D}_j\tilde{A}^{ij}\left(\mathbf{x}\right) &= \pm(\mathbf{J}_\alpha)_j{}^m\bar{D}'_m\left(\left(\frac{r'_\alpha}{a_\alpha}\right)^6\left(f^{ki} - 2n'^k_\alpha n'^i_\alpha\right)\left(f^{\ell j} - 2n'^\ell_\alpha n'^j_\alpha\right)\bar{A}_{k\ell}\left(\mathbf{x}'\right)\right)\\ &= \pm\left(\frac{r'_\alpha}{a_\alpha}\right)^8\left(\delta_k^i - 2n'^\alpha_k n'^i_\alpha\right)\bar{D}'_j\bar{A}^{kj}\left(\mathbf{x}'\right),\end{aligned} \tag{4.55}$$

where $\bar{D}'_m$ is the background covariant derivative with respect to $\mathbf{x}'$. Thus, the extrinsic curvature on the bottom sheet, as given by (4.48), satisfies the momentum constraint (4.9), if the top-sheet extrinsic curvature defining it satisfies the momentum constraint.

To check the Hamiltonian constraint, we first examine the right-hand side of (4.8). From (4.54), we find

$$\begin{aligned}\tilde{A}_{ij}\left(\mathbf{x}\right)\tilde{A}^{ij}\left(\mathbf{x}\right) &= f^{ik}f^{j\ell}\tilde{A}_{ij}\left(\mathbf{x}\right)\tilde{A}_{k\ell}\left(\mathbf{x}\right)\\ &= \left(\frac{r'_\alpha}{a_\alpha}\right)^{12}\bar{A}_{ij}\left(\mathbf{x}'\right)\bar{A}^{ij}\left(\mathbf{x}'\right),\end{aligned} \tag{4.56}$$

and, together with (4.53), this gives

$$\tilde{\psi}^{-7}\left(\mathbf{x}\right)\tilde{A}_{ij}\left(\mathbf{x}\right)\tilde{A}^{ij}\left(\mathbf{x}\right) = \left(\frac{r'_\alpha}{a_\alpha}\right)^5\psi^{-7}\left(\mathbf{x}'\right)\bar{A}_{ij}\left(\mathbf{x}'\right)\bar{A}^{ij}\left(\mathbf{x}'\right). \tag{4.57}$$

Next, the Laplacian of the conformal factor gives

$$\begin{aligned}\overline{\nabla}^2\tilde{\psi}\left(\mathbf{x}\right) &= f^{ij}\left(\mathbf{J}_\alpha\right)_i{}^k\bar{D}'_k\left[\left(\mathbf{J}_\alpha\right)_j{}^\ell\bar{D}'_\ell\left(\frac{r'_\alpha}{a_\alpha}\right)\psi\left(\mathbf{x}'\right)\right] \\ &= \left(\frac{r'_\alpha}{a_\alpha}\right)^5\overline{\nabla}'^2\psi\left(\mathbf{x}'\right).\end{aligned} \tag{4.58}$$

Thus, the Hamiltonian constraint for the conformal factor on the bottom sheet,

$$\begin{aligned}&\overline{\nabla}^2\tilde{\psi}\left(\mathbf{x}\right)+\frac{1}{8}\tilde{\psi}^{-7}\left(\mathbf{x}\right)\tilde{A}_{ij}\left(\mathbf{x}\right)\tilde{A}^{ij}\left(\mathbf{x}\right) \\ &\qquad = \left(\frac{r'_\alpha}{a_\alpha}\right)^5\left(\overline{\nabla}'^2\psi\left(\mathbf{x}'\right)+\frac{1}{8}\psi^{-7}\left(\mathbf{x}'\right)\bar{A}_{ij}\left(\mathbf{x}'\right)\bar{A}^{ij}\left(\mathbf{x}'\right)\right),\end{aligned} \tag{4.59}$$

is satisfied if the top-sheet conformal factor defining it satisfies the Hamiltonian constraint and if the extrinsic curvature is inversion-symmetric.

We can now summarize the conformal imaging method as an approach for computing initial data which represents multiple black holes with non-vanishing initial linear and angular momenta in an asypmtotically flat universe. First, demand that the initial-data slice consist of two asymptotically flat universes connected via N Einstein-Rosen bridges, one for each black hole. Next, demand that physical fields in the two universes be "identical". We choose the initial-data slice to be conformally flat and maximally embedded in the full space-time manifold.

Working in the flat conformal background space, we start by taking a full three-dimensional Eulcidean three-manifold E^3 as the domain in which we must determine the initial data. For each black hole which will be present in our universe, we choose its "position" $\mathbf{C}_\alpha$ and its "radius" $a_\alpha\,(\alpha=1,\ldots,N)$. The N spheres of radius a_α are removed from the manifold E^3 and the remainder, $E^3-\{a_\alpha\}$, is the domain in which we must determine the initial data.

In the domain $E^3-\{a_\alpha\}$, we first find solutions to the momentum constraint (4.9) which satisfy the isometry condition (4.45). By satisfying the isometry condition (4.45), the background extrinsic curvature is said to be inversion symmetric. It is guaranteed to generate a solution on the second sheet which satisfies the momentum constraint, and when combined with an inversion-symmetric conformal factor, will yield a physical extrinsic curvature which is regular everywhere and satisfies the condition (4.39) that it be "identical" on the two sheets.

Given an inversion-symmetric background extrinsic curvature, a solution must be found for the Hamiltonian constraint (4.8) which satisfies the isometry condition (4.43). By satisfying the isometry condition (4.43), the conformal factor is said to be inversion symmetric. It is guaranteed to generate a solution on the second sheet which satisfies the Hamiltonian constraint and, when combined with the flat Euclidean background metric, yields a physical metric which is regular everywhere and represents a complete manifold consisting of two "identical", asymptotically flat sheets.

Chapter 5: Solutions of the Momentum Constraint

Solving the momentum constraint equations is the first step in constructing inversion-symmetric gravitational initial data. If the initial-data slice is chosen to be maximal, or more generally if the trace of the extrinsic curvature is a constant on the initial slice, then the momentum constraint (4.2) decouples from the Hamiltonian constraint (4.1). This is one of the prime strengths of the conformal decomposition of the constraints, and can be exploited in certain cases to find analytic solutions for the background extrinsic curvature. When the initial slice is conformally and asymptotically flat, this decoupling also allows for the determination of two of the physical properties of the initial-data slice without knowing the complete initial data, as is shown below.

The momentum contained in an asymptotically flat, initial-data slice can be calculated from the integral

$$\Pi_i \xi^i{}_{(k)} = \frac{1}{\kappa} \oint_\infty \left(K_i{}^j - \delta_i^j K \right) \xi^i{}_{(k)} d^2 S_j, \tag{5.1}$$

where $\xi^i{}_{(k)}$ is a Killing vector of the spatial metric γ_{ij} (York [1980]). In the conformal imaging approach, the initial slice is conformally flat, as well as asymptotically flat. Since the background metric is flat and the conformal factor must behave like (4.10) at infinity, the integral (5.1) can be expressed equivalently in terms of the background extrinsic curvature and the flat metric. Recalling (4.5), we can now rewrite (5.1) as

$$\Pi_i \bar{\xi}^i{}_{(k)} = \frac{1}{\kappa} \oint_\infty \bar{A}_i{}^j \bar{\xi}^i{}_{(k)} d^2 \bar{S}_j. \tag{5.2}$$

Here, the integral is in terms of the flat background metric, and $\bar{\xi}^i{}_{(k)}$ is a Killing vector of the flat background metric f_{ij} to which γ_{ij} is asymptotic. If $\bar{\xi}^i{}_{(k)}$ is a translational Killing vector, then $\Pi_i \bar{\xi}^i{}_{(k)}$ is the linear momentum P_k. In terms of Cartesian coordinates, the total *physical* linear momentum of a slice is given by

$$P^i = \frac{1}{\kappa} \oint_\infty \bar{A}^{ij} d^2 \bar{S}_j. \tag{5.3}$$

If $\bar{\xi}^i{}_{(k)}$ is a rotational Killing vector, then $\Pi_i \bar{\xi}^i{}_{(k)}$ is the angular momentum S_k. In terms of Cartesian coordinates, the total *physical* angular momentum of a slice is given by

$$S_i = \frac{1}{\kappa} \epsilon_{ijk} \oint_\infty x^j \bar{A}^{k\ell} d^2 \bar{S}_\ell. \tag{5.4}$$

It should be noted that the angular momentum at infinity is not always well defined. The angular momentum S_k will be asymptotically gauge invariant, however, if $\bar{\xi}^i{}_{(k)}$ is an exact symmetry of the the physical metric γ_{ij} (*cf.* York [1980]). So, given a solution for the background extrinsic curvature, we see from (5.3) and (5.4) that two important properties of the physical initial-data set can be determined without knowing the full initial data, i.e., without solving the Hamiltonian constraint.

In the context of the conformal imaging approach, we would like to find solutions to the momentum constraint (4.9) which satisfy the isometry condition (4.45) and represent black holes with linear momentum P^i_α and angular momentum S^i_α as determined by (5.3) and (5.4). For the case of a single black hole, Bowen and York [1980] have found such solutions and they take the following form:

$$\begin{aligned}\bar{A}^{\pm}_{ij} = {} & \frac{3\kappa}{16\pi r^2}\left[P_i n_j + P_j n_i - (f_{ij} - n_i n_j)\, P^k n_k\right] \\ & \mp \frac{3\kappa a^2}{16\pi r^4}\left[P_i n_j + P_j n_i + (f_{ij} - 5 n_i n_j)\, P^k n_k\right]\end{aligned} \tag{5.5}$$

and

$$\bar{A}_{ij} = \frac{3\kappa}{8\pi r^3}\left[\epsilon_{ki\ell} S^\ell n^k n_j + \epsilon_{kj\ell} S^\ell n^k n_i\right]. \tag{5.6}$$

Note, that we have dropped the subscript α on a, r, n^i, P^i, and S^i since there is only one hole. Equation (5.5) gives the background extrinsic curvature for a hole with linear momentum P^i and is actually two solutions. The solution $\bar{A}^+_{ij}$ satisfies the isometry condition (4.45) with the plus sign, and the solution $\bar{A}^-_{ij}$ satisfies the isometry condition (4.45) with the minus sign. Only the $\mathcal{O}(r^{-2})$ term in (5.5) carries linear momentum as can be seen by evaluating (5.3). The second term is required for inversion symmetry. The two terms are individually solutions of the momentum constraint (4.9a). Equation (5.6) gives the background extrinsic curvature for a hole with angular momentum S^i. This solution satisfies the isometry condition with the minus sign only and is its own inverse.

The solutions (5.5) and (5.6) are longitudinal since they can be derived from a vector potential. Ó Murchada and York [1976a] found solution to (4.9b) for the vector potential W^i for the first term in (5.5) and for (5.6). Bowen [1979a] found the solution giving the second term in (5.5). The first term in (5.5), the part carrying linear momentum, is derived from the vector potential

$$W^i = -\frac{\kappa}{32\pi r}\left[7P^i + n^i n_j P^j\right]. \tag{5.7}$$

The second part of (5.5) can also be derived from a vector potential. It takes the form

$$W^i = \frac{\kappa a^2}{32\pi r^3}\left[P^i - 3 n^i n_j P^j\right]. \tag{5.8}$$

As previously mentioned, this term carries no linear momentum and is present only to enforce inversion symmetry. The solution representing a black hole with spin, (5.6), is derived from the vector potential

$$W^i = \frac{\kappa}{8\pi r^2}\epsilon^{ijk} n_j S_k. \tag{5.9}$$

The solutions (5.5) and (5.6) satisfy all of the conditions required by the conformal imaging approach and can be used with the Hamiltonian constraint to construct inversion-symmetric initial data for a single hole with linear and angular momentum. Such initial data has been constructed by many researchers (*cf.* York and Piran [1982], Choptuik and Unruh [1986], Rauber [1985], and Cook and York [1990]) and will be examined in later chapters. I will proceed here with the question of how to construct an inversion-symmetric solution of the momentum constraint for systems with multiple black holes.

This problem was addressed formally by Kulkarni, Shepley, and York [1983]. The approach is centered on the fact that the momentum constraint (4.9) is linear. Since this is the case, a solution representing N black holes, each with linear and angular momentum can be obtained from (5.5) and (5.6) as

$$\begin{aligned}\bar{A}_{ij} = \frac{3\kappa}{8\pi}\sum_{\alpha=1}^{N}\Bigg(&\frac{1}{2r_\alpha^2}\left[P_i^\alpha n_j^\alpha + P_j^\alpha n_i^\alpha - \left(f_{ij} - n_i^\alpha n_j^\alpha\right)P_\alpha^k n_k^\alpha\right] \\ &+\frac{1}{r_\alpha^3}\left[\epsilon_{ki\ell}S_\alpha^\ell n_\alpha^k n_j^\alpha + \epsilon_{kj\ell}S_\alpha^\ell n_\alpha^k n_i^\alpha\right]\Bigg).\end{aligned} \tag{5.10}$$

Note that the second term in (5.5) has been omitted here. The N black holes are given individual linear and angular momenta P_α^i and S_α^i in the sense that if the holes are "sufficiently far apart", then they will have such momenta as measured by (5.3) and (5.4). If the holes are close together, then all that can be measured is the total linear and angular momentum of the system.

The background extrinsic curvature given by (5.10) is longitudinal and traceless and is a solution of the momentum constraint (4.9), however, it is not inversion symmetric through any of the holes as is required. This is why the second term in (5.5) was not included for each hole in (5.10). Even though (5.10) is not inversion symmetric, Kulkarni *et al.* [1983] have shown how to take this non-invertable extrinsic curvature and make it inversion symmetric through a method of images applicable to tensors. I will outline the formal approach below.

In order for the extrinsic curvature to be inversion symmetric, it must satisfy

$$\begin{aligned}\bar{A}_{ij}(\mathbf{x}) &= \Re_\alpha^{\pm}\circ\bar{A}_{ij}(\mathbf{x}) \\ &= \pm\left(\frac{a_\alpha}{r_\alpha}\right)^2 (\mathbf{J}_\alpha)_i{}^\ell \bar{A}_{\ell m}(\mathbf{J}_\alpha(\mathbf{x}))(\mathbf{J}_\alpha)_j{}^m\end{aligned} \tag{5.11}$$

for all α. In order to simplify and clarify notation, I will drop the component indices and write (5.11) as

$$\begin{aligned}\bar{A}\,(\mathbf{x}) &= \Re^{\pm}_{\alpha}\circ\bar{A}\,(\mathbf{x}) \\ &= \pm\left(\frac{a_\alpha}{r_\alpha}\right)^2_{(\mathbf{x})}\,[\mathbf{J}_\alpha]_{(\mathbf{x})}\bar{A}\,(\mathbf{J}_\alpha\,(\mathbf{x}))\,[\mathbf{J}_\alpha]_{(\mathbf{x})}.\end{aligned} \tag{5.12}$$

Note that in order to distinguish the Jacobian from the transformation $\mathbf{J}_\alpha$, the Jacobian is enclosed in square brackets. Let $M_{ij}(\mathbf{x})$ be any second rank tensor field on E^3. It is straightforward to show the following properties of the inversion operator $\Re^{\pm}_{\alpha}$ (*cf.* Kulkarni *et at* [1983]).

$$\Re^{\pm}_{\alpha}\circ\Re^{\pm}_{\alpha} = \mathbb{I}. \tag{5.13}$$

$$\left(\Re^{\pm}_{\alpha}\circ M\right)^t = \Re^{\pm}_{\alpha}\circ\left(M^t\right), \tag{5.14}$$

where M^t is the transpose of M.

$$\left[Tr\left(\Re^{\pm}_{\alpha}\circ M\right)\right]_{(\mathbf{x})} = \pm\left(\frac{a_\alpha}{r_\alpha}\right)^6_{(\mathbf{x})}\left[(Tr\,M)_{(\mathbf{J}_\alpha(\mathbf{x}))}\right], \tag{5.15}$$

where $Tr\,M$ is the trace of M.

$$\begin{aligned}\left[\bar{D}_j\left(\Re^{\pm}_{\alpha}\circ M^{ij}\right)\right]_{(\mathbf{x})} = \pm\left(\frac{a_\alpha}{r_\alpha}\right)^6_{(\mathbf{x})}\Bigg\{&(\mathbf{J}_\alpha)_{(\mathbf{x})k}{}^{i}\left[\bar{D}_\ell M^{k\ell}\right]_{(\mathbf{J}_\alpha(\mathbf{x}))} \\ &+ 2\left(\frac{n^i_\alpha}{r_\alpha}\right)_{(\mathbf{x})}[Tr\,M]_{(\mathbf{J}_\alpha(\mathbf{x}))}\Bigg\}.\end{aligned} \tag{5.16}$$

If we start with a symmetric and traceless solution, $\bar{A}_{ij}$, to the momentum constraint (4.9a), then (5.14), (5.15), and (5.16) guarantee that the "image" of it, $\Re^{\pm}_{\alpha}\circ\bar{A}_{ij}$, will also be symmetric, traceless, and satisfy the momentum constraint. Now consider the following operator:

$$\Re^{\pm} = \mathbb{I} + \sum_{\{\alpha_i\}}\left(\prod_{i=1}^{m}\Re^{\pm}_{\alpha_i}\right). \tag{5.17}$$

The notation here needs some elaboration. The α_i label the holes as usual and the subscript i takes on the values of $1,\ldots,N$. The sum is over all unique sequences $\{\alpha_i\}$ of length m. For any sequence, $\{\alpha_i\}$, one takes the product of "image" operators corresponding to that sequence. From property (5.13), a sequence is unique if and only if $\alpha_i \neq \alpha_{i+1}$. As an example of this operator, consider the case of a single hole. The operator (5.17) takes, in this case, the form

$$\Re^{\pm} = \mathbb{I} + \Re^{\pm}_{\alpha_1}. \tag{5.18}$$

For two holes, it takes the form

$$\begin{aligned}\Re^{\pm} = \mathbb{I} &+ \Re^{\pm}_{\alpha_1} + \Re^{\pm}_{\alpha_1}\circ\Re^{\pm}_{\alpha_2} + \Re^{\pm}_{\alpha_1}\circ\Re^{\pm}_{\alpha_2}\circ\Re^{\pm}_{\alpha_1} + \Re^{\pm}_{\alpha_1}\circ\Re^{\pm}_{\alpha_2}\circ\Re^{\pm}_{\alpha_1}\circ\Re^{\pm}_{\alpha_2} + \cdots \\ &+ \Re^{\pm}_{\alpha_2} + \Re^{\pm}_{\alpha_2}\circ\Re^{\pm}_{\alpha_1} + \Re^{\pm}_{\alpha_2}\circ\Re^{\pm}_{\alpha_1}\circ\Re^{\pm}_{\alpha_2} + \Re^{\pm}_{\alpha_2}\circ\Re^{\pm}_{\alpha_1}\circ\Re^{\pm}_{\alpha_2}\circ\Re^{\pm}_{\alpha_1} + \cdots.\end{aligned} \tag{5.19}$$

It can be easily verified from (5.13), that

$$\Re^{\pm}_{\alpha} \circ \Re^{\pm} = \Re^{\pm} \tag{5.20}$$

for all α and so (5.17) can be called the inversion symmetry operator. If it acts on any arbitrary second rank tensor M_{ij}, then the result will be inversion symmetric through all N holes. In particular, if M_{ij} is symmetric, traceless, and satisfies the momentum constraint, then $\Re^{\pm} M_{ij}$ will be symmetric, traceless, satisfy the momentum constraint, and be inversion symmetric.

The formal approach for obtaining an inversion-symmetric solution of the momentum constraint (4.9a) is now obvious. Let $\hat{A}_{ij}$ represent a sum of single hole solutions to the momentum constraint. The inversion-symmetric solution is then given by

$$\bar{A}_{ij} = \Re^{\pm} \circ \hat{A}_{ij}. \tag{5.21}$$

In the case of a single hole, (5.21) will be $\hat{A}_{ij}$ plus a single image term. Specifically, it will be a combination of (5.5) and (5.6). If there is more than one hole, then (5.21) will consist of $\hat{A}_{ij}$ plus an infinite number of image terms. In this case, one must be concerned with the convergence of this infinite series. Kulkarni [1984] has shown that for any reasonable choice for $\hat{A}_{ij}$, the infinite series converges if the holes are far enough apart. In particular, if there are just two holes, then the infinite series converges absolutely provided the inversion surfaces do not overlap. This is in direct analogy with Misner's proof of convergence for the inversion-symmetric conformal factor on a time-symmetric initial slice (Misner [1963]).

To continue, we need to specify an explicit form for $\hat{A}_{ij}$. A first guess would be to use (5.10). This would lead to an error in the computation of spins since the α^{th} spin term in (5.10) is the negative of its inverse through the α^{th} hole. Using (5.10) in (5.21) would result in holes with twice the desired spin for each hole. There is no problem with the terms containing linear momentum since the full, inversion-symmetric form is not used. This error pertaining to the spin exists in Kulkarni *et al.* [1983], Kulkarni [1984], and York [1984]. Bowen, Rauber, and York [1984] correct for this error by redefining (5.21) with an overall factor of 1/2. This will work provided that the full, inversion-symmetric solutions containing linear momentum (5.5) are used. One must be careful, however, to choose the correct sign in (5.5) to match that of (5.21). The more elegant, and more computationally convenient method, is to define $\hat{A}_{ij}$ as

$$\begin{aligned} \hat{A}_{ij} = \frac{3\kappa}{16\pi} \sum_{\alpha=1}^{N} \Bigg(& \frac{1}{r_\alpha^2} \left[P_i^\alpha n_j^\alpha + P_j^\alpha n_i^\alpha - \left(f_{ij} - n_i^\alpha n_j^\alpha \right) P_\alpha^k n_k^\alpha \right] \\ & + \frac{1}{r_\alpha^3} \left[\epsilon_{ki\ell} S_\alpha^\ell n_\alpha^k n_j^\alpha + \epsilon_{kj\ell} S_\alpha^\ell n_\alpha^k n_i^\alpha \right] \Bigg). \end{aligned} \tag{5.22}$$

Consider now, the total linear and angular momenta contained in the inversion-symmetric background extrinsic curvature defined by (5.17), (5.21), and (5.22). $\bar{A}_{ij}$ will contain three types of terms. First, it will contain $\hat{A}_{ij}$ itself. It will also contain the self-image of each term in $\hat{A}_{ij}$. Finally, it will contain arbitrary image terms. Computing the total linear momentum (5.3) from $\hat{A}_{ij}$ yields the sum of the individual linear momenta P_i^α. As has already been mentioned, the self-image of the linear momentum terms carry no linear or angular momentum.

If we next assume that none of the holes has any linear momentum, then the total angular momentum (5.4) contained in $\hat{A}_{ij}$ is simply half the sum of the individual angular momenta S_{α_i}. If we choose the isometry relation with the minus sign, then the self-image of the angular momentum terms again carries half the sum of the individual angular momenta S_{α_i}. This is why (5.22) is used instead of (5.10). If the isometry relation with the plus sign is used, the angular momentum from the self-image terms will cancel that from $\hat{A}_{ij}$. If the holes have non-zero linear momentum, then the linear momentum terms in $\hat{A}_{ij}$ can contain non-zero angular momentum although their self-image terms cannot.

Remaining to be examined are the contributions to the total linear and angular momentum from the general image terms. Bowen, Rauber, and York [1984] detail an elegant proof that no general image term can carry angular momentum. Their proof, however, cannot be generalized to examine their linear momentum content. Through tedious, explicit calculations, it can be shown that at large distances from the holes, the leading behavior of all of the general image terms is $\mathcal{O}(r^{-6})$. A term with this fall-off behavior contributes nothing to the integrals (5.3) and (5.4) and thus carries no linear or angular momentum. This is a very powerful result. It means that the total linear and angular momentum content of an initial-data slice can be computed without knowing the explicit form of the general image terms. The only terms which contribute are the "base" extrinsic curvature $\hat{A}_{ij}$ and the self-image terms of the angular momentum terms (which are trivial).

As a final note to the formalism for constructing inversion-symmetric extrinsic curvature solutions, it should be pointed out that the imaging is done on the purely longitudinal field $\hat{A}_{ij}$ and not the potential W^i. For the case of a single black hole, the resulting, imaged field $\bar{A}_{ij}$ is still longitudinal. In the case of multiple black holes, this does not seem to be the case. Rauber [1985] has shown in a lengthy calculation that the resulting field $\bar{A}_{ij}$ is not derivable from a vector potential. This implies that $\bar{A}_{ij}$ contains some transverse components. This is not a problem since we are free to specify the transverse-tracefree content of the extrinsic curvature. This is the reason that the less restrictive form of the momentum constraint (4.9a) has been retained and explains further the note that the assumption (4.7) would be relaxed.

At this point, we have a *formalism* for the construction of inversion-symmetric, background extrinsic curvatures. In order to find solutions to the Hamiltonian constraint, we must be able to move past the formalism and find a concrete method for computing these extrinsic curvatures. In the case of a single hole, the resulting inversion-symmetric, background extrinsic curvature is given in (5.5) and (5.6). If we consider more than one hole, the evaluation of an infinite series must be dealt with.

The situation of primary concern is the two body problem so we need to find a method for calculating the extrinsic curvature for two holes. Bowen, Rauber, and York [1984] have addressed this problem for a certain special case. They considered the situation in which the two holes are of equal size, have no linear momentum, and have angular momenta which are equal in magnitude. With the further restriction that the direction of the angular momenta be either aligned or anti-aligned with the axis between the two holes, they found an analytic expression for each term in the infinite series. Even in this situation, which contains a high degree of symmetry, their method is tedious and results in an expression involving complicated combinations of hyperbolic and trigonometric functions. If this approach is applied to the case of axially aligned linear momentum or to the case where the linear or angular momentum is not axisymmetric, then the method becomes completely intractable. In order to proceed, another avenue must be taken. The solution which I have found to the problem is to abandon the attempt to find an analytic expression for each term in the infinite series. Instead, the solution lies in a constructive, computational approach which I detail in the next chapter.

Chapter 6: Inversion-Symmetric Extrinsic Curvature for Two Black Holes

The formalism described in the previous chapter describes a method for constructing inversion-symmetric solutions to the momentum constraint equation for N black holes. This chapter is devoted to a method for evaluating these inversion-symmetric solutions in the case of two black holes. For the construction of initial-data sets, it is sufficient to be able to evaluate numerically the formal infinite series solution described in the previous chapter (5.21). In this light, the search for an analytic expression for each term in the series is abandoned. Instead, let us consider the evaluation of the infinite series at a specific point in the domain exterior to the two holes.

Since I deal here with the case of two holes, the hole label, α, takes on the values of 1 and 2. Let $\mathbf{x}$ denote the point at which the extrinsic curvature will be evaluated, and with it define the following quantities:

$$\mathbf{x}_1 \equiv \mathbf{J}_1(\mathbf{x}), \quad \mathbf{x}_{21} \equiv \mathbf{J}_2(\mathbf{x}_1), \quad \mathbf{x}_{121} \equiv \mathbf{J}_1(\mathbf{x}_{21}), \ldots. \tag{6.1}$$

and

$$\mathbf{x}_2 \equiv \mathbf{J}_2(\mathbf{x}), \quad \mathbf{x}_{12} \equiv \mathbf{J}_1(\mathbf{x}_2), \quad \mathbf{x}_{212} \equiv \mathbf{J}_2(\mathbf{x}_{12}), \ldots. \tag{6.2}$$

With $\hat{A}_{ij}$ defined by (5.22), consider the first few terms of the infinite series (5.21).

$$\Re_1^{\pm} \circ \hat{A}(\mathbf{x}) = \pm \left(\frac{a_1}{r_1}\right)^2_{(\mathbf{x})} [\mathbf{J}_1]_{(\mathbf{x})} \hat{A}_{(\mathbf{x}_1)} [\mathbf{J}_1]_{(\mathbf{x})}. \tag{6.3}$$

$$\Re_2^{\pm} \circ \Re_1^{\pm} \circ \hat{A}(\mathbf{x}) = \left(\frac{a_2}{r_2}\right)^2_{(\mathbf{x})} \left(\frac{a_1}{r_1}\right)^2_{(\mathbf{x}_2)} [\mathbf{J}_2]_{(\mathbf{x})} [\mathbf{J}_1]_{(\mathbf{x}_2)} \hat{A}_{(\mathbf{x}_{12})} [\mathbf{J}_1]_{(\mathbf{x}_2)} [\mathbf{J}_2]_{(\mathbf{x})}. \tag{6.4}$$

$$\begin{aligned} \Re_1^{\pm} \circ \Re_2^{\pm} \circ \Re_1^{\pm} \circ \hat{A}(\mathbf{x}) = \pm &\left(\frac{a_1}{r_1}\right)^2_{(\mathbf{x})} \left(\frac{a_2}{r_2}\right)^2_{(\mathbf{x}_1)} \left(\frac{a_1}{r_1}\right)^2_{(\mathbf{x}_{21})} \times \\ &[\mathbf{J}_1]_{(\mathbf{x})} [\mathbf{J}_2]_{(\mathbf{x}_1)} [\mathbf{J}_1]_{(\mathbf{x}_{21})} \hat{A}_{(\mathbf{x}_{121})} [\mathbf{J}_1]_{(\mathbf{x}_{21})} [\mathbf{J}_2]_{(\mathbf{x}_1)} [\mathbf{J}_1]_{(\mathbf{x})}. \end{aligned} \tag{6.5}$$

The extension to higher order terms is obvious. Now, recursively define the two vectors $\mathbf{x}_1^n$ and $\mathbf{x}_2^n$ as follows.

$$\mathbf{x}_1^n \equiv \begin{cases} \mathbf{J}_1\left(\mathbf{x}_1^{n-1}\right) & : \text{for } n \text{ odd} \\ \mathbf{J}_2\left(\mathbf{x}_1^{n-1}\right) & : \text{for } n \text{ even} \\ \mathbf{x} & : \text{for } n = 0. \end{cases} \tag{6.6}$$

$$\mathbf{x}_2^n \equiv \begin{cases} \mathbf{J}_2\left(\mathbf{x}_2^{n-1}\right) & : \text{for } n \text{ odd} \\ \mathbf{J}_1\left(\mathbf{x}_2^{n-1}\right) & : \text{for } n \text{ even} \\ \mathbf{x} & : \text{for } n = 0. \end{cases} \tag{6.7}$$

In terms of $\mathbf{x}_1^n$ and $\mathbf{x}_2^n$, recursively define the following two matrices.

$$M_1^n \equiv \begin{cases} M_1^{n-1}[\mathbf{J}_1]_{\left(\mathbf{x}_1^{n-1}\right)} & : \text{for } n \text{ odd} \\ M_1^{n-1}[\mathbf{J}_2]_{\left(\mathbf{x}_1^{n-1}\right)} & : \text{for } n \text{ even} \\ \mathbb{I} & : \text{for } n = 0. \end{cases} \tag{6.8}$$

$$M_2^n \equiv \begin{cases} M_2^{n-1}[\mathbf{J}_2]_{\left(\mathbf{x}_2^{n-1}\right)} & : \text{for } n \text{ odd} \\ M_2^{n-1}[\mathbf{J}_1]_{\left(\mathbf{x}_2^{n-1}\right)} & : \text{for } n \text{ even} \\ \mathbb{I} & : \text{for } n = 0. \end{cases} \tag{6.9}$$

Finally, recursively define the following two scalar quantities.

$$F_1^n \equiv \begin{cases} F_1^{n-1}\left(\frac{a_1}{r_1}\right)^2_{\left(\mathbf{x}_1^{n-1}\right)} & : \text{for } n \text{ odd} \\ F_1^{n-1}\left(\frac{a_2}{r_2}\right)^2_{\left(\mathbf{x}_1^{n-1}\right)} & : \text{for } n \text{ even} \\ 1 & : \text{for } n = 0. \end{cases} \tag{6.10}$$

$$F_2^n \equiv \begin{cases} F_2^{n-1}\left(\frac{a_2}{r_2}\right)^2_{\left(\mathbf{x}_2^{n-1}\right)} & : \text{for } n \text{ odd} \\ F_2^{n-1}\left(\frac{a_1}{r_1}\right)^2_{\left(\mathbf{x}_2^{n-1}\right)} & : \text{for } n \text{ even} \\ 1 & : \text{for } n = 0. \end{cases} \tag{6.11}$$

In terms of these quantities, the first few terms in the series (5.19) can be written as

$$\Re_1^{\pm} \circ \hat{A}\left(\mathbf{x}\right) = \left(\pm 1\right)^1 F_1^1 M_1^1 \hat{A}_{\left(\mathbf{x}_1^1\right)} \tilde{M}_1^1, \tag{6.12}$$

$$\Re_2^{\pm} \circ \Re_1^{\pm} \circ \hat{A}\left(\mathbf{x}\right) = \left(\pm 1\right)^2 F_2^2 M_2^2 \hat{A}_{\left(\mathbf{x}_2^2\right)} \tilde{M}_2^2, \tag{6.13}$$

and

$$\Re_1^{\pm} \circ \Re_2^{\pm} \circ \Re_1^{\pm} \circ \hat{A}\left(\mathbf{x}\right) = \left(\pm 1\right)^3 F_1^3 M_1^3 \hat{A}_{\left(\mathbf{x}_1^3\right)} \tilde{M}_1^3. \tag{6.14}$$

Note that $\tilde{M}_\alpha^n$ denotes the transpose of M_α^n. By using the recursion relations defined above, it is easy to prove that (6.12), (6.13), and (6.14) are equivalent, respectively, to (6.3), (6.4), and (6.5). The pattern for a general term in the series (5.21) is now clear. The set of quantities to use, $(\mathbf{x}_1^n, M_1^n, F_1^n)$ or $(\mathbf{x}_2^n, M_2^n, F_2^n)$, is determined by the label of the left-most inversion operator, and the index of the recursion, n, is determined by the number of inversion operators. The two-hole, inversion-symmetric solution to the momentum constraint equation can now be written as

$$\begin{aligned} \bar{A}\left(\mathbf{x}\right) &= \Re^{\pm} \circ \hat{A}\left(\mathbf{x}\right) \\ &= \hat{A}\left(\mathbf{x}\right) + \sum_{n=1}^{\infty} \left(\pm 1\right)^n \left\{ F_1^n M_1^n \hat{A}_{\left(\mathbf{x}_1^n\right)} \tilde{M}_1^n + F_2^n M_2^n \hat{A}_{\left(\mathbf{x}_2^n\right)} \tilde{M}_2^n \right\}. \end{aligned} \tag{6.15}$$

Formulated in this way, any desired numerical accuracy can be obtained for the components of $\bar{A}_{ij}$. To obtain the n^{th} term in the series, one only needs to know the six quantities $\mathbf{x}_1^{n-1}$, $\mathbf{x}_2^{n-1}$,

M_1^{n-1}, M_2^{n-1}, F_1^{n-1}, and F_2^{n-1} which have already been computed in order to obtain the $(n-1)^{th}$ term. From a computational point of view, it is a simple iterative matter to keep adding terms until the value of $\bar{A}_{ij}$ converges to machine accuracy.

This formulation of the extrinsic curvature is completely general. It can be used to compute the components of the extrinsic curvature when the two holes have any relative sizes and separation, and for any values of the linear and angular momentum for each hole. In later chapters, I will explore solutions to the Hamiltonian constraint in the case of axisymmetry. In preparation for this, I will describe (6.15) explicitly for this special case.

Let us consider first the coordinate system to be used. Since the configuration is to be axisymmetric, the obvious choice is to use cylindrical coordinates. It is best to use dimensionless coordinates, so it is desirable to scale the coordinates relative to some physical length scale of the problem. There are three natural length scales in the problem: the size of each of the two holes and the separation between the two holes. I choose to use the radius of the first hole, a_1, as the natural length scale.

The two holes will be centered on the z-axis and will be positioned so that

$$\mathbf{C}_1 = [\,0 \quad 0 \quad a_1\zeta_1\,] \qquad \text{and} \qquad \mathbf{C}_2 = [\,0 \quad 0 \quad a_1\zeta_2\,]\,. \tag{6.16}$$

In order to maintain axisymmetry, we choose the linear and angular momentum vectors for the two holes to have components only in the z direction. The physical, unscaled linear and angular momentum vectors will be

$$\mathbf{P}_1 = [\,0 \quad 0 \quad P_1\,] \qquad \text{and} \qquad \mathbf{P}_2 = [\,0 \quad 0 \quad P_2\,] \tag{6.17}$$

and

$$\mathbf{S}_1 = [\,0 \quad 0 \quad S_1\,] \qquad \text{and} \qquad \mathbf{S}_2 = [\,0 \quad 0 \quad S_2\,]\,. \tag{6.18}$$

The cylindrical coordinate components of $\hat{A}_{ij}$ can now be written in dimensionless form as

$$\frac{\hat{A}_{\rho\rho}}{a_1} = -\frac{3\kappa}{16\pi}\left\{ \frac{\left(\frac{P_1}{a_1}\right)(z-\zeta_1)^3}{\left(\rho^2+(z-\zeta_1)^2\right)^{5/2}} + \frac{\left(\frac{P_2}{a_1}\right)(z-\zeta_2)^3}{\left(\rho^2+(z-\zeta_2)^2\right)^{5/2}} \right\}, \tag{6.19}$$

$$\frac{\hat{A}_{\phi\phi}}{a_1} = -\frac{3\kappa}{16\pi}\rho^2\left\{ \frac{\left(\frac{P_1}{a_1}\right)(z-\zeta_1)}{\left(\rho^2+(z-\zeta_1)^2\right)^{3/2}} + \frac{\left(\frac{P_2}{a_1}\right)(z-\zeta_2)}{\left(\rho^2+(z-\zeta_2)^2\right)^{3/2}} \right\}, \tag{6.20}$$

$$\frac{\hat{A}_{zz}}{a_1} = \frac{3\kappa}{16\pi}\left\{ \frac{\left(\frac{P_1}{a_1}\right)(z-\zeta_1)\left(\rho^2+2(z-\zeta_1)^2\right)}{\left(\rho^2+(z-\zeta_1)^2\right)^{5/2}} + \frac{\left(\frac{P_2}{a_1}\right)(z-\zeta_2)\left(\rho^2+2(z-\zeta_2)^2\right)}{\left(\rho^2+(z-\zeta_2)^2\right)^{5/2}} \right\}, \tag{6.21}$$

$$\frac{\hat{A}_{\rho z}}{a_1} = \frac{3\kappa}{16\pi}\rho\left\{ \frac{\left(\frac{P_1}{a_1}\right)\left(\rho^2+2(z-\zeta_1)^2\right)}{\left(\rho^2+(z-\zeta_1)^2\right)^{5/2}} + \frac{\left(\frac{P_2}{a_1}\right)\left(\rho^2+2(z-\zeta_2)^2\right)}{\left(\rho^2+(z-\zeta_2)^2\right)^{5/2}} \right\}, \tag{6.22}$$

$$\frac{\hat{A}_{\rho\phi}}{a_1} = \frac{3\kappa}{16\pi}\rho^3\left\{ \frac{\left(\frac{S_1}{a_1^2}\right)}{\left(\rho^2+(z-\zeta_1)^2\right)^{5/2}} + \frac{\left(\frac{S_2}{a_1^2}\right)}{\left(\rho^2+(z-\zeta_2)^2\right)^{5/2}} \right\}, \tag{6.23}$$

and

$$\frac{\hat{A}_{\phi z}}{a_1} = \frac{3\kappa}{16\pi}\rho^2\left\{ \frac{\left(\frac{S_1}{a_1^2}\right)(z-\zeta_1)}{\left(\rho^2+(z-\zeta_1)^2\right)^{5/2}} + \frac{\left(\frac{S_2}{a_1^2}\right)(z-\zeta_2)}{\left(\rho^2+(z-\zeta_2)^2\right)^{5/2}} \right\}. \tag{6.24}$$

Before describing the explicit form which the isometry map and the Jacobian will take, it is useful to examine the square of the background extrinsic curvature which is the quantity of interest in the Hamiltonian constraint. Expressed as a dimensionless quantity, it takes the form

$$\begin{aligned} a_1^2\bar{A}_{ij}\bar{A}^{ij} = &\left[\left(\Re^{\pm}\circ\left(\frac{\hat{A}}{a_1}\right)\right)_{\rho\rho}\right]^2 + \left[\frac{1}{\rho^2}\left(\Re^{\pm}\circ\left(\frac{\hat{A}}{a_1}\right)\right)_{\phi\phi}\right]^2 + \left[\left(\Re^{\pm}\circ\left(\frac{\hat{A}}{a_1}\right)\right)_{zz}\right]^2 \\ &+ 2\left[\left(\Re^{\pm}\circ\left(\frac{\hat{A}}{a_1}\right)\right)_{\rho z}\right]^2 + 2\left[\frac{1}{\rho}\left(\Re^{\pm}\circ\left(\frac{\hat{A}}{a_1}\right)\right)_{\rho\phi}\right]^2 + 2\left[\frac{1}{\rho}\left(\Re^{\pm}\circ\left(\frac{\hat{A}}{a_1}\right)\right)_{\phi z}\right]^2. \end{aligned} \tag{6.25}$$

It is clear that care will have to be taken in computing the second, fifth, and sixth terms in (6.25) so as not to encounter errors resulting from division by zero (not to mention computational roundoff errors) as the $\rho = 0$ axis is approached. The second term in (6.25) is handled easily by the property that $\bar{A}_{ij}$ is traceless. This fact immediately gives

$$\frac{1}{\rho^2}\left(\Re^{\pm}\circ\left(\frac{\hat{A}}{a_1}\right)\right)_{\phi\phi} = -\left(\left[\left(\Re^{\pm}\circ\left(\frac{\hat{A}}{a_1}\right)\right)_{\rho\rho}\right] + \left[\left(\Re^{\pm}\circ\left(\frac{\hat{A}}{a_1}\right)\right)_{zz}\right]\right), \tag{6.26}$$

so we never actually need to compute this term. The fifth and sixth terms of (6.25) cannot be handled so easily. Their resolution depends on the explicit form of the isometry and the Jacobian in the scaled cylindrical coordinate system.

In order to define the isometry conditions, one more definition must be made. The scaled centers of the holes have already been defined by (6.16). The scaled radius of the first hole is just *one* since

that length sets the scale for all quantities. All that remains is to define a dimensionless quantity to give the size of the second hole. I define this quantity by the following:

$$a_1 = \alpha a_2. \tag{6.27}$$

A straightforward calculation shows that the isometry conditions take the following dimensionless forms:

$$\mathbf{J}_1(\mathbf{x}) = \left[\tfrac{\rho}{\rho^2+(z-\zeta_1)^2} \quad , \phi \quad , \tfrac{z-\zeta_1}{\rho^2+(z-\zeta_1)^2} + \zeta_1 \right] \tag{6.28}$$

and

$$\mathbf{J}_2(\mathbf{x}) = \left[\tfrac{\alpha^{-2}\rho}{\rho^2+(z-\zeta_2)^2} \quad , \phi \quad , \tfrac{\alpha^{-2}(z-\zeta_2)}{\rho^2+(z-\zeta_2)^2} + \zeta_2 \right]. \tag{6.29}$$

Based on these two equations, the Jacobians are given by

$$[\mathbf{J}_1]_{(\mathbf{x})} = \begin{bmatrix} \frac{(z-\zeta_1)^2-\rho^2}{\left(\rho^2+(z-\zeta_1)^2\right)^2} & 0 & \frac{-2\rho(z-\zeta_1)}{\left(\rho^2+(z-\zeta_1)^2\right)^2} \\ 0 & 1 & 0 \\ \frac{-2\rho(z-\zeta_1)}{\left(\rho^2+(z-\zeta_1)^2\right)^2} & 0 & \frac{\rho^2-(z-\zeta_1)^2}{\left(\rho^2+(z-\zeta_1)^2\right)^2} \end{bmatrix} \tag{6.30}$$

and

$$[\mathbf{J}_2]_{(\mathbf{x})} = \begin{bmatrix} \frac{\alpha^{-2}\left((z-\zeta_2)^2-\rho^2\right)}{\left(\rho^2+(z-\zeta_2)^2\right)^2} & 0 & \frac{-2\alpha^{-2}\rho(z-\zeta_2)}{\left(\rho^2+(z-\zeta_2)^2\right)^2} \\ 0 & 1 & 0 \\ \frac{-2\alpha^{-2}\rho(z-\zeta_2)}{\left(\rho^2+(z-\zeta_2)^2\right)^2} & 0 & \frac{\alpha^{-2}\left(\rho^2-(z-\zeta_2)^2\right)}{\left(\rho^2+(z-\zeta_2)^2\right)^2} \end{bmatrix} \tag{6.31}$$

For completeness, I display the dimensionless form for the recursion relations (6.10) and (6.11):

$$F_1^n = \begin{cases} \left.\frac{F_1^{n-1}}{\rho^2+(z-\zeta_1)^2}\right|_{\left(\mathbf{x}_1^{n-1}\right)} & : \text{for } n \text{ odd} \\ \left.\frac{\alpha^{-2}F_1^{n-1}}{\rho^2+(z-\zeta_2)^2}\right|_{\left(\mathbf{x}_1^{n-1}\right)} & : \text{for } n \text{ even} \\ 1 & : \text{for } n = 0 \end{cases} \tag{6.32}$$

and

$$F_2^n = \begin{cases} \left.\frac{\alpha^{-2}F_2^{n-1}}{\rho^2+(z-\zeta_2)^2}\right|_{\left(\mathbf{x}_2^{n-1}\right)} & : \text{for } n \text{ odd} \\ \left.\frac{F_2^{n-1}}{\rho^2+(z-\zeta_1)^2}\right|_{\left(\mathbf{x}_2^{n-1}\right)} & : \text{for } n \text{ even} \\ 1 & : \text{for } n = 0. \end{cases} \tag{6.33}$$

Consider now, in light of the explicit form of the recurrence relations, the form of the n^{th} term in the series (6.15). Explicit calculation shows that the $\rho\rho$, ρz, and zz terms depend only on $\hat{A}_{\rho\rho}$, $\hat{A}_{\rho z}$, and $\hat{A}_{zz}$. The $\rho\phi$ and ϕz terms depend only on $\hat{A}_{\rho\phi}$ and $\hat{A}_{\phi z}$. Finally, the $\phi\phi$ term depends only on $\hat{A}_{\phi\phi}$. This means that the linear and angular momentum pieces of the inversion-symmetric extrinsic curvature are completely uncoupled and can be considered separately.

The two terms of concern in (6.25),

$$\frac{1}{\rho}\left(\Re^{\pm}\circ\left(\frac{\hat{A}}{a_1}\right)\right)_{\rho\phi} \qquad \text{and} \qquad \frac{1}{\rho}\left(\Re^{\pm}\circ\left(\frac{\hat{A}}{a_1}\right)\right)_{\phi z}, \tag{6.34}$$

are angular momentum terms and, as mentioned above, depend only on $\hat{A}_{\rho\phi}$ and $\hat{A}_{\phi z}$. Looking at (6.23) and (6.24), we see that both terms contain overall factors of ρ. This indicates that the factors of $1/\rho$ should be "commuted" with the inversion operator. Consider the n^{th} term of the first expression in (6.34).

$$\frac{1}{\rho}F_1^n\left[M_1^n\hat{A}_{(\mathbf{x}_1^n)}\tilde{M}_1^n\right]_{\rho\phi}+\frac{1}{\rho}F_2^n\left[M_2^n\hat{A}_{(\mathbf{x}_2^n)}\tilde{M}_2^n\right]_{\rho\phi}. \tag{6.35}$$

If we denote the ρ component of $\mathbf{x}_\alpha^n$ as ρ_α^n, then it is straightforward to verify that

$$\frac{1}{\rho}=\frac{F_\alpha^n}{\rho_\alpha^n}. \tag{6.36}$$

Equation (6.35) now becomes

$$(F_1^n)^2\left[M_1^n\left[\frac{\hat{A}}{\rho}\right]_{(\mathbf{x}_1^n)}\tilde{M}_1^n\right]_{\rho\phi}+(F_2^n)^2\left[M_2^n\left[\frac{\hat{A}}{\rho}\right]_{(\mathbf{x}_2^n)}\tilde{M}_2^n\right]_{\rho\phi}, \tag{6.37}$$

which is completely regular as the $\rho=0$ axis is approached since it depends only on $\hat{A}_{\rho\phi}$ and $\hat{A}_{\phi z}$, which both have overall factors of ρ. The second expression in (6.34) can be handled in exactly the same manner.

The components of the background extrinsic curvature can now be accurately calculated in cylindrical coordinates, with special care being given to the angular momentum terms. If axisymmetry is not present, then a similar construction can be obtained in terms of Cartesian coordinates. In this case, the linear and angular momentum components will not decouple, but there will be no coordinate singularities to deal with.

Chapter 7: The Hamiltonian Constraint and Boundary Conditions

The final step in the construction of initial-data sets via the conformal imaging approach is the solution of the Hamiltonian constraint (4.8). As shown in Chapter 4, the domain in which a solution of the Hamiltonian constraint must be found is $E^3 - \{a_\alpha\}$. That is, a three-dimensional Euclidean flat space with N spheres cut out, one for each black hole. If proper boundary conditions can be posed on the surfaces of these deleted spheres and at infinity, then the Hamiltonian constraint can be posed as a quasi-linear, elliptic boundary value problem. Bowen and York [1980] have derived such boundary conditions and these will be described below. I will also discuss some known, exact solutions to the Hamiltonian constraint and the approach taken for finding numerical solutions.

In order to pose the Hamiltonian constraint as a boundary value problem, boundary conditions must be found for all surfaces. The boundary condition at infinity has been discussed in Chapter 4. It is fixed by the assumption that the initial-data slice is asymptotically flat. This, together with the choice of a flat background metric, demands that the conformal factor behave like (4.10). Thus, the first boundary condition is that the conformal factor is *one* at infinity. Along with the demand that the metric be regular, this implies that the conformal factor always be greater than zero. In practice, infinity is often not part of the domain of solution for the conformal factor when numerical solutions are found. In this case, an approximate boundary condition must be used at large distances from the holes. York and Piran [1982] have suggested and used an approximate boundary condition which has become widely accepted. I will discuss it later in this chapter along with an improvement which I have derived.

In order for the solution of the Hamiltonian constraint to be inversion symmetric, it must satisfy the isometry condition (4.43) for every hole in the system. Consider the α^{th} coordinate patch and take a derivative of the isometry condition. The result is

$$\bar{D}_i\psi\left(\mathbf{x}\right) = -\frac{a_\alpha}{r_\alpha^2} n_i^\alpha \psi\left(\mathbf{J}_\alpha\left(\mathbf{x}\right)\right) + \frac{a_\alpha}{r_\alpha}\left(\mathbf{J}_\alpha\right)_i{}^j \left[\bar{D}_j\psi\left(\mathbf{x}\right)\right]_{\mathbf{J}_\alpha(\mathbf{x})}. \tag{7.1}$$

If this is contracted with the α^{th} unit normal and evaluated on the α^{th} inversion boundary, the result is

$$n_\alpha^i \bar{D}_i\psi\big|_{a_\alpha} = -\left.\frac{\psi}{2r_\alpha}\right|_{a_\alpha}, \tag{7.2}$$

where the fact that $r_\alpha = a_\alpha$ is a fixed point set of the isometry has been used. That is, $\mathbf{J}_\alpha(a_\alpha) = a_\alpha$. (7.2) represents a boundary condition which can be used on the surface of each deleted sphere. This reduces directly to the boundary condition derived by Bowen and York [1980] in the case of a single hole and to the form shown by Kulkarni *et al.* [1983] for the case of multiple holes.

Bowen and York [1980] have shown, in the case of a single hole, that the area of the inversion boundary, or "throat", is extremal. This result holds for the case of multiple holes as well and can be seen as follows. Consider the area of a sphere of radius r_α centered around the α^{th} throat.

$$A_\alpha = \oint \psi^4 r_\alpha^2 d^2\Omega_\alpha \tag{7.3}$$

The condition for extremal area is found by varying the area and setting the variation to zero.

$$\delta A_\alpha = 2 \oint r_\alpha \psi^3 \left(2 r_\alpha \bar{D}_i \psi + \psi n_i^\alpha\right) \delta x^i d^2\Omega_\alpha = 0 \tag{7.4}$$

Considering only changes normal to the surface, (7.4) gives

$$n_\alpha^i \bar{D}_i \psi + \frac{\psi}{2r_\alpha} = 0, \tag{7.5}$$

which, together with (7.2), shows that the throats must be extremal surfaces.

The Hamiltonian constraint, together with the boundary conditions of asymptotic flatness at infinity and inversion symmetry on the throats, constitutes a quasi-linear, elliptic boundary value problem. In order for this boundary value problem to be well posed, it is necessary to show that any solution satisfying the boundary conditions is unique. Two difficulties arise in trying to prove this. One arises from the non-linearity of the Hamiltonian constraint and the other from the inversion symmetry boundary condition (7.2). In order to deal with the non-linearity, one can consider a local uniqueness proof. That is, it is shown that no other solutions lie in the neighborhood of a given solution. This does not preclude the existence of other solutions which are "significantly different". If a standard, local uniqueness proof is attempted, it is found that the relative sign in (7.2) prevents any conclusion. This is because (7.2) is an "anti-Robin" boundary condition, although it appears at first sight to be a standard Robin condition (*cf.* Bergman and Schiffer [1953]). The problem arises because n_α^i points inward, into the domain of the solution, not outward.

In spite of these problems, York [1989] has proven that the solution for a single hole is locally unique. This proof depends explicitly on the inversion symmetry of both the conformal factor and the background extrinsic curvature. My attempts to generalize this proof to the case of multiple holes have been unsuccessful. The presence of extra holes makes the method inconclusive. I believe

that the solution may depend on limits on the maximum hole-radius to hole-separation ratio as do the convergence proofs of Misner [1963] and Kulkarni [1984] for the case of the infinite series which arise when multiple holes are present.

In spite of the lack of any uniqueness proof in the case of multiple holes, I will continue on the belief any solutions found will be locally unique and search for solutions. I will begin by looking at the asymptotic behavior of the solutions to the Hamiltonian constraint. In doing this, I will follow Bowen, Rauber, and York [1984] and use a "Newtonian" potential Φ instead of the conformal factor, where Φ is defined by

$$\psi = 1 - \frac{1}{2}\Phi. \tag{7.6}$$

The Hamiltonian constraint is very much like a Poisson equation except that the source term is coupled non-linearly to the conformal factor. In terms of Φ, the Hamiltonian constraint is written

$$\overline{\nabla}^2\Phi = \frac{1}{4}\psi^{-7}\bar{A}_{ij}\bar{A}^{ij} \equiv \frac{\kappa}{2}\rho_{_{eff}}, \tag{7.7}$$

where $\rho_{_{eff}}$ is defined as an effective energy density source. If we assume for a moment that $\rho_{_{eff}}$ has compact support, then a multipole expansion of Φ is well defined outside the support and is given by

$$\Phi = -\frac{\kappa}{8\pi}\left[\frac{E}{r} + \frac{d_i n^i}{r^2} + \frac{3}{2}\frac{I_{ij}\left(n^i n^j - \frac{1}{3}f^{ij}\right)}{r^3} + \mathcal{O}\left(r^{-4}\right)\right]. \tag{7.8}$$

The monopole coefficient E is the total ADM energy contained in the initial-data slice (*cf.* Arnowitt *et al.* [1962]). The other multipole coefficients are associated with the energy distribution on the initial slice. These multipole coefficients are defined in terms of the following standard Cartesian surface integrals:

$$E = \frac{2}{\kappa}\oint_\infty \bar{D}^i\Phi d^2\bar{S}_i, \tag{7.9}$$

$$d_i = \frac{2}{\kappa}\oint_\infty \left(x_i\bar{D}^j\Phi - \delta_i^j\Phi\right)d^2\bar{S}_j, \tag{7.10}$$

and

$$I_{ij} = \frac{2}{\kappa}\oint_\infty \left[\left(x_i x_j - \frac{1}{3}r^2 f_{ij}\right)\bar{D}^k\Phi - \left(x_i\delta_j^k + x_j\delta_i^k - \frac{2}{3}x^k f_{ij}\right)\Phi\right]d^2\bar{S}_k. \tag{7.11}$$

The effective source does not, of course, have compact support. Because of this, the multipole expansion will only be well defined through some given order defined by the radial fall off rate of the source. From the conditions for asymptotic flatness (4.10) and (4.11), it is seen that the effective source behaves as

$$\rho_{_{eff}} = \mathcal{O}\left(r^{-4}\right). \tag{7.12}$$

This means that the monopole term, and thus the total energy, is always well defined on an asymptotically flat slice.

The well behaved nature of the multipole expansion through monopole order is the basis of an approximate boundary condition proposed by York and Piran [1982]. The conformal factor takes the form

$$\psi = 1 + \frac{\kappa}{16\pi}\frac{E}{r} + \mathcal{O}\left(r^{-2}\right). \tag{7.13}$$

Taking the radial derivative of (7.13) and eliminating the total energy term results in the following Robin boundary condition:

$$\frac{\partial\psi}{\partial r} = \frac{1-\psi}{r} + \frac{1}{r}\,\mathcal{O}\left(r^{-2}\right). \tag{7.14}$$

Applied at large distances from the holes, (7.14) provides a good approximate outer boundary condition. Exactly how far away the outer boundary must be for (7.14) to be a good approximation depends on the explicit form of the effective source.

Evans [1989] has suggested that an improvement in the order of accuracy of the outer boundary condition would be of great use in numerical solutions as it would allow the outer boundary to be placed closer to the holes and reduce the size of the numerical problem. Prompted by this, I have explored the possibility of incorporating higher order terms into the approximation. In general, (7.8) is a valid expansion for Φ only through the monopole term. In order to make it valid for higher order terms, it must be modified. Consider a function Λ which is not annihilated by the Laplacian and which satisfies the following:

$$\overline{\nabla}^2\Lambda = \mathcal{O}\left(r^{-4}\right) = 4\pi\rho_{_{eff}} + \mathcal{O}\left(r^{-5}\right). \tag{7.15}$$

Λ is thus chosen to compensate for the highest order effects of the effective source. I demand that it have the following properties, in addition to (7.15):

$$\Lambda = \mathcal{O}\left(r^{-2}\right) \tag{7.16}$$

and

$$\bar{D}_i\Lambda = \mathcal{O}\left(r^{-3}\right). \tag{7.17}$$

Now consider expanding Φ as

$$\Phi = -\frac{\kappa}{8\pi}\left[\frac{E}{r} + \frac{\tilde{d}_i n^i}{r^2} - \Lambda + \mathcal{O}\left(r^{-3}\right)\right]. \tag{7.18}$$

The total energy given by the monopole coefficient is still defined by (7.9) because of the fall-off condition (7.17). The dipole term is modified and, in terms of (7.10), is given by

$$\tilde{d}_i = d_i - \frac{2}{\kappa} \oint_\infty \left(x_i \bar{D}^j \Lambda - \delta_i^j \Lambda \right) d^2 \bar{S}_j. \tag{7.19}$$

Given the fall-off conditions (7.16) and (7.17), the correction to the dipole moment will not, in general, vanish and, thus, the "dipole moment" of (7.18) no longer represents a multipole moment of the initial energy distribution. If the integral over Λ in (7.19) were to vanish either by some symmetry or because (7.16) and (7.17) fall off faster than necessary, then the dipole moment would retain its original interpretation and the multipole expansion would be well defined through dipole order.

To proceed, we must have an explicit form for the function Λ. In order to determine this, we must explore the asymptotic form of the effective source. Since the potential Φ is always well defined through monopole order for asymptotically flat initial data, the asymptotic form of the effective source is given by

$$\rho_{_{eff}} = \frac{1}{2\kappa} \bar{A}_{ij} \bar{A}^{ij} + \mathcal{O}\left(r^{-5}\right). \tag{7.20}$$

Thus, in order to fix Λ, we need only consider the behavior of the background extrinsic curvature. The asymptotic behavior of the extrinsic curvature is

$$\bar{A}_{ij} = \frac{3\kappa}{16\pi r^2} \sum_{\alpha=1}^{N} \left[P_i^\alpha n_j + P_j^\alpha n_i - \left(f_{ij} - n_i n_j \right) P_\alpha^k n_k \right] + \mathcal{O}\left(r^{-3}\right). \tag{7.21}$$

Using (7.21) in (7.20), the effective energy density is

$$4\pi \rho_{_{eff}} = \frac{9\kappa}{64\pi r^4} \sum_{\alpha=1}^{N} \sum_{\beta=1}^{N} \left\{ P_i^\alpha P_\beta^i + 2 P_i^\alpha n^i P_j^\beta n^j \right\} + \mathcal{O}\left(r^{-5}\right). \tag{7.22}$$

The solution of (7.15) for Λ is found by inspection to be

$$\Lambda = \frac{9\kappa}{128\pi r^2} \sum_{\alpha=1}^{N} \sum_{\beta=1}^{N} \left\{ P_i^\alpha P_\beta^i - 2 P_i^\alpha n^i P_j^\beta n^j \right\}. \tag{7.23}$$

Taking the gradient of Λ gives

$$\bar{D}^k \Lambda = -\frac{2n^k}{r} \Lambda - \frac{9\kappa n^k}{64\pi r^3} \sum_{\alpha=1}^{N} \sum_{\beta=1}^{N} \left\{ P_\alpha^k P_i^\beta n^i + P_\beta^k P_i^\alpha n^i - 2 n^k P_i^\alpha n^i P_j^\beta n^j \right\}, \tag{7.24}$$

and so (7.16) and (7.17) are satisfied.

We can now examine the effect of (7.23) on the dipole term defined by (7.19). Straightforward calculation shows

$$\begin{aligned}\tilde{d}_i &= d_i + \frac{6}{\kappa}\oint_\infty n_i \Lambda r^2 d^2\Omega \\ &= d_i + \frac{27}{16}\sum_{\alpha=1}^{N}\sum_{\beta=1}^{N}\left\{P_j^\alpha P_\beta^j \langle n_i\rangle - 2P_j^\alpha P_k^\beta \langle n_i n^j n^k\rangle\right\} \\ &= d_i,\end{aligned} \tag{7.25}$$

where $\langle\bullet\rangle$ denotes averaging over a unit two-sphere. Since the correction to the dipole term vanishes, we find that the dipole moment is well defined and retains its original meaning as a moment of the initial energy distribution, and we find that the asymptotic form for the conformal factor can be written as

$$\psi = 1 + \frac{\kappa}{16\pi}\left\{\frac{E}{r} + \frac{d_i n^i}{r^2} - \frac{9}{16r^2}\sum_{\alpha=1}^{N}\sum_{\beta=1}^{N}\left(P_i^\alpha P_\beta^i - 2P_i^\alpha n^i P_j^\beta n^j\right)\right\} + \mathcal{O}\left(r^{-3}\right). \tag{7.26}$$

I should note that both of the $\mathcal{O}(r^{-2})$ terms in (7.26) can be made to vanish by an appropriate choice for the frame of the observer. The dipole term arises if the observer is not in the "center of energy" frame. The total energy is the lowest order, non-vanishing multipole moment and is, thus, independent of the choice of the origin of coordinates. The dipole moment explicitly depends on the location of the origin of coordinates and can be made to vanish by an appropriate choice for the origin of coordinates. The second term arises if the observer is not in the "center of momentum" frame. If the observer is boosted into a frame in which the sum of the linear momenta for all N holes vanishes, then the effective energy density is, asymptotically, $\mathcal{O}(r^{-6})$. In this case, the multipole expansion (7.8) is well defined through quadrupole order with no correction terms.

We can use (7.26) as the basis of an approximate outer boundary condition. As with (7.13), by taking the radial derivative of (7.26) and eliminating the monopole term, we find

$$\frac{\partial\psi}{\partial r} = \frac{1-\psi}{r} - \frac{\kappa}{16\pi r^3}\left\{d_i n^i - \frac{9}{16}\sum_{\alpha=1}^{N}\sum_{\beta=1}^{N}\left(P_i^\alpha P_\beta^i - 2P_i^\alpha n^i P_j^\beta n^j\right)\right\} + \frac{1}{r}\mathcal{O}\left(r^{-3}\right). \tag{7.27}$$

This boundary condition is of higher order than (7.14) whenever the system is not in a center of energy *and* a center of momentum frame. The extra accuracy, however, comes at a cost. This boundary condition depends explicitly on the dipole moment which can only be determined from the solution to the Hamiltonian constraint. Thus, the boundary condition depends on the solution. This does not, however, prevent (7.27) from being a useful approximation for the outer boundary condition. The boundary condition can be used in an iterative fashion in numerical solutions to the Hamiltonian constraint. Because the dipole term in (7.27) occurs at one orders in r below the dominant term, it will constitute only a small correction and the iterative scheme will be convergent.

Before resorting to numerical methods, all analytic avenues should be explored. The only known analytic solutions to the inversion-symmetric Hamiltonian constraint which represent physical situations are time symmetric. That is, the extrinsic curvature vanishes identically and the Hamiltonian constraint reduces to a *linear* Laplace equation. In the case of a single hole, the inversion-symmetric, time-symmetric solution of the Hamiltonian constraint is a slice of the Schwarzschild solution in isotropic coordinates:

$$\psi = 1 + \frac{\kappa E}{16\pi r}. \tag{7.28}$$

E is the total energy of the solution as defined by (7.9) and there are no higher order multipole moments.

For the case of multiple holes, Misner [1963] has described the construction of inversion-symmetric, time-symmetric solutions to the Hamiltonian constraint. In the case of two holes of equal size, Misner's solution can be cast into the form of an infinite series of terms, each consisting of combinations of hyperbolic and trigonometric functions. I will generalize this to the case of two holes of any arbitrary size through the use of recurrence relations. I have not seen this calculation anywhere else, although it may have been carried out before.

In order to be inversion symmetric, the conformal factor must satisfy (4.43) for every hole. As with the extrinsic curvature tensor, we can define an inversion operator which acts on scalars. I define the inversion operator acting through the α^{th} hole by

$$\aleph_\alpha \circ \psi(\mathbf{x}) \equiv \frac{a_\alpha}{r_\alpha} \psi(\mathbf{J}_\alpha(\mathbf{x})) \tag{7.29}$$

and

$$\aleph_\alpha \circ 1 \equiv \frac{a_\alpha}{r_\alpha}. \tag{7.30}$$

An N hole inversion-symmetric and time-symmetric solution of the Hamiltonian constraint is then represented formally by

$$\psi(\mathbf{x}) = 1 + \sum_{\{\alpha_i\}} \left(\prod_{i=1}^{N} \aleph_{\alpha_i} \right). \tag{7.31}$$

In order to evaluate (7.31) for the case of two holes, I will follow Chapter 6 and use cylindrical coordinates scaled relative to the radius of the first hole, a_1. The positions of the two holes will be given by (6.16) and the radius of the second hole will be defined by (6.27). A straightforward but tedious calculation (Bowen *et al.* [1984] defines a useful notation for simplifying the calculation) reduces (7.31) to

$$\psi(\mathbf{x}) = 1 + \sum_{n=1}^{\infty} \left\{ \frac{W_1^n}{r_1^n} + \frac{W_2^n}{r_2^n} \right\}, \tag{7.32}$$

based on the following recursively defined quantities.

$$\zeta_1^n \equiv \begin{cases} \frac{1}{\zeta_1^{n-1}-\zeta_1} + \zeta_1 & : \text{for } n \text{ odd} \\ \frac{\alpha^{-2}}{\zeta_1^{n-1}-\zeta_2} + \zeta_2 & : \text{for } n \text{ even} \\ \zeta_1 & : \text{for } n = 1 \end{cases} \tag{7.33}$$

$$\zeta_2^n \equiv \begin{cases} \frac{\alpha^{-2}}{\zeta_2^{n-1}-\zeta_2} + \zeta_2 & : \text{for } n \text{ odd} \\ \frac{1}{\zeta_2^{n-1}-\zeta_1} + \zeta_1 & : \text{for } n \text{ even} \\ \zeta_2 & : \text{for } n = 1 \end{cases} \tag{7.34}$$

$$W_1^n \equiv \begin{cases} \frac{W_1^{n-1}}{\left|\zeta_1^{n-1}-\zeta_1\right|} & : \text{for } n \text{ odd} \\ \frac{\alpha^{-1}W_1^{n-1}}{\left|\zeta_1^{n-1}-\zeta_2\right|} & : \text{for } n \text{ even} \\ 1 & : \text{for } n = 1 \end{cases} \tag{7.35}$$

$$W_2^n \equiv \begin{cases} \frac{\alpha^{-1}W_2^{n-1}}{\left|\zeta_2^{n-1}-\zeta_2\right|} & : \text{for } n \text{ odd} \\ \frac{W_2^{n-1}}{\left|\zeta_2^{n-1}-\zeta_1\right|} & : \text{for } n \text{ even} \\ \alpha^{-1} & : \text{for } n = 1 \end{cases} \tag{7.36}$$

$$r_1^n \equiv \sqrt{\rho^2 + \left(z - \zeta_1^n\right)^2} \tag{7.37}$$

$$r_2^n \equiv \sqrt{\rho^2 + \left(z - \zeta_2^n\right)^2} \tag{7.38}$$

The series expansion for the conformal factor (7.32) differs for the expansion for the extrinsic curvature (6.15) in the crucial point that each term in (7.32) is evaluated at the same spatial point. In (6.15), the point of evaluation for each term is imaged. This complication was necessary in the case of the extrinsic curvature in order to make the solution tractable. Since the position dependence of (7.32) is not imaged, the series expansion can be used directly in the integrals for the multipole moments. The results for the total energy and dipole moment are

$$\frac{E}{a_1} = \frac{16\pi}{\kappa} \sum_{n=1}^{\infty} \left(W_1^n + W_2^n\right) \tag{7.39}$$

and

$$\frac{d_z}{a_1^2} = \frac{16\pi}{\kappa} \sum_{n=1}^{\infty} \left(W_1^n \zeta_1^n + W_2^n \zeta_2^n\right). \tag{7.40}$$

Since I know of no analytic methods for finding solutions to the Hamiltonian constraint in time-asymmetric situations, I will turn now to numerical techniques. The problem of solving a partial differential equation consists of two basic parts: the discretization of the continuous problem into a set of algebraic equations and the solution of the resulting large set of possibly non-linear equations. Though distinct, the two components are often treated together (*cf.* Ames [1977], Mitchel and Griffiths [1980], and Allen [1954]). The problem of discretization can be handled by several different techniques. The two main techniques are the method of finite differences and the method of finite elements and I choose to use the method of finite differences.

The problem of solving the large set of algebraic equations is the prime difficulty in finding numerical solutions. In the case of an elliptic partial differential equation, one is always faced, in the end, with the task of solving a very large matrix equation. The size of the matrix is determined by the number of spatial dimensions on which the equation depends and on the spatial resolution of the discretization, the latter determining the accuracy of the approximation. In order to reduce the size of the matrix which must be inverted, one often considers problems with sufficient symmetry to reduce the dimensional dependence of the differential equation to one or two dimensions. In subsequent chapters, I will do just this by considering only axisymmetric configurations. In the case of a single hole, this is not a serious restriction. If you do not consider the situation of a hole with *both* linear and angular momenta, then the situation is naturally axisymmetric. In the case of two holes, the restriction to axisymmetry eliminates, among other things, the possibility of exploring initial-data sets with non-zero orbital angular momentum. Such configurations are of great physical interest and will certainly be examined in the future, however, in subsequent chapters I will consider only axisymmetric configurations which can be dealt with by two-dimensional numerical techniques.

Chapter 8: Numerical Solution of the Hamiltonian Constraint for a Single, Axisymmetric Black Hole

As a first example of finding numerical solutions for the Hamiltonian constraint within the framework of the conformal imaging approach, I will examine the case of a single black hole with axisymmetric linear or angular momentum. In this chapter, I will describe in detail the procedure for differencing the Hamiltonian constraint and discuss the methods used to solve the finite difference equations. I will tabulate the numerical results obtained by sweeping through the parameter space (i.e. the magnitude of the linear and angular momenta of the hole), but I will reserve the physical interpretation for a later chapter. I should note that several authors (York and Piran [1982], Choptuik [1982], and Rauber [1985]) have examined these solutions previously. While the differencing scheme which I use is slightly different from that of any of the previous authors, the results I obtain are essentially the same.

I will begin by choosing a coordinate system which is appropriate for the physical configuration. The obvious choice is spherical polar coordinates with the center of the black hole coincident with the origin of coordinates. This coordinate system is perfectly adapted for imposing the boundary conditions at both the throat (or inversion surface) and at large distances. For numerical efficiency, I will use a logarithmically scaled, dimensionless radial coordinate x defined by

$$x = \ln\left(\frac{r}{a}\right), \tag{8.1}$$

where a is the radius of the throat. This scaling is chosen because the curvature of the initial-data slice is expected to be greatest near the throat of the black hole. In the case of the conformal factor, this curvature will show up as a gradient in the conformal factor and so the greatest changes in the conformal factor occur in the region near the throat. The coordinate choice (8.1) will tend to emphasize the region near the throat in the finite difference equations. With the coordinate transformation (8.1), the dimensionless coordinates covering the manifold are (x, θ, ϕ) and the metric is given by

$$ds^2 = a^2 e^{2x}\left(dx^2 + d\theta^2 + \sin^2\theta d\phi^2\right). \tag{8.2}$$

The domain of the top sheet in which the Hamiltonian constraint must be solved is $0 \leq x < \infty$ and the throat (or minimal surface) is located at $x = 0$.

To simplify the numerical problem of solving the Hamiltonian constraint, I will restrict myself to axisymmetric configurations. The only restriction this imposes in the case of a single hole (as mentioned in Chapter 7) occurs in the case in which the hole has *both* linear and angular momenta. In this case, to remain axisymmetric, the linear and angular momentum vectors must be parallel or anti-parallel. I will take the symmetry axis to coincide with the z-axis and so the ϕ coordinate can be ignored. From (8.2) and axisymmetry, the Laplace operator takes the form

$$\overline{\nabla}^2 = a^{-2}e^{-2x}\left\{e^{-x}\frac{\partial}{\partial x}\left(e^{x}\frac{\partial}{\partial x}\right) + \frac{1}{\sin\theta}\frac{\partial}{\partial\theta}\left(\sin\theta\frac{\partial}{\partial\theta}\right)\right\}. \tag{8.3}$$

The inversion-symmetric extrinsic curvatures for a single hole (as found by Bowen and York [1980]) were given in (5.5) and (5.6). In terms of this coordinate system, the dimensionless components are

$$\frac{\bar{A}^{+}_{ij}}{a} = 3\left(\frac{P}{a}\right)\begin{bmatrix} 2e^{-x}\cosh x\cos\theta & -e^{-x}\sinh x\sin\theta & 0 \\ -e^{-x}\sinh x\sin\theta & -e^{-x}\cosh x\cos\theta & 0 \\ 0 & 0 & -e^{-x}\cosh x\cos\theta\sin^2\theta \end{bmatrix}, \tag{8.4}$$

$$\frac{\bar{A}^{-}_{ij}}{a} = 3\left(\frac{P}{a}\right)\begin{bmatrix} 2e^{-x}\sinh x\cos\theta & -e^{-x}\cosh x\sin\theta & 0 \\ -e^{-x}\cosh x\sin\theta & -e^{-x}\sinh x\cos\theta & 0 \\ 0 & 0 & -e^{-x}\sinh x\cos\theta\sin^2\theta \end{bmatrix}, \tag{8.5}$$

and

$$\frac{\bar{A}_{ij}}{a} = 3\left(\frac{S}{a^2}\right)\begin{bmatrix} 0 & 0 & e^{-x}\sin^2\theta \\ 0 & 0 & 0 \\ e^{-x}\sin^2\theta & 0 & 0 \end{bmatrix}. \tag{8.6}$$

Note that I have chosen to use gravitational units in which the proportionality constant $\kappa = 8\pi$. Equation (8.4) gives the background extrinsic curvature for a hole with linear momentum P in the positive z direction and which obeys the extrinsic curvature isometry condition (4.45) with the plus sign. Equation (8.5) gives the background extrinsic curvature for the same physical configuration, but the extrinsic curvature obeys the isometry condition with the minus sign. Equation (8.6) gives the background extrinsic curvature for a hole with angular momentum S in the positive z direction and obeys the isometry condition with the minus sign. No single hole can have a non-vanishing angular momentum at infinity and obey the isometry condition with the plus sign.

The square of the extrinsic curvature is needed in the source term for the Hamiltonian constraint. The squares of (8.4), (8.5), and (8.6) in dimensionless form are, respectively,

$$a^2\bar{A}^{+}_{ij}\bar{A}^{+ij} = 18\left(\frac{P}{a}\right)^2 e^{-6x}\left\{\sinh^2 x\left(1+2\cos^2\theta\right)+3\cos^2\theta\right\}, \tag{8.7}$$

$$a^2\bar{A}^{-}_{ij}\bar{A}^{-ij} = 18\left(\frac{P}{a}\right)^2 e^{-6x}\left\{\cosh^2 x\left(1+2\cos^2\theta\right)-3\cos^2\theta\right\}, \tag{8.8}$$

and

$$a^2 \bar{A}_{ij} \bar{A}^{ij} = 18 \left(\frac{S}{a^2} \right)^2 e^{-6x} \sin^2 \theta. \tag{8.9}$$

Since (8.5) and (8.6) obey the extrinsic curvature isometry condition with the same sign, they can be considered together. In this case, the square of the sum is the sum of the squares since there are no cross terms and (8.8) and (8.9) can be added together. Examining (8.7), (8.8), and (8.9), we find that they are also reflection symmetric through the $\theta = \pi/2$ plane. This means that the domain in which the Hamiltonian constraint must be solved in order to specify initial data over the entire initial hypersurface is $0 \leq x < \infty$ and $0 \leq \theta \leq \pi/2$.

With the domain of the problem determined, boundary conditions must be imposed on all domain boundaries. Equation (7.5) defines the boundary condition on the throat. In terms of our coordinate system, this becomes

$$\frac{\partial \psi}{\partial x} + \frac{\psi}{2} = 0 \qquad \text{for} \qquad x = 0. \tag{8.10}$$

If the outer boundary is not taken at infinity, but at some finite radius x_f, then the outer boundary condition can be approximated by either (7.14) or (7.27). While the accuracy of (7.27) is always equal to or greater than the accuracy of (7.14), this boundary condition had not been derived at the time when this problem was studied. For this reason, I will consider only (7.14) for this particular problem. Equation (7.27) should be used in any future work on the one-hole problem, and it has been used in all work subsequent to this. With this in mind, the approximate outer boundary condition takes the following form in terms of our coordinate system:

$$\frac{\partial \psi}{\partial x} + \psi - 1 = 0 \qquad \text{for} \qquad x = x_f. \tag{8.11}$$

The two remaining boundaries are at $\theta = 0$ and $\theta = \pi/2$. To fix boundary conditions here, recall first that the configuration is axisymmetric. In order for the solution to be axisymmetric, the derivative of the conformal factor normal to the rotation axis must vanish. Similarly, because of the reflection symmetry, the derivative of the conformal factor normal to the reflection plane must also vanish. In terms of our coordinates, these two boundary conditions can be written as

$$\frac{\partial \psi}{\partial \theta} = 0 \qquad \text{at} \qquad \theta = 0 \quad \text{or} \quad \frac{\pi}{2}. \tag{8.12}$$

To difference the Hamiltonian constraint I first discretize the domain of the solution. The discretization will take the following form:

$$x_i \equiv i * h_x \qquad \text{where} \qquad i = 0, \ldots, \mathcal{I} \quad \text{and} \quad h_x \equiv \frac{x_f}{\mathcal{I}} \tag{8.13}$$

and

$$\theta_j \equiv j * h_\theta \qquad \text{where} \qquad j = 0, \ldots, \mathcal{J} \quad \text{and} \quad h_\theta \equiv \frac{\pi/2}{\mathcal{J}}. \tag{8.14}$$

Thus, the continuous domain of the solution is approximated by a discrete "mesh" of points labeled by an index pair (i, j). Any function on the space becomes a function on the mesh. For example, the conformal factor will become

$$\psi(x_i, \theta_j) \rightarrow \psi_{i,j}. \tag{8.15}$$

To difference the Laplacian (8.3), I use a second order conservative differencing scheme (*cf.* Adler and Piran [1984]). I should point out that there is no unique way to difference a differential operator. In the limit that the mesh spacings h_x and h_θ go to zero, however, all correct differencing schemes should converge to the same continuous differential operator and the results of different finite difference calculations should converge to the same continuous result. The choice of a conservative differencing scheme means that the finite difference equations will obey, locally, a discrete version of Gauss' law. As a general rule, any method for making the finite difference equations mimic any behavior of the differential equations should be used.

The finite difference form of the Hamiltonian constraint is expressed as follows:

$$\begin{aligned} &\mathcal{A}^+_{i,j}\left(\psi_{i+1,j} - \psi_{i,j}\right) + \mathcal{A}^-_{i,j}\left(\psi_{i-1,j} - \psi_{i,j}\right) + \mathcal{B}^+_{i,j}\left(\psi_{i,j+1} - \psi_{i,j}\right) \\ &\qquad + \mathcal{B}^-_{i,j}\left(\psi_{i,j-1} - \psi_{i,j}\right) + \frac{e^{2x_i}}{8}\psi^{-7}_{i,j}\left[a^2 \bar{A}_{\ell m}\bar{A}^{\ell m}\right]_{i,j} = 0, \end{aligned} \tag{8.16}$$

where

$$\mathcal{A}^\pm_{i,j} \equiv \frac{\exp\{\pm h_x\}}{h_x^2} \qquad : \qquad \text{for} \quad \begin{matrix} i = 0, \ldots, \mathcal{I} \\ j = 0, \ldots, \mathcal{J} \end{matrix} \tag{8.17}$$

and

$$\mathcal{B}^\pm_{i,j} \equiv \begin{cases} \frac{\sin\left(\theta_j \pm \frac{1}{2}h_\theta\right)}{h_\theta^2 \sin\theta_j} & : \text{for} \quad \begin{matrix} i = 0, \ldots, \mathcal{I} \\ j = 1, \ldots, \mathcal{J} \end{matrix} \\ \frac{2}{h_\theta^2} & : \text{for} \quad \begin{matrix} i = 0, \ldots, \mathcal{I} \\ j = 0 \end{matrix} \end{cases}. \tag{8.18}$$

Notice that a different form must be used for the $\mathcal{B}^\pm_{i,j}$ coefficients on the $\theta = 0$ axis. This special case occurs because of the coordinate singularity on the z-axis which is present in spherical coordinates. In the case of axisymmetry, this can be handled easily by L'Hôpital's rule given the boundary condition (8.12). For $\theta = 0$ (or π), we find that

$$\lim_{\theta \rightarrow 0} \frac{1}{\sin\theta}\frac{\partial}{\partial\theta}\left(\sin\theta \frac{\partial\psi}{\partial\theta}\right) = 2\frac{\partial^2\psi}{\partial\theta^2}, \tag{8.19}$$

which fixes the special case of (8.18). (Evans [1986a] espouses an alternate approach for differencing near coordinate singularities based on numerical regularization.) Notice also, that the differenced

form of the Hamiltonian constraint has been multiplied by an overall factor of r^2 in order to simplify the equations and to remove the overall r^{-2} scaling in the difference coefficients.

The difference equations, as given in (8.16), for points on the boundary of the domain depend on values of the conformal factor outside the computational domain. These unknowns are fixed by the boundary conditions which have, as yet, not been used. I include the boundary conditions in the one-hole problem by the *explicit* use of "virtual" boundary points. That is, the computational domain is expanded to include four sets of "virtual" mesh points, with the values of these mesh points being determined by the boundary conditions. On the inner boundary, virtual points are added for $i = -1$ and $j = 0, \ldots, \mathcal{J}$. The second order finite difference form of (8.10) fixes these virtual boundary points by

$$\psi_{-1,j} = \psi_{1,j} + h_x \psi_{0,j}. \tag{8.20}$$

On the outer boundary, virtual points are added for $i = \mathcal{I} + 1$ and $j = 0, \ldots, \mathcal{J}$. The second order finite difference form of (8.11) fixes these virtual boundary points by

$$\psi_{\mathcal{I}+1,j} = \psi_{\mathcal{I}-1,j} - 2h_x \left(\psi_{\mathcal{I},j} - 1\right). \tag{8.21}$$

Finally, the virtual points outside $\theta = 0$ and $\pi/2$ are fixed by the second order finite difference form of (8.12). These virtual points are located at $j = -1$ or $\mathcal{J} + 1$ and $i = 0, \ldots, \mathcal{I}$, and are defined by

$$\psi_{i,-1} = \psi_{i,1} \tag{8.22}$$

and

$$\psi_{i,\mathcal{J}+1} = \psi_{i,\mathcal{J}-1}. \tag{8.23}$$

The computational mesh used can be visualized as in Figure 8.1. The collection of points which "sample" the computational domain (and the virtual boundary points) are thought of as a two-dimensional object mimicking the two-dimensional domain. Each point is uniquely identified by an index pair. It is often convenient to think of the collection of points as a one-dimensional *vector* instead of a two-dimensional mesh. In this case, some ordering of the points is assumed and each mesh point (and virtual boundary point) maps to a unique element of the vector. When viewed in this manner, objects such as the conformal factor will carry a single index instead of two as in (8.15).

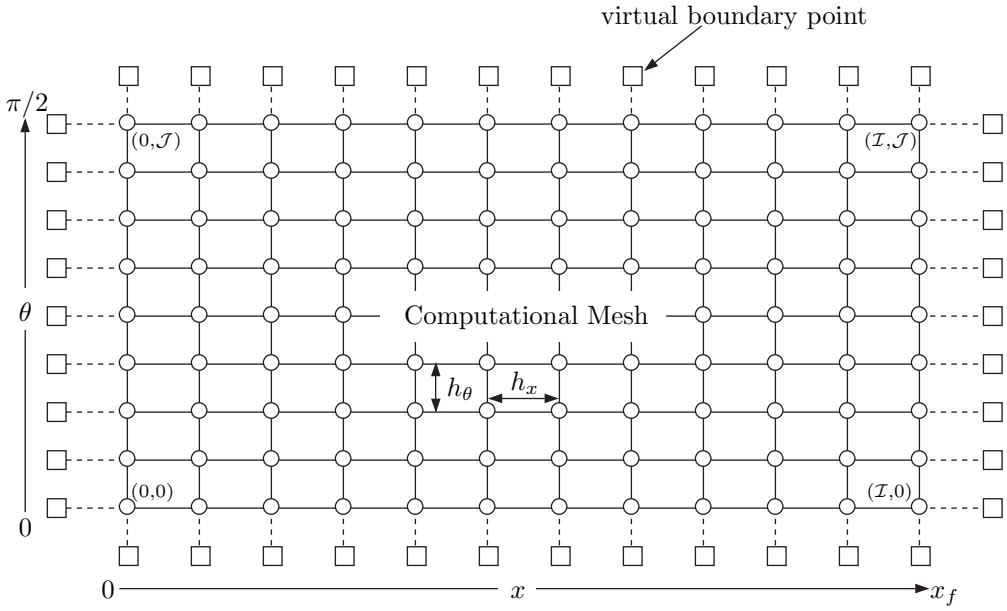


Figure 8.1: Computational mesh and "virtual" boundary points.

If we think of the conformal factor as a vector, then the set of equations given by (8.16), (8.20), (8.21), (8.22), and (8.23) can be thought of abstractly as a *vector of equations* which acts on the vector of conformal factor values

$$\mathcal{F}_a\left[\psi\right] = 0. \tag{8.24}$$

In general, $\mathcal{F}_a[\psi]$ will be a vector of nonlinear equations as is the case for the Hamiltonian constraint (8.16). If the equations were linear (i.e. the extrinsic curvature is zero), then (8.24) can be represented by a square matrix dotted into the vector ψ_a, all set equal to some constant vector containing the terms which do not depend on the conformal factor. The solution of the finite difference equations for the value of the conformal factor at the mesh points, then, reduces to the problem of inverting a large matrix.

In the case of the Hamiltonian constraint, the system is not linear and another approach must be found. There is no ideal approach for the solution of a set of nonlinear algebraic equations. One approach for solving them is the iterative Newton-Raphson method for nonlinear systems (*cf.* Press *et al.* [1988]). Assume that ψ_a is some initial guess at the solution to (8.24). Next, assume that the actual solution is given by $\psi_a + \delta\psi_a$ and expand (8.24) in a Taylor series. Truncating at linear order, we find

$$\mathcal{F}_a\left[\psi + \delta\psi\right] = \mathcal{F}_a\left[\psi\right] + \sum_b \left.\frac{\partial \mathcal{F}_a}{\partial \psi_b}\right|_\psi \delta\psi_b + \mathcal{O}\left(\delta\psi^2\right) = 0. \tag{8.25}$$

If we define the linearized coefficient matrix $\mathcal{L}_{ab}$ as

$$\mathcal{L}_{ab} \equiv \left. \frac{\partial \mathcal{F}_a}{\partial \psi_b} \right|_{\psi} \tag{8.26}$$

and the "residual" vector $\mathcal{R}_a$ as

$$\mathcal{R}_a \equiv -\mathcal{F}_a \left[\psi \right], \tag{8.27}$$

then the solution, $\delta\psi_a$, of the linearized equation

$$\sum_b \mathcal{L}_{ab} \delta\psi_b = \mathcal{R}_a \tag{8.28}$$

gives a first-order accurate correction to the initial guess ψ_a. Updating the initial guess ($\psi_a \rightarrow \psi_a + \delta\psi_a$) and iterating until the correction becomes negligible everywhere will (in the absence of pathological sets of equations) yield a solution to the nonlinear equations (8.24) to any desired accuracy.

Direct solutions of the difference equations (i.e., those which directly invert the coefficient or linearized coefficient matrix) are the preferred method of solving the finite difference equations whenever it is possible. It is often the case, however, that the coefficient matrix is too large and requires too much computer memory to be directly inverted. If this is the case, other approximation methods can be used such as simultaneous over-relaxation (SOR), alternating direction implicit (ADI), conjugate gradient (CG), and many others (*cf.* Press *et al.* [1988] or Ames [1977]). All such approximation schemes iteratively converge to the solution which would be found by a "direct" solution. The advantages of one over another deal with rates of convergence, computational efficiency, and the requirement of specific symmetries in the coefficient matrix. Perhaps the most efficient method for solving the difference equations is the multigrid (MG) approach. The use of this method for solving the Hamiltonian constraint has been discussed in Choptuik [1982], Choptuik and Unruh [1986], and Cook [1989]. I have used the MG approach for the solution of the finite difference equations in the case of a single hole. The details of the MG method are left to Appendix A and the references therein.

Given a solution to the finite difference form of the Hamiltonian constraint, it is important to extract any physically significant information about the initial data. Of fundamental interest is the total ADM energy of the initial slice defined by (7.9). In terms of the conformal factor and using gravitational units, this becomes

$$E = -\frac{1}{2\pi} \oint_{\infty} \bar{D}^i \psi d^2 \bar{S}_i. \tag{8.29}$$

This is not, however, the best form to use for computing the total energy. First, we recall that the computational domain does not extend to infinity and so this integral must be approximated by the integral over the outer boundary at a finite radius. Second, evaluating (8.29) from numerical data will require that a numerical derivative be computed in order to evaluate the integrand. Such a numerical derivative would necessarily add error to the evaluation of (8.29). An alternate method for evaluating the total energy (*cf.* Bowen and York [1980]) can be derived by applying Gauss' law to (8.29). The result is

$$\begin{aligned} E &= \frac{1}{2\pi} \oint_{r=a} \bar{D}^i \psi d^2 \bar{S}_i - \frac{1}{2\pi} \int_{r>a} \overline{\nabla}^2 \psi d^3 \bar{V} \\ &= \frac{1}{4\pi} \oint_{r=a} \frac{\psi}{r} d^2 \bar{S} + \frac{1}{16\pi} \int_{r>a} \psi^{-7} \bar{A}_{ij} \bar{A}^{ij} d^3 \bar{V}, \end{aligned} \tag{8.30}$$

where the Hamiltonian constraint (4.8) and the inner boundary condition (7.2) have been used. (Note that the unit normal for the surface integral over the inner boundary points out of the domain, i.e. toward the origin.)

This form for the total energy is much superior to (8.29). The computational approximation of a finite domain, however, means that the volume integral in (8.30) will be cut off radially at the outer boundary. Because the integrand falls off as $\mathcal{O}(r^{-2})$, the error in having a finite outer boundary will, nonetheless, be small if the boundary is far enough out. The major portion of the energy results from the surface integral and the inner regions of the volume integral. In terms of the coordinate system being used and in the case of axisymmetry, the total energy can be written in dimensionless form as

$$\frac{E}{a} \cong \frac{1}{2} \int_{\theta=0}^{\theta=\pi} \psi_{(x=0)} \sin\theta d\theta + \frac{1}{8} \int_{\theta=0}^{\theta=\pi} \int_{x=0}^{x=x_f} \psi^{-7} \left(a^2 \bar{A}_{ij} \bar{A}^{ij} \right) e^{3x} dx d\theta. \tag{8.31}$$

After computing the total energy, one might consider computing the higher order moments in the multipole expansion. Because of the reflection symmetry through $\theta = \pi/2$, the dipole moment vanishes identically. While higher moments will not vanish identically, it is not clear as to the usefulness of these quantities and they have not been calculated. A quantity that *is* of interest is the area of the throat or minimal surface *in the physical space*. This quantity is defined as

$$A_{MS} = \oint_{r=a} \psi^4 d^2 \bar{S}. \tag{8.32}$$

Associated with the area of the minimal surface is a mass defined similarly to irreducible mass by

$$M = \sqrt{\frac{A}{16\pi}}. \tag{8.33}$$

In terms of the coordinate system being used and in the case of axisymmetry, the area of the minimal surface can be written in dimensionless form as

$$\frac{A_{MS}}{a^2} = 2\pi \int_{\theta=0}^{\theta=\pi} \psi^4_{(x=0)} \sin\theta d\theta. \tag{8.34}$$

A code was constructed to solve the finite difference equations described above using the multigrid algorithm described in Appendix A. After obtaining a solution, the total energy and minimal surface area and mass are integrated numerically. In order to test the accuracy of the code, use was made of an exact solution to a fully non-linear "model" Hamiltonian constraint found by Bowen and York [1980]. The model problem is obtained by considering a non-physical, spherically symmetric extrinsic curvature whose square is given by

$$a^2 \bar{A}^T_{ij} \bar{A}^{Tij} = 24 \left(\frac{P}{a}\right)^2 e^{-6x} \sinh^2 x. \tag{8.35}$$

The solution to the model problem is

$$\psi_{model} = e^{-x/2} \left[6 + 2\cosh 2x + 4 \left(\frac{E}{a}\right) \cosh x \right]^{1/4}, \tag{8.36}$$

where

$$\frac{E}{a} = \sqrt{4 + \left(\frac{P}{a}\right)^2}. \tag{8.37}$$

From (8.34), the area of the minimal surface in the model problem is

$$\frac{A_{model}}{a^2} = 16\pi \left(2 + \frac{E}{a}\right) \tag{8.38}$$

and the mass is

$$\frac{M_{model}}{a} = \sqrt{2 + \frac{E}{a}}. \tag{8.39}$$

The code was run using (8.35) for a series of values of the momentum and using the same computational domain as was used later for the physical problem. Specifically, the outer boundary was set at $x = 10$. The radial discretization parameter was set at $\mathcal{I} = 1024$ and the angular parameter at $\mathcal{J} = 384$ on the finest grid used in the multigrid solution. Table 8.1 below summarizes the results of the computer solution compared with the exact solution. Full details on the multigrid solutions to the model problem as well as the physical problem can be found in Appendix B. The computed solution has proven to be accurate to roughly one part in 10,000 for all examined quantities.

Physical initial-data sets were generated with the same code using (8.7), (8.8), and (8.9) for the square of the extrinsic curvature. The same computational domain and discretization were used for

all cases as described above for the model problem. The results are summarized in Tables 8.2 and 8.3 below. The full details of the solutions can be found in Appendix B. In the tables below, the printed digits represent the significant digits of the printed values as determined by a conservative error estimate.

P/a	E_{exact}/a	$E_{comp.}/a$	M_{exact}/a	$M_{comp.}/a$
0.0	2.00000	1.99997	2.00000	1.99995
1.0	2.23607	2.23605	2.05817	2.05812
2.5	3.20156	3.20156	2.28069	2.28064
5.0	5.38517	5.38516	2.71757	2.71750
7.5	7.76209	7.76209	3.12443	3.12436
10.0	10.1980	10.1981	3.49257	3.49249
12.5	12.6590	12.6590	3.82871	3.82862
15.0	15.1328	15.1328	4.13917	4.13908
17.5	17.6139	17.6139	4.42876	4.42866

Table 8.1: Numerical solution of the model problem compared with the exact solution.

	$\bar{A}^{+}_{ij}$		$\bar{A}^{-}_{ij}$	
P/a	E/a	M_{MS}/a	E/a	M_{MS}/a
0.0	2.000	2.000	2.000	2.000
1.0	2.347	2.113	2.330	2.100
2.5	3.589	2.470	3.545	2.430
5.0	6.132	3.069	6.078	3.001
7.5	8.815	3.589	8.760	3.502
10.0	11.54	4.049	11.49	3.946
12.5	14.29	4.463	14.24	4.348
15.0	17.04	4.843	17.00	4.716
17.5	19.81	5.195	19.76	5.058

Table 8.2: Energy and minimal surface mass for a single black hole with linear momentum.

S/a^2	E/a	M_{MS}/a
0.0	2.000	2.000
1.0	2.048	2.033
3.0	2.328	2.227
10.0	3.477	3.034
30.0	5.759	4.673
100.0	10.41	8.071
300.0	17.99	13.67
1000.0	32.83	24.69
10000.0	103.8	77.56

Table 8.3: Energy and minimal surface mass for a single black hole with angular momentum.

Chapter 9: Axisymmetric Numerical Solutions of the Hamiltonian Constraint for Two Black Holes

To examine the case of two black holes, we must first define the configuration in the background Euclidean space. There are two natural length scales in the background space: the sizes of the throats and the separation of the centers of the throats. These length scales can be parameterized naturally by two dimensionless parameters, α and β. α has already been defined by equation (6.27) as the ratio of the sizes of the two throats. The second parameter is defined as the ratio of the separation of the centers of the two throats to the radius of the first hole. That is,

$$\beta \equiv \frac{|\mathbf{C}_1 - \mathbf{C}_2|}{a_1} = \zeta_1 - \zeta_2 \tag{9.1}$$

where the definitions in equation (6.16) have been used. In terms of scaled cylindrical coordinates, the domain of solution in the case of two holes is illustrated in Figure 9.1.

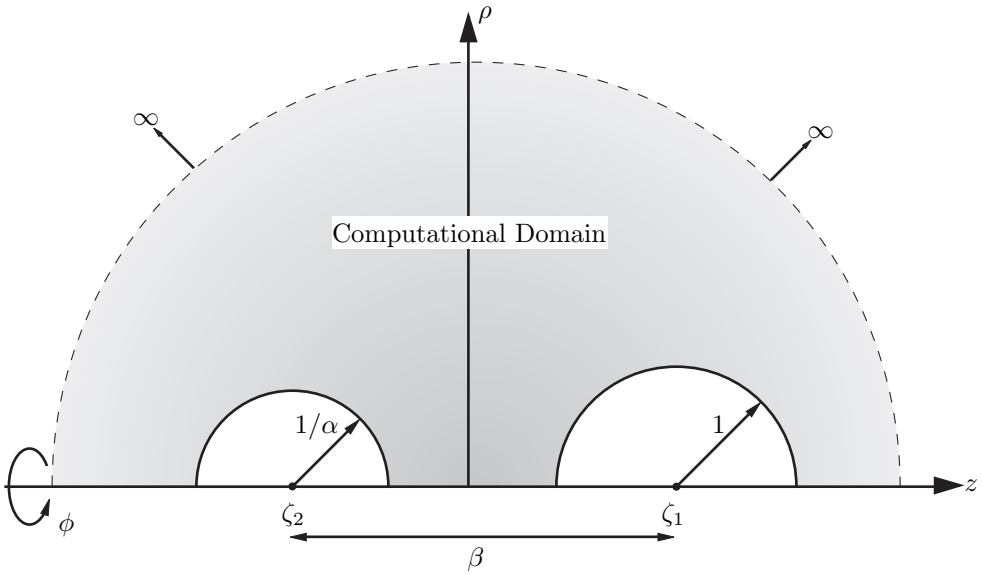


Figure 9.1: Two-hole background space parameterization and solution domain.

While cylindrical coordinates are useful for describing the configuration of the two holes in the background space, they are not well suited for use as the coordinate system in which the Hamiltonian constraint will be differenced. The primary deficiency of cylindrical coordinates is that the minimal

surfaces do not lie along constant coordinate surfaces, making the differencing of the inner boundary condition more difficult and less accurate. In choosing a coordinate system in which to difference the Hamiltonian constraint there are two primary considerations. First, the coordinate system should be orthogonal. Second, the coordinate system should possess constant coordinate surfaces which are coincident with the minimal surfaces. Because it is desired in the future to evolve these initial-data sets numerically and examine the gravitational radiation emitted, there is one additional condition on the coordinate system which should be considered. This condition is that the coordinate system should have a constant coordinate surface which is nearly spherical surrounding the two holes at large distances from the holes.

One coordinate system satisfying the three conditions listed above is known as Čadež coordinates. These coordinates were first used by Čadež [1971] in one of the early attempts at numerically solving the two-body problem. While these coordinates have all of the desired properties, there are also many difficulties associated with their use. It was, in fact, difficulties associated with the Čadež coordinates which hindered the last attempt at investigating the initial-data sets for two black holes conducted by Rauber [1985]. One difficulty associated with the use of Čadež coordinates is the fact that the coordinate system must be generated numerically. In addition, the coordinate system contains a coordinate singularity positioned at a point on the axis connecting the two holes.

While the Čadež coordinates are well suited for the numerical evolution of the two-body problem, the requirement of a nearly spherical outer boundary is not necessary for the solution of the initial-value problem. Ignoring this requirement, we find that bispherical coordinates satisfy the two primary conditions listed above. While bispherical coordinates also contain a coordinate singularity, it is located at spatial infinity and can be dealt with easily as I will show below. In the remainder of this chapter, I will describe an approach for solving the Hamiltonian constraint using the bispherical coordinate system. Using solutions generated by this approach as a guide, I will then investigate, in the next chapter, the solution of the Hamiltonian constraint using Čadež coordinates. As with the solutions to the one-hole problem, I will reserve the interpretation of the results of the numerical calculations for a later chapter.

The bispherical coordinate transformations to cylindrical coordinates are given by

$$\rho = \frac{C \sin \xi}{\cosh \eta - \cos \xi}, \tag{9.2}$$

$$z = \frac{C \sinh \eta}{\cosh \eta - \cos \xi}, \tag{9.3}$$

and

$$\phi = \phi. \tag{9.4}$$

C is a dimensionfull constant which sets the scale of the coordinates. The $\eta = constant$ surfaces are spheres centered on $z = C\coth\eta$ and with radius $C/\sinh\eta$. If we define η_0^+ to be the coordinate surface coincident with the hole of radius a_1 and η_0^- to be the coordinate surface coincident with the hole of radius a_2, then we find that the dimensioning constant is given by

$$C = a_1 \sinh\eta_0^+. \tag{9.5}$$

The configuration parameters α and β can be written as

$$\alpha = -\frac{\sinh\eta_0^-}{\sinh\eta_0^+} \tag{9.6}$$

and

$$\beta = -\frac{\sinh\left(\eta_0^+ - \eta_0^-\right)}{\sinh\eta_0^-}. \tag{9.7}$$

Using a relation similar to (9.5), but for the other hole, we find

$$\eta_0^- = -\sinh^{-1}\left[\alpha\sinh\eta_0^+\right]. \tag{9.8}$$

Using (9.8) along with (9.6) and (9.7), we find the relationship

$$\beta\sqrt{1+\alpha^2\sinh^2\eta_0^+} - \sqrt{1+\alpha^2\beta^2\sinh^2\eta_0^+} = \frac{1}{\alpha}. \tag{9.9}$$

Solving (9.9) for η_0^+ gives

$$\eta_0^+ = \ln\sqrt{\frac{\chi}{2} + \frac{1}{2}\sqrt{\chi^2-4}}, \tag{9.10}$$

where

$$\chi \equiv \beta^2 + \frac{1}{\beta^2}\left(1+\frac{1}{\alpha^4}\right) - \frac{2}{\alpha^2}\left(1+\frac{1}{\beta^2}\right). \tag{9.11}$$

Equations (9.10) and (9.8) determine the constant coordinate surfaces which are coincident with the throats of the two black holes given the background configuration parameters α and β. The dimensionfull constant C is also fixed by the choice of these two parameters and the metric becomes

$$ds^2 = \frac{a_1^2\sinh^2\eta_0^+}{\left(\cosh\eta - \cos\xi\right)^2}\left(d\eta^2 + d\xi^2 + \sin^2\xi d\phi^2\right). \tag{9.12}$$

The coordinates (η, ξ, ϕ) are dimensionless, and the domain in which the Hamiltonian constraint must be solved (the top sheet) is $\eta_0^- \le \eta \le \eta_0^+$, $0 \le \xi \le \pi$, and $0 \le \phi < 2\pi$. This coordinate range covers the entire infinite domain of the top sheet even though the coordinates vary over a finite range. This is possible because of a coordinate singularity at infinity. Examining the metric (9.12) we see that it is conformally related to a cylindrical-like coordinate system, but the conformal

factor diverges as $\eta, \xi \to 0$. Looking at the coordinate transformations (9.2) and (9.3), we see that this corresponds to $\rho, z \to \infty$. Bispherical coordinates conformally compactify infinity to a one dimensional line. This behavior is the root of the problem in using bispherical coordinates in an evolution problem. On the other hand, for the time-independent problem of solving the Hamiltonian constraint, it is a bonus. In this case, the boundary condition of asymptotic flatness can be imposed exactly since infinity can be represented in the numerical domain.

Restricting to the case of axisymmetry, the Laplacian, written conservatively in bispherical coordinates, takes the form

$$\begin{aligned}\overline{\nabla}^2\psi = \frac{(\cosh\eta - \cos\xi)^3}{a_1^2 \sinh^2\eta_0^+}\Bigg\{&\frac{\partial}{\partial\eta}\left(\frac{1}{\cosh\eta - \cos\xi}\frac{\partial\psi}{\partial\eta}\right)\\ &+\frac{1}{\sin\xi}\frac{\partial}{\partial\xi}\left(\frac{\sin\xi}{\cosh\eta - \cos\xi}\frac{\partial\psi}{\partial\xi}\right)\Bigg\}.\end{aligned} \tag{9.13}$$

The boundary conditions (7.2) on the two inversion boundaries located at $\eta = \eta_0^{\pm}$ take the following form

$$\left[-\frac{(\cosh\eta - \cos\xi)}{\sinh\eta}\frac{\partial\psi}{\partial\eta} + \frac{\psi}{2}\right]_{\eta=\eta_0^{\pm}} = 0. \tag{9.14}$$

Axisymmetry demands that on the $\xi = 0$ and $\xi = \pi$ boundaries (except at $\eta = \xi = 0$) that

$$\left.\frac{\partial\psi}{\partial\xi}\right|_{\xi=0,\pi} = 0. \tag{9.15}$$

Finally, at $\eta = \xi = 0$ we demand the Dirichlet boundary condition

$$\psi_{(\eta=0,\xi=0)} = 1, \tag{9.16}$$

which fixes the asymptotic flatness boundary condition at infinity with no approximation. As in the one-hole case, a limiting form of the Laplacian must be found along the $\rho = 0$ axis. Using the axisymmetry boundary condition (9.15) and L'Hôpital's rule, we find that

$$\lim_{\xi\to 0,\pi}\frac{1}{\sin\xi}\frac{\partial}{\partial\xi}\left(\frac{\sin\xi}{\cosh\eta - \cos\xi}\frac{\partial\psi}{\partial\xi}\right) = 2\frac{\partial}{\partial\xi}\left(\frac{1}{\cosh\eta - \cos\xi}\frac{\partial\psi}{\partial\xi}\right). \tag{9.17}$$

The Laplacian given by (9.13) and (9.17) along with the boundary conditions (9.14), (9.15), and (9.16) form the base of equations by which the Hamiltonian constraint will be differenced in bispherical coordinates. To proceed with the differencing, a discretization of the domain must be chosen. The straightforward choice is

$$\eta_i = i * h_\eta + \eta_0^- \qquad \text{where} \quad i = 0, \ldots, \mathcal{I} \quad \text{and} \quad h_\eta = \frac{\left(\eta_0^+ - \eta_0^-\right)}{\mathcal{I}} \tag{9.18}$$

and

$$\xi_j = j * h_\xi \qquad \text{where} \quad j = 0, \ldots, \mathcal{J} \quad \text{and} \quad h_\xi = \frac{\pi}{J}. \tag{9.19}$$

This discretization cannot be used, however, because (9.18) does not guarantee that $\eta = 0$ will exist in the discretization as it must in order for the asymptotic flatness boundary condition (9.16) to be applied.

In order to assure that $\eta = 0$ is in the discrete domain, I choose η to be a nonlinear function of a new coordinate variable s. The simplest choice is to choose η to be a quadratic function of the following form:

$$\eta = \eta(s) = f * s^2 + g * s, \tag{9.20}$$

where f and g are constants to be determined so that $\eta = 0$ will be contained in the discrete domain. Consider the following discretization of s,

$$s_i = i * h_s \qquad \text{where} \qquad i = -\mathcal{S}^-, \ldots, 0, \ldots, \mathcal{S}^+ \tag{9.21}$$

and

$$h_s = \frac{1}{\mathcal{S}} \qquad \text{where} \qquad \mathcal{S} = \mathcal{S}^+ + \mathcal{S}^-. \tag{9.22}$$

Together, (9.20) and (9.21) guarantee that $\eta(0) = 0$ is in the discrete domain. The two constants f and g can be chosen so that the end points of the range of s give the correct coordinate boundaries for η. Let the upper and lower limits on the range of s be defined as

$$s^+ \equiv \mathcal{S}^+ * h_s = \mathcal{S}^+ / \mathcal{S} \tag{9.23}$$

and

$$s^- \equiv -\mathcal{S}^- * h_s = -\mathcal{S}^- / \mathcal{S}. \tag{9.24}$$

The two constants f and g are fixed by the two equations

$$\eta(s^+) = \eta_0^+ \qquad \text{and} \qquad \eta(s^-) = \eta_0^- . \tag{9.25}$$

The result is

$$f = \frac{\mathcal{S}}{\mathcal{S}^+}\eta_0^+ + \frac{\mathcal{S}}{\mathcal{S}^-}\eta_0^- \tag{9.26}$$

and

$$g = \frac{\mathcal{S}^-}{\mathcal{S}^+}\eta_0^+ - \frac{\mathcal{S}^+}{\mathcal{S}^-}\eta_0^- . \tag{9.27}$$

In order for s to represent an acceptable coordinate, the coordinate transformation (9.20) must be invertible over the coordinate range in which s is used. The invertibility of the coordinate

transformation can be examined through the Jacobian of the coordinate transformation. Let $J(s)$ represent the Jacobian which is defined as

$$J(s) \equiv \frac{\partial \eta(s)}{\partial s} = 2f * s + g. \tag{9.28}$$

If the Jacobian is positive on both ends of the coordinate range in which s is used, then it will be positive everywhere in the range (since (9.20) is quadratic). We want $J(s)$ to be uniformly positive since this implies that η will be monotonically increasing as s increases. To ensure that any virtual boundary points are also located in the range in which the coordinate transformation is valid, we demand that

$$J(s^- - h_s) > 0 \qquad \text{and} \qquad J(s^+ + h_s) > 0. \tag{9.29}$$

From (9.29), a sufficient condition for the coordinate system to be well behaved is

$$\frac{\mathcal{S}^+}{\mathcal{S}^-}\frac{(2+\mathcal{S}^+)}{(2+3\mathcal{S}^-)} < \frac{\eta_0^+}{-\eta_0^+} < \frac{\mathcal{S}^+}{\mathcal{S}^-}\frac{(2+3\mathcal{S}^+)}{(2+\mathcal{S}^-)}. \tag{9.30}$$

In practice, one will choose values for α and β to fix the configuration and through (9.10), (9.11), and (9.8) these fix η_0^+ and η_0^-. Next, one chooses values for $\mathcal{S}^+$ and $\mathcal{S}^-$ so that (9.30) is satisfied. The discretization of the (s,ξ)-domain is then given by (9.19) and (9.21). The second order, conservative finite difference form of the Hamiltonian constraint is expressed as

$$\begin{aligned}\mathcal{A}^+_{i,j}\left(\psi_{i+1,j}-\psi_{i,j}\right) + \mathcal{A}^-_{i,j}\left(\psi_{i-1,j}-\psi_{i,j}\right) + \mathcal{B}^+_{i,j}\left(\psi_{i,j+1}-\psi_{i,j}\right) \\ + \mathcal{B}^-_{i,j}\left(\psi_{i,j-1}-\psi_{i,j}\right) + \frac{1}{8}\psi^{-7}_{i,j}\left[a_1^2\bar{A}_{\ell m}\bar{A}^{\ell m}\right]_{i,j} = 0,\end{aligned} \tag{9.31}$$

where

$$\mathcal{A}^{\pm}_{i,j} \equiv \frac{\left(\cosh\eta(s_i)-\cos\xi_j\right)^3}{h_s^2 J(s_i)\sinh^2\eta_o^+}\frac{1}{\left(\cosh\eta(s_i\pm h_s/2)-\cos\xi_j\right)J(s_i\pm h_s/2)} \quad : \text{for all } (i,j) \text{ except } i=j=0 \tag{9.32}$$

and

$$\mathcal{B}^{\pm}_{i,j} \equiv \begin{cases} \frac{(\cosh\eta(s_i)-\cos\xi_j)^3}{h_\xi^2\sin\xi_j\sinh^2\eta_o^+}\frac{\sin\left(\xi_j\pm h_\xi/2\right)}{\left(\cosh\eta(s_i)-\cos\left(\xi_j\pm h_\xi/2\right)\right)} & : \text{for all } i \text{ and } j\neq 0,\mathcal{J} \\ \frac{(\cosh\eta(s_i)-\cos\xi_j)^3}{h_\xi^2\sinh^2\eta_o^+}\frac{2}{\left(\cosh\eta(s_i)-\cos\left(\xi_j\pm h_\xi/2\right)\right)} & : \begin{array}{r}\text{for all } i \text{ and } j=0,\mathcal{J} \\ \text{except } i=j=0.\end{array}\end{cases} \tag{9.33}$$

The square of the extrinsic curvature appearing in (9.31) can be evaluated numerically by the technique discussed in Chapter 6.

The difference equations for points on the boundaries of the domain depend on values of the conformal factor outside the computational domain. These unknowns are eliminated from the difference equations by the *implicit* use of "virtual" boundary points. In the one-hole case, the virtual boundary points were *explicitly* included in the computational mesh. In the case of the bispherical

coordinate discretization of the Hamiltonian constraint, I have chosen the alternate, but computationally equivalent, approach. Put in a form which is most convenient for eliminating the dependence on the virtual boundary points, the inner boundary condition (9.14) at $i = -\mathcal{S}^-$ is expressed as

$$\left(\psi_{-\mathcal{S}^- -1,j} - \psi_{-\mathcal{S}^-,j}\right) = \left(\psi_{-\mathcal{S}^- +1,j} - \psi_{-\mathcal{S}^-,j}\right) + \frac{1}{\mathcal{C}_{-\mathcal{S}^-,j}}\psi_{-\mathcal{S}^-,j}, \tag{9.34}$$

where

$$\mathcal{C}_{i,j} \equiv \frac{-\left(\cosh\eta(s_i) - \cos\xi_j\right)}{h_s J(s_i)\sinh(s_i)}. \tag{9.35}$$

The inner boundary condition (9.14) at $i = \mathcal{S}^+$ is expressed as

$$\left(\psi_{\mathcal{S}^+ +1,j} - \psi_{\mathcal{S}^+,j}\right) = \left(\psi_{\mathcal{S}^+ -1,j} - \psi_{\mathcal{S}^+,j}\right) - \frac{1}{\mathcal{C}_{\mathcal{S}^+,j}}\psi_{\mathcal{S}^+,j}. \tag{9.36}$$

The axisymmetric boundary conditions (9.15) give

$$\left(\psi_{i,-1} - \psi_{i,0}\right) = \left(\psi_{i,1} - \psi_{i,0}\right) \qquad : \qquad \text{for} \quad i \neq 0 \tag{9.37}$$

and

$$\left(\psi_{i,\mathcal{J}+1} - \psi_{i,\mathcal{J}}\right) = \left(\psi_{i,\mathcal{J}-1} - \psi_{i,\mathcal{J}}\right). \tag{9.38}$$

Finally, the Dirichlet boundary condition (9.16) fixes the solution at infinity to be asymptotically flat. This final equation simply gives

$$\psi_{0,0} = 1. \tag{9.39}$$

The differencing of the Hamiltonian constraint and boundary conditions given above produces a set of second order, conservative difference equations. The equations being second order means that the *truncation* error in the difference equations behaves like $\mathcal{O}(h_s^2) + \mathcal{O}(h_\xi^2)$. In general, this implies that the *discretization* error in the solution is also second order so that halving the mesh spacing in both directions increases the accuracy of the solution by a factor of four. In the case of bispherical coordinates, however, the presence of the coordinate singularity at $\eta = \xi = 0$ spoils the behavior of the discretization error which proves to be first order.

The difference equations are solved via the Newton-Raphson method for nonlinear systems described in Chapter 8. The linearized equation for the iterative correction is solved by means of the LINPACK routines for factoring (DGBFA) and solving (DGBSL) general banded matrices. There are advantages and disadvantages to using a direct solver for this set of difference equations. The main advantage is that the solution of the difference equations can be found to nearly machine precision. Using solutions on several meshes with different mesh spacings and knowing that the

leading behavior of the discretization error of the solution is proportional to the mesh spacing, Richardson extrapolation (*cf.* Press *et al.* [1988]) can be used to estimate the solution to the *differential* equations. This procedure is limited, however, by one of the disadvantages of using a direct solver: the resolution of the mesh is limited by the physical memory of the computer. For a direct solver, there must be enough computer memory available to store and invert the coefficient matrix. Currently, the two-dimensional mesh size is limited to roughly 200×200 mesh points. Because higher order truncation error effects are totally dominated by the lower order truncation error term only in the limit that the mesh spacing becomes asymptotically small, the discretization error only becomes first order asymptotically. The limit in the mesh resolution mentioned above thus greatly limits the accuracy with which results can be obtained by Richardson extrapolation.

A solution to the finite difference equations for the Hamiltonian constraint can be used in numerical integrals for various physically significant quantities. As in the one-hole case, the total ADM energy and the areas of the minimal surfaces will be computed. In the case of two holes, the dipole moment of the energy distribution will not, in general, vanish. Since this quantity is important in the asymptotic expansion of the conformal factor (7.26) it will also be computed. One final quantity which is relevant in the case of two holes is the proper separation of the two holes in the physical space.

The total energy integral is given by (8.29) in gravitational units. Using Gauss' law, one can transform it into a form similar to (8.30), which consists of a volume integral and, in the case of two holes, two surface integrals. In terms of bispherical coordinates, the total energy for an axisymmetric system can be expressed in dimensionless form as

$$\begin{aligned}\frac{E}{a_1} = \frac{\alpha \sinh^2 \eta_0^+}{2} \int_0^\pi \frac{\psi_{(\eta=\eta_0^-)} \sin\xi}{\left(\cosh\eta_0^- - \cos\xi\right)^2} d\xi + \frac{\sinh^2 \eta_0^+}{2} \int_0^\pi \frac{\psi_{(\eta=\eta_0^+)} \sin\xi}{\left(\cosh\eta_0^+ - \cos\xi\right)^2} d\xi \\ + \frac{\sinh^3 \eta_0^+}{8} \int_{\xi=0}^{\xi=\pi} \int_{\eta=\eta_0^-}^{\eta=\eta_0^+} \frac{\psi^{-7} \left(a_1^2 \bar{A}_{ij} \bar{A}^{ij}\right) \sin\xi}{\left(\cosh\eta - \cos\xi\right)^3} d\eta d\xi.\end{aligned} \tag{9.40}$$

Note that the range of the volume integral in (9.40) covers the singular point in the coordinate system. Care must be taken in integrating this region. An extrapolative integral formula (*cf.* Press *et al.* [1988]) must be used in the numerical approximation of the integral in order to avoid the divergence of the integrand.

For an axisymmetric system, only the z-component of the dipole moment will not vanish identically. In terms of gravitational units, and written in terms of the conformal factor, (7.10) takes the form

$$d_z = -\frac{1}{2\pi} \oint_\infty \left\{ z \bar{D}^k \psi + \delta_z^k \left(1 - \psi\right) \right\} d^2 \bar{S}_k. \tag{9.41}$$

Note that this integral must be written using Cartesian components. Using Gauss' law, (9.41) becomes

$$d_z = \frac{1}{2\pi}\oint_{a_2}\left\{z\bar{D}^k\psi + \delta_z^k\left(1-\psi\right)\right\}d^2\bar{S}_k + \frac{1}{2\pi}\oint_{a_1}\left\{z\bar{D}^k\psi + \delta_z^k\left(1-\psi\right)\right\}d^2\bar{S}_k + \frac{1}{16\pi}\int_V z\psi^{-7}\bar{A}_{ij}\bar{A}^{ij}d^3\bar{V}. \tag{9.42}$$

Finally, in terms of bispherical coordinates, the z-component of the dipole moment can be written in dimensionless form as

$$\begin{aligned}\frac{d_z}{a_1^2} = \alpha\sinh^3\eta_0^+\int_0^\pi\left\{\frac{(1-\psi/2)\sinh\eta_0^-}{\left(\cosh\eta_0^- - \cos\xi\right)^3} - \frac{(1-\psi)\coth\eta_0^-}{\left(\cosh\eta_0^- - \cos\xi\right)^2}\right\}\sin\xi d\xi \\ +\sinh^3\eta_0^+\int_0^\pi\left\{\frac{(1-\psi/2)\sinh\eta_0^+}{\left(\cosh\eta_0^+ - \cos\xi\right)^3} - \frac{(1-\psi)\coth\eta_0^+}{\left(\cosh\eta_0^+ - \cos\xi\right)^2}\right\}\sin\xi d\xi \\ +\frac{\sinh^4\eta_0^+}{8}\int_{\xi=0}^{\xi=\pi}\int_{\eta=\eta_0^-}^{\eta=\eta_0^+}\frac{\psi^{-7}\left(a_1^2\bar{A}_{ij}\bar{A}^{ij}\right)}{\left(\cosh\eta-\cos\xi\right)^4}\sinh\eta\sin\xi d\eta d\xi.\end{aligned} \tag{9.43}$$

Again, care must be taken in numerically evaluating the volume integral since the coordinate singularity is in the region of integration.

The areas of the minimal surfaces are given by two integrals of the form (8.32). In terms of bispherical coordinates, the two areas, A_{MS}^+ and A_{MS}^-, are given in dimensionless form by

$$\frac{A_{MS}^\pm}{a_1^2} = 2\pi\sinh^2\eta_0^+\int_0^\pi\frac{\psi^4_{(\eta=\eta_0^\pm)}\sin\xi}{\left(\cosh\eta_0^\pm - \cos\xi\right)^2}d\xi. \tag{9.44}$$

The proper separation of the two holes is given by an integral of the physical metric along the line connecting the two holes. In terms of bispherical coordinates, this is given in dimensionless form by

$$\frac{L}{a_1} = \sinh\eta_0^+\int_{\eta_0^-}^{\eta_0^+}\frac{\psi^2_{(\xi=\pi)}}{\cosh\eta+1}d\eta. \tag{9.45}$$

Unlike the one-hole case, there is no known model problem which can be used to test the code for solving the full nonlinear difference equations. However, there are two useful scenarios which can be used to test the code. First, when the initial configuration is time-symmetric, then the exact solution is known. Equations (7.32) through (7.40) describe the numerical approach for computing the exact solution for the conformal factor as well as the total energy and dipole moment. The code can be run for several configurations which will test the validity and accuracy of the code's solution of the linear problem and the surface integral parts of the energy and dipole moment integrals. Table 9.1 below compairs the Richardson extrapolated ADM energy from the numerical solutions with the analytic result for several cases with $\alpha = 1$.

β	E/a_1 (80)	E/a_1 (120)	E/a_1 (160)	E/a_1 (*extrap.*)	E/a_1 (*analytic*)	relative error
3	6.0641	6.0902	6.1031	6.1422	6.1415	−0.01%
4	5.3215	5.3362	5.3434	5.3653	5.3642	−0.02%
5	4.9785	4.9897	4.9952	5.0118	5.0106	−0.02%
6	4.7777	4.7872	4.7918	4.8059	4.8046	−0.03%
7	4.6452	4.6538	4.6578	4.6704	4.6690	−0.03%
8	4.5511	4.5590	4.5627	4.5742	4.5727	−0.03%
9	4.4807	4.4881	4.4915	4.5024	4.5008	−0.04%
10	4.4261	4.4331	4.4364	4.4466	4.4449	−0.04%
11	4.3824	4.3892	4.3923	4.4021	4.4003	−0.04%
12	4.3468	4.3533	4.3562	4.3657	4.3639	−0.04%

Table 9.1: ADM energy of time-symmetric solutions of the Hamiltonian constraint at (80×80), (120×120), and (160×160) mesh resolutions, Richardson extrapolated and compared with the analytic solution for the ADM energy. β indicates the separation of the two holes.

To test the nonlinear aspects of the difference equations, the computation of the extrinsic curvature, and to test the accuracy of the numerical approximations of the volume integrals in the energy and dipole moment, the code can be run in a configuration in which α and β are both large. This corresponds to the case of one hole being much larger than the other and the two holes being far apart. Putting linear or angular momentum only on the larger hole results in configurations which are comparable to the case of a single hole with linear or angular momentum for which highly accurate results are available. In Tables 9.2, 9.3, and 9.4, I display the results for a set of runs for which $\alpha = 20$ and $\beta = 50$. The mesh was taken to be 160×160.

P/a_1	E/a_1	M^+/a_1	M^-/a_1	$(E - M^-)/a_1$
0.0	2.102	2.000	0.104	1.998
1.0	2.448	2.112	0.104	2.344
2.5	3.689	2.469	0.107	3.582
5.0	6.235	3.066	0.112	6.123
7.5	8.926	3.586	0.116	8.810
10.0	11.67	4.045	0.121	11.55
12.5	14.43	4.458	0.126	14.30
15.0	17.22	4.838	0.130	17.09
17.5	20.01	5.190	0.134	19.88

Table 9.2: Total energy and masses for two holes which are very far apart, the larger hole having linear momentum P. The Extrinsic Curvature obeys the isometry condition with the plus sign. $(\alpha = 20, \beta = 50)$

P/a_1	E/a_1	M^+/a_1	M^-/a_1	$(E-M^-)/a_1$
0.0	2.102	2.000	0.104	1.998
1.0	2.430	2.099	0.104	2.326
2.5	3.644	2.429	0.107	3.537
5.0	6.180	2.998	0.111	6.069
7.5	8.871	3.499	0.116	8.755
10.0	11.61	3.942	0.121	11.49
12.5	14.38	4.343	0.125	14.26
15.0	17.17	4.711	0.130	17.04
17.5	19.97	5.052	0.134	19.84

Table 9.3: Total energy and masses for two holes which are very far apart, the larger hole having linear momentum P. The Extrinsic Curvature obeys the isometry condition with the minus sign. ($\alpha = 20, \beta = 50$)

S/a_1^2	E/a_1	M^+/a_1	M^-/a_1	$(E-M^-)/a_1$
0.0	2.102	2.000	0.104	1.998
1.0	2.149	2.033	0.104	2.045
3.0	2.430	2.227	0.104	2.326
10.0	3.580	3.033	0.107	3.473
30.0	5.865	4.672	0.111	5.754
100.0	10.52	8.068	0.121	10.40
300.0	18.15	13.67	0.138	18.01
1000.0	33.12	24.68	0.172	32.95

Table 9.4: Total energy and masses for two holes which are very far apart, the larger hole having angular momentum S. The Extrinsic Curvature obeys the isometry condition with the minus sign. ($\alpha = 20, \beta = 50$)

Assume now that the two holes are far enough apart so that the binding energy is negligible compared to the total energy. Subtracting the mass of the small hole from the total energy of the system gives an energy for the single hole which has linear or angular momentum. This value, along with the mass of the larger hole, can be compared to the numerical results already calculated for a single hole in Chapter 8. Comparing the values of $(E-M^-)/a_1$ above against the values of E/a for the corresponding configurations in Tables 8.2 and 8.3 shows that all energies agree to within 0.4%. Comparing the values of M^+/a_1 to M/a shows even better agreement.

As in the case of the single hole, I will defer a physical interpretation of the initial-data sets to a later chapter. I will note now, however, that the parameter space associated with the two-hole configuration is far too large to be explored completely by numerical techniques. Unlike the case of a single hole, there is a two-dimensional parameter space (parameterized by α and β) associated with the initial positions of the two holes. There are then three more two-dimensional parameter spaces covering the choices for the linear and angular momentum vectors for the two holes and the choice of the isometry condition. If we consider these three parameter spaces separately (at most, only two can be considered at once), then the full parameter space of the two-hole problem is at least four-dimensional. There is no reasonable way to investigate the entire parameter space of the problem.

The most reasonable approach for exploring the possible configurations is to reduce the size of the parameter space by only considering configurations with some symmetry. For example, if we consider only configurations in which the two holes are of equal size, then the parameter space is restricted to the $\alpha = 1$ hyperplane. If, in addition, the magnitudes of the linear or angular momenta of the two holes are equal, then the parameter space is further reduced to two, two-dimensional parameter spaces corresponding to the cases where the momentum vectors are either parallel or anti-parallel. With these symmetries, the remaining parameter space can be sampled and the results can be effectively visualized. The results from an extensive sampling of this reduced parameter space are tabulated in Appendix C and are discussed in a later chapter.

Chapter 10: The Hamiltonian Constraint for Two Black Holes Using Čadež Coordinates

As mentioned in Chapter 9, the coordinate system first used by Čadež [1971] in his early investigations into black-hole collisions is the best coordinate system known at this time for investigating the numerical evolution of two-hole, initial-data sets. Unfortunately, this coordinate system is difficult to work with because it must be constructed numerically and because it contains a severe coordinate singularity. In this chapter, I will describe all aspects of the problem of defining Čadež coordinates and explore an approach for applying them to the problem of solving the Hamiltonian constraint for two black holes.

Čadež coordinates are defined in terms of a complex-plane transformation (*cf.* Moon and Spincer [1988]). Letting the base coordinate system be cylindrical coordinates, the complex variable ζ is defined as

$$\zeta \equiv z + i\rho. \tag{10.1}$$

The cylindrical coordinate z is then the real part of ζ and the cylindrical coordinate ρ is the imaginary part of ζ. The Čadež coordinates are defined as the real and imaginary parts of a complex function $\chi(\zeta)$. Specifically,

$$\eta(\rho, z) \equiv \Re e\chi(\zeta) \qquad \text{and} \qquad \xi(\rho, z) \equiv \Im m\chi(\zeta). \tag{10.2}$$

Defined in this way, the coordinate system is guaranteed to be orthogonal everywhere that χ is analytic. The explicit form of the complex function χ is taken to be

$$\chi(\zeta) \equiv C_0^+ \ln(\zeta - \zeta^+) + C_0^- \ln(\zeta - \zeta^-) + \sum_{n=1}^{\infty} \left\{ C_n^+ \left(\zeta - \zeta^+\right)^{-n} + C_n^- \left(\zeta - \zeta^-\right)^{-n} \right\}. \tag{10.3}$$

The coefficients $C_i^{\pm}$ are real scalars and the two complex parameters $\zeta^{\pm}$ will fix the locations of the two holes.

To see the general behavior of this transformation, consider the limit that $|\zeta|$ is large compared to $|\zeta^+|$ and $|\zeta^-|$. In this case, (10.3) becomes

$$\chi(\zeta) \approx \left(C_0^+ + C_0^-\right) \ln(\zeta) \tag{10.4}$$

and the coordinate transformations become

$$\eta(\rho, z) \approx \left(C_0^+ + C_0^-\right) \ln \sqrt{\rho^2 + z^2} \tag{10.5a}$$

and

$$\xi(\rho, z) \approx \left(C_0^+ + C_0^-\right) \arg(\zeta). \tag{10.5b}$$

We are free to scale the coordinate system so that $C_0^+ + C_0^- = 1$ and, in this limit, η is simply a logarithmically scaled, spherical-polar radial coordinate and ξ is simply the spherical-polar colatitude coordinate. This transition to spherical-polar behavior in the coordinates is precisely the desired behavior, at large distances from the holes, alluded to in Chapter 9.

If we consider only the logarithmic terms in (10.3) and take the limit that $\zeta \to \zeta^{\pm}$, then we find that the coordinates again approach logarithmically scaled, spherical-polar coordinates, but centered around $\zeta^{\pm}$. We see then that the $\eta = \textit{constant}$ surfaces near $\zeta^{\pm}$ form ovals surrounding ζ^+ and ζ^- and the coefficients in the infinite series in (10.3) can be chosen to make specific $\eta = \textit{constant}$ surfaces truly spherical. This is again the desired behavior, near the holes, for a coordinate system described in Chapter 9.

The coordinate system based on (10.3) thus has all of the properties desired for a coordinate system to be used for a two-hole manifold. Previous work (Čadež [1971], Smarr *et al.* [1976], Rauber [1985]) done with these coordinates has been restricted to the case in which the two holes are of equal size. This restriction simplifies the definition of the coordinate system (10.3). Here, however, I have extended the traditional definition of Čadež coordinates so that it can address problems in which the holes are not of equal size. The remaining task in defining the Čadež coordinates is to prescribe a method for fixing the coefficients $C_i^{\pm}$ and parameters $\zeta^{\pm}$.

As in the case of bispherical coordinates, I parameterize the configuration by the two dimensionless parameters α and β (*cf.* Chapter 9). In order to maintain the ability to transform to bispherical coordinates easily, I choose to locate the boundaries of the holes (throats) as prescribed in Chapter 9 for bispherical coordinates. This approach determines the two bispherical coordinate surfaces $\eta_0^{\pm}$ with which the throats are coincident. The two positional parameters $\zeta^{\pm}$ are then fixed as

$$\zeta^+ \equiv \cosh \eta_0^+ \qquad \text{and} \qquad \zeta^- \equiv \alpha^{-1} \cosh \eta_0^- . \tag{10.6}$$

In terms of the complex variable ζ, the two sets of points constituting the throats can be parameterized by $\theta^{\pm}$ in the following way:

$$\zeta(\theta^+) \equiv \zeta^+ + \cos\theta^+ + i \sin\theta^+ \qquad \text{for} \quad 0 \leq \theta^+ \leq \pi \tag{10.7}$$

and

$$\zeta(\theta^-) \equiv \zeta^- + \alpha^{-1}\left(\cos\theta^- + i\sin\theta^-\right) \qquad \text{for} \quad 0 \le \theta^- \le \pi. \tag{10.8}$$

Using (10.7) and (10.8), the $C_i^{\pm}$ coefficients are fixed by demanding that

$$\eta^+ = \Re e\chi(\zeta(\theta^+)) \qquad \text{and} \qquad \eta^- = \Re e\chi(\zeta(\theta^-)), \tag{10.9}$$

where $\eta^{\pm}$ are the coordinate values of the Čadež coordinate η for each of the throats and these can be freely chosen (the implications of their choice will be discussed below). The two equations in (10.9), evaluated at a large set of points on (10.7) and (10.8), yield a large set of equations which can be used to fix the $C_i^{\pm}$ coefficients numerically by a linear least squares fit. Finally, given values for the $C_i^{\pm}$ coefficients, they, and the values for $\eta^{\pm}$, are rescaled so that $C_0^+ + C_0^- = 1$.

Given a point in cylindrical coordinates, the corresponding point in Čadež coordinates is easily obtained from (10.2). However, given a point $\chi_0 = \chi(\eta, x)$ in Čadež coordinates, the corresponding point in cylindrical coordinates can only by found numerically. The inversion can be accomplished iteratively via Newton's method generalized for complex functions. The algorithm is

$$\zeta^{i+1} = \zeta^i - \left(\chi(\zeta^i) - \chi_0\right)\left(\left.\frac{\partial\chi}{\partial\zeta}\right|_{\zeta^i}\right)^{-1}. \tag{10.10}$$

Because of the behavior demanded in the coordinate system around the throats and at large distances, there is necessarily a critical point in the complex transformation (10.3). This point is defined by

$$\frac{\partial\chi(\zeta)}{\partial\zeta} = 0. \tag{10.11}$$

Recalling the Cauchy-Riemann conditions

$$\frac{\partial\eta}{\partial z} = \frac{\partial\xi}{\partial\rho} \qquad \text{and} \qquad \frac{\partial\eta}{\partial\rho} = -\frac{\partial\xi}{\partial z}, \tag{10.12}$$

the determinant of the Jacobian of the coordinate transformation becomes

$$J = \frac{\partial\eta}{\partial\rho}\frac{\partial\xi}{\partial z} - \frac{\partial\eta}{\partial z}\frac{\partial\xi}{\partial\rho} = -\left(\frac{\partial\eta}{\partial\rho}\right)^2 - \left(\frac{\partial\eta}{\partial z}\right)^2 = -\left|\frac{\partial\chi}{\partial\zeta}\right|^2. \tag{10.13}$$

Thus, the critical point in (10.3) is a saddle-point singularity of the coordinate system. This singular point will be located somewhere on the symmetry axis connecting the two throats. The exact location will be determined by the choices made for the values of $\eta^{\pm}$. In fact, the freedom to choose $\eta^{\pm}$ is used to position the singularity at some desired location.

The location of the singular point must be determined numerically. Having fixed the coefficients in the definition of (10.3) as describe above, equation (10.11) can be solved iteratively via Newton's method generalized for complex functions. The algorithm is

$$\zeta_s^{i+1} = \zeta_s^i - \left.\frac{\partial\chi}{\partial\zeta}\right|_{\zeta_s^i}\left(\left.\frac{\partial^2\chi}{\partial\zeta^2}\right|_{\zeta_s^i}\right)^{-1}, \tag{10.14}$$

where ζ_s denotes the singular value of ζ.

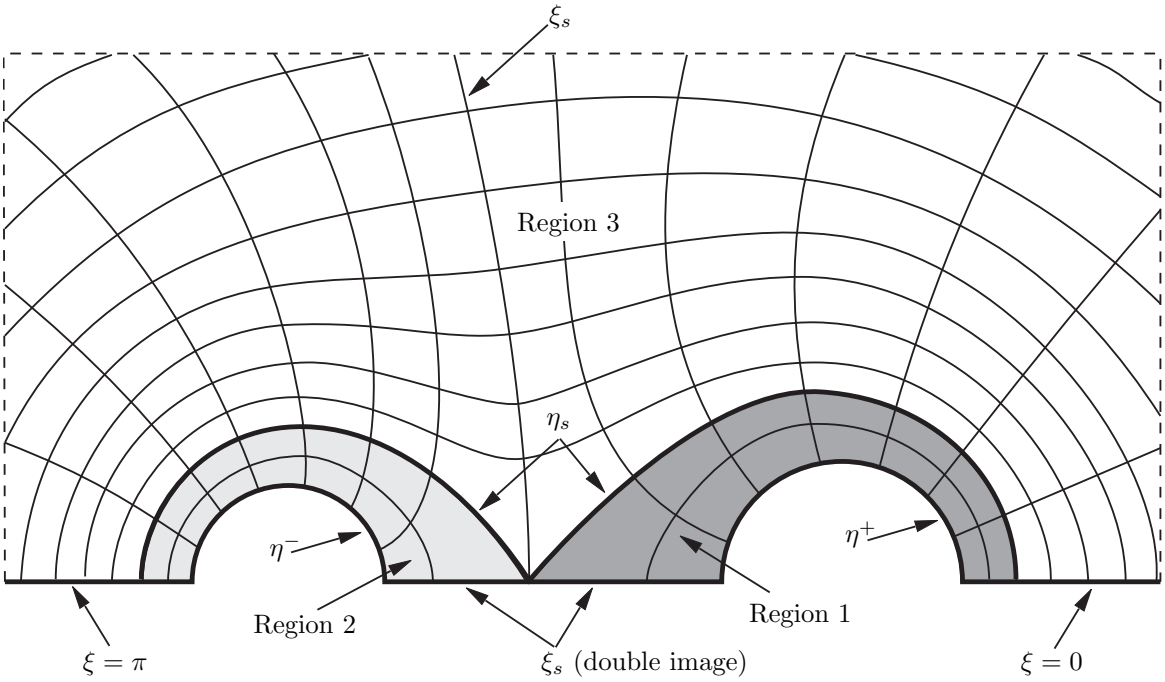


Figure 10.1: Čadež coordinates near the two holes showing important coordinate lines and the *three* region nature of the coordinate system.

Expanding (10.2) about the singular point and making use of the Cauchy-Riemann conditions, the coordinate transformation is given locally by

$$\eta(\rho, z) = \eta_s + \frac{\eta_{,\rho\rho}}{2}\left(\rho^2 - (z - z_s)^2\right) \quad \text{and} \quad \xi(\rho, z) = \xi_s - \eta_{,\rho\rho}\rho(z - z_s). \tag{10.15}$$

We see that $\xi = \xi_s$ is a double image along the z-axis and so must be handled carefully. The singular point effectively divides the Čadež coordinatization into three regions (see Figure 10.1): one surrounding each of the two throats and one region surrounding both throats and extending to infinity. With (η_s, ξ_s) denoting the singular point in Čadež coordinates, the three regions are given explicitly (assuming $C_0^+ + C_0^- = 1$) by

$$\text{Region 1} \equiv \begin{cases} \eta^+ \le \eta < \eta_s \\ 0 \le \xi \le \xi_s \end{cases}, \tag{10.16a}$$

$$\text{Region 2} \equiv \begin{cases} \eta^- \le \eta < \eta_s \\ \xi_s \le \xi \le \pi \end{cases}, \tag{10.16b}$$

and

$$\text{Region 3} \equiv \begin{cases} \eta_s \le \eta < \infty \\ 0 \le \xi \le \pi \end{cases}. \tag{10.16c}$$

The presence of this coordinate singularity places one final restriction on the definition of the Čadež coordinates. In order to handle the singular point numerically, I will demand that it always be represented in the discretization of the domain. In order to maintain a constant interval in the discretization of the η coordinate, it is necessary to demand that

$$\frac{\eta_s - \eta^+}{\eta_s - \eta^-} = \frac{\mathcal{I}^+}{\mathcal{I}^-}, \tag{10.17}$$

where $\mathcal{I}^+$ and $\mathcal{I}^-$ are positive integers. This demand can be satisfied iteratively by making initial guesses for $\eta^\pm$, solving for the Čadež coefficients, and determining an initial value for η_s. Next, if (10.17) is not satisfied, assume $\eta^+ \rightarrow \eta^+ + \varepsilon$ and $\eta^- \rightarrow \eta^- - \varepsilon$. Inserting these into (10.17) and solving for ε gives a correction for $\eta^\pm$. The new guesses for $\eta^\pm$ are used to solve again for the Čadež coefficients and for η_s and the iteration is continued until (10.17) is satisfied. This procedure has proven to be rapidly convergent.

With the Čadež coordinates fully defined, they can now be applied to the problem of solving the Hamiltonian constraint. Because of the nature of the coordinate transformations, all quantities are explicitly functions of the cylindrical coordinates and are functions of the Čadež coordinates only implicitly through the numerical inverse coordinate transformation. The Jacobian of the coordinate transformation from cylindrical to Čadež coordinates is given by

$$J_i^j = \begin{bmatrix} \eta_{,\rho} & 0 & \eta_{,z} \\ 0 & 1 & 0 \\ \eta_{,z} & 0 & -\eta_{,\rho} \end{bmatrix} \tag{10.18}$$

and the inverse Jacobian by

$$\left(J^{-1}\right)_i^j = \begin{bmatrix} \frac{\eta_{,\rho}}{\left(\eta_{,\rho}^2+\eta_{,z}^2\right)} & 0 & \frac{\eta_{,z}}{\left(\eta_{,\rho}^2+\eta_{,z}^2\right)} \\ 0 & 1 & 0 \\ \frac{\eta_{,z}}{\left(\eta_{,\rho}^2+\eta_{,z}^2\right)} & 0 & \frac{-\eta_{,\rho}}{\left(\eta_{,\rho}^2+\eta_{,z}^2\right)} \end{bmatrix}. \tag{10.19}$$

The metric is given by

$$ds^2 = \frac{a_1^2}{\eta_{,\rho}^2 + \eta_{,z}^2}\left(d\eta^2 + d\xi^2\right) + a_1^2\rho^2 d\phi^2, \tag{10.20}$$

where ρ and z are dimensionless coordinates scaled relative to a_1.

The Laplacian can be written in Čadež coordinates by applying the chain rule to the Laplacian in cylindrical coordinates as done by Rauber [1985]. The Laplacian, in this form, cannot be conservatively differenced which is a significant disadvantage to finding numerical solutions. However, by making use of the explicit form of the inverse Jacobian, the Laplacian can be rewritten in a form which can be conservatively differenced. Restricting to the case of axisymmetry, the Laplacian, written conservatively in Čadež coordinates, takes the form

$$\overline{\nabla}^2\psi = \frac{\eta_{,\rho}^2 + \eta_{,z}^2}{a_1^2\rho}\left\{\frac{\partial}{\partial\eta}\left(\rho\frac{\partial\psi}{\partial\eta}\right) + \frac{\partial}{\partial\xi}\left(\rho\frac{\partial\psi}{\partial\xi}\right)\right\}. \tag{10.21}$$

The boundary conditions (7.2) on the two inversion boundaries located at $\eta = \eta^{\pm}$ take the following forms,

$$\left[\sqrt{\eta_{,\rho}^2 + \eta_{,z}^2}\frac{\partial\psi}{\partial\eta} + \frac{\psi}{2}\right]_{\eta=\eta^+} = 0 \tag{10.22a}$$

and

$$\left[\sqrt{\eta_{,\rho}^2 + \eta_{,z}^2}\frac{\partial\psi}{\partial\eta} + \frac{\alpha\psi}{2}\right]_{\eta=\eta^-} = 0. \tag{10.22b}$$

On the z-axis, axisymmetry must be used to impose a boundary condition on this coordinate boundary. The z-axis exists on four separate segments in the Čadež coordinate system. The two boundaries for which $\xi = 0$ and $\xi = \pi$ correspond, respectively, to the z-axis extending to infinity from the right of the right-most hole and to the left of the left-most hole. The boundaries in Regions 1 and 2 (10.16a,b) for which $\xi = \xi_s$ and $\eta \leq \eta_s$ also correspond to the z-axis located between the holes. On these boundaries, axisymmetry demands that

$$\left.\frac{\partial\psi}{\partial\xi}\right|_{\rho=0} = 0. \tag{10.23}$$

As usual, a limiting form of the Laplacian must be found along the $\rho = 0$ axis. Using the axisymmetry boundary condition (10.23) and L'Hôpital's rule, the Laplacian takes the form

$$\left.\overline{\nabla}^2\psi\right|_{\rho=0} = \frac{\eta_{,z}^2}{a_1^2}\left\{\frac{\partial^2\psi}{\partial\eta^2} + 2\frac{\partial^2\psi}{\partial\xi^2}\right\} + \frac{\eta_{,\rho\rho}}{a_1^2}\frac{\partial\psi}{\partial\eta}. \tag{10.24}$$

The outer boundary of the domain in which the Hamiltonian constraint will be found does not conveniently extend to infinity where the boundary condition of asymptotic flatness is naturally applied. Instead, the approximate outer boundary condition (7.27) is applied at a finite but large radius. For the case of two black holes with axisymmetric linear momentum, and assuming gravitational units, (7.27) takes the form

$$\frac{\partial\psi}{\partial r} = \frac{1-\psi}{r} - \frac{1}{2r^3}\left\{d_z\cos\theta + \frac{9}{16}(P_1+P_2)^2\cos 2\theta\right\} + \frac{1}{r}\,\mathcal{O}(r^{-3}). \tag{10.25}$$

While Čadež coordinates do approach spherical coordinates at large distances from the holes, they are not exactly spherical coordinates and so the radial derivative must be handled carefully. The radial derivative can be written in terms of Čadež coordinates by the use of the chain rule as follows:

$$\begin{aligned}\frac{\partial}{\partial r} &= \cos\theta\frac{\partial}{\partial z} + \sin\theta\frac{\partial}{\partial\rho} \\ &= \frac{(z\eta_{,z} + \rho\eta_{,\rho})}{r}\frac{\partial}{\partial\eta} - \frac{(z\eta_{,\rho} - \rho\eta_{,z})}{r}\frac{\partial}{\partial\xi}.\end{aligned} \tag{10.26}$$

The outer boundary condition (10.25) can thus be written as

$$(z\eta_{,z} + \rho\eta_{,\rho})\frac{\partial\psi}{\partial\eta} - (z\eta_{,\rho} - \rho\eta_{,z})\frac{\partial\psi}{\partial\xi} + \frac{d_z z}{2(\rho^2+z^2)^{3/2}} + \frac{9}{32}(P_1+P_2)^2\frac{\left(z^2-\rho^2\right)}{\left(\rho^2+z^2\right)^2} = 0, \tag{10.27}$$

and is applied at an outer boundary where $\eta = \eta_f$. As discussed in Chapter 7, this boundary condition must be applied iteratively since it depends on the dipole moment d_z which must be determined from the solution.

The differencing of the Hamiltonian constraint is complicated by the discretization of the computational domain which, as mentioned above, is naturally divided into three regions. The η coordinate is discretized as

$$\eta_i = i * h_\eta + \eta_s \qquad \text{where} \qquad \begin{cases} i = -\mathcal{I}^+, \ldots, -1 & : \text{Region 1} \\ i = -\mathcal{I}^-, \ldots, -1 & : \text{Region 2} \\ i = 0, \ldots, \mathcal{I} & : \text{Region 3} \end{cases} \tag{10.28}$$

and

$$h_\eta = \frac{\eta_f - \eta_s}{\mathcal{I}} = \frac{\eta_s - \eta^+}{\mathcal{I}^+} = \frac{\eta_s - \eta^-}{\mathcal{I}^-}. \tag{10.29}$$

The discretization of the ξ coordinate cannot be done directly. The singular value of ξ must always occur in the discretization and this will not, in general, be compatible with a uniform discretization. This situation is analogous to that already dealt with for the discretization of the η coordinate in bispherical coordinates. I reparameterize ξ in terms of an auxiliary variable s so that

$$\xi = \xi(s) = f * s^2 + g * s + \xi_s. \tag{10.30}$$

The new coordinate s is then discretized as follows

$$s_j = j * h_s \qquad \text{where} \qquad j = -\mathcal{S}^+, \ldots, 0, \ldots, \mathcal{S}^- \tag{10.31}$$

and

$$h_s = \frac{1}{\mathcal{S}} \qquad \text{where} \qquad \mathcal{S} = \mathcal{S}^+ + \mathcal{S}^-. \tag{10.32}$$

Together, (10.31) and (10.32) guarantee that $\xi(0) = \xi_s$ is in the discrete domain. The two constants f and g are chosen so that the end points of the range of s give the correct coordinate boundaries for ξ. Let the upper and lower limits on the range of s be defined as

$$s^- \equiv \mathcal{S}^- * h_s = \mathcal{S}^- / \mathcal{S} \tag{10.33}$$

and

$$s^+ \equiv -\mathcal{S}^+ * h_s = -\mathcal{S}^+ / \mathcal{S}. \tag{10.34}$$

The two constants f and g are fixed by the two equations

$$\xi(s^+) = 0 \qquad \text{and} \qquad \xi(s^-) = \pi. \tag{10.35}$$

The result is

$$f = \frac{\mathcal{S}}{\mathcal{S}^-}\pi - \frac{\mathcal{S}^2}{\mathcal{S}^+\mathcal{S}^-}\xi_s \tag{10.36}$$

and

$$g = \frac{\mathcal{S}^+}{\mathcal{S}^-}\pi + \frac{\mathcal{S}\left(\mathcal{S}^- - \mathcal{S}^+\right)}{\mathcal{S}^+\mathcal{S}^-}\xi_s. \tag{10.37}$$

As was the case for bispherical coordinates, the Jacobian of the reparameterization is given by

$$J(s) \equiv \frac{\partial \xi(s)}{\partial s} = 2f * s + g, \tag{10.38}$$

and ξ will be monotonically increasing as s increases if and only if

$$J(s^+ - h_s) > 0 \qquad \text{and} \qquad J(s^- + h_s) > 0. \tag{10.39}$$

From (10.39), a sufficient condition for the coordinate system to be well behaved is

$$\frac{\mathcal{S}\left(2+\mathcal{S}\right)}{\mathcal{S}^+\left(2+\mathcal{S}+\mathcal{S}^-\right)} < \frac{\pi}{\xi_s} < \frac{\mathcal{S}\left(2+\mathcal{S}\right)}{\mathcal{S}^+\left(2+\mathcal{S}^+\right)}. \tag{10.40}$$

In practice, one chooses values for α and β to fix the configuration and also a value for the ratio $\mathcal{I}^+/\mathcal{I}^-$ (see (10.17)) to position the singular point. Next, one chooses values for $\mathcal{S}^+$ and $\mathcal{S}^-$ so that (10.40) is satisfied. The discretization of the (η, s)-domain is then given by (10.28) and (10.31). The second order, conservative finite difference form of the Hamiltonian constraint is expressed (except at the singular point $i = j = 0$) as

$$\begin{aligned}\mathcal{A}^+_{i,j}\left(\psi_{i+1,j} - \psi_{i,j}\right) + \mathcal{A}^-_{i,j}\left(\psi_{i-1,j} - \psi_{i,j}\right) + \mathcal{B}^+_{i,j}\left(\psi_{i,j+1} - \psi_{i,j}\right) \\ + \mathcal{B}^-_{i,j}\left(\psi_{i,j-1} - \psi_{i,j}\right) + \frac{1}{8}\psi^{-7}_{i,j}\left[a_1^2 \bar{A}_{\ell m}\bar{A}^{\ell m}\right]_{i,j} = 0,\end{aligned} \tag{10.41}$$

where

$$\mathcal{A}^{\pm}_{i,j} \equiv \begin{cases} \dfrac{\left(\eta^2_{,\rho}\big|_{(\eta_i,\xi(s_j))} + \eta^2_{,z}\big|_{(\eta_i,\xi(s_j))}\right)}{h_\eta^2 \rho_{(\eta_i,\xi(s_j))}} \rho_{(\eta_i \pm h_\eta/2, \xi(s_j))} & : \begin{array}{r}\text{for all } (i,j) \text{ except } i=j=0; \\ \text{or all } i \text{ and } j = -\mathcal{S}^+, \mathcal{S}^-; \\ \text{or } i<0 \text{ and } j = 0\end{array} \\ \dfrac{\eta^2_{,z}\big|_{(\eta_i,\xi(s_j))}}{h_\eta^2} \pm \dfrac{\eta_{,\rho\rho}\big|_{(\eta_i,\xi(s_j))}}{2h_\eta} & : \begin{array}{r}\text{for all } i \text{ and } j = -\mathcal{S}^+, \mathcal{S}^-; \\ \text{and } i<0 \text{ and } j = 0\end{array} \end{cases} \tag{10.42}$$

and

$$\mathcal{B}^{\pm}_{i,j} \equiv \begin{cases} \dfrac{\left(\eta^2_{,\rho}\big|_{(\eta_i,\xi(s_j))} + \eta^2_{,z}\big|_{(\eta_i,\xi(s_j))}\right)}{h_s^2 J(s_j) \rho_{(\eta_i,\xi(s_j))}} \dfrac{\rho_{(\eta_i,\xi(s_j \pm h_s/2))}}{J(s_j \pm h_s/2)} & : \begin{array}{r}\text{for all } (i,j) \text{ except } i=j=0; \\ \text{or all } i \text{ and } j = -\mathcal{S}^+, \mathcal{S}^-; \\ \text{or } i<0 \text{ and } j = 0\end{array} \\ \dfrac{\left(2\,\eta^2_{,z}\big|_{(\eta_i,\xi(s_j))}\right)}{h_s^2 J(s_j)} \dfrac{1}{J(s_j \pm h_s/2)} & : \begin{array}{r}\text{for all } i \text{ and } j = -\mathcal{S}^+, \mathcal{S}^-; \\ \text{and } i<0 \text{ and } j = 0\end{array}. \end{cases} \tag{10.43}$$

The differencing of the Laplacian at the singular point must be handled as a special case and will be discussed below.

The boundary conditions will be handled through the *implicit* use of "virtual" boundary points as in the case of bispherical coordinates. The finite difference form for the inner boundary condition for Region 1 (10.22a), put in a form which is most convenient for eliminating the dependence on the virtual boundary points, is given by

$$\left(\psi_{-\mathcal{I}^+-1,j}-\psi_{-\mathcal{I}^+,j}\right)=\left(\psi_{-\mathcal{I}^++1,j}-\psi_{-\mathcal{I}^+,j}\right)+\frac{h_\eta\psi_{-\mathcal{I}^+,j}}{\sqrt{\eta_{,\rho}^2\big|_{(\eta^+,\xi(s_j))}+\eta_{,z}^2\big|_{(\eta^+,\xi(s_j))}}}, \tag{10.44}$$

and the inner boundary condition for Region 2 (10.22b) is given by

$$\left(\psi_{-\mathcal{I}^--1,j}-\psi_{-\mathcal{I}^-,j}\right)=\left(\psi_{-\mathcal{I}^-+1,j}-\psi_{-\mathcal{I}^-,j}\right)+\frac{\alpha h_\eta\psi_{-\mathcal{I}^-,j}}{\sqrt{\eta_{,\rho}^2\big|_{(\eta^-,\xi(s_j))}+\eta_{,z}^2\big|_{(\eta^-,\xi(s_j))}}}. \tag{10.45}$$

The finite difference form for the outer boundary condition of Region 3 (10.27) is expressed as

$$\begin{aligned}\left(\psi_{\mathcal{I}+1,j}-\psi_{\mathcal{I},j}\right)=&\left(\psi_{\mathcal{I}-1,j}-\psi_{\mathcal{I},j}\right)+\frac{2h_\eta\left(1-\psi_{\mathcal{I},j}\right)}{\left(z\eta_{,z}+\rho\eta_{,\rho}\right)_{(\eta_f,\xi(s_j))}}\\&+\frac{h_\eta}{h_sJ(s_j)}\left(\frac{z\eta_{,\rho}-\rho\eta_{,z}}{z\eta_{,z}+\rho\eta_{,\rho}}\right)_{(\eta_f,\xi(s_j))}\left(\left(\psi_{\mathcal{I},j+1}-\psi_{\mathcal{I},j}\right)-\left(\psi_{\mathcal{I},j-1}-\psi_{\mathcal{I},j}\right)\right)\\&-d_z\left(\frac{h_\eta z\left(\rho^2+z^2\right)^{-3/2}}{z\eta_{,z}+\rho\eta_{,\rho}}\right)_{(\eta_f,\xi(s_j))}\\&-\frac{9(P_1+P_2)^2}{16}\left(\frac{h_\eta\left(z^2-\rho^2\right)\left(\rho^2+z^2\right)^{-2}}{z\eta_{,z}+\rho\eta_{,\rho}}\right)_{(\eta_f,\xi(s_j))}.\end{aligned} \tag{10.46}$$

The axisymmetry boundary conditions (10.23) give

$$\left(\psi_{i,-\mathcal{S}^+-1}-\psi_{i,-\mathcal{S}^+}\right)=\left(\psi_{i,-\mathcal{S}^++1}-\psi_{i,-\mathcal{S}^+}\right), \tag{10.47}$$

$$\left(\psi_{i,\mathcal{S}^-+1}-\psi_{i,\mathcal{S}^-}\right)=\left(\psi_{i,\mathcal{S}^--1}-\psi_{i,\mathcal{S}^-}\right), \tag{10.48}$$

$$\left(\psi_{i,1}-\psi_{i,0}\right)=\left(\psi_{i,-1}-\psi_{i,0}\right)\qquad\text{for}\quad i<0\text{ in Region 1}, \tag{10.49}$$

and

$$\left(\psi_{i,-1}-\psi_{i,0}\right)=\left(\psi_{i,1}-\psi_{i,0}\right)\qquad\text{for}\quad i<0\text{ in Region 2}. \tag{10.50}$$

As mentioned above, the differencing of the Laplacian at the singular point cannot be handled in the usual manner since even the limiting behavior of the Laplacian, as the singular point is approached, is not well defined. One approach to differencing the Laplacian at the singular point is obtained by considering the mesh in the neighborhood of the singular point not as a regularly spaced mesh in Čadež coordinates, but rather as an irregularly spaced mesh in cylindrical coordinates. For an axisymmetric configuration, the Laplacian at the singular point takes the cylindrical coordinate form of

$$\overline{\nabla}^2\psi\Big|_{(\rho=0,z=z_s)}=2\frac{\partial^2\psi}{\partial\rho^2}+\frac{\partial^2\psi}{\partial z^2}. \tag{10.51}$$

To express (10.51) by finite differences, discrete approximations to both second derivatives must be found which can be constructed from the irregular distribution of mesh point in the cylindrical coordinate system.

Assuming axisymmetry in the conformal factor, the general Taylor series expansion about the singular point takes the form

$$\begin{aligned}\psi(z_s+h,k) = \psi_s + \psi_{,z}h + \frac{1}{2}\psi_{,zz}h^2 + \frac{1}{2}\psi_{,\rho\rho}k^2 + \frac{1}{2}\psi_{,z\rho\rho}hk^2 + \frac{1}{6}\psi_{,zzz}h^3 \\ + \left\{\frac{1}{4}\psi_{,zz\rho\rho}h^2k^2 + \frac{1}{24}\psi_{,zzzz}h^4 + \frac{1}{24}\psi_{,\rho\rho\rho\rho}k^4 + \cdots\right\}.\end{aligned} \tag{10.52}$$

If this series is truncated at some level and the difference between the value of the conformal factor at the singular point and a sufficient number of neighboring points are taken in (10.52), then the result is a matrix problem for the derivatives of the conformal factor at the singular point. In order for the truncation error in the approximations of the second derivatives to be second order in h and k, all of the terms not bracketed in (10.52) must be included in the expansion. This means that five points neighboring the singular point must be used. If there happens to be a reflection symmetry in the coordinate system in the z direction through the singular point, then three of the terms in (10.52) will vanish identically. In order for the matrix constructed from (10.52) not to be singular in this case, at least three pairs of points must be used for which $h \neq 0$. This means that at least six points must be used and thus at least one of the fourth order terms in (10.52) must be included. Finally, in order to symmetrize the differencing scheme as much as possible, I have chosen to include one extra point and a second fourth order term from (10.52). The resulting eight-point differencing molecule is illustrated below in Figure 10.2.

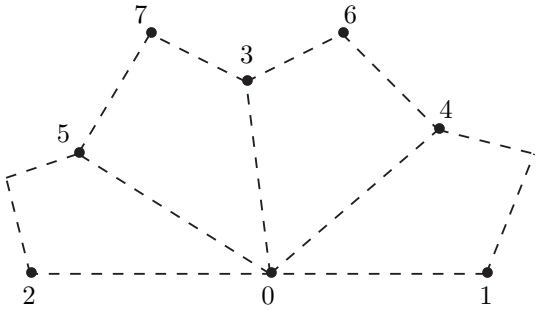


Figure 10.2: Eight-point differencing molecule used for singular point.

Using the labeling in Figure 10.2, the matrix problem for the derivatives becomes

$$\begin{bmatrix} h_1 & h_1^2 & 0 & 0 & h_1^3 & h_1^4 & 0 \\ h_2 & h_2^2 & 0 & 0 & h_2^3 & h_2^4 & 0 \\ h_3 & h_3^2 & k_3^2 & h_3k_3^2 & h_3^3 & h_3^4 & k_3^4 \\ h_4 & h_4^2 & k_4^2 & h_4k_4^2 & h_4^3 & h_4^4 & k_4^4 \\ h_5 & h_5^2 & k_5^2 & h_5k_5^2 & h_5^3 & h_5^4 & k_5^4 \\ h_6 & h_6^2 & k_6^2 & h_6k_6^2 & h_6^3 & h_6^4 & k_6^4 \\ h_7 & h_7^2 & k_7^2 & h_7k_7^2 & h_7^3 & h_7^4 & k_7^4 \end{bmatrix} \begin{bmatrix} \psi_{,z} \\ \frac{1}{2}\psi_{,zz} \\ \frac{1}{2}\psi_{,\rho\rho} \\ \frac{1}{2}\psi_{,z\rho\rho} \\ \frac{1}{6}\psi_{,zzz} \\ \frac{1}{24}\psi_{,zzzz} \\ \frac{1}{24}\psi_{,\rho\rho\rho\rho} \end{bmatrix} = \begin{bmatrix} \psi_1 - \psi_0 - \mathcal{O}(h_1^5) \\ \psi_2 - \psi_0 - \mathcal{O}(h_2^5) \\ \psi_3 - \psi_0 - \mathcal{O}(h_3^2k_3^2) \\ \psi_4 - \psi_0 - \mathcal{O}(h_4^2k_4^2) \\ \psi_5 - \psi_0 - \mathcal{O}(h_5^2k_5^2) \\ \psi_6 - \psi_0 - \mathcal{O}(h_6^2k_6^2) \\ \psi_7 - \psi_0 - \mathcal{O}(h_7^2k_7^2) \end{bmatrix}, \tag{10.53}$$

where

$$h_i \equiv z_i - z_0 \qquad \text{and} \qquad k_i \equiv \rho_i. \tag{10.54}$$

Having chosen a discretization for the domain of the problem being solved, all quantities in the matrix of (10.53) are fixed and the inverse matrix can be computed numerically. If the elements of the inverse matrix are denoted by $M_{i,j}^{-1}$, then the differenced form of the Laplacian at the singular point can be written as

$$\overline{\nabla}^2\psi = \sum_{i=1}^{7} \left\{ \left(2M_{2,i}^{-1} + 4M_{3,i}^{-1}\right)(\psi_i - \psi_0) \right\} - \sum_{i=3}^{7} \left\{ \left(2M_{2,i}^{-1} + 4M_{3,i}^{-1}\right)\mathcal{O}(h_i^2k_i^2) \right\}. \tag{10.55}$$

The overall truncation error to this scheme is $\mathcal{O}(h^2 + k^2 + hk)$ and so the rate of decrease in the error is quadratic as h and k decrease. This does not, however, accurately describe the reduction in the truncation error as the discretization size in Čadež coordinates is reduced. If the discretization of the Čadež coordinates is fine enough so that the local expansion of the coordinate transformation (10.15) is valid, then it is seen that the reduction in the cylindrical discretization length goes as the square root of the reduction of the Čadež discretization length. This means that the limiting behavior of the truncation error of (10.55) will be first-order or linear, not quadratic. As in the case of bispherical coordinates, the presence of this sort of coordinate singularity leads to first-order behavior for the discretization error.

The difference equations described above for the Hamiltonian constraint in Čadež coordinates are solved via the Newton-Raphson method for nonlinear systems as described in Chapter 8. As with the bispherical coordinates, the linearized equations for the iterative correction have been solved directly by means of the LINPACK routines for factoring (DGBFA) and solving (DGBSL) general banded matrices. Because of the multiple region nature of the Čadež coordinate system, the number of bands and the maximum separation of the bands from the diagonal of the matrix are larger than in the case of bispherical coordinates. The effect of this is that the size of the matrix which can be solved with these LINPACK routines is substantially less than in the case of bispherical coordinates. This means that the discretization of the domain cannot be done as finely

as is possible with bispherical coordinates and, consequently, the accuracy of the solution will not be as great. An alternate approach for solving the Čadež coordinate difference equations would be of great help in this regard. Some work has been done on applying the multigrid approach to this problem, but with only modest success. It is likely that the multiple region nature of the domain and difficulties associated with the coordinate singularity are responsible for the less than satisfactory behavior of the multigrid solver written for this problem. A detailed investigation of the applicability of the multigrid method to the Čadež coordinate system will be necessary in order to advance this approach.

Given a solution to the difference equations, the total ADM energy and dipole moment as well as the minimal surface masses and the physical hole separations can be computed via numerical integrals. As in the case of bispherical coordinates, care must be taken in numerically integrating near the singular point. Extrapolative integral formulas have been used unless otherwise stated. In terms of Čadež coordinates, the total energy is given in dimensionless form by

$$\begin{aligned}\frac{E}{a_1} = \frac{1}{2}\int_0^{\xi_s} \left.\frac{\psi\rho d\xi}{\sqrt{\eta_{,\rho}^2+\eta_{,z}^2}}\right|_{(\eta=\eta^+)} + \frac{\alpha}{2}\int_{\xi_s}^{\pi} \left.\frac{\psi\rho d\xi}{\sqrt{\eta_{,\rho}^2+\eta_{,z}^2}}\right|_{(\eta=\eta^-)} \\ + \frac{1}{8}\int_{\xi=0}^{\xi=\xi_s}\int_{\eta=\eta^+}^{\eta=\eta_s} \frac{\left(a_1^2\bar{A}_{ij}\bar{A}^{ij}\right)}{\psi^7}\frac{\rho d\eta d\xi}{\eta_{,\rho}^2+\eta_{,z}^2} + \frac{1}{8}\int_{\xi=\xi_s}^{\xi=\pi}\int_{\eta=\eta^-}^{\eta=\eta_s} \frac{\left(a_1^2\bar{A}_{ij}\bar{A}^{ij}\right)}{\psi^7}\frac{\rho d\eta d\xi}{\eta_{,\rho}^2+\eta_{,z}^2} \\ + \frac{1}{8}\int_{\xi=0}^{\xi=\pi}\int_{\eta=\eta_s}^{\eta=\infty} \frac{\left(a_1^2\bar{A}_{ij}\bar{A}^{ij}\right)}{\psi^7}\frac{\rho d\eta d\xi}{\eta_{,\rho}^2+\eta_{,z}^2}.\end{aligned} \tag{10.56}$$

The z component of the dipole moment is given in dimensionless form by

$$\begin{aligned}\frac{d_z}{a_1^2} = \int_0^{\xi_s}\left\{\frac{z\psi}{2}+\frac{\eta_{,z}(1-\psi)}{\sqrt{\eta_{,\rho}^2+\eta_{,z}^2}}\right\}\left.\frac{\rho d\xi}{\sqrt{\eta_{,\rho}^2+\eta_{,z}^2}}\right|_{(\eta=\eta^+)} + \frac{1}{8}\int_{\xi=0}^{\xi=\xi_s}\int_{\eta=\eta^+}^{\eta=\eta_s} \frac{\left(a_1^2\bar{A}_{ij}\bar{A}^{ij}\right)}{\psi^7}\frac{z\rho d\eta d\xi}{\eta_{,\rho}^2+\eta_{,z}^2} \\ + \int_{\xi_s}^{\pi}\left\{\frac{\alpha z\psi}{2}+\frac{\eta_{,z}(1-\psi)}{\sqrt{\eta_{,\rho}^2+\eta_{,z}^2}}\right\}\left.\frac{\rho d\xi}{\sqrt{\eta_{,\rho}^2+\eta_{,z}^2}}\right|_{(\eta=\eta^-)} + \frac{1}{8}\int_{\xi=\xi_s}^{\xi=\pi}\int_{\eta=\eta^-}^{\eta=\eta_s} \frac{\left(a_1^2\bar{A}_{ij}\bar{A}^{ij}\right)}{\psi^7}\frac{z\rho d\eta d\xi}{\eta_{,\rho}^2+\eta_{,z}^2} \\ + \frac{1}{8}\int_{\xi=0}^{\xi=\pi}\int_{\eta=\eta_s}^{\eta=\infty} \frac{\left(a_1^2\bar{A}_{ij}\bar{A}^{ij}\right)}{\psi^7}\frac{z\rho d\eta d\xi}{\eta_{,\rho}^2+\eta_{,z}^2}.\end{aligned} \tag{10.57}$$

The areas of the minimal surfaces are given in dimensionless form by

$$\frac{A_{MS}^+}{a_1^2} = 2\pi\int_0^{\xi_s}\left.\frac{\psi^4\rho d\xi}{\sqrt{\eta_{,\rho}^2+\eta_{,z}^2}}\right|_{(\eta=\eta^+)} \tag{10.58a}$$

and

$$\frac{A^-_{MS}}{a_1^2} = 2\pi \int_{\xi_s}^{\pi} \left. \frac{\psi^4 \rho d\xi}{\sqrt{\eta_{,\rho}^2 + \eta_{,z}^2}} \right|_{(\eta=\eta^-)} . \tag{10.58b}$$

Finally, the proper separation of the two holes is given in dimensionless form by

$$\frac{L}{a_1} = -\int_{\eta^+}^{\eta_s} \left. \frac{\psi^2 d\eta}{\eta_{,z}} \right|_{(\xi=\xi_s)} + \int_{\eta^-}^{\eta_s} \left. \frac{\psi^2 d\eta}{\eta_{,z}} \right|_{(\xi=\xi_s)} . \tag{10.59}$$

The numerical approximation of (10.59) tends to be a poor approximation because of the relative sparseness of mesh points between the two holes. The accuracy of the approximation can be greatly increased by replacing (10.59) with an integral over three separate regions. (10.59) consists of an integral along the z-axis between the holes in Regions 1 and 2. The third integral is taken to be from one mesh point to the left of the singular point in Region 2 to one mesh point to the right of the singular point in Region 1. The two integrals in (10.59) are adjusted so as not to include this section. The value of the conformal factor in the intermediate section can be approximated by a quadratic polynomial fit to the three values of the conformal factor at the singular point and its nearest neighbors. This interpolated conformal factor can then be integrated analytically in cylindrical coordinates giving a more accurate result than can be achieved by a standard, extrapolative numerical integral. Using the notation of Figure 10.2, the contribution of this section to the total proper separation is given by

$$\begin{aligned} \frac{\bar{L}}{a_1} = \psi_1^2 \frac{(z_1 - z_2)}{6(z_1 - z_0)}(2z_1 - 3z_0 + z_2) + \psi_0^2 \frac{(z_1 - z_2)^3}{6(z_1 - z_0)(z_0 - z_2)} \\ - \psi_2^2 \frac{(z_1 - z_2)}{6(z_0 - z_2)}(z_1 - 3z_0 + 2z_2). \end{aligned} \tag{10.60}$$

Because the numerical integrals for the total energy and dipole moment cannot extend past the outer boundary of the computational domain, the integrals (10.56) and (10.57) necessarily incorporate error beyond that introduced by the numerical approximations. An understanding of the nature of this error as well as a first-order correction to the numerical result can be obtained by examining the asymptotic forms of the integrands of (10.56) and (10.57) and estimating the contribution from the integral over the domain exterior to the outer boundary.

For the case of two holes with axisymmetric linear and angular momenta, we find (see (7.22)) that at large radius the square of the extrinsic curvature takes the dimensionless form

$$a_1^2 \bar{A}_{ij} \bar{A}^{ij} \approx \frac{9}{2r^4} (P_1/a_1 + P_2/a_1)^2 \left(1 + 2\cos^2\theta\right) . \tag{10.61}$$

(Note that r is dimensionless.) Similarly, from (7.26) we find for the conformal factor

$$\psi \approx 1 + \frac{E/a_1}{2r} + \frac{d_z/a_1^2}{2r^2} \cos\theta - \frac{9}{32} \frac{(P_1/a_1 + P_2/a_1)^2}{r^2} (1 - 2\cos^2\theta). \tag{10.62}$$

Using (10.61) and (10.62), the leading order contributions to the total energy and dipole moment, resulting from the integral over the region exterior to a sphere of radius r_b, are

$$\Delta E/a_1 \approx \frac{15}{8}\frac{\left(P_1/a_1 + P_2/a_1\right)^2}{r_b} - \frac{105}{32}\frac{\left(P_1/a_1 + P_2/a_1\right)^2}{r_b^2}\frac{E}{a_1} \tag{10.63}$$

and

$$\Delta d_z/a_1^2 \approx -\frac{231}{160}\frac{\left(P_1/a_1 + P_2/a_1\right)^2}{r_b^2}\frac{d_z}{a_1^2}. \tag{10.64}$$

If results of the numerical integration over the finite domain for the total energy and dipole moment are denoted respectively by E_N/a_1 and d_N/a_1^2, then first-order corrected values are given by

$$\frac{E}{a_1} \approx \frac{E_N/a_1 + \frac{15}{8}\frac{\left(P_1/a_1+P_2/a_1\right)^2}{r_b}}{1 + \frac{105}{32}\frac{\left(P_1/a_1+P_2/a_1\right)^2}{r_b^2}} \tag{10.65}$$

and

$$\frac{d_z}{a_1^2} \approx \frac{d_N/a_1^2}{1 + \frac{231}{160}\frac{\left(P_1/a_1+P_2/a_1\right)^2}{r_b^2}}. \tag{10.66}$$

It is easy to see from (10.65) and (10.66) that configurations with a non-vanishing net linear momentum will suffer the worst errors from the approximation of a finite computational domain and this error can, for the most part, be compensated for by the use of (10.65) and (10.66).

Appendix D contains the results from computational solutions covering a large set of configurations and grid resolutions. Each of these computations, performed in Čadež coordinates, can be directly compared to an identical computation performed in bispherical coordinates and tabulated in Appendix C. Because of the behavior of the discretization between the holes, configurations with small β require very fine discretizations in Region 3 in order to have a moderate discretization in Regions 1 and 2. The end result of this is that with the current solution method, only very coarse grids can be used when β is small. Consequently, the accuracy of the solution is rather poor in these cases. For the case of $\beta = 3$, the errors in the total energy where on the order of 20% and the errors in the separation were roughly 30%. This is not at all surprising considering that only 12 discrete zones were present between the holes while in bispherical coordinates, 160 where used in the finest discretization. On the other hand, when β reached 6, the errors were down to less than 1% when there was no net momentum and to 5% when there was. This is an encouraging level of error for the cases with no net momenta. The higher error in the cases with a net momentum indicate that the outer boundary, placed at radius of roughly $200a_1$, was somewhat too close.

These preliminary solutions using Čadež coordinates, while less accurate than those obtained with bispherical coordinates, show that there is no fundamental problem with the use of Čadež

coordinates for work on the two-hole initial-value and evolution problems. The differencing scheme discussed above appears to work adequately. The remaining difficuly lies in finding computational routines for solving the large, poorly banded matrices which result from the differencing scheme.

Chapter 11: Apparent Horizons on Inversion-Symmetric Initial-Data Sets

The inversion-symmetric initial-data sets discussed in the preceding chapters are all assumed to contain one or more black holes. If we do not violate the cosmic-censorship conjecture, then each initial-data slice will necessarily intersect the null surface of at least one event horizon. Ideally, we would like to be able to determine the locations of these intersections on the initial-data slice. Unfortunately, determining the location of an event horizon on any given slice requires the full future evolution of the data on that slice. Similar in concept, though not equivalent, to an event horizon is an apparent horizon. This surface, unlike the event horizon, can be located solely in terms of the initial data. Hawking and Ellis [1973] show that if an apparent horizon exists, then an event horizon necessarily exists outside or coincident with the apparent horizon. The area of the apparent horizon thus gives a lower bound on the area of the event horizon. With this information, Hawking's [1971] area theorem can be used to compute an upper limit on the total amount of energy which can be radiated from the black-hole system via gravitational radiation. We see, then, that in order to understand fully the physical content of an initial-data slice, it is necessary to know the location of the apparent horizons on the initial slice.

In order to locate apparent horizons, it is first necessary to clarify their definition. As discussed in Cook and York [1990], Hawking and Ellis [1973] define an apparent horizon as the outer boundary of a connected component of a trapped region. A trapped region, then, is defined as the collection of all points within all compact, orientable spacelike two-surfaces for which the surface-orthogonal outgoing null geodesics have nonpositive expansion. If a spacelike hypersurface is asymptotically flat, then the expansion of null geodesics emanating from a compact two-surface far from any holes will be positive. The search for apparent horizons can thus be formulated in terms of the search for compact, orientable two surfaces on which the outgoing null geodesics have *zero* expansion.

Following York [1989], consider a spacelike hypersurface Σ with timelike unit normal n^μ. Let S be a compact, orientable spacelike two-surface embedded in Σ with unit normal s^μ (see Figure 11.1). Two orthogonal null vectors k^μ and ℓ^μ can be constructed from n^μ and s^μ as

$$k^\mu \equiv \frac{1}{\sqrt{2}}(n^\mu + s^\mu) \qquad \text{and} \qquad \ell^\mu \equiv \frac{1}{\sqrt{2}}(n^\mu - s^\mu). \tag{11.1}$$

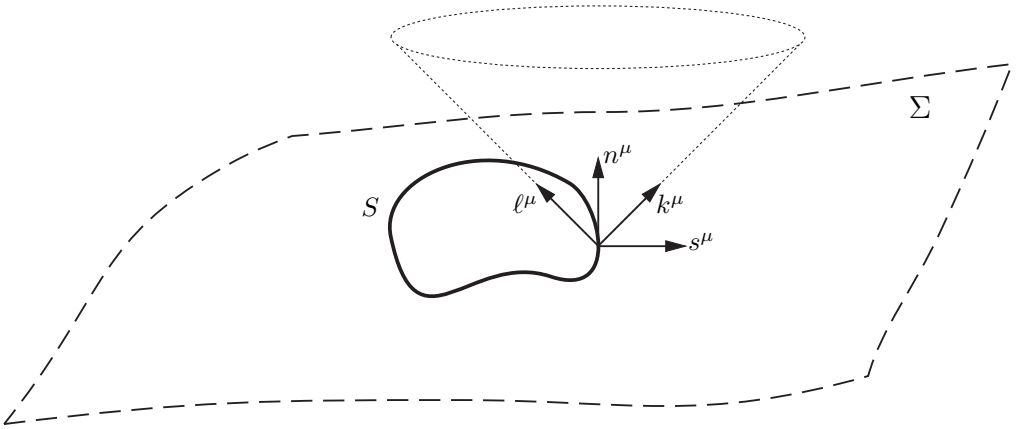


Figure 11.1: An apparent horizon S intersecting the initial-data surface Σ. n^μ is the timelike unit normal vector for the initial-data surface and s^μ is the *outward* pointing spacelike unit normal to the apparent horizon.

The null surface η, generated by k^μ, has an induced metric $S_{\mu\nu}$ given by

$$\begin{aligned} S_{\mu\nu} &= g_{\mu\nu} + k_\mu \ell_\nu + k_\nu \ell_\mu \\ &= g_{\mu\nu} + n_\mu n_\nu - s_\mu s_\nu \\ &= \gamma_{\mu\nu} - s_\mu s_\nu \\ &= P^\alpha_\mu P^\beta_\nu g_{\alpha\beta}, \end{aligned} \tag{11.2}$$

where $\gamma_{\mu\nu}$ is the induced metric of Σ and where P^μ_ν is the operator for projection onto the null surface generated by k^μ:

$$P^\mu_\nu \equiv \delta^\mu_\nu + n^\mu n_\nu - s^\mu s_\nu. \tag{11.3}$$

The extrinsic curvature of the null surface η is defined similarly to (2.19), by

$$\kappa_{\mu\nu} \equiv -P^\alpha_\mu P^\beta_\nu \nabla_{(\alpha} k_{\beta)}, \tag{11.4}$$

where ∇_μ is the full, four-dimensional covariant derivative. Because k^μ is the null vector tangent to the outgoing null geodesic at the surface S, the surface S will be an apparent horizon if the expansion (trace of (11.4)) vanishes.

Consider now the extrinsic curvature of the surface S embedded in Σ. It is given by

$$\chi_{\mu\nu} \equiv -P^\alpha_\mu P^\beta_\nu D_{(\alpha} s_{\beta)} \tag{11.5}$$

where D_μ is the spatial covariant derivative induced on Σ. Expanding (11.4) and imposing the apparent horizon condition that the trace of $\kappa_{\mu\nu}$ vanish gives

$$\sqrt{2}\kappa^\mu_\mu = \chi^\mu_\mu + P^\nu_\mu K_\nu{}^\mu = 0, \tag{11.6}$$

where $K_{\mu\nu}$ is the extrinsic curvature of Σ embedded in the full space-time. This can be simplified to

$$D_i s^i - K + K_{ij} s^i s^j = 0, \tag{11.7a}$$

or in terms of (3.8),

$$D_i s^i - \frac{2}{3} K + A_{ij} s^i s^j = 0. \tag{11.7b}$$

Equation (11.7), thus, represents a necessary condition that s^i be the outward-pointing unit-normal to an apparent horizon. If the surface to which s^i is normal is the outer-most such surface, then that surface is an apparent horizon. Equation (11.7b) can be expressed in terms of the conformal background space and the background quantities defined on it. For a unit normal vector, the natural conformal weighting is given by

$$s^i = \psi^{-2} \bar{s}^i, \tag{11.8}$$

where $\bar{s}^i$ is the background unit-normal vector. Using the conformal weightings for the metric and extrinsic curvature from Chapter 3, (11.7b) becomes

$$\bar{D}_i \bar{s}^i + 4 \bar{s}^i \bar{D}_i \ln \psi - \frac{2}{3} \psi^2 K + \psi^{-4} \bar{A}_{ij} \bar{s}^i \bar{s}^j = 0. \tag{11.9}$$

Equation (11.9) is a single equation for a three-dimensional vector and so it seems at first that it cannot uniquely determine $\bar{s}^i$. Recalling that $\bar{s}^i$ must be a unit vector removes one degree of freedom from $\bar{s}^i$ and the fact that the surface of the apparent horizon must be a closed two-surface removes a second. Together, these conditions demand that

$$\bar{s}_i = \lambda \bar{D}_i \tau \qquad \text{where} \qquad \lambda = \left[(\bar{D}^i \tau)(\bar{D}_i \tau) \right]^{-1/2}, \tag{11.10}$$

and where τ is a scalar function whose level surface $\tau = \tau_0$ defines the position of the apparent horizon. Using (11.10) in (11.9) gives the final form for the apparent-horizon equation

$$\lambda \overline{\nabla}^2 \tau + (\bar{D}^i \lambda)(\bar{D}_i \tau) + 4\lambda (\bar{D}^i \ln \psi)(\bar{D}_i \tau) - \frac{2}{3} \psi^2 K + \psi^{-4} \lambda^2 \bar{A}_{ij} (\bar{D}^i \tau)(\bar{D}^j \tau) = 0. \tag{11.11}$$

The apparent-horizon equation is thus in the form of a highly nonlinear partial differential equation for the scalar function τ which can be solved numerically by a variety of means.

If the manifold on which the initial data is specified is inversion-symmetric, as is the case for the initial data described in earlier chapters, then the apparent horizon must be inversion-symmetric as well. The unit normal to the surface of the apparent horizon, as with all vector fields defined on the manifold, must satisfy isometry condition (4.36), so

$$s^i(\mathbf{x}) = \pm (\mathbf{J}_\alpha^{-1})_j{}^i s^j(\mathbf{J}_\alpha(\mathbf{x})). \tag{11.12}$$

In terms of the conformal background fields, this becomes

$$\bar{s}^i(\mathbf{x}) = \pm\left(\frac{a_\alpha}{r_\alpha}\right)^2 (\mathbf{J}_\alpha^{-1})_j{}^i \bar{s}^j(\mathbf{J}_\alpha(\mathbf{x})). \tag{11.13}$$

To prove that apparent horizons on initial-data slices which contain inversion-symmetric initial data are themselves inversion-symmetric, let us assume that $\bar{s}^i(\mathbf{x})$ is a solution of the apparent-horizon equation (11.9), where $\mathbf{x}$ belongs to the set of points which satisfies $\tau(\mathbf{x}) = \tau_0$. The inversion-symmetric counterpart must then be the vector field $\tilde{s}^i(\mathbf{x})$ defined by

$$\tilde{s}^i(\mathbf{x}) = \pm\left(\frac{a_\alpha}{r_\alpha}\right)^2 (\mathbf{J}_\alpha^{-1})_j{}^i \bar{s}^j(\mathbf{J}_\alpha(\mathbf{x})). \tag{11.14}$$

In terms of Cartesian coordinates and using (4.40) and (4.49)–(4.54), direct calculation shows that

$$\bar{D}_i \tilde{s}^i(\mathbf{x}) = \pm\left(\frac{r'_\alpha}{a_\alpha}\right)^2 \left[\bar{D}'_i \bar{s}^i(\mathbf{x}') - \frac{4}{r'_\alpha} n'^\alpha_i \bar{s}^i(\mathbf{x}')\right], \tag{11.15}$$

$$\tilde{s}^i(\mathbf{x}) \bar{D}_i \ln\psi(\mathbf{x}) = \pm\left(\frac{r'_\alpha}{a_\alpha}\right)^2 \bar{s}^i(\mathbf{x}') \left[\bar{D}'_i \ln\psi(\mathbf{x}') + \frac{1}{r'_\alpha} n'^\alpha_i\right], \tag{11.16}$$

$$\psi^{-2}(\mathbf{x}) K(\mathbf{x}) = \pm\left(\frac{r'_\alpha}{a_\alpha}\right)^2 \psi^{-2}(\mathbf{x}') K(\mathbf{x}'), \tag{11.17}$$

and

$$\psi^{-4}(\mathbf{x}) \bar{A}_{ij}(\mathbf{x}) \tilde{s}^i(\mathbf{x}) \tilde{s}^j(\mathbf{x}) = \pm\left(\frac{r'_\alpha}{a_\alpha}\right)^2 \left[\psi^{-4}(\mathbf{x}') \bar{A}_{ij}(\mathbf{x}') \bar{s}^i(\mathbf{x}') \bar{s}^j(\mathbf{x}')\right]. \tag{11.18}$$

Thus, we find that the apparent-horizon equation for $\tilde{s}^i(\mathbf{x})$ becomes

$$\begin{aligned} &\bar{D}_i \tilde{s}^i(\mathbf{x}) + 4\tilde{s}^i(\mathbf{x}) \bar{D}_i \ln\psi(\mathbf{x}) - \frac{2}{3}\psi^2(\mathbf{x}) K(\mathbf{x}) + \psi^{-4}(\mathbf{x}) \bar{A}_{ij}(\mathbf{x}) \tilde{s}^i(\mathbf{x}) \tilde{s}^{\mathrm{j}}(\mathbf{x}) \\ &\quad = \pm\left(\frac{r'_\alpha}{a_\alpha}\right)^2 \Bigg[\bar{D}'_i \bar{s}^i(\mathbf{x}') + 4\bar{s}^i(\mathbf{x}') \bar{D}'_i \ln\psi(\mathbf{x}') - \frac{2}{3}\psi^2(\mathbf{x}') K(\mathbf{x}') \\ &\qquad\qquad + \psi^{-4}(\mathbf{x}') \bar{A}_{ij}(\mathbf{x}') \bar{s}^i(\mathbf{x}') \bar{s}^j(\mathbf{x}')\Bigg]. \end{aligned} \tag{11.19}$$

Since the right-hand side of (11.19) satisfies the apparent-horizon equation for $\mathbf{x}'$ such that $\tau(\mathbf{x}') = \tau_0$, we find that $\tilde{s}^i(\mathbf{x})$ satisfies the apparent-horizon equation for $\mathbf{x}$ such that $\tau(\mathbf{J}_\alpha(\mathbf{x})) = \tau_0$.

Many methods can be used to locate apparent horizons by solving the apparent-horizon equation (11.11). For the case of two black holes on a time-symmetric slice, several authors (Čadež [1974] and Bishop [1982] and [1984]) have searched for apparent horizons (minimal surfaces in the time-symmetric case) by means of "shooting" methods. Unfortunately, this method is applicable only to axisymmetric initial-data sets since it is an inherently one-dimensional method. Nakamura *et al.* [1984] and [1985] have developed and tested a method for locating apparent horizons based on an expansion in spherical harmonics. This approach is applicable to full, three-dimensional initial-data sets. An alternative approach which I have developed (Cook and York [1990]) is to solve

(11.11) directly as a boundary value problem. This approach is also applicable to three-dimensional initial-data sets.

I have applied this approach to the problem of locating the apparent horizons in the one-hole initial-data sets discussed in Chapter 8. In the next chapter, I will describe the method and the solutions found. In the future, it will be essential to locate the apparent horizons in the two-hole initial-data sets. This work has not yet been undertaken, although it is planned for the near future.

Chapter 12: Apparent Horizons for a Single Black Hole with Linear or Angular Momentum

Given the initial data for a single black hole with non-zero linear or angular momentum as described in Chapter 8, the apparent-horizon equation (11.11) can be solved to locate any apparent horizons on the initial-data slice. Because part of the initial data is only known numerically, it will be necessary to solve (11.11) numerically. As described in Chapter 11, this will be accomplished by posing the apparent-horizon equation as a boundary value problem.

As stated in Chapter 11, the location of apparent horizons is determined by solving (11.11) for the scalar function τ of which the level surface $\tau = \tau_0$ is the apparent horizon. For this approach to work, the functional form for τ must be chosen carefully. The apparent horizons for the case of a single hole are expected to be located near to the minimal surface. Using the logarithmically scaled dimensionless radial coordinates (8.1) from Chapter 8, an appropriate choice for τ is

$$\tau(x, \theta, \phi) = x - h(\theta, \phi). \tag{12.1}$$

Choosing the level surface $\tau = 0$ to locate the apparent horizon then means that the radius of the apparent horizon is given parametrically by

$$x = h(\theta, \phi). \tag{12.2}$$

From (11.10) we find that

$$\lambda = a e^{h(\theta,\phi)} (1 + h_{,\theta}^2 + h_{,\phi}^2/\sin^2\theta)^{-1/2} \tag{12.3}$$

and

$$\bar{s}^i = \frac{1}{a e^{h(\theta,\phi)} \sqrt{1 + h_{,\theta}^2 + h_{,\phi}^2/\sin^2\theta}} \left[1 \quad -h_{,\theta} \quad -h_{,\phi}/\sin^2\theta \right]. \tag{12.4}$$

Note that any occurrence of the coordinate x must be evaluated at $x = h(\theta, \phi)$. From (12.4) it is seen that $\bar{s}^i$ is indeed an outward pointing unit normal from the point of view of an observer on the top sheet ($x > 0$).

Since the initial-data slices constructed in Chapter 8 for a single hole are inversion symmetric, any solution of the apparent-horizon equation must have an inversion-symmetric counterpart. To

examine it's form, it is necessary to construct the isometry relations in our coordinate system. From the coordinate transformations and from (4.31) it is easily seen that the isometry map takes the form

$$(x = -x', \theta = \theta', \varphi = \varphi'). \tag{12.5}$$

We find then, that if (12.2) defines one apparent horizon, its inversion symmetric counterpart is located at

$$x = -h(\theta, \phi) \tag{12.6}$$

and the outward pointing unit normal is

$$\tilde{s}^i = \frac{1}{ae^{h(\theta,\phi)}\sqrt{1 + h_{,\theta}^2 + h_{,\phi}^2/\sin^2\theta}} \left[-1 \quad -h_{,\theta} \quad -h_{,\phi}/\sin^2\theta \right]. \tag{12.7}$$

The outward-pointing normal in (12.7) is outward pointing from the point of view of an observer on the bottom sheet ($x < 0$). Thus, the inversion-symmetric counterpart to an apparent horizon for the top sheet is an apparent horizon for the bottom sheet.

To proceed in locating the apparent horizons for the initial-data sets constructed in Chapter 8, I will now restrict to the case of axisymmetry so the apparent-horizon function $h(\theta, \phi)$ now becomes a function only of θ. Expanding (11.11) in terms of (12.1) (and recalling $K = 0$), we find

$$\begin{aligned} h_{,\theta\theta} + \left[\cot\theta + 4\psi^{-1}\psi_{,\theta}\right] h_{,\theta}(1 + h_{,\theta}^2) + \left[-2 - 4\psi^{-1}\psi_{,x}\right](1 + h_{,\theta}^2) \\ - e^{-h}\sqrt{1 + h_{,\theta}^2}\psi^{-4}\left[\frac{\bar{A}_{xx}}{a} + \frac{\bar{A}_{\theta\theta}}{a}h_{,\theta}^2 - 2\frac{\bar{A}_{x\theta}}{a}h_{,\theta}\right] = 0. \end{aligned} \tag{12.8}$$

The domain in which (12.8) must be solved is $0 \leq \theta \leq \pi$. Axisymmetry demands that $\partial h/\partial\theta = 0$ on the boundaries $\theta = 0, \pi$. The demand that $\tau = 0$ define the apparent horizon is imposed by evaluating all functions of x (ψ, $\bar{A}_{ij}$, and the exponential function) at $x = h(\theta)$. The functional forms for the components of the extrinsic curvature are given in (8.4), (8.5), and (8.6). The functional form for the conformal factor ψ is only known numerically. This fact adds greatly to the difficulty in finding solutions to (12.8).

A great deal about the solutions to (12.8) can be determined without actually solving this equation. For the case of a hole with angular momentum, examining (8.6) shows that the three components of the extrinsic curvature which appear in (12.8) vanish identically. If we consider the apparent-horizon equation in the case in which the extrinsic curvature vanishes, then from (11.7) we see that it reduces to the equation for an extremal surface (vanishing of the divergence of the normal vector field). This means that in the case of a spinning hole, the apparent-horizon equation also reduces to an extremal-surface equation. But we already know that the minimal surface will

satisfy this equation and so we find that the minimal surface and the apparent horizon coincide. York and Piran [1982] have previously noted this behavior for the apparent horizons for the spinning hole solutions.

Solutions for a hole with linear momentum can be generated in one of two ways depending on the sign of the isometry condition imposed on the extrinsic curvature. Considering the case of the isometry condition with the minus sign (same as for a spinning hole), then from (8.5) we see that $\bar{A}_{xx}$ and $\bar{A}_{\theta\theta}$ both vanish on the minimal surface. If we consider the case of $h(\theta) = constant$, then (12.8) reduces again to an extremal surface equation and the surface $h = 0$ is seen to satisfy the apparent-horizon equation. While there is no evidence to suggest that other solutions exist, the non-linearity of (12.8) prevents them from being ruled out. A numerical search for other solutions must be conducted to determine if the minimal surface truly is the apparent horizon. York and Piran [1982] stated in error that $\bar{A}_{ij}\bar{s}^i\bar{s}^j \neq 0$ on the minimal surface in this case, and thus that the minimal surface and apparent horizon cannot coincide. They also claim to have found numerical solutions to the apparent-horizon equation which were not coincident with the minimal surface. As I will show later, I have found no such solutions and believe that the minimal surface and apparent horizon do in fact coincide.

The final case to consider is that of a hole with linear momentum constructed from an extrinsic curvature obeying the isometry condition with the plus sign. Examination of (8.4) shows that $\bar{A}_{xx} = 0$ only if $P/a = 0$ which is simply the Schwarzschild solution. This means that $h = 0$ cannot be a solution to the apparent-horizon equation and thus the minimal surface and apparent horizon cannot coincide.

Some understanding of the form which the apparent horizon will take in this case can be obtained by examining the case of an infinitesimally boosted hole. Bowen and York [1980] examined the effect of Lorentz boosting a Schwarzschild black hole to first order in the boost velocity. After demanding that the boosted slice be maximal, the metric is found to be unchanged to first order in the boost velocity. This metric is thus given in our coordinates by

$$g_{ij} = a^2\left(1 + e^{-x}\right)^4 f_{ij} = a^2\psi^4 f_{ij}. \tag{12.9}$$

Again to first order, the boosted form of the extrinsic curvature is given by

$$A_{ij} = \psi^{-2}\bar{A}^{\pm}{}_{ij} \tag{12.10}$$

where the two forms of (12.10) correspond to two possible inversion symmetric choices for the lapse function and $\bar{A}^{\pm}_{ij}$ is given by (5.5). The momentum used in (12.10) is defined by $P^i = MV^i = 2aV^i$

where V^i is the boost velocity of the hole. A non-numerical, first order form for the apparent horizon equation can thus be obtained by using the Schwarzschild conformal factor from (12.9) and the extrinsic curvature $\bar{A}^+_{ij}$ given in (8.4). The result is

$$\begin{aligned} h_{,\theta\theta} + \cot\theta h_{,\theta}(1+h_{,\theta}^2) + \left[-2 + \frac{2e^{-h/2}}{\cosh(h/2)}\right](1+h_{,\theta}^2) \\ - \frac{3(P/a)}{16\cosh^2(h/2)}\sqrt{1+h_{,\theta}^2}\left[\cosh h\cos\theta(2-h_{,\theta}^2) + 2\sinh h\sin\theta h_{,\theta}\right] = 0. \end{aligned} \tag{12.11}$$

If we assume that the horizon does not deviate far from the minimal surface during an infinitesimal boost, then we can expand (12.11) to first order in the apparent horizon function h. The result is

$$\frac{1}{\sin\theta}\frac{\partial}{\partial\theta}\left(\sin\theta\frac{\partial h(\theta)}{\partial\theta}\right) - h(\theta) = \frac{3}{8}\frac{P}{a}\cos\theta. \tag{12.12}$$

The solution to (12.12) compatible with the boundary conditions is

$$h(\theta) = -\frac{1}{8}\frac{P}{a}\cos\theta. \tag{12.13}$$

(Note that the corresponding equation in Cook and York [1990] is incorrect by a factor of three.) To first order in the standard radial coordinate, the apparent horizon is located at

$$r = a(1 - \frac{1}{8}\frac{P}{a}\cos\theta) \tag{12.14}$$

and we see that the apparent horizon takes the form of a *translation* ($P_\ell = \cos\theta; \ell = 1$) of the minimal surface.

With some understanding of the expected behavior of the solutions to (12.8), I turn now to the problem of solving it numerically. To simplify and clearify the expression, let me define the following quantities:

$$\mathcal{A}(h,\theta,\psi) \equiv \cot\theta + \frac{4}{\psi(h,\theta)}\left.\frac{\partial\psi(x,\theta)}{\partial\theta}\right|_{x=h(\theta)}, \tag{12.15}$$

$$\mathcal{B}(h,\theta,\psi) \equiv -2 - \frac{4}{\psi(h,\theta)}\left.\frac{\partial\psi(x,\theta)}{\partial x}\right|_{x=h(\theta)}, \tag{12.16}$$

and

$$\mathcal{C}(h,\theta,\psi) \equiv \frac{e^{-h(\theta)}}{\psi^4_{(h,\theta)}}\sqrt{1+\left(\frac{\partial h}{\partial\theta}\right)^2}. \tag{12.17}$$

The apparent-horizon equation now takes the form

$$h_{,\theta\theta} + (\mathcal{A}h_{,\theta} + \mathcal{B})(1+h_{,\theta}^2) - \mathcal{C}\left[\frac{\bar{A}_{xx}}{a} + \frac{\bar{A}_{\theta\theta}}{a}h_{,\theta}^2 - 2\frac{\bar{A}_{x\theta}}{a}h_{,\theta}\right] = 0 \quad \text{for} \quad 0 < \theta < \pi. \tag{12.18}$$

On the boundaries at the z-axis, the limiting form of (12.18) can be obtained from L'Hôpital's rule and the boundary condition that $h_{,\theta} = 0$. The result is

$$2h_{,\theta\theta} + \mathcal{B} - \mathcal{C}\frac{\bar{A}_{xx}}{a} = 0 \quad \text{for} \quad \theta = 0, \pi. \tag{12.19}$$

To difference (12.18) and (12.19), I first discretize the domain of the solution. The discretization will take the following form:

$$\theta_j \equiv j * \delta_\theta \qquad \text{where} \qquad j = 0, \ldots, \mathcal{J} \quad \text{and} \quad \delta_\theta \equiv \frac{\pi}{\mathcal{J}}. \tag{12.20}$$

The derivatives in (12.18) and (12.19) are differenced using second order central differencing. Explicitly, this gives

$$\left.\frac{\partial h}{\partial \theta}\right|_{\theta=\theta_j} = \frac{h_{j+1} - h_{j-1}}{2\delta_\theta} \equiv \mathcal{D}_j \tag{12.21}$$

and

$$\left.\frac{\partial^2 h}{\partial \theta^2}\right|_{\theta=\theta_j} = \frac{h_{j+1} - 2h_j + h_{j-1}}{\delta_\theta^2}. \tag{12.22}$$

The set of nonlinear difference equations derived from (12.18) and (12.19) can be written as $\mathcal{F}_j[h] = 0$ where

$$\begin{aligned} \mathcal{F}_j[h] \equiv & \frac{1}{\delta_\theta^2}(h_{j+1} - 2h_j + h_{j-1}) + (\mathcal{A}_j\mathcal{D}_j + \mathcal{B}_j)(1 + \mathcal{D}_j^2) \\ & - \mathcal{C}_j \left[\frac{\bar{A}_{xx}(h_j, \theta_j)}{a} + \frac{\bar{A}_{\theta\theta}(h_j, \theta_j)}{a}\mathcal{D}_j^2 - 2\frac{\bar{A}_{x\theta}(h_j, \theta_j)}{a}\mathcal{D}_j \right] \end{aligned} \qquad \text{for} \quad j = 1, \ldots, \mathcal{J} - 1, \tag{12.23}$$

$$\mathcal{F}_0[h] \equiv \frac{4}{\delta_\theta^2}(h_1 - h_0) + \mathcal{B}_0 - \mathcal{C}_0\frac{\bar{A}_{xx}(h_0, \theta_0)}{a}, \tag{12.24}$$

and

$$\mathcal{F}_\mathcal{J}[h] \equiv \frac{4}{\delta_\theta^2}(h_{\mathcal{J}-1} - h_\mathcal{J}) + \mathcal{B}_\mathcal{J} - \mathcal{C}_\mathcal{J}\frac{\bar{A}_{xx}(h_\mathcal{J}, \theta_\mathcal{J})}{a}. \tag{12.25}$$

Because of their nonlinearity, these difference equations cannot be solved directly. As in the case of the differenced Hamiltonian constraint, the nonlinear difference equations can be solved iteratively by the Newton-Raphson method for nonlinear systems described in (8.24)–(8.28). The linearized coefficient matrix $\mathcal{L}_{ab}$ is far more complicated for the apparent-horizon difference equations than it is for the case of the Hamiltonian constraint. For clarity, I give them explicitly. Let me first define the following quantities:

$$\mathcal{A'}_j \equiv \frac{\partial \mathcal{A}}{\partial h_j} = \frac{4}{\psi^2_{(\tilde{h}_j, \theta_j)}} \left[-\left(\frac{\partial \psi(x,\theta)}{\partial x}\right)\left(\frac{\partial \psi(x,\theta)}{\partial \theta}\right) + \psi(x,\theta)\left(\frac{\partial^2 \psi(x,\theta)}{\partial x \partial \theta}\right) \right] \begin{array}{l} x = \tilde{h}_j \\ \theta = \theta_j \end{array}, \tag{12.26}$$

$$\mathcal{B'}_j \equiv \frac{\partial \mathcal{B}}{\partial h_j} = \frac{4}{\psi^2_{(\tilde{h}_j, \theta_j)}} \left[\left(\frac{\partial \psi(x,\theta)}{\partial x}\right)^2 - \psi(x,\theta)\left(\frac{\partial^2 \psi(x,\theta)}{\partial x^2}\right) \right] \begin{array}{l} x = \tilde{h}_j \\ \theta = \theta_j \end{array}, \tag{12.27}$$

$$\mathcal{C'}_j \equiv \frac{\partial \mathcal{C}}{\partial h_j} = \mathcal{C}_j(1 + \mathcal{B}_j), \tag{12.28}$$

and

$$\bar{A}'_{\ell m} \equiv \left.\frac{\partial \bar{A}_{\ell m}}{\partial x}\right|_{\substack{x=\tilde{h}_j \\ \theta=\theta_j}} \tag{12.29}$$

where $\tilde{h}$ is the current estimate for the apparent horizon function. The non-zero elements of the linearized coefficient matrix are

$$\begin{aligned}\mathcal{L}_{j,j}[\tilde{h}] = -\frac{2}{\delta_\theta^2} + (\mathcal{A}'_j\mathcal{D}_j + \mathcal{B}'_j)(1+\mathcal{D}_j^2) - \mathcal{C}_j\left[\frac{\bar{A}'_{xx}}{a} + \frac{\bar{A}'_{\theta\theta}}{a}\mathcal{D}_j^2 - 2\frac{\bar{A}'_{x\theta}}{a}\mathcal{D}_j\right] \\ +\mathcal{C}'_j\left[\frac{\bar{A}_{xx}(\tilde{h}_j,\theta_j)}{a} + \frac{\bar{A}_{\theta\theta}(\tilde{h}_j,\theta_j)}{a}\mathcal{D}_j^2 - 2\frac{\bar{A}_{x\theta}(\tilde{h}_j,\theta_j)}{a}\mathcal{D}_j\right] \\ \text{for} \quad j = 1,\ldots,\mathcal{J}-1,\end{aligned} \tag{12.30}$$

$$\mathcal{L}_{j,j}[\tilde{h}] = -\frac{4}{\delta_\theta^2} + \mathcal{B}'_j - \mathcal{C}_j\left[\frac{\bar{A}'_{xx}}{a} + (1+\mathcal{B}_j)\frac{\bar{A}_{xx}(\tilde{h}_j,\theta_j)}{a}\right] \quad \text{for} \quad j = 0,\mathcal{J}, \tag{12.31}$$

$$\begin{aligned}\mathcal{L}_{j,j\pm1}[\tilde{h}] = \frac{1}{\delta_\theta^2} \pm \left\{\mathcal{A}_j\frac{1+\mathcal{D}_j^2}{2\delta_\theta} + (\mathcal{A}_j\mathcal{D}_j + \mathcal{B}_j)\frac{\mathcal{D}_j}{\delta_\theta} - \frac{\mathcal{C}_j}{(1+\mathcal{D}_j^2)\delta_\theta}\left[\frac{\bar{A}_{xx}(\tilde{h}_j,\theta_j)}{a}\frac{\mathcal{D}_j}{2}\right.\right. \\ \left.\left. +\frac{\bar{A}_{\theta\theta}(\tilde{h}_j,\theta_j)}{a}\frac{(3\mathcal{D}_j^2+2)\mathcal{D}_j}{2} - \frac{\bar{A}_{x\theta}(\tilde{h}_j,\theta_j)}{a}(2\mathcal{D}_j^2+1)\right]\right\} \\ \text{for} \quad j = 1,\ldots,\mathcal{J}-1,\end{aligned} \tag{12.32}$$

and

$$\mathcal{L}_{0,1}[\tilde{h}] = \frac{4}{\delta_\theta^2} \qquad \text{and} \qquad \mathcal{L}_{\mathcal{J},\mathcal{J}-1}[\tilde{h}] = \frac{4}{\delta_\theta^2}. \tag{12.33}$$

Inspection of the linearized coefficient matrix shows it to be tridiagonal and so it can be easily inverted directly by a tridiagonal matrix solver.

There is one difficult point in evaluating the intermediate functions (12.15), (12.16), and (12.17) and their derivatives (12.26), (12.27), and (12.28). These functions depend upon the conformal factor ψ and its derivatives which are known only numerically on a discrete mesh. From the form of the discretization of the conformal factor ψ (8.13) and (8.14), and from the form of the discretization of the apparent-horizon function h (12.20), it is apparent that the discretization of h can be chosen to match that of the conformal factor. This means that the conformal factor and its derivatives need only be evaluated along lines of constant θ on which values of the conformal factor are known numerically. Unfortunately, the radial position at which the conformal factor must be evaluated is not discretized and will, in general, not occur at a location at which the conformal factor is known. The evaluation of the conformal factor will thus require interpolation in the radial direction.

The main criterion for choosing an interpolation algorithm is the requirement that the conformal factor and its derivatives be continuous functions. From (12.15), (12.16), (12.26), and (12.27) we find that the highest order radial derivative needed is a second derivative. Interpolation by cubic

splines (*cf.* Press *et al.* [1988]) has sufficient smoothness so that its second derivatives are continuous (though not smooth) and I have chosen to use this approach for the radial interpolation. The radial derivatives can be evaluated by analytically differentiating the cubic spline interpolation formula. Angular derivatives of the conformal factor can be evaluated using second order centered difference approximations.

The possibility of the introduction of high frequency noise must always be considered when numerical data is differentiated. The use of cubic splines and the analytic differentiation of these, rather than the numerical data itself, helps to eliminate possible high frequency noise in radial derivatives. Another step which can be taken to eliminate such effects is to factor out the gross variations in the numerical data into an analytic prefactor (Piran [1988]). For the case of the one-hole initial-data sets, such a factorization can take the form

$$\psi(x,\theta) = f(x)\mathcal{N}(x,\theta) \qquad \text{where} \qquad f(x) \equiv 1 + \frac{1}{2}\frac{E}{a}e^{-x}. \tag{12.34}$$

The prefactor $f(x)$ is simply the conformal factor for a time-symmetric solution with scaled total energy E/a. By factoring this out of the numerical solution, the resulting numerical data $\mathcal{N}(x,\theta)$ will be a more slowly varying function of x and the interpolation of this data will be less prone to high frequency noise. No extra effort was needed to reduce noise for the numerical derivatives in the θ direction since the conformal factor is already a slowly varying function in this direction.

One final point needs to be explained regarding the evaluation of the conformal factor and its derivatives. The Hamiltonian constraint was solved over the finite range of $0 \le x \le x_f$ and $0 \le \theta \le \pi/2$. The range over which the apparent-horizon equation must be solved is $0 \le \theta \le \pi$. The extension of the numerical data to cover this region is easily achieved since

$$\psi(x,\theta) = \psi(x,\pi-\theta) \qquad \text{for} \qquad \pi/2 \le \theta \le \pi. \tag{12.35}$$

It will also be necessary to evaluate the conformal factor for $x < 0$. Values in this range can be obtained from the isometry condition (4.53). Written in terms of the logarithmically scaled radial coordinates we find

$$\psi(x,\theta) = e^{|x|}\psi(|x|,\theta) \qquad \text{for} \qquad x < 0. \tag{12.36}$$

Finally, if the conformal factor is needed in the region outside the outer boundary of the domain $x > x_f$, this can be approximated by (7.13) (same as $f(x)$ from (12.34)) which is the basis for the outer boundary condition imposed at x_f.

A computer code based on the method described above was constructed to solve for the apparent-horizon function $h(\theta)$ and was used to locate the apparent horizons on all of the initial-data

sets described in Chapter 8. In addition to computing the location of the apparent horizon, the code also computed the area and mass (via (8.33)) of the apparent horizon. The integral for the area of the apparent horizon is obtained by starting with the physical metric for the initial-data slice

$$ds^2 = a^2 e^{2x} \psi^4 (dx^2 + d\theta^2 + \sin^2\theta d\phi^2) \tag{12.37}$$

and using the parametrically defined location of the apparent horizon (12.2) to reduce (12.37) to the induced metric on the apparent horizon

$$ds^2 = a^2 e^{2h(\theta)} \psi^4_{(h(\theta),\theta)} ((1 + h^2_{,\theta}) d\theta^2 + \sin^2\theta d\phi^2). \tag{12.38}$$

From (12.38), the integral for the physical area of the apparent horizon is given in dimensionless form by

$$\frac{A_{AH}}{a^2} = 2\pi \int_0^\pi \psi^4_{(h(\theta),\theta)} e^{2h(\theta)} \sqrt{1 + h^2_{,\theta}} \sin\theta d\theta. \tag{12.39}$$

For the case of a hole with linear or angular momentum generated from an extrinsic curvature obeying the isometry condition with the minus sign, no solutions except the one coincident with the minimal surface were found. Other solutions were sought by varying the initial guess for the location of the apparent horizon. Convergence to the minimal surface solution was always direct, with no indication of other possible solutions.

For the case of a hole with linear momentum generated from an extrinsic curvature obeying the isometry condition with the plus sign, a single solution, not coincident with the minimal surface, was found for each initial-data set. The apparent-horizon function for the case of $P/a = 10$ is shown in Figure 12.1. The general sinusoidal shape is inherent for all values of the momentum. In fact, to within the truncation error of the problem, the solution is given by

$$h(\theta) = \mathcal{H}(P/a) \cos\theta \tag{12.40}$$

where the amplitude $\mathcal{H}$ is a function of the scaled momentum only. Table 12.1 lists the masses for the minimal surface M_{MS} and the apparent horizon M_{AH} along with the value of the amplitude $\mathcal{H}$ and its standard deviation σ resulting from a least-squares fit of the numerical data for $h(\theta)$ to the functional form (12.40).

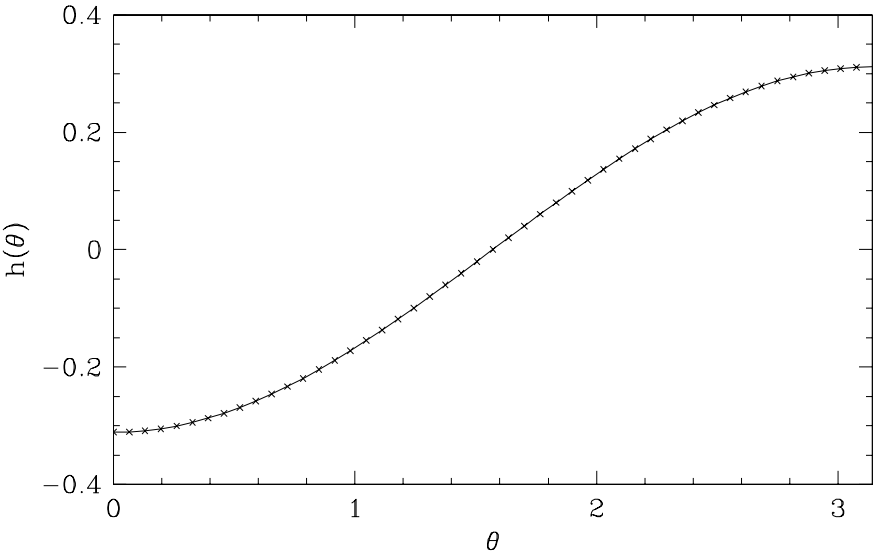


Figure 12.1: Apparent-horizon function $h(\theta)$ for a hole with linear momentum $P/a = 10$ generated by $\bar{A}^{+}_{ij}$.

P/a	M_{MS}/a	M_{AH}/a	$\mathcal{H}$	σ
1.0	2.113	2.119	−0.112291	0.000012
2.5	2.470	2.496	−0.206398	0.000087
5.0	3.069	3.121	−0.269071	0.00021
7.5	3.589	3.662	−0.295948	0.00029
10.0	4.049	4.138	−0.310731	0.00034
12.5	4.463	4.567	−0.320063	0.00039
15.0	4.843	4.959	−0.326486	0.00041
17.5	5.195	5.324	−0.331175	0.00043

Table 12.1: Minimal-surface mass and apparent-horizon mass for a hole with linear momentum P generatedfrom $\bar{A}^{+}_{ij}$. Also tabulated are the apparent-horizon amplitude $\mathcal{H}$ and its standard deviation σ.

It is seen immediately that the area of the apparent horizon is always greater than that of the minimal surface as it must be. We also see that the slope of the apparent-horizon amplitude $\mathcal{H}$ is very close to $-1/8$ at $P/a = 1$ and, so, matches well to the solution for an infinitesimally boosted hole. Further interpretation of these results will be held for the next chapter.

Chapter 13: Inversion-Symmetric, Single-Hole Initial-Data Sets

In Chapter 8, a technique for solving the Hamiltonian constraint and for extracting physically relevant information for a single hole with linear or angular momentum was described. In this chapter, I will discuss the interpretation of the content of these initial-data sets. As mentioned in Chapter 8, this has been done previously by several authors. I am including a discussion of these single-hole initial-data sets, both for completeness, and because of new information concerning the location of the apparent horizons surrounding the holes. As discussed in Chapter 12, the behavior of apparent horizons for a single boosted hole has not been understood correctly in the past, and the new understanding of the apparent-horizon structure does affect the interpretation of the initial-data sets.

Because all of the single-hole initial-data sets described here are constructed following the conformal imaging approach, they necessarily exist on a *complete*, space-like hypersurface consisting of two asymptotically-flat "sheets" joined by a single throat. The existence of an event horizon in the spacetime is confirmed by the existence of an inversion-symmetric pair of apparent horizons, one for each "universe" or "sheet".

Associated with each initial-data set is a total energy for the system. The mass associated with this energy is, in fact, the Keplerian mass which an observer at infinity on either sheet would measure by examining the orbit of a test particle. It is quite likely that the total energy in any of these initial-data sets is not entirely bound to the black hole. Some of the energy in the initial slice can be in the form of gravitational radiation which may escape to infinity. With this in mind, it is useful to consider the *irreducible mass* M_{IR} of the black hole. This mass is given by (8.33) and is associated with the area of the event horizon which (classically) can never decrease.

Given the initial data, observers at infinity on either slice can determine the total linear and angular momentum of the slice in addition to the total energy. For a boosted hole, the total energy in the slice consists of the kinetic energy of the boosted hole in addition to the energy bound to the hole and any gravitational radiation outside the hole. In this case, the rest energy of the hole will be of more importance than the total energy since it does not include the kinetic energy. For a hole

in simple translation with linear momentum P, the rest energy can be calculated simply from

$$E^2_{total} = E^2_{rest} + P^2. \tag{13.1}$$

For a spinning hole with angular momentum S, some of the energy in the system is in the form of rotational kinetic energy. Instead of associating it with the total energy of the system, however, it is traditional, and somewhat more natural, to associate this extra energy with the mass of the hole. Using the Christodoulou [1970] formula, the mass of the hole can be defined from

$$M^2 = M^2_{IR} + \frac{S^2}{4M^2_{IR}}. \tag{13.2}$$

By taking translational and rotational kinetic energy into account as in (13.1) and (13.2), and if there are no other sources of energy, then the rest energy of the system and the mass of the hole should be equivalent. If they are not equal, then, for a vacuum configuration, the only other way that energy can be present in the system is in the form of gravitational radiation. This radiation may or may not be bound to the black hole. If it is, then as the data is evolved in time, the radiation will fall into the hole and the mass of the hole will increase. If it is not bound to the hole, then eventually, it will propagate to infinity.

It is possible to obtain an upper limit on the amount of gravitational radiation which can reach infinity. It is not possible to determine the *irreducible mass* of a hole in these initial-data set since this requires knowledge of the area of the *event* horizon. However, we do know that the event horizon will necessarily be outside of or coincident with the apparent horizon, the mass of which is a lower limit on the irreducible mass. Using the total energy in the slice, the value of the linear and angular momenta at infinity and the mass of the *apparent* horizon, the upper limit to the amount of gravitational radiation which can escape to infinity is given by

$$E_{rad} \leq \sqrt{E^2_{total} - P^2} - \sqrt{M^2_{AH} + \frac{S^2}{4M^2_{AH}}}. \tag{13.3}$$

Similarly, the maximum "efficiency" with which a given configuration can produce gravitational radiation is given by

$$\text{Efficiency} \leq \frac{E_{rad}}{\sqrt{E^2_{total} - P^2}}. \tag{13.4}$$

Figures 13.1, 13.2 and 13.3 display the physical content of the initial data sets corresponding, respectively, to a hole with linear momentum generated by $\bar{A}^+_{ij}$, a hole with linear momentum generated by $\bar{A}^-_{ij}$, and a hole with angular momentum generated by $\bar{A}_{ij}$. I should note that the data in these figures are presented differently than they have been in the past. The data is displayed

in terms of *naturally* dimensionless quantities. Specifically, all quantities are scaled relative to the mass of the hole as given in (13.2) where M_{IR} is replaced by the mass of the apparent horizon which is a very good approximation to the irreducible mass. Historically (*cf.* York and Piran [1982], Choptuik [1984], and Cook and York [1990]), all quantities have been examined, either directly or effectively, scaled relative to the conformal radius of the minimal surface, ie. E/a, P/a, etc. This seems, initially, to be of trivial importance in the case of a single hole. However, it can lead to subtle misinterpretations of the physical content of the initial-data sets. For example, for a given value of P/a as measured at infinity, the initial-data sets constructed from $\bar{A}^{+}_{ij}$ and $\bar{A}^{-}_{ij}$ give different value for the total energy of the slice E/a. This fact was used in Cook and York [1990] to argue that the two initial-data slices cannot be different slicings of the same global space-time. While the conclusion may be true, it cannot be made based on this argument because the mass (and thus the proper area) of the apparent horizons in the two cases are also different. The two physical configurations are not directly comparable.

Postponing for the moment any comparison between the two, consider the initial data for a hole with linear momentum generated by either $\bar{A}^{+}_{ij}$ or $\bar{A}^{-}_{ij}$. Figures 13.1 and 13.2 display, respectively for these cases, the *naturally* scaled total energy, rest energy, maximum radiation energy, and radiation efficiency as a function of the *naturally* scaled linear momentum. Also shown for each computed value of the momentum is the velocity of the hole. This quantity is plotted adjacent to the value of the total energy and is given by $V = P/E$. We see in both cases, that the total energy follows the general behavior of a boosted point particle. In addition, the velocity of the hole is less than one in all cases and the general trend suggests that it will not exceed unity.

If the initial data being examined were that of a simple, boosted Schwarzschild black hole, then the naturally scaled rest energy should be unity for all values of the momentum. We see immediately in Figures 13.1 and 13.2 that this is not the case and so there must be gravitational radiation present in the initial-data slice. This was anticipated because, as Bowen and York [1980] pointed out, the boosted Schwarzschild metric is not conformally flat. Since it is the conformal three-geometry which carries the gravitational degrees of freedom for the metric, the choice of conformal flatness requires the presence of gravitational radiation in the initial slice. Plotted along with the maximum radiation content of the slice in Figures 13.1 and 13.2 is the maximum percentage of the rest energy which is present in the form of radiation.

Figure 13.3 displays the naturally scaled total energy, maximum radiation energy, and radiation efficiency as a function of the *naturally* scaled angular momentum. For a spinning hole, the total energy equals the rest energy since the hole has no linear momentum. In the absence of gravitational

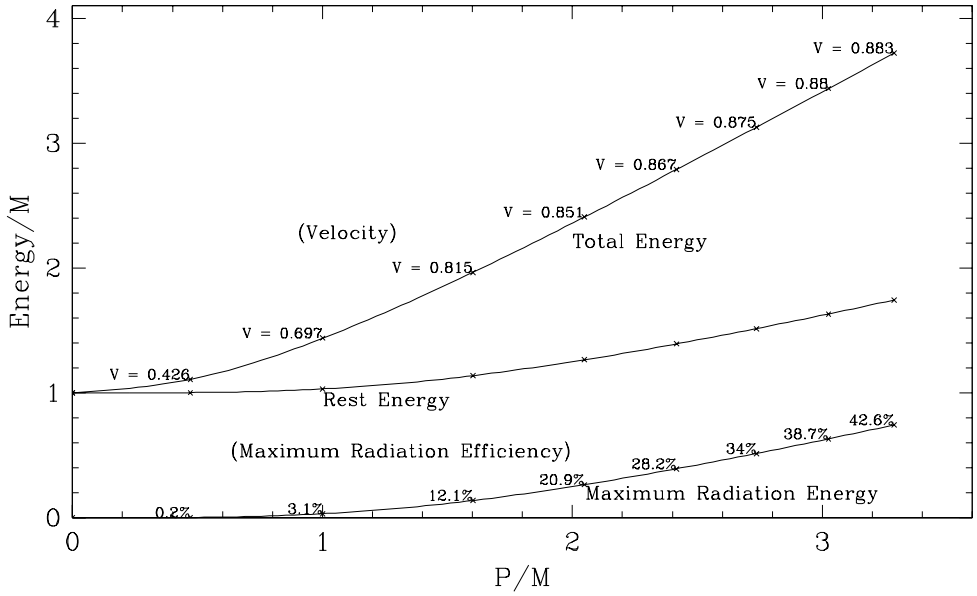


Figure 13.1: Energy and velocity for a boosted black hole with linear momentum P generated from the extrinsic curvature $\bar{A}^{+}_{ij}$.

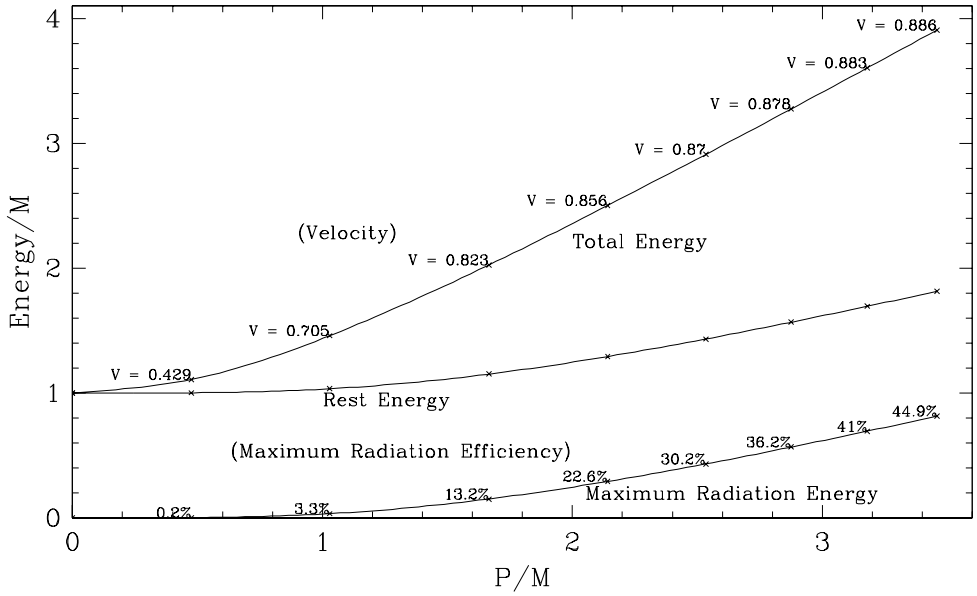


Figure 13.2: Energy and velocity for a boosted black hole with linear momentum P generated from the extrinsic curvature $\bar{A}^{-}_{ij}$.

radiation in the slice, the naturally scaled total energy should be *one* since the mass of the hole (13.2) to which the energy is scaled includes the rotational kinetic energy. From Figure 13.3, we see that the scaled total energy does deviate from unity and so there must be gravitational radiation in the slice. This, too, was anticipated because, as Bowen and York [1980] pointed out, a $t = constant$ slice

(Boyer-Lindquist time) of the Kerr metric, like the boosted Schwarzschild metric, is not conformally flat. The maximum radiation content of the slice is plotted in Figure 13.3 to a different scale than the total energy. Plotted along with the maximum radiation content of the slice in Figure 13.3 is the maximum percentage of the rest energy which is present in the form of radiation.

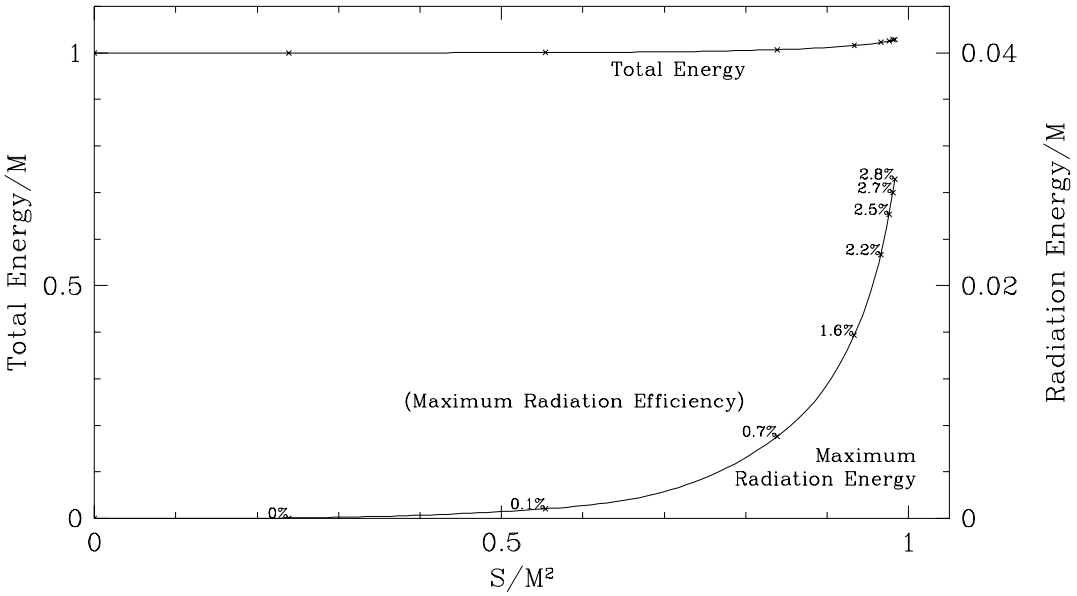


Figure 13.3: Energy of a spinning black hole with angular momentum S.

Note that in Figures 13.1 and 13.2, it appears that the scaled linear momentum may increase without bound. On the other hand, in Figure 13.3, the scaled angular momentum is asymptotic to unity. This behavior is explained by noting that an extreme Kerr metric occurs when $S/M^2 = 1$. The asymptotic behavior of the scaled angular momentum simply indicates that initial-data sets for rotating holes constructed via the conformal-imaging approach will not violate cosmic censureship.

Returning to the case of a hole with linear momentum, it is useful to compare in more detail the differences between the two sets of initial data generated from $\bar{A}^+_{ij}$ and $\bar{A}^-_{ij}$. In Chapter 12, it was discovered that the apparent horizons for the initial-data sets associated with $\bar{A}^+_{ij}$ and $\bar{A}^-_{ij}$ behave differently. For the case of $\bar{A}^-_{ij}$, the apparent horizon for the top sheet is coincident with the minimal surface. From Chapter 12, we know that the inversion-symmetric counterpart for this apparent horizon will be an apparent horizon for the bottom sheet which is also coincident with the minimal surface. This apparent horizon structure is exactly that found in $t = constant$ slices of the Schwarzschild metric in isotropic coordinates.

For the case of $\bar{A}^+_{ij}$, the position of the apparent horizon in the top sheet is given by (12.40). We see that half of the apparent horizon is on one side of the minimal surface and half is on the

other. For an observer at infinity on the top sheet, a positive value of the linear momentum will be pointed in the positive z (or $\theta = 0$) direction. From (12.40), we see that the the apparent horizon on the "leading" side of the hole ($\theta = 0$) is positioned interior to the minimal surface from the point of view of an observer on the top sheet. The apparent horizon crosses the minimal surface at $\theta = \pi/2$ and is exterior to it on the "trailing" side. Figure 13.4 illustrates this behavior by plotting the position of the apparent horizon in the conformal background space using standard spherical coordinates. These coordinates are the natural coordinate patch for the top sheet. The bottom sheet, as mentioned in Chapter 4, is the region interior to the minimal surface and infinity on the bottom sheet is compactified to the origin.

The inversion-symmetric counterpart for this apparent horizon, as described in Chapter 12, is positioned analogously from the point of view of an observer at infinity on the "bottom" sheet. Examining $\bar{A}^{+}_{ij}$ carefully, we find that an observer at infinity on the bottom sheet also finds a positive value of the momentum to point toward infinity in the $\theta = 0$ direction (see Figure 13.5). This observer will also find that the apparent horizon is interior to the minimal surface on the leading edge of the hole, crosses the minimal surface at $\theta = \pi/2$, and is exterior to the minimal surface on the trailing edge.

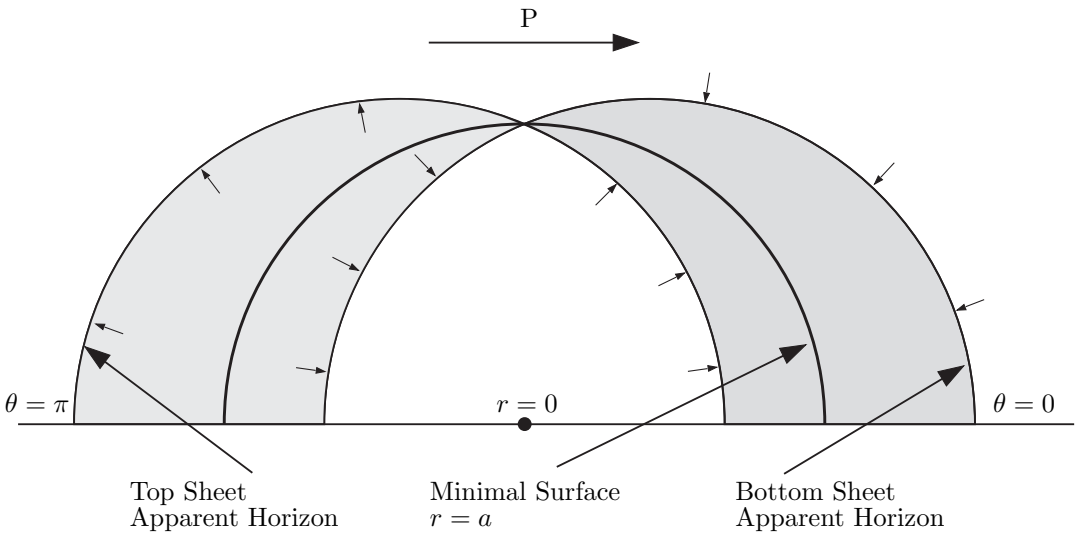


Figure 13.4: The location of the top and bottom apparent horizons (for data sets generated from $\bar{A}^{+}_{ij}$) and the minimal surface in the conformal background space. Also plotted are the spatial projections of various "outgoing" null vectors with negative expansion.

As seen from either Figure 13.4 or 13.5, the behavior of the apparent horizons means that an observer on one sheet will "see" the apparent horizon for the other sheet on the leading edge of the hole. This alternate apparent horizon is more correctly a "past" apparent horizon. Interpreted in this way, we see that the initial-data hypersurface resulting from $\bar{A}^+_{ij}$ is a slice of a global space-time which intersects the past apparent horizon for values of $\theta < \pi/2$, intersects the bifurcation point at $\theta = \pi/2$, and intersects the future apparent horizon for $\theta > \pi/2$. In contrast to this, the initial-data hypersurface resulting from $\bar{A}^-_{ij}$ is a slice of a global space-time which intersects the bifurcation point for all θ.

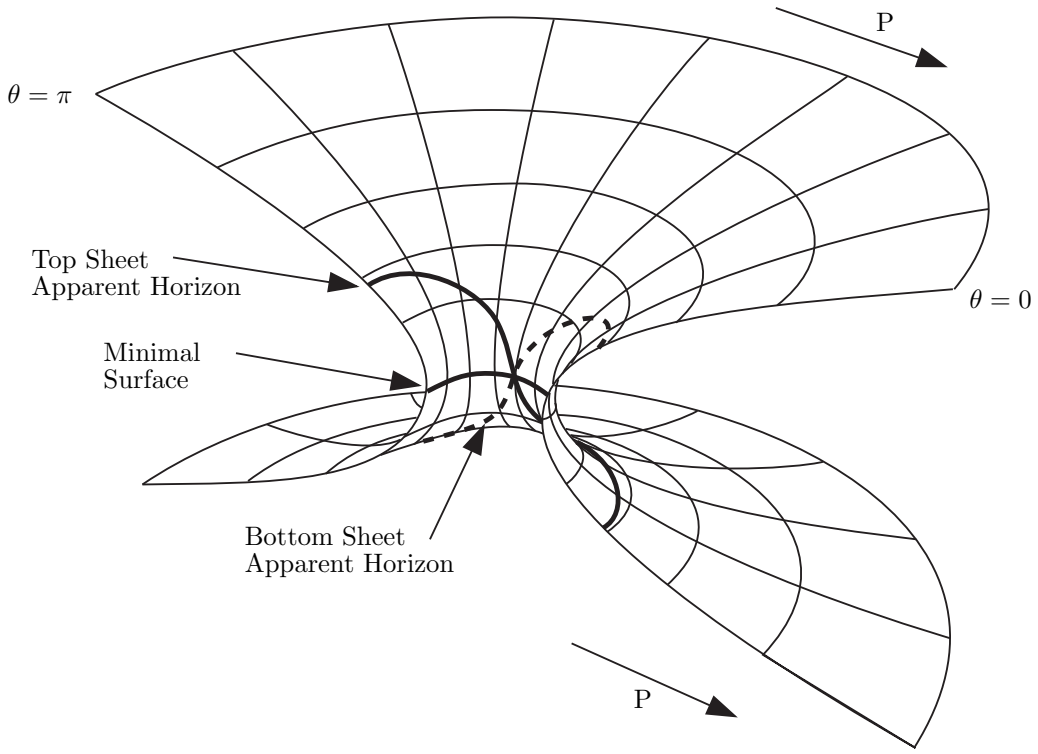


Figure 13.5: The location of the apparent horizons (for data sets generated from $\bar{A}^+_{ij}$) and the minimal surface illustrated on an embedding diagram of the geometry.

To examine the connection between these two families of initial-data sets for boosted black holes, and to understand them better, it is useful to return to the example of the first-order, boosted Schwarzschild initial data discussed in Chapter 12. While the metric, to first order, is simply the Schwarzschild metric, the extrinsic curvature and apparent horizon structure can be given either by $\bar{A}^+_{ij}$ or $\bar{A}^-_{ij}$ and their corresponding apparent horizons as described above. The choice of $\bar{A}^+_{ij}$ or $\bar{A}^-_{ij}$ is determined by the choice of the isometry condition which the lapse function must satisfy

and thus, the isometry condition which the extrinsic curvatures must satisfy. In the case of these first-order initial-data sets, we find that the choice of the isometry condition simply distinguishes two different maximal slices of the same global space-time and the evolution of either initial-data set must generate the same global space-time.

The question now is whether or not the two initial data sets given by $\bar{A}^{+}_{ij}$ or $\bar{A}^{-}_{ij}$ and their respective solutions of the Hamiltonian constraint are two different slicings of the same global space-time. Cook and York [1990] concluded that this was not the case since the total energy for the two cases, with the same linear momentum, were different. As I have discussed above, this conclusion cannot be made on this basis. If the naturally scaled initial data is compared by using cubic-spline interpolation to facilitate a direct comparison, then one finds that the scaled energies differ on at a level of less than 0.1%. This level of error is too close to the level of the discretization error in the solution for a conclusion to be drawn. This question may only be answerable by evolving the initial-data sets and examining the gravitational radiation emitted during the two evolutions.

The apparent-horizon structure found for the $\bar{A}^{+}_{ij}$ initial data in Chapter 12, in addition to illuminating the structure of the initial-data slice, also lends support to the use of the conformal imaging approach. As mentioned in Chapter 4, Thornburg [1987] has proposed using $N+1$ sheeted initial-data hypersurfaces as opposed to the two sheeted initial-data hypersurfaces of the conformal imaging approach. The use of these hypersurfaces is accompanied by the use of an apparent-horizon inner boundary condition in place of the minimal surface boundary condition of the conformal imaging approach. By using the apparent-horizon boundary condition, no information about the geometry interior to the apparent horizon can be determined. It is argued that this information is irrelevant since no information can propagate through the apparent horizon and so it can have no effect on the future evolution of the initial data. What this argument ignores, however, is the fact that the geometry interior to the apparent horizon does affect the exterior geometry in the sense that they are both part of a global construction. We see from the example of the apparent horizon structure for $\bar{A}^{+}_{ij}$ that knowing only the incomplete initial data exterior to the apparent horizon would not allow the past apparent horizon to be found. The construction of initial data sets on *complete* manifolds is crucial to assuring that the maximum amount of information can be extracted both from the initial-data set and from its evolution.

Chapter 14: Inversion-Symmetric, Two-Hole Initial-Data Sets

The previous chapter discussed the physical content and interpretation of the one-hole initial-data sets. The successful interpretation of these data sets was facilitated by the understanding of closely related analytic initial data (the boosted Schwarzschild and the Kerr solutions) to which the numerical data could be compared. Furthermore, these data sets do not involve a gravitational interaction with another object. In the case of two holes, each with linear or angular momentum, the task of interpreting the content of the initial data sets is not aided in any of these ways. There are no known analogous exact solutions for the case of two holes with linear or angular momentum to which the initial data can be compared. Further, one's intuition must be suspect in the face of the nonlinearities and non-localizability inherent in Einstein's equations. With this in mind, I will strive to attach some interpretation to the content of the two-hole initial-data sets, the construction of which was detailed in previous chapters.

The initial-data sets which will be discussed below were all constructed following the conformal imaging approach. The topology of the initial-data slice is thus that of two asymptotically flat universes connected by two Einstein-Rosen bridges. In addition, physical fields in the two universes are identified, leading to "inversion symmetry" in the initial data. Because of current computational limitations, only axisymmetric configurations of the two holes are considered. Thus, we are limited to considering a pair of holes with linear and angular momentum vectors aligned parallel to the axis joining the centers of the two holes. Further, to reduce the size of the parameter space governing the initial configuration, I will consider here only the case in which the two holes are of equal size and have linear or angular momenta of equal magnitude. Recalling the choice in sign when applying the isometry condition to the extrinsic curvature (*cf.* Chapters 5 and 6) and only considering the application of linear or angular momenta separately, we find six separate classes of configurations to consider. The first two cases are defined by the holes having linear momenta generated from the extrinsic curvature obeying the isometry condition with a plus sign. The first case has the linear momentum vectors aligned anti-parallel to each other so that there is no net momentum at infinity, and the second case has the linear momentum vectors aligned parallel to each other. The second pair of cases are defined by the holes having linear momenta generated from the extrinsic curvature

obeying the isometry condition with a minus sign. Again, the two cases are distinguished by having the linear momentum vectors aligned either anti-parallel or parallel. The final pair of cases represent holes with angular momenta aligned either anti-parallel or parallel. For clarity and brevity in the discussion below, I will refer to these configurations, respectively, as Cases 1 through 6.

For each of these cases, there are two remaining parameters to be explored. The separation between the two holes can be varied and this quantity is roughly parameterized by the "conformal separation" parameter β (*cf.* equation (9.1)). The second parameter to be varied in each initial-data set is the magnitude of the linear momentum P or angular momentum S for each of the holes. We recall from Chapter 5 that the two-hole solution for the inversion-symmetric extrinsic curvature was constructed from the superposition of *two* single-hole solutions with the addition of image terms which carry no momenta. In this way, each of the holes is assigned its own value of linear and angular momentum. An observer at infinity will measure a total linear or angular momentum for the system which is given by the vector sum of the individual linear or angular momenta. A point which must be kept in mind, however, is that when the two holes are close to each other, the value of the linear or angular momentum assigned to each hole may not have a well-defined physical interpretation.

For each point in the parameter space, there are three important physical quantities which can be directly calculated. First is the total ADM energy E of the slice. To be completely explicit, this is equivalent to the Keplerian mass of the system which an observer at infinity will measure by examining the orbits of test particles. The second quantity which can be measured is the mass of the apparent horizon surrounding each hole. At present, the search for apparent horizons in these data sets has not been undertaken and we can only approximate it with the mass of the minimal surface which will be a lower bound on the mass of the apparent horizon. The third quantity which is measured is the proper separation L, defined here as the minimum proper distance between the two minimal surfaces. It would be more nearly correct to define the proper separation as the minimum distance between the apparent horizons surrounding the two holes; however, as mentioned above, the positions of the apparent horizons are not yet known. A fourth quantity which can be measured is the dipole moment of the system. However, because of the symmetry in the problem, this quantity is identically zero.

Given this information about an initial-data set, the behavior of many quantities can be explored. As in the case of a single hole, one must be careful when examining any quantity individually as a function of the configuration parameters. We would like to use some kind of *natural* scaling as was used in the case of a single hole. The separation of the two holes, for example, is less meaningful

than the separation-to-mass ratio. The question, of course, is how to scale the quantities in such a way as to clarify the problem.

In addition to the total energy of the initial slice, there are two other basic masses in the problem. The first is the mass of the apparent horizon which is a measure of the proper surface area of the hole. The second is what I would call the mass of the hole itself and is given by the Christodoulou [1970] formula (13.2). In scaling the total energy, it is perhaps most natural to choose the Christodoulou mass M of a single hole as the natural scaling. If we consider the case of two Kerr holes infinitely far apart, then E/M for the system will be *two* regardless of the magnitude of the angular momenta on the holes. The correct choice for scaling the proper separation is less clear. For consistency, I choose to scale it with respect to the Christodoulou mass as well.

Figures 14.1–14.6 below display the naturally scaled physical quantities corresponding respectively to Cases 1–6. Each plot is derived from Richardson extrapolated initial data tabulated in Appendix C. Figures 14.1–14.4 show all quantities as a function of the scaled linear momentum P/M on *one* of the holes. In these cases where the holes only have linear momentum, the mass of the hole M and the mass of the apparent horizon M_{AH} are the same. For Figures 14.5 and 14.6, all quantities are given as a function of the scaled angular momentum S/M^2 on *one* of the holes. The mass in these two cases is the Christodoulou mass of *one* of the holes. It is given by (13.2), where the irreducible mass is approximated by the mass of the minimal surface and the spin of the individual hole is given by the angular momentum parameter S. In all plots, 10 separate configurations are displayed, each representing a different value of the separation parameter β.

Each of the six figures contains four separate plots. Plot (a) in each figure displays the scaled total ADM energy of the slice E/M. Plot (b) in each figure displays the scaled proper separation of the two holes. If we assume that the two holes will eventually coalesce into a single boosted Schwarzschild or Kerr hole, then we can use Hawking's [1971] area theorem to determine a lower limit on the final mass of the resulting black hole. Using the mass of the minimal surface M_{MS} as a lower limit on the masses of the two initial event horizons, we find that the mass of the final event horizon M_{IR} must be larger than

$$M_{IR} > \sqrt{2} M_{MS}. \tag{14.1}$$

If S_1 and S_2 are the signed magnitudes of the spins on the two initial holes, then the final mass of the hole M_f must be larger than

$$M_f > M_{MS} \sqrt{2 + \frac{1}{8} \left(\frac{S_1}{M_{MS}^2} + \frac{S_1}{M_{MS}^2} \right)^2}. \tag{14.2}$$

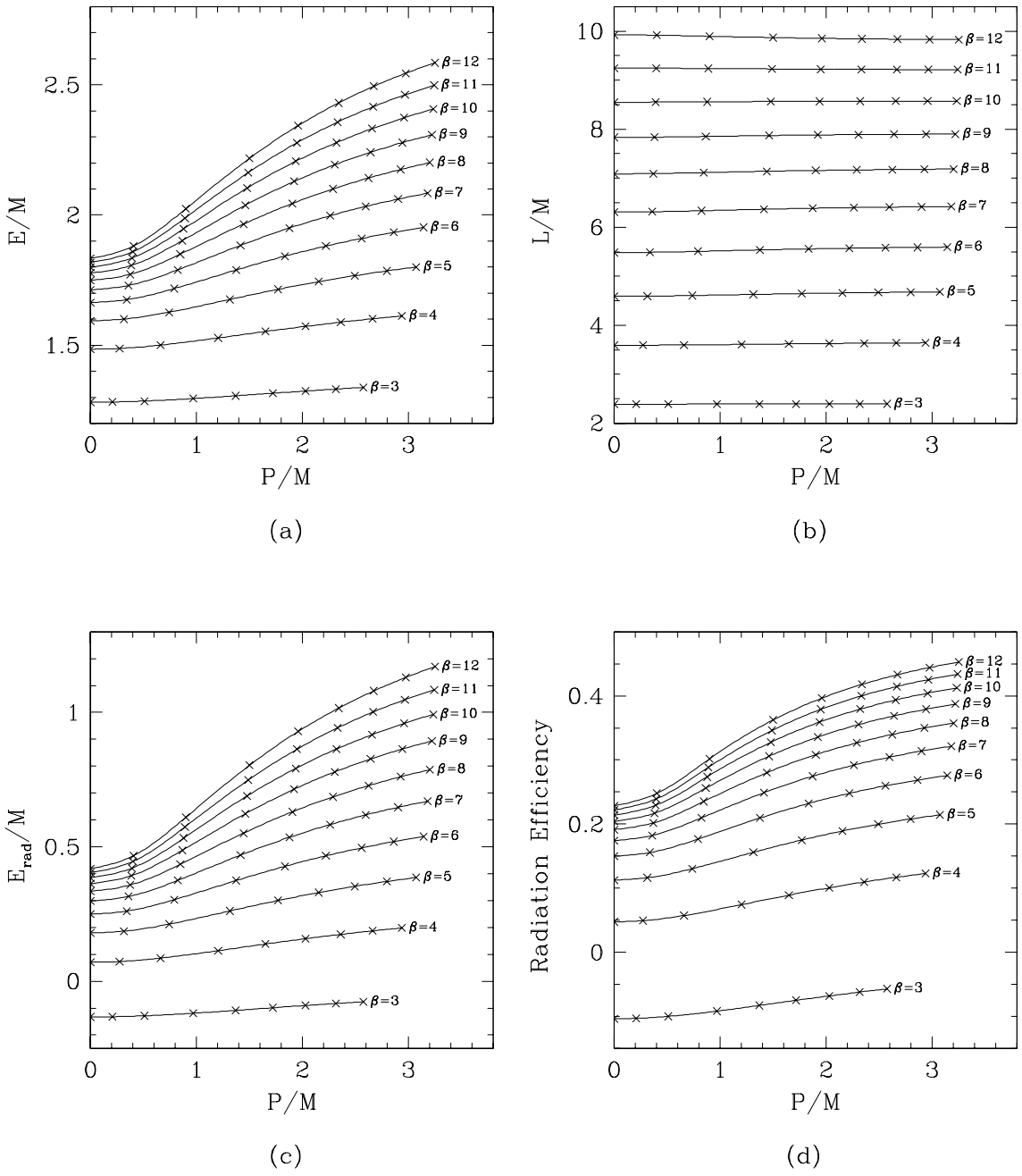


Figure 14.1: (a) total energy, (b) separation, (c) maximum radiation energy, and (d) maximum radiation efficiency for two holes with linear momenta P aligned anti-parallel to each other and generated by an inversion-symmetric extrinsic curvature obeying the isometry condition with a plus sign.

If P_1 and P_2 are the signed magnitudes of the linear momenta of the two initial holes, then an upper limit on the amount of energy which can possibly be radiated from the system is

$$E_{rad} < \sqrt{E^2 - (P_1 + P_2)^2} - M_{MS}\sqrt{2 + \frac{1}{8}\left(\frac{S_1}{M_{MS}^2} + \frac{S_1}{M_{MS}^2}\right)^2}. \tag{14.3}$$

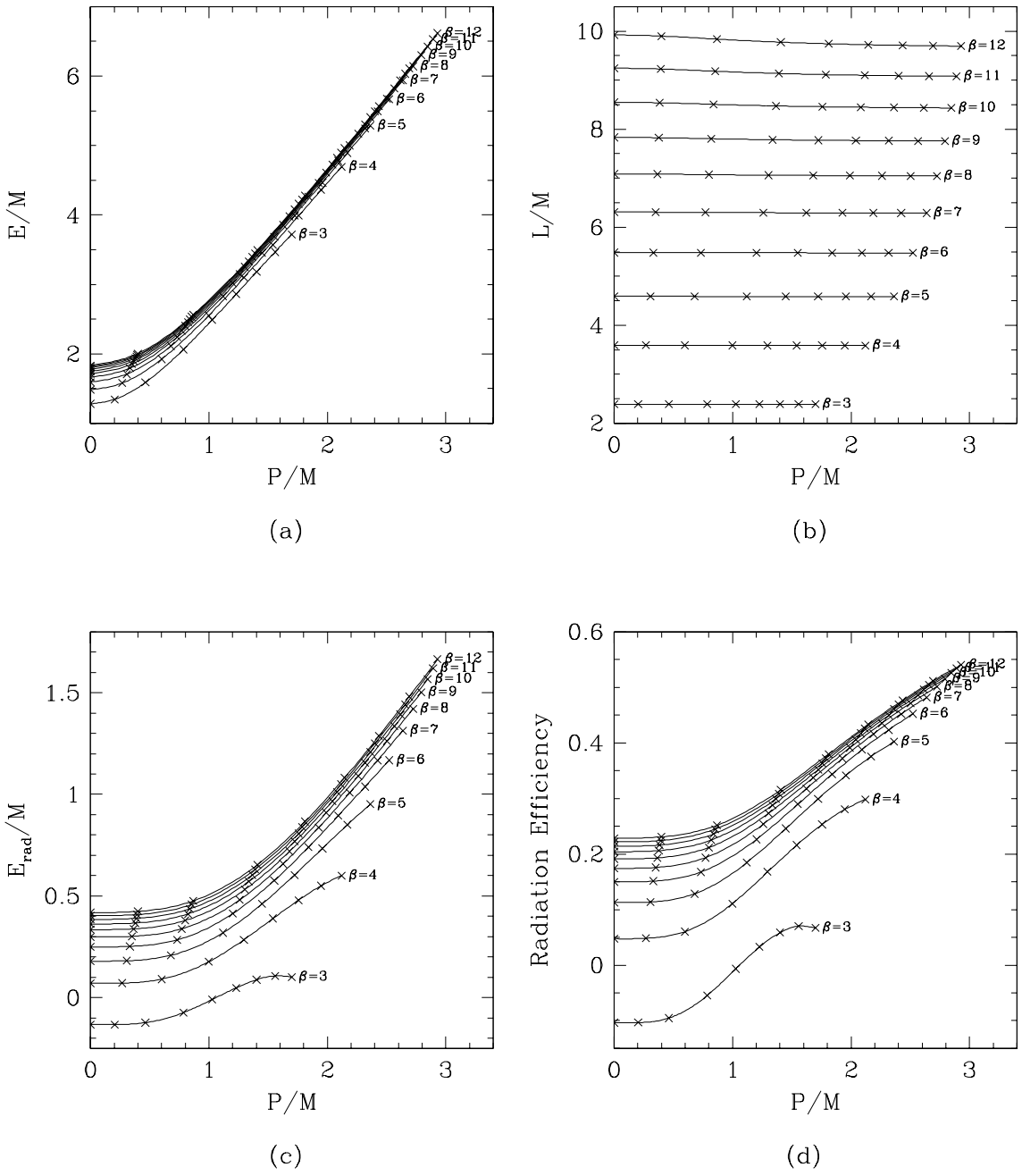


Figure 14.2: (a) total energy, (b) separation, (c) maximum radiation energy, and (d) maximum radiation efficiency for two holes with linear momenta P aligned parallel to each other and generated by an inversion-symmetric extrinsic curvature obeying the isometry condition with a plus sign.

The maximum possible radiation content of the slice scaled to the mass of one of the holes E_{rad} is displayed in Plot (c). Finally, Plot (d) in each figure displays the maximum radiation efficiency of

each slice which is given by

$$\text{efficiency} < \frac{E_{rad}}{\sqrt{E^2 - (P_1 + P_2)^2}}. \tag{14.4}$$

Consider first Cases 1 and 3, which represent two holes with anti-parallel linear momentum vectors. These two cases, representing both choices in the isometry, can represent either two holes headed directly toward each other or directly away from each other. Because the holes are of equal size and have momenta of equal magnitude, the energy, mass, and separation are identical in either instance.

The first question related to these two cases is whether the two choices for the isometry condition lead to two different global spacetimes or two different slicings of the same global spacetime? All four plots in each case are qualitatively the same although there are discernible differences. Because we do not know the true mass of the apparent horizon, the question posed above cannot be definitively answered. Carefully examining the differences between the two cases does show that if they are two different slicings of the same spacetime, then the mass of the apparent horizon in Case 3 must increase from its current estimate by a factor larger than the increase in Case 1.

Consider now the total energy of the system. If the two holes are at rest infinitely far apart, then E/M should be *two*. Thus, any configuration with $E/M < 2$ should be gravitationally bound. Plot (a) in Figures 14.1 and 14.3 shows that if the two holes are far enough apart and have large enough momenta, then it is energetically feasible (if the momenta are directed away from each other) for the two holes to be unbound. One must keep in mind, however, that some of the excess energy may be in the form of gravitational radiation, as in the case of a single boosted hole.

Examining Plot (b) in Figures 14.1 and 14.3, we find that the conformal separation parameter β has a strong correlation with the physical separation to mass ratio L/M. For each of the ten values of β, L/M is surprisingly constant for all values of P/M. This is somewhat unexpected given the nonlinearity of Einstein's equations.

If the two holes do coalesce, then Plot (c) in Figures 14.1 and 14.2 shows the scaled maximum amount of energy which can be emitted by gravitational radiation. As expected, E_{rad}/M increases as both separation and momentum increase. An unusual feature is seen for $\beta = 3$. In this case, the energy available for radiation is negative. To understand this behavior we note that if two Schwarzschild holes, infinitely separated and initially at rest, are allowed to coalesce with the maximum release of energy, then E/M for the resulting hole is $\sqrt{2}$. We expect, then, that an apparent horizon will form around the two holes when their separation gives an E/M value near $\sqrt{2}$. This corresponds to a value of $\beta \sim 3.6$ and corresponds to $L/E \sim 2.2$, which is in rough agreement with

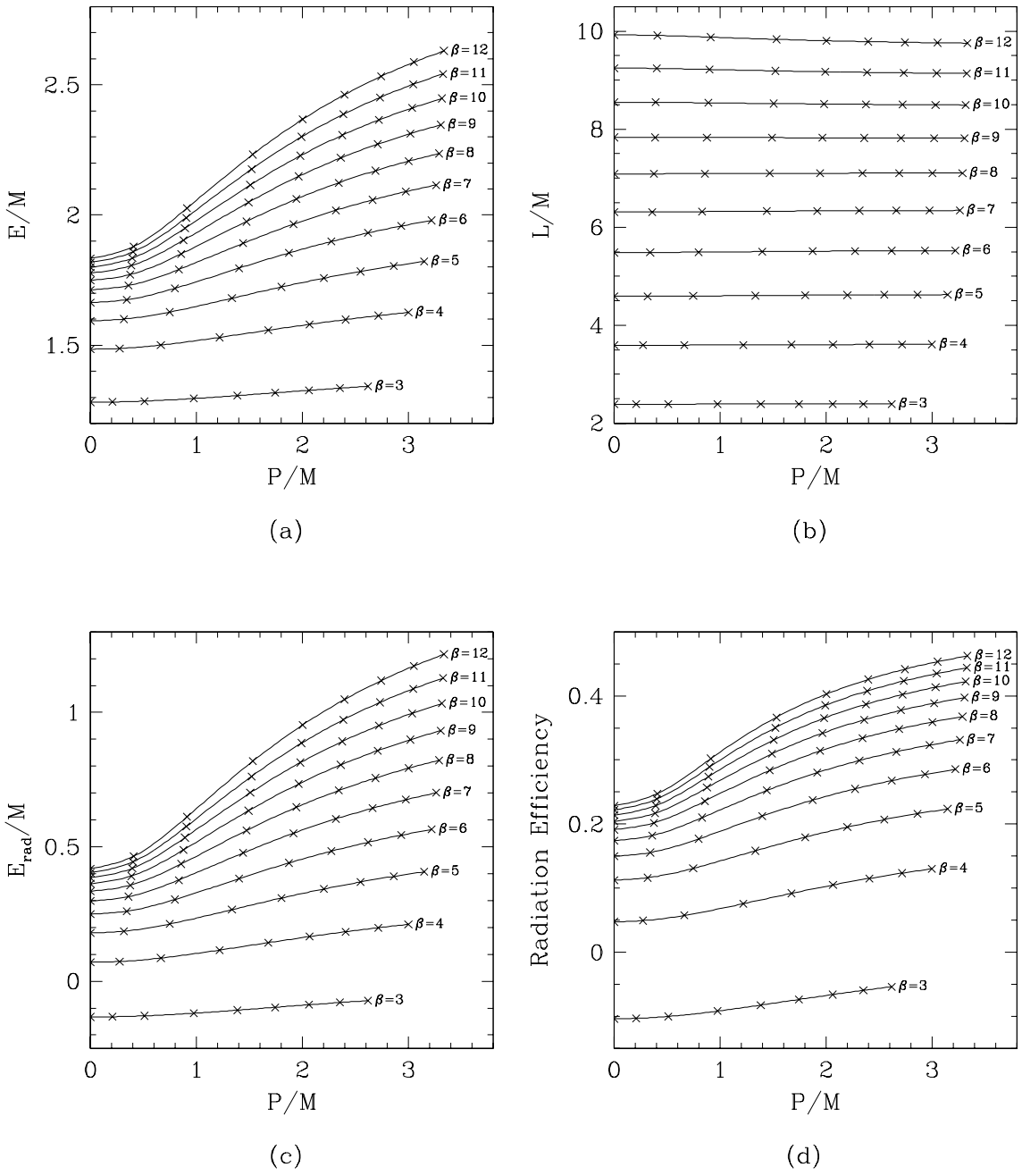


Figure 14.3: (a) total energy, (b) separation, (c) maximum radiation energy, and (d) maximum radiation efficiency for two holes with linear momenta P aligned anti-parallel to each other and generated by an inversion-symmetric extrinsic curvature obeying the isometry condition with a minus sign.

the numerical results of Smarr *et al.* [1976]. The negative value of E_{rad}/M for $\beta = 3$ *must* stem from the inappropriate use of equation (14.3) when the two holes are surrounded by a third apparent horizon.

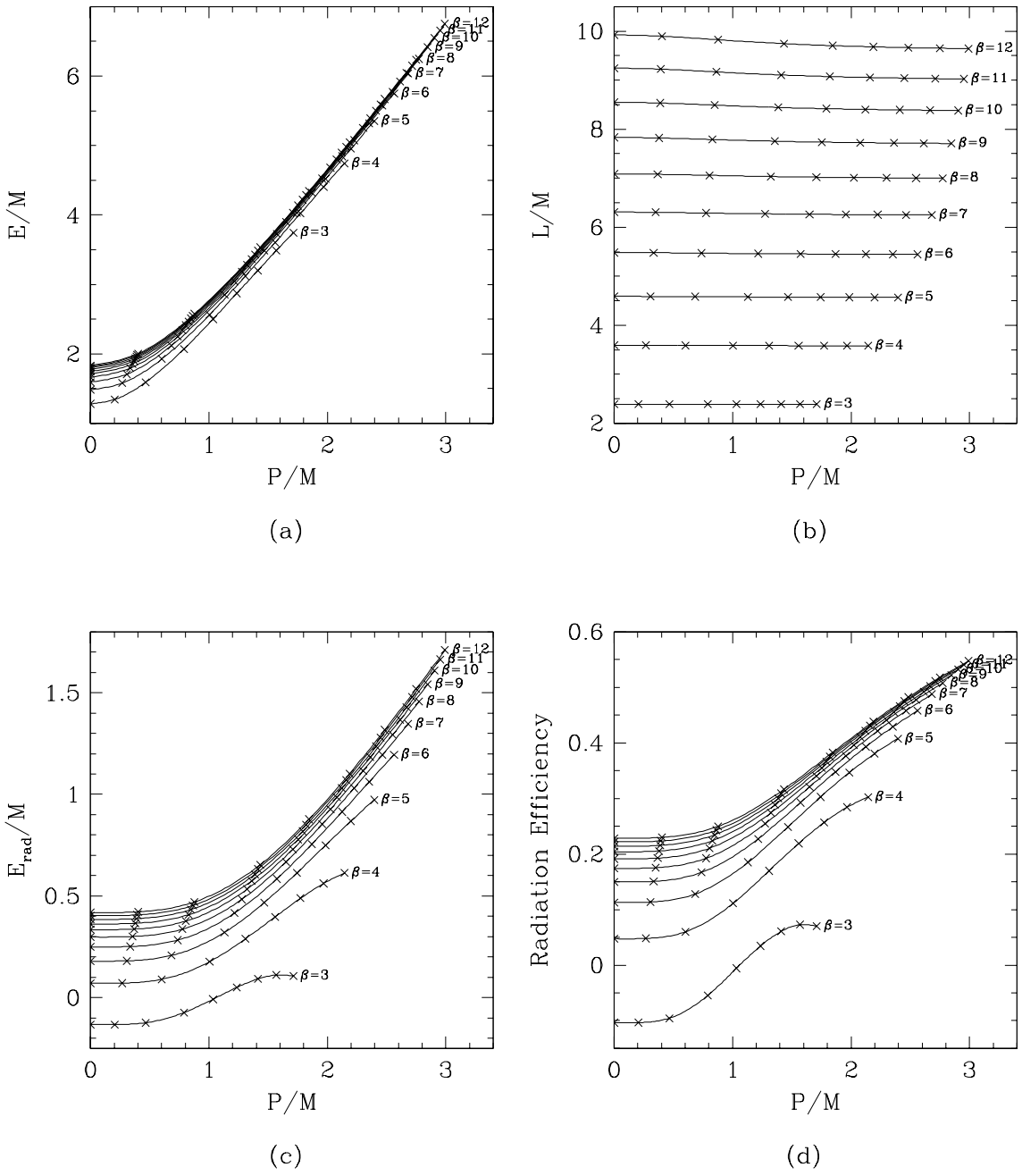


Figure 14.4: (a) total energy, (b) separation, (c) maximum radiation energy, and (d) maximum radiation efficiency for two holes with linear momenta P aligned parallel to each other and generated by an inversion-symmetric extrinsic curvature obeying the isometry condition with a minus sign.

Let us move now to the case of two holes with parallel linear momenta represented in Cases 2 and 4. The plots displaying the physical content of these two cases are found respectively in Figures 14.2 and 14.4. As for Cases 1 and 3, we find that the initial data generated from the two choices of the

isometry condition are qualitatively the same although there are discernible differences. Again, we find that the mass of the apparent horizon in Case 4 (minus isometry) must increase from its current estimate by a factor larger than the increase in Case 2 if the two cases are to represent different slicings of the same global spacetime.

Examining the behavior of the total energy in Plot (a) of Figures 14.2 and 14.4 shows the gross behavior of a single boosted particle. At lower values of the momentum, the lowering of the total energy, due to increased binding energy as the holes move closer, is also clearly visible. Plot (b) shows that the L/M ratio is again fairly insensitive to P/M. Plots (c) and (d) show little new information about the radiation content of the initial slice beyond that already seen for a single boosted hole. The primary difference results from the effects of binding energy.

The most interesting of the cases to examine are Cases 5 and 6 which involve two holes with, respectively, anti-parallel and parallel angular momentum vectors. The behavior of the scaled total energy in the slice, seen in Plot (a) in Figures 14.5 and 14.6, is surprising and unintuitive. While it clearly shows the effects of increased binding energy as the holes are brought closer together, it also indicates that the total energy-to-mass ratio decreases as the angular momenta increase, with the decrease being most dramatic when the spins are anti-parallel.

Examining the L/M ratio in Plot (b) in Figures 14.5 and 14.6 shows that it is much more strongly affected by the spin of the holes than by their linear momenta. Lines of constant β can no longer be considered to represent a constant L/M ratio. This fact complicates the interpretation of the total energy of the slice seen in Plot (a) in Figures 14.5 and 14.6. Because the holes are getting closer, for constant β as the angular momenta is increased, they necessarily have a greater binding energy and the decrease in E/M must be due, in part, to this effect. However, rough interpolations along lines of constant L/M shows clearly that the decrease in separation is not the dominant contribution to the decrease in E/M. It is possible that the Christodoulou mass is not the correct quantity with which to scale the total energy and separation. On the other hand, its use in scaling the angular momentum does have the correct limiting behavior as the angular momentum is increased. That is, S/M^2 appears to be asymptotic to *one*, which is the "Kerr" limit.

Moving on to examine the radiation content of the slices, consider first Plots (c) and (d) in Figure 14.5. We see, in the case of two holes with anti-parallel spins, that the amount of energy which is potentially available for radiation does increase initially as the angular momentum is increased. However, after a certain point, the available energy rapidly diminishes with increased angular momentum. These effects are seen not only in Plot (c), which is scaled with respect to the Christodoulou mass, but also in Plot (d), which shows the ratio of the maximum radiation content

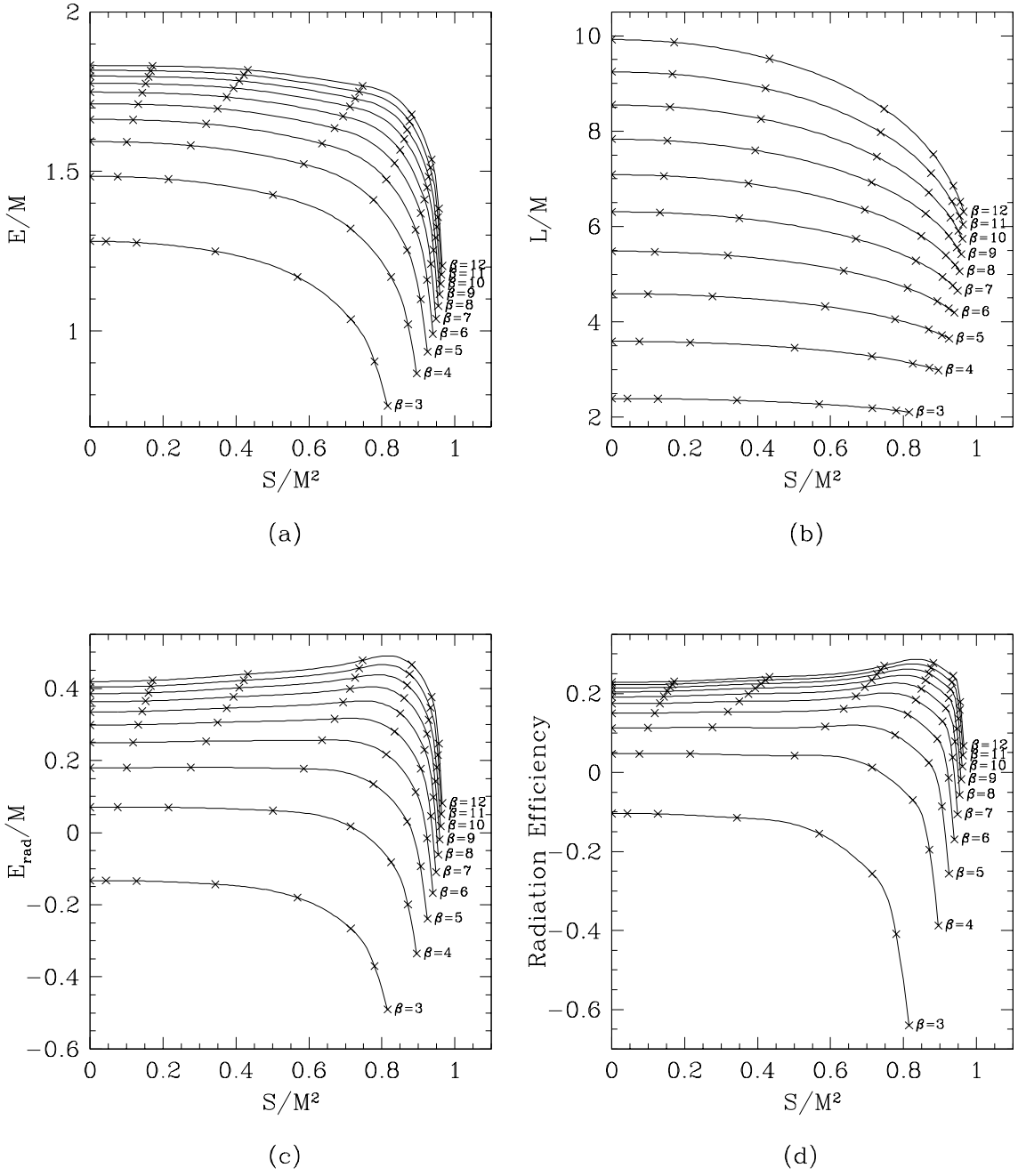


Figure 14.5: (a) total energy, (b) separation, (c) maximum radiation energy, and (d) maximum radiation efficiency for two holes with angular momenta S aligned anti-parallel to each other and generated by an inversion-symmetric extrinsic curvature obeying the isometry condition with a minus sign.

to the total energy. This last ratio is independent of the choice of a scaling parameter and indicates that the drop in total energy is a physical effect independent of the choice of the scaling parameter. Examining Plots (c) and (d) in Figure 14.6 shows, in the case of two holes with parallel spins,

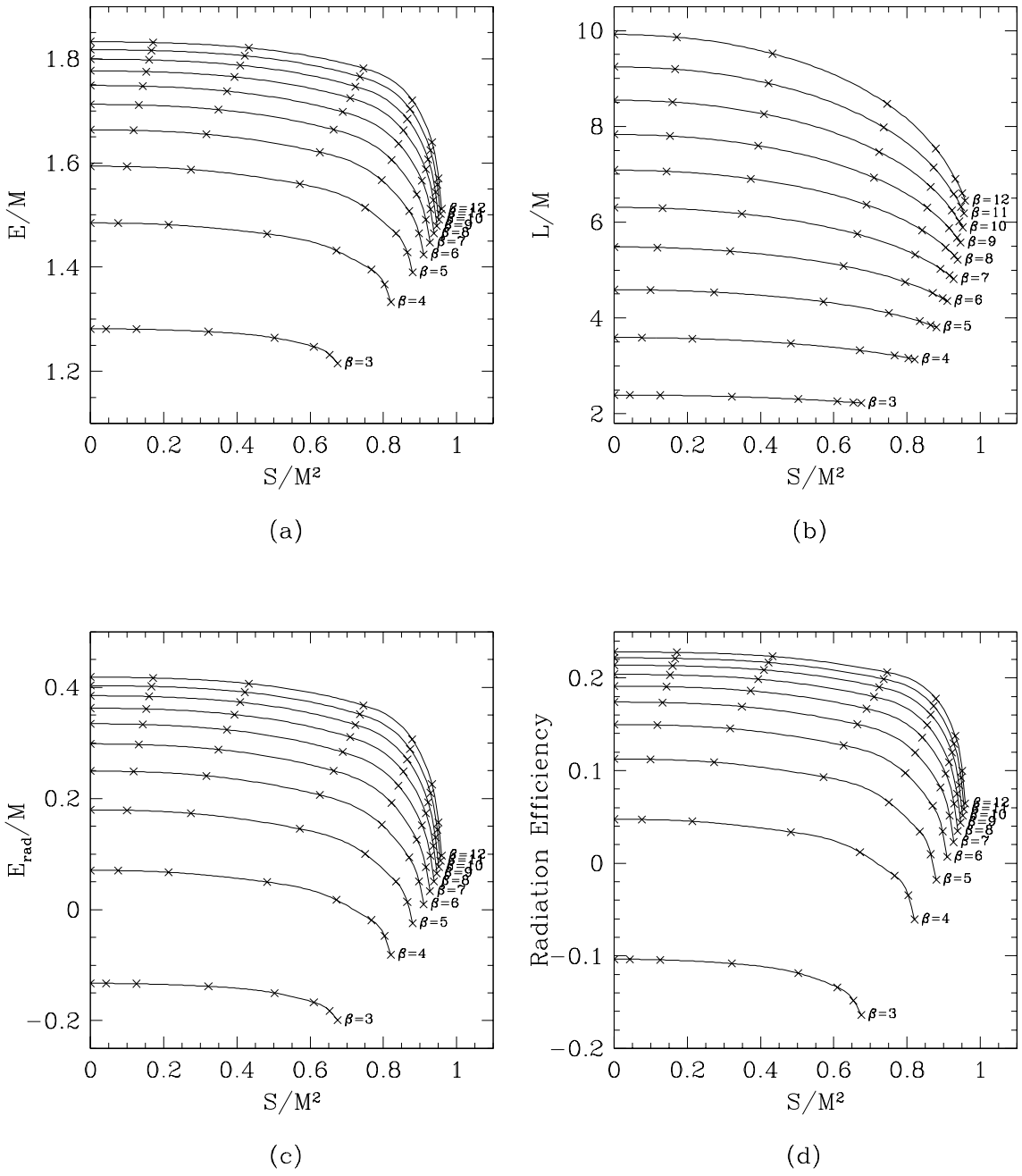


Figure 14.6: (a) total energy, (b) separation, (c) maximum radiation energy, and (d) maximum radiation efficiency for two holes with angular momenta S aligned parallel to each other and generated by an inversion-symmetric extrinsic curvature obeying the isometry condition with a minus sign.

that the amount of energy which is potentially available for radiation decreases continuously as the angular momentum is increased.

The decrease in the total energy as the spin of the holes (either parallel or anti-parallel) is

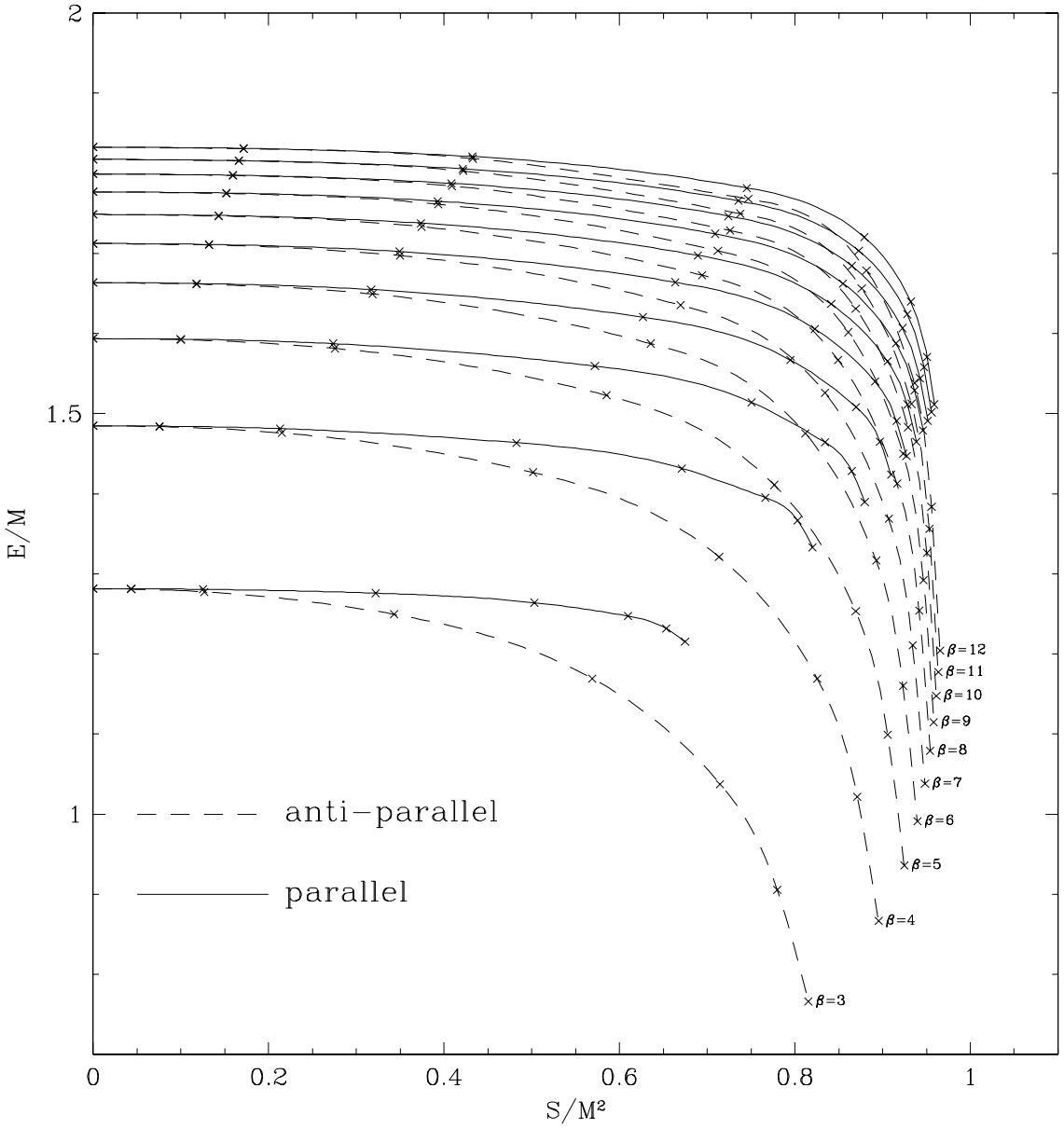


Figure 14.7: Comparison of the scaled total energy for two holes with angular momenta S aligned anti-parallel and parallel to each other showing the spin-spin interaction.

increased may indicate that there is an additional attractive interaction between the holes which is a result of the spins and is independent of the orientation of the spins. Such an attractive force would add to the binding energy of the configuration and decrease the total energy. Beyond this, there is clear evidence of an orientation-dependent, spin-spin interaction between the two holes. Figure 14.7 shows an overlay of Plot (a) from Figures 14.5 and 14.6 which compares the total energy of the slice for the parallel and anti-parallel oriented spins. Even though the sequences of constant β do not

represent a constant L/M ratio, the L/M curves for constant β are nearly identical for both the parallel and anti-parallel spin scenarios. This allows us to directly compare the E/M ratio in the two cases for the same values of β. For each value of β, we find that the E/M ratio is lower when the spins are oriented anti-parallel than when parallel. This indicates that there is a spin-spin force which is attractive when the spins are anti-aligned and repulsive when aligned. Such an interaction is in agreement with the gravitational spin-spin interaction investigated by Wald [1972] for the case of a spinning test particle in the exterior field of an arbitrary, stationary, rotating source. We can also see that the magnitude of the spin-spin force decreases as the separation between the holes increases. This is apparent from the fact that the difference in the energy levels for the aligned and anti-aligned cases decreases as the separation increases.

As evidenced by the discussion above, the understanding of the content of the two-hole initial-data sets is far from complete. Many uncertainties should be resolved when the location and areas of the apparent horizons are determined. This knowledge will allow for much more accurate estimates of the irreducible mass of the holes and will greatly change many of the estimates for the radiation content of the initial-data slices since the current method of estimating the radiation content assumes that there is not a third horizon surrounding both holes. In any case, it will probably be the case that a complete understanding of the content of these two-hole initial-data sets will be found only by evolving them in time.

Chapter 15: Conclusion

The primary motivation for undertaking an investigation of methods for computing initial-data sets containing one or more black holes is the desire to simulate black hole collisions. In particular, we wish to evolve data which represent two black holes in a bound orbit, spiralling toward a collision. During this evolution, we wish to examine the gravitational radiation which is being emitted during the spiralling infall, the collision, and the subsequent transition to quiescence. With this in mind, I will discuss the usefulness and limitations of initial-data sets constructed following the conformal imaging approach. I will also discuss some of the problems remaining to be investigated regarding the generation and evolution of these initial-data sets.

The most obvious advantage of the conformal imaging approach over other methods for constructing initial-data sets containing black holes (*cf.* Thornburg [1987]) is that it allows for the construction of initial data on a *complete* manifold. During an evolution of this initial data, more of the global structure of the space-time should be accessible because the initial-data manifold is complete. The "price" which is paid for having a complete manifold is that all of the fields which reside on the manifold must obey an isometry condition which identifies the physical fields on the two "sheets" (or universes) which the manifold comprises. At first, this identification may seem unnatural. The imposition of such an isometry condition is possible only when topological vacuum solutions are considered. If the black hole is produced from a matter source, then there can be no "alternate" universe to identify with the "physical" universe. The existence of multiple, causally disconnected, asymptotically flat regions seems to be a generic feature of vacuum black-hole space-times. Unless there is some reason that these additional universes should be considered physically relevant and distinct from the "real" universe, it actually seems most natural to identify these causally disconnected regions mathematically.

One of the most important reasons for pursuing the evolution of the two black hole collision problem is the desire to obtain accurate waveforms for the gravitational radiation which results from the collision. In order to be able to compare waveforms generated by numerical means confidently against waveforms which should be available in the future from gravity-wave detectors, it will be important to be able to distinguish between waveforms which result from the dynamics of the

evolution and those which are present in the initial data. As has been shown, initial-data sets constructed by the conformal imaging approach must contain gravitational radiation in the field exterior to the apparent horizon. This is not a condition inherent only to the conformal imaging approach, however. Any initial-data sets constructed on a space-like slice will most likely contain gravitational radiation. Even if the trace-free background extrinsic curvature is purely longitudinal, the physical extrinsic curvature may have a non-vanishing, transverse-traceless part.

Since these initial-data sets do contain gravitational radiation from the start, it will be necessary to determine its content in some quantitative way so that its contribution to the dynamical waveform can be determined. It is likely that any gravitational radiation present in the initial slice can be made to propagate away from or fall into the holes before any of the interesting dynamics takes place. In addition, some hope for finding methods of examining the gravitational radiation content of initial-data sets has been expressed by Abrahams [1990] based on experience in extracting waveforms from numerical evolutions of Einstein's equations (*cf.* Abrahams and Evans [1988], [1990]). I feel that this avenue of investigating the radiation content of the initial data should be vigorously pursued.

Beyond these questions regarding the content of the initial-data sets, there are problems which have yet to be addressed regarding their numerical generation. The research described in this work has dealt with the generation of axisymmetric initial-data sets. I have found a general, explicit approach for evaluating the two-hole, inversion-symmetric extrinsic curvature and I have demonstrated two approaches for solving the two-hole Hamiltonian constraint numerically. With regard to these axisymmetric data sets, the task of increasing the accuracy of the numerical solutions still remains as does the problem of locating the apparent horizons in these data sets.

In order to model the *spiralling* collision of two black holes, three-dimensional initial-data sets will be required. Many of the techniques developed for constructing axisymmetric data sets can be applicable to the three-dimensional problems. The method I have developed for evaluating the axisymmetric, inversion-symmetric extrinsic curvature is directly generalizable to three-dimensional situations. The general approaches for differencing the Hamiltonian constraint should also be applicable. However, some effort will be needed with regard to differencing near the coordinate singularity along the z-axis in the absence of axisymmetry. Also, much work will be required in finding an efficient approach for solving the resulting difference equations. The size of this set of equations will be significantly larger than that resulting from differencing the axisymmetric problem and will tax the memory limitations of even the most powerful supercomputers.

I would like to turn now to the problem of evolving inversion-symmetric initial-data sets. As was mentioned earlier, the use of initial data on a *complete* manifold should allow for more of the global

space-time to be covered during a numerical evolution. Initial data constructed by the conformal imaging approach allows for the efficient construction of initial data on a complete manifold because only half of the full manifold must be considered. The other half is known by identification through the isometry condition. Because the two sheets of the manifold contain identical Cauchy data, the two causally disconnected spacetimes which evolve from these data will be identical and there will therefore exist a spacetime isometry between them. If *efficient* use is to be made of the initial data, however, then each spatial slice in the subsequent evolution should *also* consist of a complete three-manifold on which the data obey a spatial isometry condition which is either similar or identical to the isometry condition on the initial-data slice. This means that the question of the compatibility of the isometry condition and the evolution equations must be considered.

A full investigation of this problem is beyond the scope of this concluding chapter, but I do wish to discuss some of the more general points. To begin with, all of the fields which are relevant to the evolution equations will be required to satisfy some isometry condition. The isometry condition includes, in some cases, the freedom of choice in the sign of the identified field. For example, we have seen in Chapter 4 that the extrinsic curvature can obey the isometry condition with either a plus or a minus sign. The metric, on the other hand, must obey the isometry condition only with a plus sign in order for the metric to be non-singular on the inversion surfaces. To determine the sign of the isometry condition for the other fields we must examine the vacuum Einstein equations

$$R + \frac{2}{3}K^2 - A_{ij}A^{ij} = 0, \tag{15.1}$$

$$D_j(A^{ij} - \frac{2}{3}\gamma^{ij}K) = 0, \tag{15.2}$$

$$\begin{aligned}\partial_t A_{ij} = &- D_i D_j \alpha + \alpha R_{ij} - 2\alpha A_{i\ell}A_j{}^{\ell} + \alpha A_{ij}(\frac{1}{3}K) + 3\alpha\gamma_{ij}(\frac{1}{3}K)^2 \\ &- \gamma_{ij}\partial_t(\frac{1}{3}K) + \gamma_{ij}\beta^{\ell}D_{\ell}(\frac{1}{3}K) + \beta^{\ell}D_{\ell}A_{ij} + A_{i\ell}D_j\beta^{\ell} + A_{\ell j}D_i\beta^{\ell},\end{aligned} \tag{15.3}$$

and

$$\partial_t \gamma_{ij} = -2\alpha A_{ij} - \frac{2}{3}\alpha\gamma_{ij}K + D_i\beta_j + D_j\beta_i. \tag{15.4}$$

We see immediately that the lapse α and the trace of the extrinsic curvature K must obey the isometry condition with the same sign as the extrinsic curvature

$$\alpha(\mathbf{x}) = \pm\alpha(\mathbf{J}_\alpha(\mathbf{x})) \tag{15.5}$$

and

$$K(\mathbf{x}) = \pm K(\mathbf{J}_\alpha(\mathbf{x})). \tag{15.6}$$

(The subscript α on the isometry condition $\mathbf{J}_\alpha$ designates the throat through which the isometry is applied and should not be confused with the lapse function.) We also find that the shift vector β^i must obey the isometry condition with the plus sign

$$\beta^i(\mathbf{x}) = (\mathbf{J}_\alpha^{-1})_j{}^i \beta^j(\mathbf{J}_\alpha(\mathbf{x})). \tag{15.7}$$

The isometry conditions (15.5)–(15.7) along with similar conditions for the metric and extrinsic curvature (4.38) and (4.39) can be used to generate boundary conditions which these fields must obey at the inversion surfaces which are fixed point sets of the isometry. Using the isometry condition which we know is obeyed on the initial hypersurface and going to a local spherical coordinate system (r, θ, ϕ) centered around any given throat, we can read off boundary conditions for each component of each field. The boundary condition will be such that either the normal derivative of a given component vanishes at the throat or the value of the component vanishes at the throat. Since there is no choice in the sign of the isometry condition for the metric, we find immediately that the normal derivatives of γ_{rr}, $\gamma_{\theta\theta}$, $\gamma_{\phi\phi}$, and $\gamma_{\theta\phi}$ must vanish at a throat and $\gamma_{r\theta}$ and $\gamma_{r\phi}$ must vanish in value at a throat. There is also no choice in the sign of the isometry condition for the shift vector and we find that β^r must vanish in value at a throat and also that the normal derivatives of β^θ and β^ϕ must vanish at a throat. The boundary condition for the remaining quantities depends on the choice in sign for the isometry condition. If the isometry condition with a plus sign is chosen for α, K, and A_{ij}, then we find that the normal derivatives of α, K, A_{rr}, $A_{\theta\theta}$, $A_{\phi\phi}$, and $A_{\theta\phi}$ must vanish on a throat and so $A_{r\theta}$ and $A_{r\phi}$ must vanish in value on a throat. If the isometry condition with a minus sign is chosen, then the conditions are reversed. Boundary conditions of this sort are being used by Bernstein and Hobill [1990] in their investigations into the evolution of a single, perturbed black hole.

We can now consider whether the imposition of these boundary conditions in conjuction with the evolution equations (15.3) and (15.4) is sufficient to guarantee that the fields on subsequent slices will be inversion symmetric. The imposition of the boundary conditions described above should ensure that the surfaces identified with fixed-point sets of the isometry remain fixed-point sets throughout the evolution. What it may not do, however, is determine what the explicit form of the isometry conditions (or maps) will be. It is the explicit form of the isometry maps which, given a coordinate map defined by the isometry, allows for the smooth continuation of fields through the inversion surfaces. This, in turn, allows global structures such as apparent horizons, which may cross the inversion surface, to be located.

To exploit fully the conformal imaging approach, it will be necessary to understand better the relation between the isometry maps and the evolution equations, and also their relation with the constraint equations on evolved slices which will not be conformally flat. While I do not claim to have come to any complete understanding of this problem, I would like to discuss a few important points. It seems likely to me that the explicit form of the isometry condition will be dependent on the choice of the shift vector. This can be seen from the fact that the isometry condition is defined to identify points in the two identical sheets which the manifold comprises. Since the shift vector determines which coordinate point is associated with a physical point in the manifold, it must be closely associated with the evolution of the isometry condition. Another point of consideration is the connection between the isometry condition and the choice of hypersurfaces throughout the evolution. It is evident that not just any general hypersurface will allow for the identification of data in the two sheets. Thus, the choice of the lapse function must be made in such a way which as to be compatible with the isometry. Some clue to possible constraints on the choice of the lapse function may be found in the evolution equations.

A clear understanding of the relationships mentioned above will be very important to our undertaking of the evolution of these inversion-symmetric initial-data sets. A successful combination of isometry conditions and the evolution equations will allow for evolution on complete manifolds which I feel will be of benefit. We know implicitly, from the uniqueness of the evolution of the Cauchy data, that the two universes are identical. What technical difficulties exist in finding an explicit, spatial isometry condition remain to be determined. In any event, it is clear that the work presented here is but a small part of the effort which will be required in the quest for the evolution of a spiralling binary coalescence.

Appendix A: The Multigrid Algorithm

The problem of numerically solving an elliptic boundary value problem is usually reduced to the problem of solving a large matrix equation. The task of solving this system of equations can be handled in a variety of ways. The equations can be solved by direct matrix inversion or by iterative techniques. The accuracy of direct solutions is usually limited by the computational storage requirements of large matrices, although the number of computational operations is also a limiting factor. For iterative schemes, it is the number of computational operations which usually limits the accuracy of solutions. Some of the most promising approaches for bypassing the time and memory problems and finding fast, accurate solutions are offered by multigrid techniques (*cf.* Brandt [1977], Hackbusch and Trottenberg [1982], Choptuik [1982], Hackbusch [1985], Choptuik and Unruh [1986], and Cook [1989]).

Probably the most widely used multigrid algorithm for non-linear problems is the full approximation storage (FAS) algorithm proposed by Brandt [1977]. Its use in numerical relativity has been advocated by Choptuik and Unruh [1986] and Cook [1989]. The following discussion closely follows Cook [1989].

Let the differential equation to be solved be denoted by

$$\mathcal{F}\varphi = f, \tag{A.1}$$

where $\mathcal{F}$ is a non-linear differential operator acting on φ, and f is a source term. Now let $\mathcal{P}^k$ be an operator which projects a scalar function onto a discrete mesh $\mathcal{M}^k$ labeled by k and covering the computational domain. The representation of the source function f on the mesh $\mathcal{M}^k$ is thus $\mathcal{P}^k f = f^k$. The finite difference approximation of (A.1) on $\mathcal{M}^k$ will be denoted by

$$\mathcal{F}^k\varphi^k = f^k. \tag{A.2}$$

$\mathcal{F}^k$ is the set of possibly non-linear algebraic equations obtained from finite differencing $\mathcal{F}$ and $\varphi^k \neq \mathcal{P}^k\varphi$ since φ^k is the set of values which must satisfy the difference equations (A.2). The difference $\varphi^k - \mathcal{P}^k\varphi$ is known as the discretization error in the solution and results from the truncation

error inherent in the finite difference approximation. The *local truncation error* τ^k of the finite difference operator $\mathcal{F}^k$ is given by

$$\tau^k \equiv \mathcal{F}^k(\mathcal{P}^k\varphi) - f^k = \mathcal{F}^k(\mathcal{P}^k\varphi) - \mathcal{P}^k(\mathcal{F}\varphi). \tag{A.3}$$

If, somehow, τ^k could be found without knowing the exact solution φ, then the solution to

$$\mathcal{F}^k\varphi^k = f^k + \tau^k \tag{A.4}$$

would be the projection of the exact solution φ and there would be no discretization error.

While it is not possible, in general, to determine τ^k exactly, there is a great deal of information about the discretization which is not used in traditional direct or iterative solution techniques which can be used to approximate τ^k. Consider two different discretizations of the computational domain, $\mathcal{M}^k$ and $\mathcal{M}^{k-1}$, where the discretization of $\mathcal{M}^{k-1}$ is coarser than that of $\mathcal{M}^k$. Now define two operators which smoothly interpolate values from one mesh to the other. The prolongation operator $\mathcal{I}_{k-1}^k$ takes values from the coarse mesh to the finer mesh, and the restriction operator $\mathcal{I}_k^{k-1}$ takes values from the fine mesh to the coarse mesh. If we have a solution on the fine mesh satisfying (A.2), then we can define, in a manner similar to (A.3), the *relative local truncation error* τ_k^{k-1}

$$\tau_k^{k-1} \equiv \mathcal{F}^{k-1}(\mathcal{I}_k^{k-1}\varphi^k) - \mathcal{I}_k^{k-1}(\mathcal{F}^k\varphi^k). \tag{A.5}$$

The relative local truncation error can be used as an estimate of the local truncation error of the difference operator on $\mathcal{M}^{k-1}$. If we now solve

$$F^{k-1}\tilde{\varphi}^{k-1} = f^{k-1} + \tau_k^{k-1}, \tag{A.6}$$

then $\tilde{\varphi}^{k-1}$ will be a better approximation of $\mathcal{P}^{k-1}\varphi$ since the discretization error of (A.6) will be on the order of that on $\mathcal{M}^k$, as opposed to that on $\mathcal{M}^{k-1}$.

To this point, solving (A.6) does not aid in the solution of the problem on $\mathcal{M}^k$ since the solution on $\mathcal{M}^k$ was needed to generate τ_k^{k-1}. To proceed, instead of using an actual solution to (A.2) in (A.5) consider φ^k now to be only an approximate solution. If the approximate solution is sufficiently close to the true solution, then the solution to (A.6) will be a good approximation of the solution to (A.2) and, since (A.6) is defined on the coarser mesh, it will require less work than (A.2) to solve. Once the solution $\tilde{\varphi}^{k-1}$ is known, then subtracting $\mathcal{I}_k^{k-1}\varphi^k$ gives the amount by which the approximate solution on $\mathcal{M}^k$ has been corrected. The *coarse grid correction* is thus defined as

$$\tilde{\varphi}^{k-1} - I_k^{k-1}\varphi^k. \tag{A.7}$$

Projecting this onto the finer mesh $\mathcal{M}^k$ gives an update to the approximate solution given by

$$\varphi^k \to \varphi^k + \mathcal{I}_{k-1}^k \left(\tilde{\varphi}^{k-1} - I_k^{k-1} \varphi^k \right). \tag{A.8}$$

The update (A.8) gives a substantially improved solution on $\mathcal{M}^k$ without ever solving the equations on $\mathcal{M}^k$. Of course, it may be the case that the difference equations on $\mathcal{M}^{k-1}$ are, like those on $\mathcal{M}^k$, too difficult to solve efficiently. If this is the case, then the problem can be shifted to mesh $\mathcal{M}^{k-2}$ which is coarser yet. In this way, the problem of solving the finite difference equations can always be pushed to a grid which is coarse enough for the difference equations to be solved efficiently.

An alternate, and somewhat more general, derivation of the multigrid approach for non-linear problems is given by Hackbusch [1985]. Consider again the two-level system labeled by $\mathcal{M}^k$ and $\mathcal{M}^{k-1}$. Let φ^k be an approximate solution to (A.2) which satisfies

$$\mathcal{F}^k \varphi^k - f^k = d^k, \tag{A.9}$$

where d^k is the residual or defect in the solution which is assumed to be a smooth function over the mesh. If $\varphi^k + \delta\varphi^k$ is the actual solution to (A.2), then the correction can be written (remembering that $\mathcal{F}^k$ is non-linear) as

$$\delta\varphi^k = \left(\mathcal{F}^k\right)^{-1} f^k - \left(\mathcal{F}^k\right)^{-1} (d^k + f^k), \tag{A.10}$$

where $(\mathcal{F}^k)^{-1}$ denotes the operator inverse of $\mathcal{F}^k$. Expanding (A.10) in a Taylor series about f^k gives

$$\begin{aligned} \delta\varphi^k &= \left(\mathcal{F}^k\right)^{-1} f^k - \left(\mathcal{F}^k\right)^{-1} f^k - \left(\left(\mathcal{F}^k\right)^{-1} \right)'_{(f^k)} d^k + \cdots \\ &\approx - \left(\left(\mathcal{F}^k\right)^{-1} \right)'_{(f^k)} d^k \end{aligned}, \tag{A.11}$$

where $\left((\mathcal{F}^k)^{-1} \right)'_{(f^k)}$ is the Jacobian of $(\mathcal{F}^k)^{-1}$ evaluated at f^k. Solving (A.11) is, of course, no easier than solving (A.2). We will want to solve, not for $\delta\varphi^k$, but for a quantity $\delta\varphi^{k-1}$ which approximates it on $\mathcal{M}^{k-1}$.

Let φ^{k-1} be a solution to the following equation on $\mathcal{M}^{k-1}$

$$\mathcal{F}^{k-1} \varphi^{k-1} = \Phi^{k-1}, \tag{A.12}$$

where $\Phi^{k-1} \neq f^{k-1}$, but is constructed to satisfy (A.12) exactly for the given φ^{k-1} . Next, define a coarse grid defect by

$$d^{k-1} \equiv \Phi^{k-1} - s(\mathcal{I}_k^{k-1} d^k), \tag{A.13}$$

where s is simply a weighting coefficient in the linear combination. Finally, the coarse grid function $\tilde{\varphi}^{k-1}$ is defined by

$$\begin{aligned} \tilde{\varphi}^{k-1} &\equiv \left(\mathcal{F}^{k-1}\right)^{-1} d^{k-1} \\ &= \left(\mathcal{F}^{k-1}\right)^{-1} (\Phi^{k-1} - s\mathcal{I}_k^{k-1} d^k) \end{aligned} . \tag{A.14}$$

Expanding (A.14) in a Taylor series about Φ^{k-1} gives

$$\begin{aligned} \tilde{\varphi}^{k-1} &= \left(\mathcal{F}^{k-1}\right)^{-1} \Phi^{k-1} - s\Big(\left(\mathcal{F}^{k-1}\right)^{-1}\Big)'_{(\Phi^k)} (\mathcal{I}_k^{k-1} d^k) + \cdots \\ &\approx \varphi^{k-1} - s\Big(\left(\mathcal{F}^{k-1}\right)^{-1}\Big)'_{(\Phi^k)} (\mathcal{I}_k^{k-1} d^k) \end{aligned} . \tag{A.15}$$

Comparing (A.15) to (A.11) leads us to define the coarse grid correction as

$$\delta\varphi^{k-1} \equiv \frac{1}{s}(\tilde{\varphi}^{k-1} - \varphi^{k-1}). \tag{A.16}$$

Projecting this onto the fine mesh gives the update to the approximate solution

$$\varphi^k \rightarrow \varphi^k + \mathcal{I}_{k-1}^k \left(\frac{1}{s}(\tilde{\varphi}^{k-1} - \varphi^{k-1})\right). \tag{A.17}$$

As in the FAS algorithm, the problem of solving a set of difference equations on a fine mesh is transferred to a coarser mesh where it is either solved or passed to an even coarser mesh.

As mentioned previously, this second derivation of the multigrid approach is more general than the FAS algorithm. In fact, it contains the FAS algorithm. If the weighting parameter s is taken to be one, and if $\varphi^{k-1} = \mathcal{I}_k^{k-1}\varphi^k$, then this second approach reduces identically to the FAS algorithm. Even though the second method contains the first, the philosophy of the two algorithms is quite different. In the case of the FAS algorithm, the quantity added to the source term on each level (the relative local truncation error) is chosen to correct for the truncation error in the difference equations on that level. In this way, the solutions of the difference equations constructed on each level are always approximations of the same differential equation. This leads to the name of the method, since the full approximation of the solution is solved and stored on each level. This is not the case in the second approach except in the limiting case mentioned above. Here, the coarse grid solution $\tilde{\varphi}^{k-1}$ can be thought of as resulting from a perturbation of the solution to (A.12). The perturbation is driven by the defect in the approximate solution on $\mathcal{M}^k$ and is weighted by s. The size of this weighting parameter is restricted only by the need for the Taylor expansion in (A.15) to be well defined. In practice, it can be made quite small so that the perturbation from $\tilde{\varphi}^{k-1}$ is small. One approach which I have used for fixing a value for s is to choose it to satisfy

$$\|s(\mathcal{I}_k^{k-1} d^k)\| = \varepsilon_s \|\Phi^{k-1}\| \qquad \text{or} \qquad s = \frac{\varepsilon_s \|\Phi^{k-1}\|}{\|(\mathcal{I}_k^{k-1} d^k)\|}, \tag{A.18}$$

where $\| \bullet \|$ is some appropriate vector norm and ε_s is an "adaptive scaling" parameter.

Appendix B contains the results for the solutions to the one-hole Hamiltonian constraint described in Chapter 8. These solutions were obtained from a multigrid code based on the approach outlined above. (For a detailed description of the construction of a multigrid code, see Brandt [1977], [1982] and Choptuik [1982].) The solutions to the model problem were obtained using the FAS limit of the code. The solutions to the physical problem of a hole with linear or angular momentum were obtained both in the FAS limit and using adaptive scaling as described above, where $\varepsilon_s = 0.1$.

Appendix B: Numerical Solutions of the One-Hole Hamiltonian Constraint

This appendix contains the most important details from the numerical solutions of the one-hole Hamiltonian constraint described in Chapter 8. The code which produced these results was a multigrid code based on the ideas outlined in Appendix A. In all cases, the solutions were found on a multigrid hierarchy consisting of seven separate grids or meshes. The coarsest mesh, labeled level zero, was discretized into 16 radial zones and six angular zones. This discretization was doubled for each finer mesh and the finest mesh on level six was discretized into 1024 radial zones and 384 angular zones. The outer boundary on which the approximate outer boundary condition was specified was placed at $x = 10$ which places it at $\sim 22,000$ radii in the conformal space.

Seven sets of output are listed below. To gauge the accuracy of the code, the first set of outputs lists the results from the numerical solution of the model problem described in Chapter 8. The total energy and minimal surface mass were computed for nine separate values of the "momentum" parameter. The values of these quantities are listed for each multigrid level and the analytic solution is listed at the bottom of each table. Also listed for each level are two values for the L_1 norm of the relative error in the conformal factor. Since the solution is known analytically, the exact L_1 error is given as well as an estimated error for level ℓ computed by comparing the result on level ℓ with that on level $\ell - 1$. The code was configured to solve the difference equations using the FAS limit of the code described in Appendix A.

The next three sets of output tables contain, respectively, the results for a hole with linear momentum based on an extrinsic curvature obeying the isometry condition with a plus sign, a hole with linear momentum based on an extrinsic curvature obeying the isometry condition with a minus sign, and a hole with angular momentum based on an extrinsic curvature obeying the isometry condition with a minus sign. The code was configured to solve the difference equations using adaptive scaling as described in Appendix A. The adaptive scaling parameter was set at $\varepsilon_s = 0.1$. The final three sets of output tables consist of the same solution set as the previous three except that the code was configured to solve the difference equations using the FAS limit of the code.

– Model Problem Set –

Level	E/a	M/a	L_1 Estimate	L_1
0	1.88126	1.77173	N/A	18.4148
1	1.98729	1.97465	16.8755	1.30273
2	1.99461	1.98922	0.593958	0.647151
3	1.99703	1.99406	0.265249	0.36502
4	1.99928	1.99857	0.269975	0.0930136
5	1.99987	1.99973	0.075652	0.0171719
6	1.99997	1.99995	0.0136947	0.00345789
Analytic	2.00000	2.00000		

Table B.1: Multigrid solution of the model problem compared with the analytic solution for $P/a = 0$.

Level	E/a	M/a	L_1 Estimate	L_1
0	2.13881	1.831	N/A	17.3906
1	2.22493	2.03316	15.9607	1.20308
2	2.23157	2.04735	0.526089	0.617516
3	2.23365	2.05225	0.255	0.346291
4	2.2355	2.05674	0.255836	0.0884995
5	2.23596	2.0579	0.071875	0.0164409
6	2.23605	2.05812	0.0131075	0.00331472
Analytic	2.23607	2.05817		

Table B.2: Multigrid solution of the model problem compared with the analytic solution for $P/a = 1.0$.

Level	E/a	M/a	L_1 Estimate	L_1
0	3.16028	2.04926	N/A	14.9109
1	3.19397	2.25567	13.7324	0.975064
2	3.19963	2.26949	0.384193	0.537859
3	3.2007	2.27467	0.226123	0.297224
4	3.20142	2.27924	0.21904	0.0764276
5	3.20154	2.28042	0.0618241	0.0144363
6	3.20156	2.28064	0.0114914	0.00292773
Analytic	3.20156	2.28069		

Table B.3: Multigrid solution of the model problem compared with the analytic solution for $P/a = 2.5$.

Level	E/a	M/a	L_1 Estimate	L_1
0	5.40404	2.46167	N/A	12.7531
1	5.38031	2.69011	11.7688	0.800096
2	5.38631	2.70508	0.313773	0.459622
3	5.38615	2.71097	0.196951	0.249785
4	5.38533	2.71691	0.222119	0.0270176
5	5.38511	2.71751	0.0272101	0.00141964
6	5.38516	2.7175	0.00215859	0.00193588
Analytic	5.38517	2.71757		

Table B.4: Multigrid solution of the model problem compared with the analytic solution for $P/a = 5.0$.

Level	E/a	M/a	L_1 Estimate	L_1
0	7.81623	2.83896	N/A	11.8536
1	7.75843	3.09375	10.9376	0.738881
2	7.76517	3.11048	0.309136	0.424543
3	7.7642	3.11714	0.184089	0.228286
4	7.7624	3.1237	0.202703	0.0249653
5	7.76202	3.12437	0.0251515	0.00134353
6	7.76209	3.12436	0.00202864	0.00181608
Analytic	7.76209	3.12443		

Table B.5: Multigrid solution of the model problem compared with the analytic solution for $P/a = 7.5$.

Level	E/a	M/a	L_1 Estimate	L_1
0	10.2772	3.17807	N/A	11.3959
1	10.1952	3.45866	10.5092	0.712923
2	10.2025	3.47718	0.311281	0.406113
3	10.201	3.48458	0.177587	0.21674
4	10.1985	3.49175	0.192252	0.023888
5	10.198	3.4925	0.0240053	0.00129538
6	10.1981	3.49249	0.00191836	0.00177774
Analytic	10.1980	3.49257		

Table B.6: Multigrid solution of the model problem compared with the analytic solution for $P/a = 10.0$.

Level	E/a	M/a	L_1 Estimate	L_1
0	12.7581	3.48669	N/A	11.1285
1	12.6569	3.79171	10.2558	0.700624
2	12.6647	3.81196	0.314684	0.395145
3	12.6626	3.82005	0.173897	0.209695
4	12.6595	3.82782	0.185848	0.0232604
5	12.6589	3.82863	0.0232931	0.00128323
6	12.659	3.82862	0.00183219	0.00177894
Analytic	12.6590	3.82871		

Table B.7: Multigrid solution of the model problem compared with the analytic solution for $P/a = 12.5$.

Level	E/a	M/a	L_1 Estimate	L_1
0	15.2488	3.77122	N/A	10.9573
1	15.1315	4.09926	10.0916	0.694589
2	15.1394	4.12115	0.317998	0.388047
3	15.1369	4.12989	0.171637	0.205016
4	15.1333	4.13822	0.181567	0.0228726
5	15.1327	4.13909	0.0228154	0.00130033
6	15.1328	4.13908	0.00176446	0.00180388
Analytic	15.1328	4.13917		

Table B.8: Multigrid solution of the model problem compared with the analytic solution for $P/a = 15.0$.

Level	E/a	M/a	L_1 Estimate	L_1
0	17.7449	4.03631	N/A	10.8407
1	17.6134	4.38608	9.97836	0.691766
2	17.6215	4.40953	0.320859	0.383178
3	17.6185	4.41888	0.170181	0.201721
4	17.6146	4.42774	0.178526	0.0226272
5	17.6138	4.42867	0.0224768	0.00133455
6	17.6139	4.42866	0.00171017	0.00184542
Analytic	17.6139	4.42876		

Table B.9: Multigrid solution of the model problem compared with the analytic solution for $P/a = 17.5$.

– Physical Problem Sets (Adaptive Scaling) –

Linear Momentum, + isometry

Level	E/a	M/a	L_1
0	2.27118	1.90016	N/A
1	2.33728	2.08729	14.1696
2	2.34372	2.10275	0.599614
3	2.34538	2.10719	0.215799
4	2.34685	2.11138	0.228649
5	2.3472	2.11244	0.0634737
6	2.34726	2.11263	0.0114474

Table B.10: Adaptive multigrid solution for a single hole with linear momentum $P/a = 1.0$ generated from $\bar{A}^+_{ij}$.

Level	E/a	M/a	L_1
0	3.58275	2.27377	N/A
1	3.58475	2.44426	10.1188
2	3.58867	2.46147	0.547304
3	3.58888	2.47027	0.391994
4	3.58927	2.46983	0.0510522
5	3.58925	2.47009	0.0130427
6	3.58923	2.47043	0.0157145

Table B.11: Adaptive multigrid solution for a single hole with linear momentum $P/a = 2.5$ generated from $\bar{A}^+_{ij}$.

Level	E/a	M/a	L_1
0	6.17888	2.86364	N/A
1	6.13279	3.03946	7.72502
2	6.13428	3.05955	0.485525
3	6.13215	3.06842	0.28416
4	6.1329	3.06824	0.0304917
5	6.1328	3.06849	0.00853165
6	6.13267	3.06881	0.0112497

Table B.12: Adaptive multigrid solution for a single hole with linear momentum $P/a = 5.0$ generated from $\bar{A}^+_{ij}$.

Level	E/a	M/a	L_1
0	8.88952	3.36622	N/A
1	8.81718	3.55645	6.85398
2	8.81735	3.57932	0.460271
3	8.81403	3.58884	0.245491
4	8.81496	3.58878	0.0232719
5	8.81481	3.58903	0.0070166
6	8.81463	3.58938	0.00961275

Table B.13: Adaptive multigrid solution for a single hole with linear momentum $P/a = 7.5$ generated from $\bar{A}^+_{ij}$.

Level	E/a	M/a	L_1
0	11.6364	3.80639	N/A
1	11.5449	4.01229	6.42244
2	11.5441	4.03774	0.448654
3	11.54	4.04801	0.226421
4	11.541	4.04803	0.0197016
5	11.5409	4.0483	0.00629121
6	11.5406	4.04867	0.00878817

Table B.14: Adaptive multigrid solution for a single hole with linear momentum $P/a = 10.0$ generated from $\bar{A}^+_{ij}$.

Level	E/a	M/a	L_1
0	14.3999	4.20188	N/A
1	14.2925	4.42321	6.17005
2	14.291	4.45107	0.443361
3	14.2862	4.46209	0.215272
4	14.2873	4.46216	0.0175899
5	14.2871	4.46245	0.00587456
6	14.2868	4.46285	0.00829641

Table B.15: Adaptive multigrid solution for a single hole with linear momentum $P/a = 12.5$ generated from $\bar{A}^+_{ij}$.

Level	E/a	M/a	L_1
0	17.1724	4.56374	N/A
1	17.051	4.79992	6.00681
2	17.0489	4.83003	0.441576
3	17.0435	4.84177	0.208048
4	17.0447	4.84189	0.0162105
5	17.0445	4.8422	0.00560799
6	17.0442	4.84262	0.00797158

Table B.16: Adaptive multigrid solution for a single hole with linear momentum $P/a = 15.0$ generated from $\bar{A}^+_{ij}$.

Level	E/a	M/a	L_1
0	19.9505	4.8992	N/A
1	19.8164	5.14958	5.89386
2	19.8137	5.18181	0.441517
3	19.8078	5.19424	0.203033
4	19.8091	5.19441	0.0153403
5	19.8088	5.19473	0.00542486
6	19.8085	5.19517	0.00774191

Table B.17: Adaptive multigrid solution for a single hole with linear momentum $P/a = 17.5$ generated from $\bar{A}^{+}_{ij}$.

Linear Momentum, − isometry

Level	E/a	M/a	L_1
0	2.24839	1.88262	N/A
1	2.31919	2.07431	14.7024
2	2.32571	2.08941	0.575997
3	2.32747	2.09399	0.227557
4	2.32902	2.09827	0.236393
5	2.3294	2.09936	0.065833
6	2.32947	2.09956	0.0119361

Table B.18: Adaptive multigrid solution for a single hole with linear momentum $P/a = 1.0$ generated from $\bar{A}^{-}_{ij}$.

Level	E/a	M/a	L_1
0	3.53242	2.22443	N/A
1	3.5393	2.40394	11.011
2	3.54386	2.42068	0.524756
3	3.54444	2.42499	0.163016
4	3.54464	2.429	0.175416
5	3.54461	2.42999	0.0480308
6	3.5446	2.43017	0.00874135

Table B.19: Adaptive multigrid solution for a single hole with linear momentum $P/a = 2.5$ generated from $\bar{A}^{-}_{ij}$.

Level	E/a	M/a	L_1
0	6.12118	2.78323	N/A
1	6.0766	2.97079	8.62898
2	6.07923	2.99066	0.481417
3	6.07897	2.99522	0.122633
4	6.07803	2.99938	0.134004
5	6.07767	3.00037	0.0359193
6	6.0776	3.00055	0.0065615

Table B.20: Adaptive multigrid solution for a single hole with linear momentum $P/a = 5.0$ generated from $\bar{A}^{-}_{ij}$.

Level	E/a	M/a	L_1
0	8.83381	3.26467	N/A
1	8.76099	3.46863	7.73617
2	8.76254	3.49147	0.466121
3	8.75894	3.50174	0.281434
4	8.76005	3.50154	0.0298021
5	8.75987	3.50183	0.00862492
6	8.75968	3.5022	0.0107975

Table B.21: Adaptive multigrid solution for a single hole with linear momentum $P/a = 7.5$ generated from $\bar{A}^{-}_{ij}$.

Level	E/a	M/a	L_1
0	11.5839	3.6878	N/A
1	11.4906	3.90916	7.29002
2	11.4914	3.93475	0.460578
3	11.4869	3.94583	0.260407
4	11.4881	3.94571	0.0251472
5	11.4879	3.94602	0.00773244
6	11.4877	3.94642	0.00988517

Table B.22: Adaptive multigrid solution for a single hole with linear momentum $P/a = 10.0$ generated from $\bar{A}^{-}_{ij}$.

Level	E/a	M/a	L_1
0	14.3505	4.06858	N/A
1	14.2404	4.30695	7.02799
2	14.2406	4.33507	0.459733
3	14.2353	4.34696	0.248029
4	14.2367	4.3469	0.0223645
5	14.2364	4.34723	0.00721265
6	14.2362	4.34765	0.00933885

Table B.23: Adaptive multigrid solution for a single hole with linear momentum $P/a = 12.5$ generated from $\bar{A}^{-}_{ij}$.

Level	E/a	M/a	L_1
0	17.1259	4.41729	N/A
1	17.0011	4.67194	6.85803
2	17.0007	4.70242	0.46087
3	16.9948	4.71509	0.239969
4	16.9963	4.71508	0.0204899
5	16.996	4.71543	0.00687665
6	16.9957	4.71588	0.00897717

Table B.24: Adaptive multigrid solution for a single hole with linear momentum $P/a = 15.0$ generated from $\bar{A}^{-}_{ij}$.

Level	E/a	M/a	L_1
0	19.9065	4.74074	N/A
1	19.7685	5.01093	6.74019
2	19.7675	5.04362	0.462799
3	19.761	5.05704	0.234352
4	19.7626	5.05707	0.0192142
5	19.7623	5.05744	0.00664377
6	19.762	5.05791	0.00872102

Table B.25: Adaptive multigrid solution for a single hole with linear momentum $P/a = 17.5$ generated from $\bar{A}^{-}_{ij}$.

Angular Momentum, − isometry

Level	E/a	M/a	L_1
0	1.9453	1.81683	N/A
1	2.03568	2.00718	15.5057
2	2.04302	2.02274	0.658644
3	2.0451	2.02721	0.235656
4	2.04706	2.03147	0.249537
5	2.04756	2.03255	0.0693041
6	2.04765	2.03275	0.0124626

Table B.26: Adaptive multigrid solution for a single hole with angular momentum $S/a^2 = 1.0$ generated from $\bar{A}_{ij}$.

Level	E/a	M/a	L_1
0	2.28436	2.05537	N/A
1	2.32101	2.20191	10.7183
2	2.32632	2.21919	0.731421
3	2.32828	2.22655	0.400527
4	2.32834	2.22642	0.0372912
5	2.32838	2.2266	0.0109158
6	2.32844	2.22687	0.0154346

Table B.27: Adaptive multigrid solution for a single hole with angular momentum $S/a^2 = 3.0$ generated from $\bar{A}_{ij}$.

Level	E/a	M/a	L_1
0	3.50209	2.9152	N/A
1	3.47917	3.01279	5.23388
2	3.47786	3.02864	0.501918
3	3.47704	3.03356	0.1872
4	3.47718	3.03385	0.00755355
5	3.47717	3.03394	0.00398086
6	3.47712	3.03413	0.00731379

Table B.28: Adaptive multigrid solution for a single hole with angular momentum $S/a^2 = 10.0$ generated from $\bar{A}_{ij}$.

Level	E/a	M/a	L_1
0	5.81325	4.56595	N/A
1	5.76641	4.6525	3.20339
2	5.76092	4.66807	0.337921
3	5.75878	4.67254	0.116625
4	5.75881	4.67294	0.00489168
5	5.75864	4.67319	0.00808768
6	5.75868	4.67317	0.00142925

Table B.29: Adaptive multigrid solution for a single hole with angular momentum $S/a^2 = 30.0$ generated from $\bar{A}_{ij}$.

Level	E/a	M/a	L_1
0	10.4867	7.94041	N/A
1	10.4185	8.04484	2.4779
2	10.4089	8.06426	0.27204
3	10.4053	8.06966	0.0925639
4	10.4051	8.07025	0.00691291
5	10.4049	8.07053	0.00607274
6	10.4049	8.07053	0.000639976

Table B.30: Adaptive multigrid solution for a single hole with angular momentum $S/a^2 = 100.0$ generated from $\bar{A}_{ij}$.

Level	E/a	M/a	L_1
0	18.1138	13.4829	N/A
1	18.0098	13.6343	2.30948
2	17.9944	13.6627	0.259295
3	17.9884	13.6705	0.0881838
4	17.988	13.6714	0.00841928
5	17.9875	13.6719	0.00565544
6	17.9876	13.6719	0.000415205

Table B.31: Adaptive multigrid solution for a single hole with angular momentum $S/a^2 = 300.0$ generated from $\bar{A}_{ij}$.

Level	E/a	M/a	L_1
0	33.0444	24.3724	N/A
1	32.8654	24.6271	2.32567
2	32.839	24.6753	0.267809
3	32.8281	24.6885	0.0904453
4	32.8273	24.69	0.00946999
5	32.8264	24.6909	0.00646133
6	32.8265	24.6909	0.000595018

Table B.32: Adaptive multigrid solution for a single hole with angular momentum $S/a^2 = 1000.0$ generated from $\bar{A}_{ij}$.

Level	E/a	M/a	L_1
0	104.446	76.5926	N/A
1	103.911	77.3671	2.54212
2	103.837	77.5149	0.311267
3	103.802	77.5550	0.100746
4	103.799	77.5604	0.0131785
5	103.796	77.5626	0.00623526
6	103.796	77.5627	0.000612333

Table B.33: Adaptive multigrid solution for a single hole with angular momentum $S/a^2 = 10000.0$ generated from $\bar{A}_{ij}$.

– Physical Problem Sets (FAS) –

Linear Momentum, + isometry

Level	E/a	M/a	L_1
0	2.27118	1.90016	N/A
1	2.33728	2.08729	14.1696
2	2.34372	2.10274	0.599539
3	2.34538	2.10718	0.215515
4	2.34685	2.11138	0.228794
5	2.3472	2.11244	0.063629
6	2.34726	2.11263	0.0114756

Table B.34: FAS multigrid solution for a single hole with linear momentum $P/a = 1.0$ generated from $\bar{A}^+_{ij}$.

Level	E/a	M/a	L_1
0	3.58275	2.27377	N/A
1	3.58475	2.44426	10.1188
2	3.58867	2.46147	0.54721
3	3.58888	2.47026	0.3914
4	3.58927	2.46983	0.0503605
5	3.58921	2.47034	0.0266914
6	3.58922	2.47046	0.00375036

Table B.35: FAS multigrid solution for a single hole with linear momentum $P/a = 2.5$ generated from $\bar{A}^+_{ij}$.

Level	E/a	M/a	L_1
0	6.17888	2.86364	N/A
1	6.13279	3.03946	7.72502
2	6.13428	3.05955	0.485477
3	6.13216	3.06841	0.283678
4	6.1329	3.06824	0.029911
5	6.13266	3.06871	0.0178838
6	6.13266	3.06884	0.00305324

Table B.36: FAS multigrid solution for a single hole with linear momentum $P/a = 5.0$ generated from $\bar{A}^+_{ij}$.

Level	E/a	M/a	L_1
0	8.88952	3.36622	N/A
1	8.81718	3.55645	6.85398
2	8.81735	3.57932	0.460246
3	8.81404	3.58883	0.24508
4	8.81496	3.58878	0.0228025
5	8.81463	3.58926	0.014813
6	8.81461	3.58941	0.00278446

Table B.37: FAS multigrid solution for a single hole with linear momentum $P/a = 7.5$ generated from $\bar{A}^+_{ij}$.

Level	E/a	M/a	L_1
0	11.6364	3.80639	N/A
1	11.5449	4.01229	6.42244
2	11.5441	4.03774	0.44864
3	11.54	4.048	0.226049
4	11.541	4.04803	0.0193
5	11.5406	4.04854	0.0133003
6	11.5406	4.0487	0.0026534

Table B.38: FAS multigrid solution for a single hole with linear momentum $P/a = 10.0$ generated from $\bar{A}^+_{ij}$.

Level	E/a	M/a	L_1
0	14.3999	4.20188	N/A
1	14.2925	4.42321	6.17005
2	14.291	4.45107	0.443353
3	14.2862	4.46208	0.214925
4	14.2873	4.46217	0.0172251
5	14.2868	4.46271	0.0124096
6	14.2868	4.46288	0.00257952

Table B.39: FAS multigrid solution for a single hole with linear momentum $P/a = 12.5$ generated from $\bar{A}^+_{ij}$.

Level	E/a	M/a	L_1
0	17.1724	4.56374	N/A
1	17.051	4.79992	6.00681
2	17.0489	4.83003	0.441572
3	17.0435	4.84176	0.207717
4	17.0447	4.84189	0.0158799
5	17.0442	4.84247	0.0118264
6	17.0442	4.84265	0.00253397

Table B.40: FAS multigrid solution for a single hole with linear momentum $P/a = 15.0$ generated from $\bar{A}^+_{ij}$.

Level	E/a	M/a	L_1
0	19.9505	4.8992	N/A
1	19.8164	5.14958	5.89386
2	19.8137	5.18181	0.441515
3	19.8078	5.19423	0.202714
4	19.8091	5.19441	0.0150376
5	19.8085	5.19501	0.0114166
6	19.8085	5.19521	0.00250416

Table B.41: FAS multigrid solution for a single hole with linear momentum $P/a = 17.5$ generated from $\bar{A}^{+}_{ij}$.

Linear Momentum, − isometry

Level	E/a	M/a	L_1
0	2.24839	1.88262	N/A
1	2.31919	2.07431	14.7024
2	2.32571	2.08941	0.575936
3	2.32747	2.09399	0.227287
4	2.32902	2.09827	0.236527
5	2.3294	2.09936	0.0659768
6	2.32947	2.09956	0.0119618

Table B.42: FAS multigrid solution for a single hole with linear momentum $P/a = 1.0$ generated from $\bar{A}^{-}_{ij}$.

Level	E/a	M/a	L_1
0	3.53242	2.22443	N/A
1	3.5393	2.40394	11.011
2	3.54386	2.42068	0.52466
3	3.54445	2.42498	0.162606
4	3.54464	2.429	0.175624
5	3.54461	2.42999	0.0482485
6	3.5446	2.43017	0.00877865

Table B.43: FAS multigrid solution for a single hole with linear momentum $P/a = 2.5$ generated from $\bar{A}^{-}_{ij}$.

Level	E/a	M/a	L_1
0	6.12118	2.78323	N/A
1	6.0766	2.97079	8.62898
2	6.07923	2.99065	0.481356
3	6.07897	2.99521	0.122286
4	6.07804	2.99937	0.134175
5	6.07767	3.00037	0.0360939
6	6.0776	3.00055	0.00659

Table B.44: FAS multigrid solution for a single hole with linear momentum $P/a = 5.0$ generated from $\bar{A}^{-}_{ij}$.

Level	E/a	M/a	L_1
0	8.83381	3.26467	N/A
1	8.76099	3.46863	7.73617
2	8.76254	3.49147	0.466083
3	8.75895	3.50173	0.280972
4	8.76005	3.50154	0.0292591
5	8.75967	3.50208	0.0174626
6	8.75965	3.50226	0.00363022

Table B.45: FAS multigrid solution for a single hole with linear momentum $P/a = 7.5$ generated from $\bar{A}^{-}_{ij}$.

Level	E/a	M/a	L_1
0	11.5839	3.6878	N/A
1	11.4906	3.90916	7.29002
2	11.4914	3.93475	0.460554
3	11.4869	3.94582	0.259985
4	11.4881	3.94571	0.0246665
5	11.4877	3.94628	0.0156611
6	11.4877	3.94644	0.0023109

Table B.46: FAS multigrid solution for a single hole with linear momentum $P/a = 10.0$ generated from $\bar{A}^{-}_{ij}$.

Level	E/a	M/a	L_1
0	14.3505	4.06858	N/A
1	14.2404	4.30695	7.02799
2	14.2406	4.33507	0.459717
3	14.2353	4.34694	0.24763
4	14.2367	4.3469	0.0219194
5	14.2362	4.3475	0.0145924
6	14.2362	4.34768	0.00229527

Table B.47: FAS multigrid solution for a single hole with linear momentum $P/a = 12.5$ generated from $\bar{A}^{-}_{ij}$.

Level	E/a	M/a	L_1
0	17.1259	4.41729	N/A
1	17.0011	4.67194	6.85803
2	17.0007	4.70242	0.46086
3	16.9948	4.71508	0.239586
4	16.9963	4.71509	0.0200749
5	16.9957	4.71572	0.0138894
6	16.9957	4.71591	0.0022915

Table B.48: FAS multigrid solution for a single hole with linear momentum $P/a = 15.0$ generated from $\bar{A}^{-}_{ij}$.

Level	E/a	M/a	L_1
0	19.9065	4.74074	N/A
1	19.7685	5.01093	6.74019
2	19.7675	5.04362	0.462792
3	19.7611	5.05703	0.233981
4	19.7626	5.05708	0.0188294
5	19.762	5.05774	0.0133939
6	19.762	5.05795	0.0022932

Table B.49: FAS multigrid solution for a single hole with linear momentum $P/a = 17.5$ generated from $\bar{A}^{-}_{ij}$.

Angular Momentum, − isometry

Level	E/a	M/a	L_1
0	1.9453	1.81683	N/A
1	2.03568	2.00718	15.5057
2	2.04302	2.02274	0.658592
3	2.0451	2.02721	0.235507
4	2.04706	2.03147	0.249625
5	2.04756	2.03255	0.0693884
6	2.04765	2.03275	0.0124742

Table B.50: FAS multigrid solution for a single hole with angular momentum $S/a^2 = 1.0$ generated from $\bar{A}_{ij}$.

Level	E/a	M/a	L_1
0	2.28436	2.05537	N/A
1	2.32101	2.20191	10.7183
2	2.32632	2.21919	0.731384
3	2.32827	2.22654	0.399879
4	2.32834	2.22642	0.0364626
5	2.32838	2.2266	0.0107395
6	2.32844	2.22687	0.0154423

Table B.51: FAS multigrid solution for a single hole with angular momentum $S/a^2 = 3.0$ generated from $\bar{A}_{ij}$.

Level	E/a	M/a	L_1
0	3.50209	2.9152	N/A
1	3.47917	3.01279	5.23388
2	3.47786	3.02864	0.501975
3	3.47705	3.03356	0.186861
4	3.47718	3.03385	0.00737905
5	3.47717	3.03394	0.00389055
6	3.47713	3.03411	0.0064444

Table B.52: FAS multigrid solution for a single hole with angular momentum $S/a^2 = 10.0$ generated from $\bar{A}_{ij}$.

Level	E/a	M/a	L_1
0	5.81325	4.56595	N/A
1	5.76641	4.6525	3.20339
2	5.76092	4.66807	0.337955
3	5.75879	4.67254	0.1165
4	5.75881	4.67294	0.00497109
5	5.75864	4.67319	0.00803859
6	5.75868	4.67317	0.00140094

Table B.53: FAS multigrid solution for a single hole with angular momentum $S/a^2 = 30.0$ generated from $\bar{A}_{ij}$.

Level	E/a	M/a	L_1
0	10.4867	7.94041	N/A
1	10.4185	8.04484	2.4779
2	10.4089	8.06426	0.272064
3	10.4053	8.06966	0.0925007
4	10.4051	8.07025	0.00695548
5	10.4049	8.07053	0.00605396
6	10.4049	8.07053	0.00062889

Table B.54: FAS multigrid solution for a single hole with angular momentum $S/a^2 = 100.0$ generated from $\bar{A}_{ij}$.

Level	E/a	M/a	L_1
0	18.1138	13.4829	N/A
1	18.0098	13.6343	2.30948
2	17.9944	13.6627	0.259315
3	17.9884	13.6705	0.0881372
4	17.988	13.6714	0.00844824
5	17.9875	13.6719	0.00564414
6	17.9876	13.6719	0.000411762

Table B.55: FAS multigrid solution for a single hole with angular momentum $S/a^2 = 300.0$ generated from $\bar{A}_{ij}$.

Level	E/a	M/a	L_1
0	33.0444	24.3724	N/A
1	32.8654	24.6271	2.32567
2	32.839	24.6753	0.26783
3	32.8281	24.6885	0.090403
4	32.8273	24.69	0.00949345
5	32.8264	24.6909	0.00645202
6	32.8265	24.6909	0.000591245

Table B.56: FAS multigrid solution for a single hole with angular momentum $S/a^2 = 1000.0$ generated from $\bar{A}_{ij}$.

Level	E/a	M/a	L_1
0	104.446	76.5926	N/A
1	103.911	77.3671	2.54212
2	103.837	77.5149	0.311291
3	103.802	77.555	0.100703
4	103.799	77.5604	0.0132001
5	103.796	77.5626	0.00622809
6	103.796	77.5627	0.000613726

Table B.57: FAS multigrid solution for a single hole with angular momentum $S/a^2 = 10000.0$ generated from $\bar{A}_{ij}$.

Appendix C: Numerical Solutions of the Two-Hole Hamiltonian Constraint in Bispherical Coordinates

This appendix contains the most important details from the numerical solution of the two-hole Hamiltonian constraint described in Chapter 9. The difference equations for this approach were solved by Newton's method for systems of equations and each linearized equation for the iterative correction was solved directly by means of the LINPACK routines for factoring (DGBFA) and solving (DGBSL) general banded matrices. The solution for each configuration was obtained at three different mesh resolutions. The coarsest discretization consisted of a mesh of (80×80) zones. The intermediate discretization consisted of a mesh of (120×120) zones. The finest discretization consisted of a mesh of (160×160) zones. It was possible, though not practicle, to use a discretization of (200×200) zones. One set of runs was obtained for configurations with $\beta = 3$ to see if the results were significantly better. They were not, and the results of this run are not included in this appendix. (They are, however, included in the Richardson extrapolated data used to construct Figures 14.1 through 14.7.)

The 60 tables which follow can be considered as ten groups of six tables. Each group of six tables corresponds to the six cases described in Chapter 14. The ten groups of six tables represent ten values of the separation parameter $\beta = 3 \rightarrow 12$. Finally, each table lists results from the numerical computations for the scaled total energy E/a_1, the scaled minimal surface mass M/a_1, and the scaled proper separation L/a_1 as the linear or angular momentum parameter is varied. For each of the physical quantities listed in each table, the value for each of the three mesh resolutions is listed along with the average Richardson extrapolated value $\Re$ obtaind by assuming the error scales as first order in the mesh spacing.

P/a_1	E/a_1 80	120	160	$\Re$	M/a_1 80	120	160	$\Re$	L/a_1 80	120	160	$\Re$
0.0	6.064	6.090	6.103	6.108	4.675	4.714	4.734	4.740	11.186	11.278	11.325	11.340
1.0	6.092	6.118	6.130	6.135	4.694	4.733	4.752	4.759	11.231	11.323	11.369	11.384
2.5	6.231	6.254	6.265	6.269	4.786	4.823	4.842	4.848	11.453	11.541	11.585	11.600
5.0	6.633	6.649	6.657	6.660	5.053	5.087	5.105	5.110	12.097	12.178	12.219	12.232
7.5	7.129	7.139	7.144	7.146	5.382	5.415	5.431	5.436	12.891	12.967	13.005	13.017
10.0	7.645	7.651	7.653	7.655	5.726	5.757	5.772	5.777	13.720	13.792	13.829	13.840
12.5	8.154	8.156	8.155	8.157	6.065	6.095	6.110	6.115	14.539	14.608	14.643	14.654
15.0	8.646	8.645	8.642	8.644	6.393	6.422	6.437	6.442	15.331	15.399	15.433	15.444
17.5	9.119	9.115	9.111	9.113	6.709	6.738	6.752	6.757	16.093	16.160	16.194	16.205

Table C.1: Scaled energy, mass, and proper separation for two equal sized holes, each with anti-parallel linear momenta P/a_1 generated from an inversion symmetric extrinsic curvature obeying the isometry condition with a plus sign. The conformal separation is $\beta = 3$.

P/a_1	E/a_1 80	120	160	$\Re$	M/a_1 80	120	160	$\Re$	L/a_1 80	120	160	$\Re$
0.0	6.064	6.090	6.103	6.108	4.675	4.714	4.734	4.740	11.186	11.278	11.325	11.340
1.0	6.089	6.115	6.127	6.132	4.692	4.731	4.750	4.756	11.226	11.317	11.363	11.378
2.5	6.213	6.236	6.248	6.252	4.773	4.810	4.829	4.835	11.421	11.509	11.554	11.569
5.0	6.583	6.600	6.609	6.612	5.015	5.049	5.067	5.073	12.003	12.085	12.127	12.140
7.5	7.053	7.064	7.069	7.071	5.321	5.354	5.371	5.376	12.742	12.818	12.857	12.869
10.0	7.550	7.556	7.558	7.560	5.647	5.678	5.694	5.699	13.526	13.599	13.636	13.647
12.5	8.046	8.048	8.048	8.050	5.973	6.003	6.018	6.023	14.309	14.379	14.414	14.425
15.0	8.529	8.529	8.526	8.528	6.290	6.319	6.334	6.339	15.072	15.140	15.175	15.185
17.5	8.996	8.993	8.988	8.990	6.597	6.625	6.640	6.645	15.809	15.876	15.910	15.921

Table C.2: Scaled energy, mass, and proper separation for two equal sized holes, each with anti-parallel linear momenta P/a_1 generated from an inversion symmetric extrinsic curvature obeying the isometry condition with a minus sign. The conformal separation is $\beta = 3$.

S/a_1^2	E/a_1 80	120	160	$\Re$	M/a_1 80	120	160	$\Re$	L/a_1 80	120	160	$\Re$
0.0	6.064	6.090	6.103	6.108	4.675	4.714	4.734	4.740	11.186	11.278	11.325	11.340
1.0	6.073	6.099	6.112	6.116	4.683	4.722	4.741	4.748	11.204	11.296	11.342	11.357
3.0	6.142	6.167	6.179	6.183	4.741	4.779	4.798	4.804	11.341	11.430	11.475	11.490
10.0	6.705	6.719	6.726	6.729	5.219	5.252	5.268	5.274	12.473	12.551	12.590	12.602
30.0	8.501	8.498	8.496	8.495	6.846	6.874	6.888	6.892	16.326	16.392	16.425	16.436
100.0	12.363	12.331	12.316	12.311	10.813	10.843	10.858	10.863	25.719	25.789	25.824	25.836
300.0	17.991	17.914	17.875	17.862	17.577	17.613	17.632	17.638	41.730	41.817	41.860	41.874
1000.0	27.379	27.194	27.102	27.070	30.967	31.018	31.043	31.052	73.426	73.546	73.606	73.626

Table C.3: Scaled energy, mass, and proper separation for two equal sized holes, each with anti-parallel angular momenta S/a_1^2 generated from an inversion symmetric extrinsic curvature obeying the isometry condition with a minus sign. The conformal separation is $\beta = 3$.

P/a_1	E/a_1 80	120	160	$\Re$	M/a_1 80	120	160	$\Re$	L/a_1 80	120	160	$\Re$
0.0	6.064	6.090	6.103	6.108	4.675	4.714	4.734	4.740	11.186	11.278	11.325	11.340
1.0	6.476	6.519	6.541	6.548	4.797	4.836	4.856	4.862	11.476	11.568	11.614	11.629
2.5	8.155	8.287	8.357	8.375	5.274	5.315	5.335	5.341	12.613	12.708	12.755	12.771
5.0	11.782	12.199	12.427	12.477	6.238	6.283	6.305	6.313	14.910	15.017	15.069	15.088
7.5	15.400	16.218	16.681	16.764	7.147	7.199	7.224	7.233	17.078	17.200	17.259	17.281
10.0	18.779	20.071	20.821	20.932	7.973	8.031	8.059	8.070	19.048	19.185	19.252	19.277
12.5	21.902	23.711	24.787	24.917	8.729	8.793	8.824	8.836	20.850	21.003	21.077	21.105
15.0	24.793	27.141	28.570	28.706	9.427	9.498	9.532	9.545	22.516	22.684	22.765	22.796
17.5	27.478	30.376	32.177	32.308	10.078	10.155	10.192	10.206	24.070	24.253	24.341	24.374

Table C.4: Scaled energy, mass, and proper separation for two equal sized holes, each with parallel linear momenta P/a_1 generated from an inversion symmetric extrinsic curvature obeying the isometry condition with a plus sign. The conformal separation is $\beta = 3$.

P/a_1	E/a_1 80	120	160	$\Re$	M/a_1 80	120	160	$\Re$	L/a_1 80	120	160	$\Re$
0.0	6.064	6.090	6.103	6.108	4.675	4.714	4.734	4.740	11.186	11.278	11.325	11.340
1.0	6.471	6.514	6.536	6.543	4.793	4.832	4.852	4.858	11.466	11.558	11.605	11.620
2.5	8.136	8.268	8.338	8.356	5.257	5.298	5.318	5.325	12.574	12.669	12.716	12.732
5.0	11.753	12.170	12.398	12.448	6.204	6.249	6.272	6.280	14.830	14.937	14.991	15.009
7.5	15.369	16.187	16.650	16.733	7.100	7.152	7.178	7.187	16.968	17.091	17.152	17.173
10.0	18.748	20.040	20.790	20.901	7.917	7.975	8.004	8.014	18.916	19.054	19.122	19.147
12.5	21.873	23.681	24.757	24.886	8.664	8.729	8.760	8.772	20.698	20.853	20.928	20.956
15.0	24.764	27.112	28.541	28.677	9.355	9.426	9.461	9.474	22.347	22.516	22.598	22.630
17.5	27.451	30.348	32.148	32.279	9.999	10.077	10.114	10.129	23.885	24.070	24.159	24.193

Table C.5: Scaled energy, mass, and proper separation for two equal sized holes, each with parallel linear momenta P/a_1 generated from an inversion symmetric extrinsic curvature obeying the isometry condition with a minus sign. The conformal separation is $\beta = 3$.

S/a_1^2	E/a_1 80	120	160	$\Re$	M/a_1 80	120	160	$\Re$	L/a_1 80	120	160	$\Re$
0.0	6.064	6.090	6.103	6.108	4.675	4.714	4.734	4.740	11.186	11.278	11.325	11.340
1.0	6.079	6.105	6.118	6.122	4.686	4.725	4.745	4.751	11.212	11.304	11.350	11.365
3.0	6.196	6.219	6.231	6.234	4.768	4.806	4.825	4.831	11.408	11.496	11.541	11.556
10.0	7.090	7.097	7.100	7.101	5.401	5.433	5.449	5.455	12.912	12.988	13.026	13.039
30.0	9.852	9.820	9.805	9.798	7.369	7.398	7.412	7.417	17.597	17.664	17.698	17.709
100.0	16.436	16.263	16.186	16.147	12.026	12.058	12.074	12.079	28.692	28.766	28.804	28.816
300.0	28.099	27.478	27.188	27.065	19.957	19.999	20.019	20.026	47.597	47.694	47.741	47.758
1000.0	52.484	51.001	49.981	50.013	35.706	35.771	35.801	35.814	85.146	85.295	85.364	85.394

Table C.6: Scaled energy, mass, and proper separation for two equal sized holes, each with parallel angular momenta S/a_1^2 generated from an inversion symmetric extrinsic curvature obeying the isometry condition with a minus sign. The conformal separation is $\beta = 3$.

P/a_1	E/a_1 80	120	160	$\Re$	M/a_1 80	120	160	$\Re$	L/a_1 80	120	160	$\Re$
0.0	5.321	5.336	5.343	5.346	3.557	3.576	3.585	3.588	12.782	12.848	12.882	12.893
1.0	5.381	5.395	5.402	5.404	3.589	3.608	3.617	3.620	12.902	12.968	13.001	13.012
2.5	5.654	5.664	5.669	5.671	3.737	3.754	3.763	3.766	13.454	13.515	13.546	13.556
5.0	6.335	6.339	6.340	6.341	4.106	4.122	4.130	4.132	14.832	14.887	14.914	14.923
7.5	7.068	7.066	7.065	7.066	4.504	4.519	4.526	4.529	16.316	16.367	16.392	16.401
10.0	7.774	7.768	7.765	7.765	4.888	4.902	4.910	4.912	17.745	17.794	17.819	17.827
12.5	8.440	8.431	8.425	8.425	5.250	5.265	5.272	5.274	19.093	19.141	19.165	19.173
15.0	9.066	9.054	9.047	9.046	5.592	5.606	5.613	5.615	20.362	20.409	20.433	20.441
17.5	9.658	9.643	9.634	9.633	5.914	5.928	5.935	5.938	21.559	21.607	21.631	21.638

Table C.7: Scaled energy, mass, and proper separation for two equal sized holes, each with anti-parallel linear momenta P/a_1 generated from an inversion symmetric extrinsic curvature obeying the isometry condition with a plus sign. The conformal separation is $\beta = 4$.

P/a_1	E/a_1 80	120	160	$\Re$	M/a_1 80	120	160	$\Re$	L/a_1 80	120	160	$\Re$
0.0	5.321	5.336	5.343	5.346	3.557	3.576	3.585	3.588	12.782	12.848	12.882	12.893
1.0	5.375	5.389	5.396	5.398	3.585	3.604	3.613	3.616	12.885	12.951	12.983	12.995
2.5	5.624	5.635	5.640	5.642	3.716	3.734	3.743	3.746	13.365	13.427	13.458	13.468
5.0	6.267	6.272	6.274	6.275	4.056	4.072	4.080	4.082	14.605	14.661	14.689	14.698
7.5	6.978	6.977	6.976	6.976	4.432	4.447	4.454	4.457	15.977	16.029	16.056	16.064
10.0	7.671	7.666	7.663	7.663	4.799	4.814	4.821	4.824	17.317	17.367	17.393	17.401
12.5	8.330	8.321	8.315	8.315	5.148	5.163	5.170	5.173	18.589	18.639	18.664	18.672
15.0	8.952	8.939	8.932	8.931	5.479	5.493	5.500	5.503	19.792	19.841	19.866	19.874
17.5	9.540	9.525	9.516	9.515	5.792	5.806	5.813	5.816	20.931	20.980	21.004	21.012

Table C.8: Scaled energy, mass, and proper separation for two equal sized holes, each with anti-parallel linear momenta P/a_1 generated from an inversion symmetric extrinsic curvature obeying the isometry condition with a minus sign. The conformal separation is $\beta = 4$.

S/a_1^2	E/a_1 80	120	160	$\Re$	M/a_1 80	120	160	$\Re$	L/a_1 80	120	160	$\Re$
0.0	5.321	5.336	5.343	5.346	3.557	3.576	3.585	3.588	12.782	12.848	12.882	12.893
1.0	5.340	5.354	5.361	5.364	3.569	3.588	3.597	3.600	12.824	12.890	12.923	12.935
3.0	5.473	5.486	5.492	5.494	3.658	3.676	3.685	3.688	13.136	13.199	13.231	13.241
10.0	6.358	6.362	6.364	6.364	4.266	4.281	4.289	4.291	15.266	15.319	15.346	15.355
30.0	8.594	8.585	8.581	8.579	5.938	5.951	5.958	5.961	21.116	21.166	21.190	21.198
100.0	12.960	12.929	12.914	12.909	9.687	9.703	9.711	9.714	34.240	34.297	34.325	34.335
300.0	19.168	19.098	19.063	19.051	15.959	15.979	15.989	15.993	56.189	56.263	56.299	56.312
1000.0	29.441	29.279	29.199	29.172	28.320	28.349	28.363	28.368	99.448	99.553	99.605	99.623

Table C.9: Scaled energy, mass, and proper separation for two equal sized holes, each with anti-parallel angular momenta S/a_1^2 generated from an inversion symmetric extrinsic curvature obeying the isometry condition with a minus sign. The conformal separation is $\beta = 4$.

P/a_1	E/a_1 80	120	160	$\Re$	M/a_1 80	120	160	$\Re$	L/a_1 80	120	160	$\Re$
0.0	5.321	5.336	5.343	5.346	3.557	3.576	3.585	3.588	12.782	12.848	12.882	12.893
1.0	5.819	5.844	5.856	5.860	3.675	3.694	3.704	3.707	13.206	13.273	13.306	13.317
2.5	7.778	7.859	7.901	7.913	4.115	4.134	4.144	4.147	14.781	14.850	14.884	14.896
5.0	11.953	12.221	12.363	12.399	4.949	4.972	4.983	4.987	17.774	17.853	17.891	17.905
7.5	16.205	16.752	17.048	17.116	5.714	5.740	5.752	5.757	20.518	20.608	20.651	20.667
10.0	20.299	21.193	21.688	21.790	6.402	6.431	6.445	6.450	22.983	23.085	23.134	23.153
12.5	24.195	25.490	26.219	26.354	7.027	7.059	7.075	7.081	25.226	25.340	25.394	25.415
15.0	27.898	29.633	30.626	30.789	7.603	7.639	7.656	7.662	27.292	27.418	27.477	27.501
17.5	31.421	33.624	34.905	35.093	8.139	8.178	8.197	8.204	29.216	29.353	29.418	29.444

Table C.10: Scaled energy, mass, and proper separation for two equal sized holes, each with parallel linear momenta P/a_1 generated from an inversion symmetric extrinsic curvature obeying the isometry condition with a plus sign. tThe conformal separation is $\beta = 4$.

P/a_1	E/a_1 80	120	160	$\Re$	M/a_1 80	120	160	$\Re$	L/a_1 80	120	160	$\Re$
0.0	5.321	5.336	5.343	5.346	3.557	3.576	3.585	3.588	12.782	12.848	12.882	12.893
1.0	5.810	5.835	5.848	5.852	3.670	3.689	3.698	3.701	13.185	13.252	13.285	13.296
2.5	7.752	7.833	7.875	7.887	4.094	4.113	4.123	4.127	14.698	14.767	14.802	14.814
5.0	11.916	12.184	12.327	12.363	4.909	4.931	4.942	4.946	17.610	17.689	17.728	17.742
7.5	16.168	16.714	17.011	17.078	5.660	5.686	5.698	5.703	20.294	20.386	20.430	20.446
10.0	20.262	21.156	21.651	21.753	6.336	6.366	6.380	6.385	22.712	22.816	22.866	22.885
12.5	24.160	25.455	26.184	26.318	6.952	6.985	7.000	7.007	24.914	25.030	25.085	25.107
15.0	27.865	29.599	30.592	30.755	7.520	7.556	7.573	7.580	26.944	27.072	27.133	27.157
17.5	31.389	33.591	34.872	35.059	8.048	8.088	8.106	8.114	28.835	28.975	29.041	29.068

Table C.11: Scaled energy, mass, and proper separation for two equal sized holes, each with parallel linear momenta P/a_1 generated from an inversion symmetric extrinsic curvature obeying the isometry condition with a minus sign. The conformal separation is $\beta = 4$.

S/a_1^2	E/a_1 80	120	160	$\Re$	M/a_1 80	120	160	$\Re$	L/a_1 80	120	160	$\Re$
0.0	5.321	5.336	5.343	5.346	3.557	3.576	3.585	3.588	12.782	12.848	12.882	12.893
1.0	5.346	5.360	5.367	5.369	3.571	3.590	3.599	3.602	12.832	12.898	12.931	12.942
3.0	5.521	5.532	5.538	5.540	3.675	3.693	3.702	3.705	13.199	13.262	13.293	13.304
10.0	6.660	6.661	6.661	6.661	4.362	4.377	4.385	4.387	15.612	15.666	15.692	15.701
30.0	9.644	9.619	9.607	9.602	6.195	6.210	6.217	6.219	22.066	22.117	22.142	22.150
100.0	16.262	16.145	16.092	16.067	10.300	10.316	10.324	10.327	36.545	36.603	36.632	36.642
300.0	27.665	27.198	27.002	26.886	17.200	17.222	17.233	17.237	60.919	60.995	61.032	61.046
1000.0	52.050	50.110	49.220	48.817	30.859	30.891	30.906	30.913	109.198	109.308	109.362	109.382

Table C.12: Scaled energy, mass, and proper separation for two equal sized holes, each with parallel angular momenta S/a_1^2 generated from an inversion symmetric extrinsic curvature obeying the isometry condition with a minus sign. The conformal separation is $\beta = 4$.

	E/a_1				M/a_1				L/a_1			
P/a_1	80	120	160	$\Re$	80	120	160	$\Re$	80	120	160	$\Re$
0.0	4.979	4.990	4.995	4.997	3.104	3.118	3.125	3.127	14.257	14.317	14.347	14.357
1.0	5.073	5.083	5.088	5.089	3.149	3.162	3.169	3.171	14.474	14.532	14.561	14.571
2.5	5.474	5.481	5.484	5.485	3.341	3.353	3.359	3.361	15.399	15.452	15.479	15.488
5.0	6.378	6.378	6.377	6.378	3.772	3.783	3.789	3.791	17.476	17.524	17.547	17.555
7.5	7.283	7.278	7.275	7.274	4.205	4.216	4.221	4.223	19.556	19.600	19.623	19.630
10.0	8.127	8.117	8.111	8.110	4.609	4.620	4.625	4.627	21.491	21.535	21.557	21.564
12.5	8.908	8.894	8.886	8.885	4.984	4.994	5.000	5.001	23.283	23.327	23.348	23.356
15.0	9.636	9.618	9.608	9.606	5.333	5.344	5.349	5.351	24.952	24.995	25.017	25.024
17.5	10.319	10.297	10.285	10.283	5.660	5.671	5.676	5.678	26.516	26.560	26.582	26.589

Table C.13: Scaled energy, mass, and proper separation for two equal sized holes, each with anti-parallel linear momenta P/a_1 generated from an inversion symmetric extrinsic curvature obeying the isometry condition with a plus sign. The conformal separation is $\beta = 5$.

	E/a_1				M/a_1				L/a_1			
P/a_1	80	120	160	$\Re$	80	120	160	$\Re$	80	120	160	$\Re$
0.0	4.979	4.990	4.995	4.997	3.104	3.118	3.125	3.127	14.257	14.317	14.347	14.357
1.0	5.063	5.073	5.078	5.080	3.143	3.157	3.163	3.165	14.440	14.499	14.528	14.538
2.5	5.434	5.440	5.444	5.445	3.314	3.327	3.333	3.335	15.243	15.298	15.325	15.334
5.0	6.299	6.299	6.299	6.299	3.715	3.726	3.731	3.733	17.118	17.167	17.191	17.199
7.5	7.185	7.180	7.177	7.176	4.126	4.137	4.142	4.144	19.041	19.087	19.110	19.118
10.0	8.020	8.010	8.004	8.003	4.514	4.524	4.529	4.531	20.851	20.896	20.919	20.927
12.5	8.796	8.782	8.774	8.772	4.875	4.885	4.891	4.893	22.537	22.582	22.604	22.612
15.0	9.521	9.503	9.493	9.491	5.213	5.223	5.228	5.230	24.111	24.157	24.179	24.187
17.5	10.202	10.180	10.168	10.166	5.530	5.541	5.546	5.548	25.591	25.637	25.659	25.667

Table C.14: Scaled energy, mass, and proper separation for two equal sized holes, each with anti-parallel linear momenta P/a_1 generated from an inversion symmetric extrinsic curvature obeying the isometry condition with a minus sign. The conformal separation is $\beta = 5$.

	E/a_1				M/a_1				L/a_1			
S/a_1^2	80	120	160	$\Re$	80	120	160	$\Re$	80	120	160	$\Re$
0.0	4.979	4.990	4.995	4.997	3.104	3.118	3.125	3.127	14.257	14.317	14.347	14.357
1.0	5.005	5.016	5.021	5.023	3.120	3.133	3.140	3.142	14.325	14.384	14.414	14.424
3.0	5.193	5.201	5.206	5.207	3.230	3.243	3.249	3.251	14.807	14.863	14.891	14.901
10.0	6.292	6.293	6.294	6.294	3.902	3.913	3.918	3.920	17.739	17.787	17.810	17.819
30.0	8.800	8.790	8.785	8.783	5.581	5.591	5.596	5.598	25.065	25.112	25.135	25.143
100.0	13.535	13.504	13.488	13.482	9.235	9.247	9.253	9.255	41.020	41.077	41.104	41.114
300.0	20.218	20.147	20.112	20.100	15.307	15.323	15.331	15.333	67.535	67.610	67.647	67.660
1000.0	31.254	31.093	31.014	30.987	27.256	27.279	27.290	27.294	119.716	119.823	119.877	119.895

Table C.15: Scaled energy, mass, and proper separation for two equal sized holes, each with anti-parallel angular momenta S/a_1^2 generated from an inversion symmetric extrinsic curvature obeying the isometry condition with a minus sign. The conformal separation is $\beta = 5$.

P/a_1	E/a_1 80	120	160	$\Re$	M/a_1 80	120	160	$\Re$	L/a_1 80	120	160	$\Re$
0.0	4.979	4.990	4.995	4.997	3.104	3.118	3.125	3.127	14.257	14.317	14.347	14.357
1.0	5.521	5.539	5.548	5.551	3.222	3.235	3.242	3.244	14.795	14.855	14.885	14.895
2.5	7.619	7.676	7.705	7.714	3.643	3.657	3.664	3.667	16.728	16.789	16.820	16.831
5.0	12.060	12.249	12.349	12.375	4.420	4.436	4.443	4.446	20.288	20.358	20.393	20.405
7.5	16.637	17.029	17.238	17.290	5.121	5.140	5.148	5.152	23.506	23.587	23.626	23.641
10.0	21.118	21.769	22.122	22.203	5.749	5.769	5.779	5.783	26.384	26.475	26.519	26.536
12.5	25.455	26.413	26.939	27.052	6.318	6.341	6.352	6.356	28.995	29.097	29.145	29.164
15.0	29.643	30.946	31.670	31.815	6.842	6.867	6.879	6.884	31.398	31.509	31.563	31.584
17.5	33.684	35.365	36.310	36.486	7.329	7.356	7.369	7.375	33.632	33.754	33.812	33.835

Table C.16: Scaled energy, mass, and proper separation for two equal sized holes, each with parallel linear momenta P/a_1 generated from an inversion symmetric extrinsic curvature obeying the isometry condition with a plus sign. The conformal separation is $\beta = 5$.

P/a_1	E/a_1 80	120	160	$\Re$	M/a_1 80	120	160	$\Re$	L/a_1 80	120	160	$\Re$
0.0	4.979	4.990	4.995	4.997	3.104	3.118	3.125	3.127	14.257	14.317	14.347	14.357
1.0	5.510	5.528	5.537	5.540	3.215	3.229	3.235	3.238	14.760	14.820	14.850	14.860
2.5	7.586	7.643	7.673	7.681	3.619	3.633	3.640	3.642	16.595	16.657	16.688	16.699
5.0	12.016	12.205	12.305	12.332	4.373	4.390	4.398	4.400	20.028	20.100	20.136	20.148
7.5	16.593	16.985	17.194	17.246	5.060	5.078	5.087	5.091	23.154	23.237	23.277	23.292
10.0	21.075	21.726	22.079	22.161	5.675	5.696	5.706	5.710	25.957	26.051	26.096	26.113
12.5	25.414	26.372	26.898	27.011	6.234	6.257	6.268	6.273	28.504	28.608	28.658	28.678
15.0	29.604	30.907	31.631	31.776	6.748	6.774	6.786	6.791	30.849	30.964	31.019	31.041
17.5	33.647	35.328	36.273	36.449	7.227	7.255	7.268	7.274	33.032	33.158	33.217	33.241

Table C.17: Scaled energy, mass, and proper separation for two equal sized holes, each with parallel linear momenta P/a_1 generated from an inversion symmetric extrinsic curvature obeying the isometry condition with a minus sign. The conformal separation is $\beta = 5$.

S/a_1^2	E/a_1 80	120	160	$\Re$	M/a_1 80	120	160	$\Re$	L/a_1 80	120	160	$\Re$
0.0	4.979	4.990	4.995	4.997	3.104	3.118	3.125	3.127	14.257	14.317	14.347	14.357
1.0	5.010	5.021	5.026	5.028	3.121	3.135	3.141	3.144	14.331	14.391	14.420	14.431
3.0	5.230	5.239	5.243	5.244	3.241	3.254	3.260	3.262	14.857	14.913	14.940	14.950
10.0	6.525	6.524	6.523	6.523	3.958	3.968	3.973	3.975	17.995	18.043	18.066	18.074
30.0	9.638	9.616	9.605	9.601	5.730	5.741	5.746	5.748	25.784	25.831	25.854	25.863
100.0	16.303	16.209	16.165	16.146	9.606	9.619	9.625	9.627	42.870	42.927	42.955	42.965
300.0	27.577	27.211	27.056	26.966	16.086	16.103	16.111	16.114	71.502	71.577	71.614	71.627
1000.0	51.469	49.716	49.002	48.548	28.894	28.918	28.930	28.934	128.168	128.275	128.327	128.347

Table C.18: Scaled energy, mass, and proper separation for two equal sized holes, each with parallel angular momenta S/a_1^2 generated from an inversion symmetric extrinsic curvature obeying the isometry condition with a minus sign. The conformal separation is $\beta = 5$.

P/a_1	E/a_1 80	120	160	$\Re$	M/a_1 80	120	160	$\Re$	L/a_1 80	120	160	$\Re$
0.0	4.778	4.787	4.792	4.794	2.856	2.867	2.873	2.875	15.670	15.728	15.756	15.766
1.0	4.906	4.914	4.918	4.919	2.912	2.922	2.928	2.930	15.989	16.045	16.073	16.082
2.5	5.424	5.428	5.430	5.431	3.136	3.146	3.151	3.153	17.283	17.333	17.358	17.367
5.0	6.510	6.507	6.506	6.505	3.607	3.616	3.621	3.622	19.987	20.032	20.054	20.062
7.5	7.554	7.546	7.541	7.540	4.061	4.070	4.074	4.075	22.583	22.626	22.647	22.655
10.0	8.510	8.497	8.489	8.488	4.476	4.485	4.490	4.491	24.957	25.000	25.021	25.029
12.5	9.388	9.370	9.360	9.358	4.858	4.867	4.872	4.873	27.137	27.179	27.201	27.208
15.0	10.202	10.179	10.167	10.164	5.213	5.222	5.226	5.228	29.155	29.198	29.220	29.227
17.5	10.962	10.936	10.921	10.918	5.544	5.553	5.557	5.559	31.041	31.084	31.106	31.113

Table C.19: Scaled energy, mass, and proper separation for two equal sized holes, each with anti-parallel linear momenta P/a_1 generated from an inversion symmetric extrinsic curvature obeying the isometry condition with a plus sign. The conformal separation is $\beta = 6$.

P/a_1	E/a_1 80	120	160	$\Re$	M/a_1 80	120	160	$\Re$	L/a_1 80	120	160	$\Re$
0.0	4.778	4.787	4.792	4.794	2.856	2.867	2.873	2.875	15.670	15.728	15.756	15.766
1.0	4.893	4.902	4.906	4.907	2.904	2.915	2.920	2.922	15.940	15.996	16.024	16.034
2.5	5.375	5.380	5.382	5.382	3.106	3.116	3.121	3.123	17.068	17.120	17.145	17.154
5.0	6.423	6.421	6.419	6.419	3.545	3.555	3.559	3.561	19.522	19.569	19.592	19.600
7.5	7.452	7.443	7.439	7.438	3.978	3.987	3.991	3.993	21.931	21.976	21.998	22.006
10.0	8.400	8.387	8.379	8.378	4.377	4.386	4.390	4.392	24.156	24.201	24.223	24.230
12.5	9.275	9.256	9.247	9.244	4.746	4.755	4.759	4.761	26.207	26.252	26.274	26.282
15.0	10.087	10.064	10.051	10.049	5.089	5.098	5.102	5.104	28.113	28.158	28.180	28.188
17.5	10.846	10.819	10.804	10.801	5.410	5.419	5.423	5.425	29.896	29.942	29.964	29.972

Table C.20: Scaled energy, mass, and proper separation for two equal sized holes, each with anti-parallel linear momenta P/a_1 generated from an inversion symmetric extrinsic curvature obeying the isometry condition with a minus sign. The conformal separation is $\beta = 6$.

S/a_1^2	E/a_1 80	120	160	$\Re$	M/a_1 80	120	160	$\Re$	L/a_1 80	120	160	$\Re$
0.0	4.778	4.787	4.792	4.794	2.856	2.867	2.873	2.875	15.670	15.728	15.756	15.766
1.0	4.811	4.821	4.825	4.827	2.874	2.885	2.891	2.893	15.761	15.819	15.847	15.857
3.0	5.043	5.050	5.053	5.055	3.000	3.010	3.015	3.017	16.396	16.450	16.476	16.486
10.0	6.297	6.297	6.296	6.296	3.707	3.716	3.720	3.722	19.980	20.026	20.049	20.057
30.0	9.005	8.993	8.987	8.985	5.385	5.394	5.398	5.399	28.484	28.531	28.554	28.563
100.0	14.039	14.006	13.989	13.984	8.985	8.995	9.000	9.002	46.743	46.802	46.831	46.841
300.0	21.126	21.053	21.017	21.005	14.948	14.962	14.968	14.971	76.998	77.077	77.116	77.129
1000.0	32.827	32.664	32.582	32.555	26.673	26.692	26.702	26.705	136.499	136.615	136.672	136.692

Table C.21: Scaled energy, mass, and proper separation for two equal sized holes, each with anti-parallel angular momenta S/a_1^2 generated from an inversion symmetric extrinsic curvature obeying the isometry condition with a minus sign. The conformal separation is $\beta = 6$.

P/a_1	E/a_1 80	120	160	$\Re$	M/a_1 80	120	160	$\Re$	L/a_1 80	120	160	$\Re$
0.0	4.778	4.787	4.792	4.794	2.856	2.867	2.873	2.875	15.670	15.728	15.756	15.766
1.0	5.349	5.363	5.371	5.373	2.973	2.984	2.990	2.992	16.309	16.367	16.395	16.405
2.5	7.531	7.574	7.596	7.602	3.384	3.395	3.401	3.403	18.554	18.614	18.643	18.653
5.0	12.130	12.271	12.345	12.365	4.126	4.139	4.145	4.147	22.614	22.681	22.715	22.727
7.5	16.905	17.198	17.354	17.394	4.791	4.806	4.813	4.816	26.254	26.332	26.369	26.383
10.0	21.629	22.120	22.383	22.447	5.384	5.401	5.409	5.412	29.500	29.587	29.629	29.645
12.5	26.251	26.979	27.373	27.464	5.921	5.940	5.949	5.952	32.441	32.538	32.585	32.603
15.0	30.760	31.758	32.304	32.424	6.415	6.435	6.445	6.449	35.145	35.252	35.302	35.323
17.5	35.153	36.453	37.169	37.319	6.874	6.897	6.907	6.911	37.660	37.775	37.830	37.852

Table C.22: Scaled energy, mass, and proper separation for two equal sized holes, each with parallel linear momenta P/a_1 generated from an inversion symmetric extrinsic curvature obeying the isometry condition with a plus sign. The conformal separation is $\beta = 6$.

P/a_1	E/a_1 80	120	160	$\Re$	M/a_1 80	120	160	$\Re$	L/a_1 80	120	160	$\Re$
0.0	4.778	4.787	4.792	4.794	2.856	2.867	2.873	2.875	15.670	15.728	15.756	15.766
1.0	5.335	5.350	5.357	5.360	2.966	2.977	2.982	2.984	16.260	16.318	16.346	16.356
2.5	7.493	7.535	7.558	7.564	3.357	3.368	3.374	3.376	18.373	18.433	18.463	18.474
5.0	12.080	12.221	12.295	12.315	4.075	4.089	4.095	4.098	22.263	22.333	22.367	22.380
7.5	16.855	17.148	17.304	17.344	4.724	4.740	4.747	4.750	25.781	25.861	25.900	25.914
10.0	21.581	22.072	22.335	22.399	5.304	5.321	5.330	5.333	28.927	29.017	29.061	29.077
12.5	26.205	26.933	27.327	27.418	5.831	5.850	5.858	5.862	31.782	31.883	31.931	31.950
15.0	30.716	31.715	32.260	32.380	6.315	6.335	6.345	6.349	34.410	34.520	34.573	34.594
17.5	35.112	36.411	37.127	37.277	6.765	6.788	6.798	6.803	36.855	36.975	37.032	37.055

Table C.23: Scaled energy, mass, and proper separation for two equal sized holes, each with parallel linear momenta P/a_1 generated from an inversion symmetric extrinsic curvature obeying the isometry condition with a minus sign. The conformal separation is $\beta = 6$.

S/a_1^2	E/a_1 80	120	160	$\Re$	M/a_1 80	120	160	$\Re$	L/a_1 80	120	160	$\Re$
0.0	4.778	4.787	4.792	4.794	2.856	2.867	2.873	2.875	15.670	15.728	15.756	15.766
1.0	4.815	4.824	4.829	4.830	2.875	2.886	2.892	2.894	15.767	15.824	15.852	15.862
3.0	5.072	5.079	5.082	5.083	3.007	3.017	3.022	3.024	16.434	16.488	16.514	16.523
10.0	6.480	6.477	6.476	6.475	3.742	3.750	3.755	3.756	20.171	20.217	20.239	20.247
30.0	9.688	9.667	9.657	9.653	5.481	5.490	5.494	5.495	29.046	29.093	29.117	29.125
100.0	16.405	16.322	16.283	16.267	9.233	9.244	9.249	9.250	48.281	48.339	48.368	48.378
300.0	27.617	27.312	27.180	27.108	15.486	15.500	15.506	15.509	80.442	80.520	80.558	80.572
1000.0	51.062	49.564	48.975	48.566	27.833	27.853	27.863	27.866	144.080	144.191	144.245	144.265

Table C.24: Scaled energy, mass, and proper separation for two equal sized holes, each with parallel angular momenta S/a_1^2 generated from an inversion symmetric extrinsic curvature obeying the isometry condition with a minus sign. The conformal separation is $\beta = 6$.

P/a_1	E/a_1 80	120	160	$\Re$	M/a_1 80	120	160	$\Re$	L/a_1 80	120	160	$\Re$
0.0	4.645	4.654	4.658	4.659	2.699	2.709	2.713	2.715	17.038	17.095	17.123	17.133
1.0	4.805	4.812	4.816	4.817	2.763	2.772	2.777	2.778	17.460	17.515	17.542	17.552
2.5	5.427	5.430	5.431	5.431	3.012	3.021	3.025	3.026	19.100	19.149	19.173	19.182
5.0	6.667	6.663	6.660	6.660	3.510	3.517	3.521	3.523	22.364	22.408	22.430	22.438
7.5	7.830	7.820	7.814	7.812	3.976	3.984	3.988	3.990	25.418	25.462	25.483	25.490
10.0	8.884	8.868	8.859	8.857	4.400	4.408	4.412	4.413	28.185	28.228	28.249	28.257
12.5	9.847	9.826	9.814	9.812	4.787	4.795	4.799	4.801	30.710	30.754	30.775	30.783
15.0	10.737	10.710	10.696	10.693	5.145	5.153	5.157	5.159	33.043	33.087	33.109	33.117
17.5	11.567	11.536	11.519	11.515	5.479	5.488	5.492	5.493	35.218	35.263	35.285	35.293

Table C.25: Scaled energy, mass, and proper separation for two equal sized holes, each with anti-parallel linear momenta P/a_1 generated from an inversion symmetric extrinsic curvature obeying the isometry condition with a plus sign. The conformal separation is $\beta = 7$.

P/a_1	E/a_1 80	120	160	$\Re$	M/a_1 80	120	160	$\Re$	L/a_1 80	120	160	$\Re$
0.0	4.645	4.654	4.658	4.659	2.699	2.709	2.713	2.715	17.038	17.095	17.123	17.133
1.0	4.790	4.797	4.801	4.802	2.755	2.764	2.769	2.770	17.397	17.452	17.479	17.489
2.5	5.372	5.375	5.376	5.377	2.980	2.988	2.992	2.994	18.836	18.886	18.911	18.920
5.0	6.576	6.572	6.569	6.569	3.446	3.454	3.458	3.459	21.816	21.862	21.885	21.893
7.5	7.725	7.714	7.709	7.707	3.892	3.900	3.903	3.905	24.663	24.708	24.730	24.738
10.0	8.773	8.757	8.748	8.746	4.299	4.307	4.311	4.313	27.262	27.307	27.329	27.337
12.5	9.733	9.712	9.700	9.697	4.673	4.681	4.685	4.687	29.644	29.690	29.712	29.720
15.0	10.622	10.595	10.581	10.578	5.020	5.028	5.032	5.033	31.850	31.896	31.919	31.927
17.5	11.451	11.420	11.403	11.399	5.343	5.352	5.356	5.357	33.910	33.957	33.980	33.988

Table C.26: Scaled energy, mass, and proper separation for two equal sized holes, each with anti-parallel linear momenta P/a_1 generated from an inversion symmetric extrinsic curvature obeying the isometry condition with a minus sign. The conformal separation is $\beta = 7$.

S/a_1^2	E/a_1 80	120	160	$\Re$	M/a_1 80	120	160	$\Re$	L/a_1 80	120	160	$\Re$
0.0	4.645	4.654	4.658	4.659	2.699	2.709	2.713	2.715	17.038	17.095	17.123	17.133
1.0	4.685	4.693	4.697	4.698	2.719	2.729	2.733	2.735	17.152	17.208	17.235	17.246
3.0	4.952	4.958	4.961	4.962	2.855	2.864	2.868	2.870	17.921	17.974	17.999	18.009
10.0	6.324	6.322	6.321	6.321	3.585	3.592	3.596	3.597	22.046	22.092	22.114	22.122
30.0	9.189	9.176	9.170	9.168	5.261	5.268	5.272	5.273	31.531	31.580	31.604	31.612
100.0	14.476	14.442	14.425	14.420	8.826	8.835	8.839	8.841	51.733	51.795	51.825	51.836
300.0	21.917	21.843	21.806	21.793	14.719	14.731	14.737	14.739	85.156	85.241	85.283	85.297
1000.0	34.208	34.041	33.958	33.929	26.303	26.320	26.329	26.332	150.873	150.997	151.059	151.080

Table C.27: Scaled energy, mass, and proper separation for two equal sized holes, each with anti-parallel angular momenta S/a_1^2 generated from an inversion symmetric extrinsic curvature obeying the isometry condition with a minus sign. The conformal separation is $\beta = 7$.

P/a_1	E/a_1 80	120	160	$\Re$	M/a_1 80	120	160	$\Re$	L/a_1 80	120	160	$\Re$
0.0	4.645	4.654	4.658	4.659	2.699	2.709	2.713	2.715	17.038	17.095	17.123	17.133
1.0	5.237	5.249	5.255	5.257	2.816	2.825	2.830	2.832	17.768	17.825	17.853	17.863
2.5	7.475	7.508	7.525	7.531	3.219	3.229	3.233	3.235	20.295	20.353	20.382	20.393
5.0	12.178	12.286	12.343	12.359	3.938	3.949	3.954	3.957	24.806	24.873	24.906	24.918
7.5	17.085	17.311	17.431	17.462	4.579	4.592	4.598	4.600	28.831	28.908	28.945	28.959
10.0	21.974	22.353	22.556	22.606	5.149	5.164	5.171	5.174	32.414	32.500	32.542	32.558
12.5	26.792	27.356	27.660	27.732	5.666	5.682	5.689	5.693	35.659	35.754	35.800	35.817
15.0	31.526	32.303	32.725	32.821	6.140	6.158	6.166	6.170	38.640	38.744	38.794	38.814
17.5	36.171	37.187	37.741	37.864	6.582	6.601	6.610	6.613	41.412	41.525	41.579	41.601

Table C.28: Scaled energy, mass, and proper separation for two equal sized holes, each with parallel linear momenta P/a_1 generated from an inversion symmetric extrinsic curvature obeying the isometry condition with a plus sign. The conformal separation is $\beta = 7$.

P/a_1	E/a_1 80	120	160	$\Re$	M/a_1 80	120	160	$\Re$	L/a_1 80	120	160	$\Re$
0.0	4.645	4.654	4.658	4.659	2.699	2.709	2.713	2.715	17.038	17.095	17.123	17.133
1.0	5.221	5.233	5.239	5.241	2.807	2.817	2.821	2.823	17.706	17.763	17.791	17.801
2.5	7.432	7.465	7.483	7.488	3.190	3.200	3.204	3.206	20.069	20.129	20.159	20.169
5.0	12.122	12.231	12.289	12.304	3.884	3.896	3.901	3.904	24.375	24.445	24.478	24.491
7.5	17.030	17.256	17.376	17.407	4.509	4.522	4.528	4.531	28.252	28.331	28.369	28.384
10.0	21.921	22.300	22.503	22.553	5.066	5.080	5.088	5.090	31.713	31.803	31.846	31.862
12.5	26.742	27.306	27.610	27.682	5.571	5.587	5.595	5.598	34.854	34.953	35.000	35.019
15.0	31.478	32.255	32.677	32.773	6.035	6.053	6.061	6.065	37.743	37.851	37.903	37.924
17.5	36.125	37.141	37.696	37.818	6.467	6.486	6.495	6.499	40.430	40.548	40.604	40.627

Table C.29: Scaled energy, mass, and proper separation for two equal sized holes, each with parallel linear momenta P/a_1 generated from an inversion symmetric extrinsic curvature obeying the isometry condition with a minus sign. The conformal separation is $\beta = 7$.

S/a_1^2	E/a_1 80	120	160	$\Re$	M/a_1 80	120	160	$\Re$	L/a_1 80	120	160	$\Re$
0.0	4.645	4.654	4.658	4.659	2.699	2.709	2.713	2.715	17.038	17.095	17.123	17.133
1.0	4.688	4.696	4.700	4.701	2.720	2.729	2.734	2.736	17.156	17.212	17.239	17.249
3.0	4.975	4.981	4.983	4.984	2.860	2.869	2.873	2.875	17.950	18.002	18.028	18.037
10.0	6.469	6.466	6.464	6.464	3.608	3.615	3.619	3.620	22.191	22.237	22.260	22.268
30.0	9.756	9.736	9.726	9.723	5.326	5.333	5.337	5.338	31.982	32.031	32.055	32.063
100.0	16.527	16.452	16.416	16.402	9.001	9.011	9.015	9.017	53.044	53.105	53.136	53.147
300.0	27.712	27.448	27.331	27.271	15.113	15.125	15.131	15.133	88.217	88.300	88.340	88.355
1000.0	50.814	49.536	49.034	48.683	27.173	27.191	27.200	27.203	157.821	157.939	157.997	158.017

Table C.30: Scaled energy, mass, and proper separation for two equal sized holes, each with parallel angular momenta S/a_1^2 generated from an inversion symmetric extrinsic curvature obeying the isometry condition with a minus sign. The conformal separation is $\beta = 7$.

P/a_1	E/a_1 80	120	160	$\Re$	M/a_1 80	120	160	$\Re$	L/a_1 80	120	160	$\Re$
0.0	4.551	4.559	4.563	4.564	2.590	2.599	2.603	2.605	18.372	18.429	18.457	18.467
1.0	4.741	4.747	4.750	4.751	2.661	2.670	2.674	2.675	18.893	18.948	18.974	18.984
2.5	5.454	5.456	5.456	5.457	2.929	2.937	2.940	2.942	20.852	20.901	20.925	20.934
5.0	6.829	6.823	6.820	6.820	3.445	3.452	3.456	3.457	24.622	24.666	24.688	24.696
7.5	8.097	8.085	8.078	8.076	3.922	3.929	3.932	3.934	28.091	28.135	28.157	28.165
10.0	9.239	9.220	9.211	9.208	4.351	4.358	4.362	4.363	31.214	31.258	31.280	31.287
12.5	10.278	10.254	10.242	10.239	4.742	4.749	4.753	4.755	34.056	34.101	34.123	34.131
15.0	11.237	11.208	11.192	11.188	5.103	5.110	5.114	5.116	36.676	36.721	36.744	36.752
17.5	12.131	12.096	12.078	12.073	5.439	5.447	5.451	5.452	39.116	39.163	39.186	39.194

Table C.31: Scaled energy, mass, and proper separation for two equal sized holes, each with anti-parallel linear momenta P/a_1 generated from an inversion symmetric extrinsic curvature obeying the isometry condition with a plus sign. The conformal separation is $\beta = 8$.

P/a_1	E/a_1 80	120	160	$\Re$	M/a_1 80	120	160	$\Re$	L/a_1 80	120	160	$\Re$
0.0	4.551	4.559	4.563	4.564	2.590	2.599	2.603	2.605	18.372	18.429	18.457	18.467
1.0	4.723	4.730	4.733	4.734	2.652	2.661	2.665	2.666	18.817	18.872	18.898	18.908
2.5	5.395	5.397	5.397	5.398	2.895	2.903	2.906	2.908	20.548	20.598	20.623	20.632
5.0	6.735	6.729	6.726	6.725	3.380	3.388	3.391	3.392	24.009	24.055	24.078	24.086
7.5	7.990	7.978	7.971	7.970	3.836	3.843	3.847	3.848	27.254	27.300	27.323	27.331
10.0	9.127	9.108	9.099	9.096	4.249	4.257	4.260	4.262	30.196	30.243	30.265	30.273
12.5	10.164	10.140	10.128	10.124	4.627	4.635	4.638	4.640	32.884	32.931	32.954	32.962
15.0	11.123	11.093	11.077	11.073	4.976	4.984	4.988	4.989	35.367	35.415	35.438	35.447
17.5	12.016	11.981	11.963	11.958	5.302	5.310	5.314	5.315	37.683	37.732	37.755	37.764

Table C.32: Scaled energy, mass, and proper separation for two equal sized holes, each with anti-parallellinear momenta P/a_1 generated from an inversion symmetric extrinsic curvature obeying the isometry condition with a minus sign. The conformal separation is $\beta = 8$.

S/a_1^2	E/a_1 80	120	160	$\Re$	M/a_1 80	120	160	$\Re$	L/a_1 80	120	160	$\Re$
0.0	4.551	4.559	4.563	4.564	2.590	2.599	2.603	2.605	18.372	18.429	18.457	18.467
1.0	4.596	4.603	4.607	4.608	2.612	2.620	2.624	2.626	18.505	18.561	18.588	18.599
3.0	4.892	4.897	4.900	4.901	2.756	2.764	2.768	2.769	19.392	19.445	19.470	19.480
10.0	6.356	6.354	6.353	6.353	3.501	3.507	3.511	3.512	23.978	24.024	24.047	24.055
30.0	9.351	9.338	9.332	9.330	5.174	5.181	5.184	5.185	34.302	34.352	34.377	34.386
100.0	14.859	14.824	14.807	14.801	8.714	8.722	8.726	8.728	56.182	56.247	56.280	56.291
300.0	22.614	22.538	22.500	22.487	14.560	14.571	14.576	14.578	92.353	92.444	92.489	92.504
1000.0	35.436	35.265	35.180	35.151	26.047	26.063	26.071	26.074	163.468	163.602	163.667	163.691

Table C.33: Scaled energy, mass, and proper separation for two equal sized holes, each with anti-parallel angular momenta S/a_1^2 generated from an inversion symmetric extrinsic curvature obeying the isometry condition with a minus sign. The conformal separation is $\beta = 8$.

P/a_1	E/a_1 80	120	160	$\Re$	M/a_1 80	120	160	$\Re$	L/a_1 80	120	160	$\Re$
0.0	4.551	4.559	4.563	4.564	2.590	2.599	2.603	2.605	18.372	18.429	18.457	18.467
1.0	5.157	5.168	5.173	5.175	2.707	2.715	2.719	2.721	19.185	19.242	19.269	19.279
2.5	7.436	7.463	7.477	7.481	3.104	3.113	3.117	3.119	21.967	22.026	22.055	22.065
5.0	12.212	12.298	12.343	12.355	3.807	3.817	3.822	3.824	26.894	26.961	26.993	27.005
7.5	17.212	17.391	17.485	17.510	4.431	4.442	4.448	4.450	31.275	31.352	31.389	31.403
10.0	22.219	22.517	22.677	22.716	4.985	4.998	5.005	5.007	35.171	35.257	35.299	35.314
12.5	27.179	27.623	27.862	27.919	5.487	5.502	5.508	5.511	38.698	38.792	38.838	38.856
15.0	32.076	32.689	33.021	33.097	5.948	5.964	5.971	5.974	41.938	42.041	42.091	42.111
17.5	36.906	37.709	38.145	38.243	6.376	6.393	6.401	6.405	44.949	45.062	45.115	45.137

Table C.34: Scaled energy, mass, and proper separation for two equal sized holes, each with parallel linear momenta P/a_1 generated from an inversion symmetric extrinsic curvature obeying the isometry condition with a plus sign. The conformal separation is $\beta = 8$.

P/a_1	E/a_1 80	120	160	$\Re$	M/a_1 80	120	160	$\Re$	L/a_1 80	120	160	$\Re$
0.0	4.551	4.559	4.563	4.564	2.590	2.599	2.603	2.605	18.372	18.429	18.457	18.467
1.0	5.140	5.151	5.156	5.158	2.698	2.706	2.710	2.712	19.111	19.168	19.196	19.206
2.5	7.389	7.416	7.430	7.434	3.073	3.083	3.087	3.089	21.703	21.764	21.793	21.804
5.0	12.152	12.239	12.284	12.296	3.751	3.762	3.766	3.768	26.394	26.463	26.497	26.509
7.5	17.153	17.332	17.427	17.451	4.358	4.370	4.375	4.378	30.604	30.683	30.722	30.736
10.0	22.162	22.461	22.621	22.660	4.899	4.912	4.918	4.921	34.361	34.450	34.493	34.510
12.5	27.125	27.569	27.809	27.865	5.389	5.403	5.410	5.413	37.768	37.867	37.914	37.933
15.0	32.025	32.638	32.970	33.046	5.839	5.855	5.862	5.866	40.902	41.010	41.062	41.082
17.5	36.857	37.660	38.097	38.194	6.258	6.275	6.283	6.286	43.817	43.934	43.990	44.012

Table C.35: Scaled energy, mass, and proper separation for two equal sized holes, each with parallel linear momenta P/a_1 generated from an inversion symmetric extrinsic curvature obeying the isometry condition with a minus sign. The conformal separation is $\beta = 8$.

S/a_1^2	E/a_1 80	120	160	$\Re$	M/a_1 80	120	160	$\Re$	L/a_1 80	120	160	$\Re$
0.0	4.551	4.559	4.563	4.564	2.590	2.599	2.603	2.605	18.372	18.429	18.457	18.467
1.0	4.598	4.606	4.609	4.611	2.612	2.621	2.625	2.627	18.508	18.564	18.591	18.602
3.0	4.910	4.915	4.918	4.919	2.759	2.767	2.771	2.772	19.414	19.467	19.492	19.501
10.0	6.474	6.471	6.469	6.469	3.516	3.523	3.526	3.527	24.090	24.137	24.160	24.168
30.0	9.829	9.810	9.801	9.797	5.220	5.227	5.230	5.232	34.671	34.722	34.747	34.756
100.0	16.655	16.586	16.553	16.540	8.844	8.853	8.856	8.858	57.319	57.384	57.417	57.428
300.0	27.835	27.599	27.492	27.441	14.860	14.871	14.876	14.879	95.116	95.204	95.247	95.262
1000.0	50.682	49.576	49.137	48.839	26.727	26.743	26.751	26.754	169.926	170.052	170.114	170.136

Table C.36: Scaled energy, mass, and proper separation for two equal sized holes, each with parallel angular momenta S/a_1^2 generated from an inversion symmetric extrinsic curvature obeying the isometry condition with a minus sign. The conformal separation is $\beta = 8$.

P/a_1	E/a_1 80	120	160	$\Re$	M/a_1 80	120	160	$\Re$	L/a_1 80	120	160	$\Re$
0.0	4.481	4.488	4.492	4.493	2.511	2.519	2.522	2.524	19.678	19.735	19.762	19.773
1.0	4.697	4.703	4.706	4.707	2.587	2.595	2.599	2.600	20.292	20.347	20.373	20.383
2.5	5.493	5.493	5.494	5.494	2.869	2.876	2.880	2.881	22.546	22.595	22.619	22.628
5.0	6.988	6.981	6.977	6.976	3.400	3.406	3.409	3.411	26.777	26.822	26.844	26.852
7.5	8.351	8.337	8.330	8.328	3.883	3.890	3.893	3.894	30.627	30.672	30.694	30.702
10.0	9.572	9.552	9.542	9.539	4.317	4.323	4.327	4.328	34.078	34.123	34.146	34.154
12.5	10.683	10.657	10.643	10.639	4.711	4.718	4.721	4.723	37.212	37.259	37.282	37.290
15.0	11.706	11.673	11.657	11.652	5.074	5.081	5.084	5.086	40.099	40.146	40.169	40.178
17.5	12.658	12.620	12.600	12.595	5.412	5.419	5.423	5.424	42.785	42.834	42.857	42.866

Table C.37: Scaled energy, mass, and proper separation for two equal sized holes, each with anti-parallel linear momenta P/a_1 generated from an inversion symmetric extrinsic curvature obeying the isometry condition with a plus sign. The conformal separation is $\beta = 9$.

P/a_1	E/a_1 80	120	160	$\Re$	M/a_1 80	120	160	$\Re$	L/a_1 80	120	160	$\Re$
0.0	4.481	4.488	4.492	4.493	2.511	2.519	2.522	2.524	19.678	19.735	19.762	19.773
1.0	4.678	4.684	4.687	4.688	2.578	2.586	2.589	2.591	20.205	20.260	20.286	20.297
2.5	5.430	5.431	5.431	5.432	2.834	2.841	2.845	2.846	22.209	22.259	22.283	22.292
5.0	6.891	6.884	6.881	6.880	3.334	3.341	3.344	3.345	26.111	26.158	26.181	26.190
7.5	8.242	8.229	8.222	8.220	3.797	3.804	3.807	3.808	29.726	29.772	29.795	29.804
10.0	9.460	9.440	9.429	9.426	4.215	4.222	4.225	4.226	32.986	33.033	33.057	33.065
12.5	10.569	10.543	10.529	10.525	4.596	4.603	4.606	4.608	35.957	36.006	36.030	36.038
15.0	11.591	11.559	11.542	11.538	4.947	4.954	4.958	4.959	38.698	38.748	38.772	38.781
17.5	12.544	12.506	12.486	12.481	5.275	5.282	5.286	5.287	41.253	41.304	41.329	41.338

Table C.38: Scaled energy, mass, and proper separation for two equal sized holes, each with anti-parallel linear momenta P/a_1 generated from an inversion symmetric extrinsic curvature obeying the isometry condition with a minus sign. The conformal separation is $\beta = 9$.

S/a_1^2	E/a_1 80	120	160	$\Re$	M/a_1 80	120	160	$\Re$	L/a_1 80	120	160	$\Re$
0.0	4.481	4.488	4.492	4.493	2.511	2.519	2.522	2.524	19.678	19.735	19.762	19.773
1.0	4.530	4.537	4.540	4.541	2.533	2.541	2.545	2.546	19.828	19.884	19.912	19.922
3.0	4.850	4.855	4.857	4.858	2.684	2.691	2.694	2.696	20.820	20.872	20.898	20.907
10.0	6.390	6.387	6.386	6.386	3.439	3.445	3.448	3.449	25.803	25.850	25.874	25.882
30.0	9.494	9.481	9.475	9.473	5.110	5.116	5.119	5.120	36.859	36.911	36.937	36.946
100.0	15.196	15.161	15.143	15.137	8.632	8.639	8.643	8.644	60.214	60.284	60.318	60.330
300.0	23.234	23.157	23.119	23.106	14.443	14.453	14.458	14.460	98.810	98.907	98.955	98.971
1000.0	36.540	36.366	36.279	36.250	25.860	25.875	25.882	25.885	174.693	174.837	174.907	174.932

Table C.39: Scaled energy, mass, and proper separation for two equal sized holes, each with anti-parallel angular momenta S/a_1^2 generated from an inversion symmetric extrinsic curvature obeying the isometry condition with a minus sign. The conformal separation is $\beta = 9$.

P/a_1	E/a_1 80	120	160	$\Re$	M/a_1 80	120	160	$\Re$	L/a_1 80	120	160	$\Re$
0.0	4.481	4.488	4.492	4.493	2.511	2.519	2.522	2.524	19.678	19.735	19.762	19.773
1.0	5.098	5.108	5.112	5.114	2.627	2.635	2.638	2.640	20.566	20.623	20.651	20.661
2.5	7.407	7.430	7.441	7.444	3.020	3.028	3.032	3.034	23.585	23.644	23.672	23.683
5.0	12.237	12.307	12.343	12.353	3.710	3.719	3.724	3.726	28.896	28.963	28.996	29.008
7.5	17.306	17.449	17.526	17.545	4.321	4.332	4.337	4.339	33.610	33.687	33.724	33.738
10.0	22.400	22.638	22.766	22.797	4.864	4.876	4.882	4.884	37.799	37.885	37.927	37.943
12.5	27.465	27.819	28.011	28.055	5.355	5.368	5.374	5.377	41.590	41.685	41.731	41.749
15.0	32.486	32.974	33.239	33.299	5.806	5.820	5.827	5.830	45.073	45.177	45.227	45.246
17.5	37.456	38.094	38.443	38.520	6.224	6.240	6.247	6.250	48.310	48.423	48.477	48.498

Table C.40: Scaled energy, mass, and proper separation for two equal sized holes, each with parallel linear momenta P/a_1 generated from an inversion symmetric extrinsic curvature obeying the isometry condition with a plus sign. The conformal separation is $\beta = 9$.

P/a_1	E/a_1 80	120	160	$\Re$	M/a_1 80	120	160	$\Re$	L/a_1 80	120	160	$\Re$
0.0	4.481	4.488	4.492	4.493	2.511	2.519	2.522	2.524	19.678	19.735	19.762	19.773
1.0	5.079	5.089	5.094	5.095	2.617	2.625	2.629	2.630	20.482	20.539	20.567	20.577
2.5	7.357	7.379	7.391	7.394	2.988	2.996	3.000	3.002	23.287	23.347	23.376	23.387
5.0	12.174	12.243	12.280	12.290	3.653	3.662	3.667	3.669	28.336	28.406	28.439	28.452
7.5	17.243	17.387	17.463	17.482	4.246	4.257	4.263	4.265	32.860	32.940	32.979	32.994
10.0	22.339	22.578	22.706	22.737	4.775	4.787	4.793	4.795	36.896	36.986	37.029	37.046
12.5	27.408	27.762	27.954	27.998	5.254	5.267	5.273	5.276	40.555	40.654	40.702	40.720
15.0	32.432	32.919	33.185	33.245	5.694	5.708	5.715	5.718	43.920	44.029	44.081	44.101
17.5	37.404	38.043	38.391	38.468	6.103	6.118	6.126	6.129	47.050	47.168	47.224	47.246

Table C.41: Scaled energy, mass, and proper separation for two equal sized holes, each with parallel linear momenta P/a_1 generated from an inversion symmetric extrinsic curvature obeying the isometry condition with a minus sign. The conformal separation is $\beta = 9$.

S/a_1^2	E/a_1 80	120	160	$\Re$	M/a_1 80	120	160	$\Re$	L/a_1 80	120	160	$\Re$
0.0	4.481	4.488	4.492	4.493	2.511	2.519	2.522	2.524	19.678	19.735	19.762	19.773
1.0	4.532	4.539	4.542	4.543	2.534	2.542	2.545	2.547	19.830	19.887	19.914	19.924
3.0	4.865	4.869	4.871	4.872	2.686	2.693	2.697	2.698	20.837	20.889	20.914	20.924
10.0	6.487	6.483	6.481	6.481	3.450	3.456	3.459	3.460	25.893	25.940	25.963	25.972
30.0	9.902	9.883	9.874	9.871	5.144	5.150	5.153	5.154	37.167	37.220	37.246	37.255
100.0	16.784	16.719	16.688	16.676	8.731	8.739	8.742	8.744	61.214	61.283	61.317	61.329
300.0	27.972	27.757	27.658	27.613	14.679	14.689	14.694	14.696	101.330	101.424	101.470	101.486
1000.0	50.630	49.659	49.266	49.011	26.406	26.421	26.429	26.432	180.753	180.887	180.953	180.977

Table C.42: Scaled energy, mass, and proper separation for two equal sized holes, each with parallel angular momenta S/a_1^2 generated from an inversion symmetric extrinsic curvature obeying the isometry condition with a minus sign. The conformal separation is $\beta = 9$.

P/a_1	E/a_1 80	120	160	$\Re$	M/a_1 80	120	160	$\Re$	L/a_1 80	120	160	$\Re$
0.0	4.426	4.433	4.436	4.438	2.450	2.457	2.461	2.462	20.960	21.017	21.045	21.056
1.0	4.668	4.673	4.675	4.676	2.531	2.538	2.542	2.543	21.662	21.717	21.743	21.754
2.5	5.536	5.537	5.536	5.537	2.824	2.831	2.834	2.835	24.188	24.237	24.261	24.270
5.0	7.140	7.132	7.128	7.127	3.365	3.372	3.375	3.376	28.843	28.889	28.912	28.920
7.5	8.590	8.575	8.567	8.565	3.854	3.861	3.864	3.865	33.047	33.093	33.116	33.124
10.0	9.886	9.864	9.853	9.850	4.291	4.298	4.301	4.302	36.803	36.850	36.873	36.882
12.5	11.062	11.034	11.019	11.015	4.688	4.695	4.698	4.699	40.211	40.259	40.283	40.291
15.0	12.145	12.110	12.092	12.087	5.053	5.060	5.063	5.064	43.346	43.396	43.420	43.429
17.5	13.152	13.111	13.090	13.084	5.392	5.399	5.403	5.404	46.263	46.313	46.338	46.347

Table C.43: Scaled energy, mass, and proper separation for two equal sized holes, each with anti-parallel linear momenta P/a_1 generated from an inversion symmetric extrinsic curvature obeying the isometry condition with a plus sign. The conformal separation is $\beta = 10$.

P/a_1	E/a_1 80	120	160	$\Re$	M/a_1 80	120	160	$\Re$	L/a_1 80	120	160	$\Re$
0.0	4.426	4.433	4.436	4.438	2.450	2.457	2.461	2.462	20.960	21.017	21.045	21.056
1.0	4.647	4.653	4.655	4.656	2.521	2.528	2.532	2.533	21.565	21.620	21.647	21.657
2.5	5.471	5.471	5.471	5.472	2.789	2.795	2.798	2.800	23.822	23.873	23.897	23.907
5.0	7.042	7.034	7.030	7.029	3.299	3.306	3.309	3.310	28.135	28.183	28.206	28.215
7.5	8.481	8.466	8.458	8.456	3.768	3.774	3.777	3.779	32.093	32.141	32.164	32.173
10.0	9.774	9.752	9.740	9.737	4.189	4.196	4.199	4.200	35.651	35.700	35.724	35.732
12.5	10.949	10.920	10.906	10.901	4.572	4.579	4.583	4.584	38.888	38.939	38.963	38.972
15.0	12.031	11.996	11.978	11.973	4.926	4.933	4.936	4.938	41.872	41.924	41.949	41.958
17.5	13.039	12.998	12.977	12.971	5.255	5.262	5.266	5.267	44.651	44.704	44.730	44.739

Table C.44: Scaled energy, mass, and proper separation for two equal sized holes, each with anti-parallel linear momenta P/a_1 generated from an inversion symmetric extrinsic curvature obeying the isometry condition with a minus sign. The conformal separation is $\beta = 10$.

S/a_1^2	E/a_1 80	120	160	$\Re$	M/a_1 80	120	160	$\Re$	L/a_1 80	120	160	$\Re$
0.0	4.426	4.433	4.436	4.438	2.450	2.457	2.461	2.462	20.960	21.017	21.045	21.056
1.0	4.479	4.485	4.488	4.490	2.473	2.481	2.484	2.486	21.126	21.182	21.210	21.220
3.0	4.819	4.824	4.826	4.826	2.629	2.635	2.639	2.640	22.210	22.263	22.288	22.298
10.0	6.422	6.419	6.417	6.417	3.392	3.397	3.400	3.401	27.544	27.592	27.616	27.624
30.0	9.621	9.608	9.601	9.599	5.061	5.066	5.069	5.070	39.247	39.302	39.328	39.338
100.0	15.496	15.460	15.442	15.436	8.568	8.575	8.579	8.580	63.917	63.990	64.026	64.039
300.0	23.791	23.713	23.674	23.661	14.353	14.363	14.368	14.369	104.680	104.783	104.833	104.851
1000.0	37.541	37.364	37.276	37.246	25.717	25.732	25.739	25.741	184.832	184.985	185.060	185.087

Table C.45: Scaled energy, mass, and proper separation for two equal sized holes, each with anti-parallel angular momenta S/a_1^2 generated from an inversion symmetric extrinsic curvature obeying the isometry condition with a minus sign. The conformal separation is $\beta = 10$.

P/a_1	E/a_1 80	120	160	$\Re$	M/a_1 80	120	160	$\Re$	L/a_1 80	120	160	$\Re$
0.0	4.426	4.433	4.436	4.438	2.450	2.457	2.461	2.462	20.960	21.017	21.045	21.056
1.0	5.053	5.061	5.065	5.067	2.565	2.573	2.576	2.578	21.918	21.976	22.003	22.014
2.5	7.385	7.404	7.413	7.416	2.955	2.963	2.967	2.968	25.155	25.214	25.243	25.254
5.0	12.257	12.313	12.343	12.351	3.636	3.644	3.649	3.650	30.826	30.894	30.927	30.939
7.5	17.378	17.494	17.556	17.571	4.237	4.247	4.252	4.254	35.852	35.930	35.968	35.982
10.0	22.537	22.730	22.834	22.859	4.771	4.782	4.787	4.789	40.318	40.405	40.447	40.463
12.5	27.684	27.969	28.123	28.158	5.253	5.265	5.271	5.273	44.359	44.455	44.502	44.519
15.0	32.800	33.191	33.404	33.451	5.696	5.709	5.715	5.718	48.071	48.176	48.227	48.246
17.5	37.878	38.389	38.669	38.729	6.107	6.122	6.128	6.131	51.522	51.636	51.690	51.711

Table C.46: Scaled energy, mass, and proper separation for two equal sized holes, each with parallel linear momenta P/a_1 generated from an inversion symmetric extrinsic curvature obeying the isometry condition with a plus sign. The conformal separation is $\beta = 10$.

P/a_1	E/a_1 80	120	160	$\Re$	M/a_1 80	120	160	$\Re$	L/a_1 80	120	160	$\Re$
0.0	4.426	4.433	4.436	4.438	2.450	2.457	2.461	2.462	20.960	21.017	21.045	21.056
1.0	5.033	5.041	5.045	5.047	2.556	2.563	2.567	2.568	21.824	21.882	21.910	21.921
2.5	7.332	7.351	7.360	7.363	2.922	2.930	2.934	2.936	24.827	24.888	24.918	24.929
5.0	12.190	12.247	12.277	12.285	3.577	3.586	3.590	3.592	30.214	30.285	30.319	30.332
7.5	17.312	17.428	17.490	17.506	4.161	4.171	4.176	4.178	35.036	35.117	35.156	35.171
10.0	22.474	22.667	22.771	22.796	4.680	4.691	4.696	4.699	39.336	39.426	39.470	39.487
12.5	27.624	27.909	28.064	28.099	5.150	5.162	5.168	5.171	43.234	43.334	43.382	43.401
15.0	32.742	33.134	33.348	33.394	5.582	5.595	5.602	5.604	46.819	46.929	46.981	47.002
17.5	37.823	38.334	38.615	38.675	5.983	5.998	6.005	6.008	50.154	50.273	50.330	50.352

Table C.47: Scaled energy, mass, and proper separation for two equal sized holes, each with parallel linear momenta P/a_1 generated from an inversion symmetric extrinsic curvature obeying the isometry condition with a minus sign. The conformal separation is $\beta = 10$.

S/a_1^2	E/a_1 80	120	160	$\Re$	M/a_1 80	120	160	$\Re$	L/a_1 80	120	160	$\Re$
0.0	4.426	4.433	4.436	4.438	2.450	2.457	2.461	2.462	20.960	21.017	21.045	21.056
1.0	4.480	4.487	4.490	4.491	2.474	2.481	2.484	2.486	21.127	21.184	21.211	21.222
3.0	4.831	4.835	4.837	4.838	2.630	2.637	2.640	2.642	22.223	22.276	22.302	22.312
10.0	6.502	6.499	6.497	6.496	3.400	3.406	3.408	3.409	27.616	27.664	27.688	27.697
30.0	9.971	9.954	9.945	9.942	5.086	5.092	5.095	5.096	39.507	39.562	39.589	39.599
100.0	16.909	16.848	16.818	16.807	8.646	8.653	8.657	8.658	64.804	64.877	64.913	64.926
300.0	28.115	27.917	27.824	27.784	14.543	14.552	14.557	14.559	106.996	107.095	107.144	107.162
1000.0	50.634	49.768	49.410	49.190	26.166	26.181	26.187	26.190	190.554	190.697	190.767	190.792

Table C.48: Scaled energy, mass, and proper separation for two equal sized holes, each with parallel angular momenta S/a_1^2 generated from an inversion symmetric extrinsic curvature obeying the isometry condition with a minus sign. The conformal separation is $\beta = 10$.

P/a_1	E/a_1 80	120	160	$\Re$	M/a_1 80	120	160	$\Re$	L/a_1 80	120	160	$\Re$
0.0	4.382	4.389	4.392	4.394	2.401	2.409	2.412	2.413	22.221	22.279	22.307	22.318
1.0	4.646	4.651	4.654	4.655	2.487	2.494	2.497	2.498	23.006	23.061	23.088	23.098
2.5	5.582	5.582	5.581	5.581	2.789	2.796	2.798	2.800	25.784	25.834	25.858	25.867
5.0	7.285	7.276	7.272	7.271	3.339	3.345	3.348	3.349	30.833	30.881	30.904	30.912
7.5	8.815	8.799	8.791	8.789	3.832	3.838	3.841	3.842	35.367	35.415	35.438	35.447
10.0	10.181	10.158	10.146	10.142	4.271	4.278	4.281	4.282	39.411	39.459	39.483	39.492
12.5	11.419	11.389	11.373	11.369	4.670	4.677	4.680	4.681	43.075	43.125	43.150	43.159
15.0	12.558	12.521	12.502	12.496	5.036	5.043	5.046	5.048	46.445	46.496	46.521	46.531
17.5	13.617	13.574	13.551	13.545	5.377	5.384	5.388	5.389	49.579	49.632	49.657	49.667

Table C.49: Scaled energy, mass, and proper separation for two equal sized holes, each with anti-parallel linear momenta P/a_1 generated from an inversion symmetric extrinsic curvature obeying the isometry condition with a plus sign. The conformal separation is $\beta = 11$.

P/a_1	E/a_1 80	120	160	$\Re$	M/a_1 80	120	160	$\Re$	L/a_1 80	120	160	$\Re$
0.0	4.382	4.389	4.392	4.394	2.401	2.409	2.412	2.413	22.221	22.279	22.307	22.318
1.0	4.625	4.630	4.632	4.633	2.477	2.484	2.487	2.488	22.900	22.956	22.983	22.993
2.5	5.514	5.514	5.514	5.514	2.753	2.759	2.762	2.764	25.394	25.445	25.470	25.480
5.0	7.186	7.177	7.173	7.171	3.272	3.278	3.281	3.283	30.089	30.138	30.161	30.170
7.5	8.706	8.690	8.682	8.680	3.745	3.752	3.755	3.756	34.369	34.418	34.442	34.451
10.0	10.069	10.045	10.033	10.030	4.169	4.176	4.179	4.180	38.208	38.258	38.283	38.292
12.5	11.306	11.276	11.260	11.256	4.555	4.561	4.565	4.566	41.696	41.749	41.774	41.783
15.0	12.445	12.408	12.389	12.383	4.909	4.916	4.920	4.921	44.910	44.963	44.989	44.999
17.5	13.505	13.461	13.439	13.432	5.240	5.247	5.250	5.252	47.901	47.956	47.983	47.993

Table C.50: Scaled energy, mass, and proper separation for two equal sized holes, each with anti-parallel linear momenta P/a_1 generated from an inversion symmetric extrinsic curvature obeying the isometry condition with a minus sign. The conformal separation is $\beta = 11$.

S/a_1^2	E/a_1 80	120	160	$\Re$	M/a_1 80	120	160	$\Re$	L/a_1 80	120	160	$\Re$
0.0	4.382	4.389	4.392	4.394	2.401	2.409	2.412	2.413	22.221	22.279	22.307	22.318
1.0	4.438	4.445	4.447	4.449	2.426	2.433	2.436	2.438	22.402	22.459	22.486	22.497
3.0	4.796	4.800	4.802	4.803	2.585	2.592	2.595	2.596	23.569	23.623	23.648	23.658
10.0	6.451	6.448	6.447	6.446	3.354	3.360	3.362	3.363	29.214	29.264	29.288	29.297
30.0	9.733	9.720	9.713	9.711	5.021	5.027	5.029	5.030	41.498	41.554	41.582	41.592
100.0	15.764	15.728	15.710	15.704	8.518	8.525	8.528	8.529	67.351	67.428	67.466	67.480
300.0	24.296	24.217	24.178	24.164	14.282	14.291	14.296	14.298	110.073	110.181	110.234	110.253
1000.0	38.455	38.277	38.188	38.157	25.605	25.619	25.625	25.628	194.088	194.250	194.329	194.358

Table C.51: Scaled energy, mass, and proper separation for two equal sized holes, each with anti-parallel angular momenta S/a_1^2 generated from an inversion symmetric extrinsic curvature obeying the isometry condition with a minus sign. The conformal separation is $\beta = 11$.

P/a_1	E/a_1 80	120	160	$\Re$	M/a_1 80	120	160	$\Re$	L/a_1 80	120	160	$\Re$
0.0	4.382	4.389	4.392	4.394	2.401	2.409	2.412	2.413	22.221	22.279	22.307	22.318
1.0	5.017	5.024	5.028	5.029	2.517	2.524	2.527	2.529	23.245	23.303	23.331	23.342
2.5	7.368	7.384	7.392	7.394	2.904	2.911	2.915	2.916	26.685	26.745	26.774	26.785
5.0	12.272	12.319	12.343	12.350	3.577	3.585	3.589	3.591	32.694	32.763	32.796	32.809
7.5	17.434	17.529	17.580	17.592	4.170	4.180	4.184	4.186	38.016	38.095	38.133	38.147
10.0	22.645	22.802	22.887	22.906	4.696	4.707	4.712	4.714	42.743	42.832	42.874	42.891
12.5	27.855	28.085	28.211	28.239	5.172	5.183	5.189	5.191	47.022	47.119	47.166	47.184
15.0	33.045	33.360	33.534	33.570	5.608	5.621	5.627	5.629	50.952	51.059	51.110	51.129
17.5	38.209	38.618	38.845	38.892	6.014	6.027	6.034	6.036	54.606	54.721	54.776	54.798

Table C.52: Scaled energy, mass, and proper separation for two equal sized holes, each with parallel linear momenta P/a_1 generated from an inversion symmetric extrinsic curvature obeying the isometry condition with a plus sign. The conformal separation is $\beta = 11$.

P/a_1	E/a_1 80	120	160	$\Re$	M/a_1 80	120	160	$\Re$	L/a_1 80	120	160	$\Re$
0.0	4.382	4.389	4.392	4.394	2.401	2.409	2.412	2.413	22.221	22.279	22.307	22.318
1.0	4.995	5.003	5.007	5.008	2.507	2.514	2.517	2.519	23.143	23.201	23.229	23.240
2.5	7.312	7.328	7.336	7.339	2.871	2.878	2.882	2.883	26.331	26.393	26.423	26.434
5.0	12.202	12.249	12.274	12.281	3.517	3.525	3.529	3.531	32.037	32.109	32.143	32.156
7.5	17.365	17.460	17.511	17.524	4.092	4.102	4.107	4.108	37.142	37.224	37.263	37.278
10.0	22.579	22.736	22.822	22.841	4.604	4.615	4.620	4.622	41.693	41.785	41.829	41.847
12.5	27.792	28.023	28.149	28.176	5.067	5.079	5.084	5.087	45.820	45.921	45.970	45.989
15.0	32.986	33.301	33.474	33.511	5.492	5.505	5.511	5.514	49.615	49.726	49.780	49.800
17.5	38.152	38.562	38.789	38.835	5.888	5.902	5.908	5.911	53.147	53.266	53.324	53.346

Table C.53: Scaled energy, mass, and proper separation for two equal sized holes, each with parallel linear momenta P/a_1 generated from an inversion symmetric extrinsic curvature obeying the isometry condition with a minus sign. The conformal separation is $\beta = 11$.

S/a_1^2	E/a_1 80	120	160	$\Re$	M/a_1 80	120	160	$\Re$	L/a_1 80	120	160	$\Re$
0.0	4.382	4.389	4.392	4.394	2.401	2.409	2.412	2.413	22.221	22.279	22.307	22.318
1.0	4.440	4.446	4.449	4.450	2.426	2.433	2.436	2.438	22.403	22.460	22.488	22.499
3.0	4.806	4.810	4.812	4.812	2.587	2.593	2.596	2.597	23.580	23.633	23.659	23.669
10.0	6.519	6.516	6.514	6.513	3.360	3.366	3.368	3.369	29.273	29.323	29.347	29.356
30.0	10.038	10.021	10.012	10.009	5.041	5.047	5.049	5.050	41.720	41.777	41.805	41.815
100.0	17.030	16.972	16.943	16.933	8.580	8.587	8.590	8.591	68.145	68.222	68.260	68.273
300.0	28.261	28.076	27.989	27.952	14.437	14.447	14.451	14.453	112.213	112.319	112.371	112.389
1000.0	50.677	49.894	49.565	49.372	25.980	25.994	26.000	26.003	199.515	199.667	199.741	199.768

Table C.54: Scaled energy, mass, and proper separation for two equal sized holes, each with parallel angular momenta S/a_1^2 generated from an inversion symmetric extrinsic curvature obeying the isometry condition with a minus sign. The conformal separation is $\beta = 11$.

P/a_1	E/a_1 80	120	160	$\Re$	M/a_1 80	120	160	$\Re$	L/a_1 80	120	160	$\Re$
0.0	4.347	4.353	4.356	4.358	2.362	2.369	2.372	2.374	23.466	23.524	23.552	23.564
1.0	4.631	4.636	4.638	4.639	2.451	2.458	2.461	2.462	24.327	24.383	24.410	24.420
2.5	5.628	5.627	5.626	5.626	2.761	2.767	2.770	2.771	27.339	27.390	27.414	27.424
5.0	7.422	7.413	7.408	7.407	3.317	3.323	3.326	3.327	32.757	32.806	32.829	32.838
7.5	9.028	9.011	9.003	9.000	3.814	3.820	3.823	3.824	37.602	37.651	37.675	37.684
10.0	10.459	10.435	10.422	10.418	4.256	4.262	4.265	4.266	41.916	41.967	41.991	42.000
12.5	11.755	11.724	11.707	11.703	4.656	4.662	4.665	4.667	45.824	45.876	45.901	45.910
15.0	12.947	12.909	12.889	12.883	5.024	5.030	5.033	5.035	49.416	49.469	49.495	49.505
17.5	14.056	14.010	13.987	13.980	5.365	5.372	5.376	5.377	52.755	52.810	52.837	52.847

Table C.55: Scaled energy, mass, and proper separation for two equal sized holes, each with anti-parallel linear momenta P/a_1 generated from an inversion symmetric extrinsic curvature obeying the isometry condition with a plus sign. The conformal separation is $\beta = 12$.

P/a_1	E/a_1 80	120	160	$\Re$	M/a_1 80	120	160	$\Re$	L/a_1 80	120	160	$\Re$
0.0	4.347	4.353	4.356	4.358	2.362	2.369	2.372	2.374	23.466	23.524	23.552	23.564
1.0	4.609	4.613	4.616	4.617	2.441	2.447	2.450	2.452	24.213	24.270	24.297	24.308
2.5	5.558	5.558	5.557	5.557	2.724	2.730	2.733	2.734	26.929	26.981	27.006	27.016
5.0	7.322	7.313	7.308	7.307	3.251	3.257	3.259	3.261	31.982	32.032	32.056	32.065
7.5	8.919	8.902	8.893	8.891	3.727	3.733	3.736	3.738	36.566	36.617	36.642	36.651
10.0	10.347	10.322	10.310	10.306	4.154	4.160	4.163	4.164	40.670	40.723	40.748	40.758
12.5	11.642	11.611	11.595	11.590	4.541	4.547	4.550	4.552	44.398	44.452	44.478	44.488
15.0	12.835	12.796	12.776	12.770	4.897	4.904	4.907	4.908	47.829	47.885	47.912	47.922
17.5	13.944	13.898	13.875	13.868	5.228	5.235	5.238	5.240	51.022	51.080	51.108	51.118

Table C.56: Scaled energy, mass, and proper separation for two equal sized holes, each with anti-parallel linear momenta P/a_1 generated from an inversion symmetric extrinsic curvature obeying the isometry condition with a minus sign. The conformal separation is $\beta = 12$.

S/a_1^2	E/a_1 80	120	160	$\Re$	M/a_1 80	120	160	$\Re$	L/a_1 80	120	160	$\Re$
0.0	4.347	4.353	4.356	4.358	2.362	2.369	2.372	2.374	23.466	23.524	23.552	23.564
1.0	4.405	4.411	4.414	4.415	2.388	2.394	2.397	2.399	23.659	23.717	23.744	23.756
3.0	4.778	4.782	4.783	4.784	2.550	2.556	2.559	2.560	24.902	24.956	24.982	24.992
10.0	6.479	6.476	6.474	6.474	3.324	3.329	3.331	3.332	30.827	30.878	30.902	30.911
30.0	9.834	9.820	9.813	9.811	4.989	4.995	4.997	4.998	43.634	43.693	43.722	43.732
100.0	16.006	15.970	15.952	15.946	8.477	8.483	8.486	8.488	70.564	70.645	70.684	70.698
300.0	24.756	24.676	24.636	24.623	14.225	14.233	14.238	14.239	115.070	115.184	115.240	115.260
1000.0	39.297	39.117	39.027	38.996	25.515	25.528	25.534	25.537	202.611	202.782	202.866	202.896

Table C.57: Scaled energy, mass, and proper separation for two equal sized holes, each with anti-parallel angular momenta S/a_1^2 generated from an inversion symmetric extrinsic curvature obeying the isometry condition with a minus sign. The conformal separation is $\beta = 12$.

P/a_1	E/a_1 80	120	160	$\Re$	M/a_1 80	120	160	$\Re$	L/a_1 80	120	160	$\Re$
0.0	4.347	4.353	4.356	4.358	2.362	2.369	2.372	2.374	23.466	23.524	23.552	23.564
1.0	4.987	4.994	4.998	4.999	2.478	2.485	2.488	2.489	24.550	24.609	24.636	24.648
2.5	7.354	7.367	7.374	7.376	2.863	2.870	2.873	2.874	28.180	28.241	28.270	28.282
5.0	12.284	12.323	12.343	12.349	3.529	3.537	3.540	3.542	34.508	34.578	34.612	34.625
7.5	17.479	17.557	17.599	17.609	4.116	4.125	4.129	4.131	40.110	40.190	40.229	40.244
10.0	22.731	22.859	22.929	22.945	4.636	4.646	4.650	4.652	45.088	45.177	45.220	45.237
12.5	27.991	28.178	28.282	28.303	5.106	5.117	5.122	5.124	49.592	49.691	49.738	49.757
15.0	33.241	33.495	33.636	33.664	5.537	5.549	5.554	5.557	53.731	53.839	53.890	53.910
17.5	38.473	38.802	38.986	39.021	5.938	5.950	5.956	5.959	57.579	57.695	57.751	57.773

Table C.58: Scaled energy, mass, and proper separation for two equal sized holes, each with parallel linear momenta P/a_1 generated from an inversion symmetric extrinsic curvature obeying the isometry condition with a plus sign. The conformal separation is $\beta = 12$.

P/a_1	E/a_1 80	120	160	$\Re$	M/a_1 80	120	160	$\Re$	L/a_1 80	120	160	$\Re$
0.0	4.347	4.353	4.356	4.358	2.362	2.369	2.372	2.374	23.466	23.524	23.552	23.564
1.0	4.965	4.972	4.975	4.977	2.468	2.474	2.478	2.479	24.440	24.499	24.527	24.539
2.5	7.295	7.309	7.316	7.319	2.828	2.836	2.839	2.840	27.804	27.866	27.896	27.908
5.0	12.211	12.251	12.272	12.277	3.468	3.476	3.480	3.482	33.813	33.885	33.920	33.933
7.5	17.407	17.486	17.528	17.538	4.037	4.046	4.050	4.052	39.187	39.270	39.310	39.325
10.0	22.663	22.791	22.862	22.877	4.542	4.553	4.557	4.559	43.979	44.072	44.117	44.134
12.5	27.926	28.114	28.217	28.238	5.000	5.011	5.016	5.018	48.324	48.427	48.476	48.496
15.0	33.179	33.434	33.575	33.603	5.420	5.432	5.438	5.440	52.321	52.434	52.487	52.508
17.5	38.415	38.743	38.927	38.962	5.810	5.824	5.830	5.832	56.040	56.162	56.220	56.242

Table C.59: Scaled energy, mass, and proper separation for two equal sized holes, each with parallel linear momenta P/a_1 generated from an inversion symmetric extrinsic curvature obeying the isometry condition with a minus sign. The conformal separation is $\beta = 12$.

S/a_1^2	E/a_1 80	120	160	$\Re$	M/a_1 80	120	160	$\Re$	L/a_1 80	120	160	$\Re$
0.0	4.347	4.353	4.356	4.358	2.362	2.369	2.372	2.374	23.466	23.524	23.552	23.564
1.0	4.406	4.412	4.415	4.416	2.388	2.395	2.398	2.399	23.660	23.718	23.746	23.757
3.0	4.786	4.790	4.791	4.792	2.551	2.557	2.560	2.561	24.910	24.964	24.990	25.000
10.0	6.537	6.533	6.531	6.530	3.329	3.334	3.336	3.337	30.876	30.926	30.951	30.960
30.0	10.100	10.083	10.075	10.072	5.005	5.010	5.013	5.014	43.826	43.885	43.914	43.924
100.0	17.146	17.091	17.063	17.053	8.527	8.534	8.537	8.538	71.279	71.359	71.399	71.413
300.0	28.407	28.233	28.151	28.117	14.353	14.362	14.367	14.368	117.058	117.169	117.223	117.243
1000.0	50.748	50.032	49.727	49.556	25.833	25.846	25.852	25.855	207.777	207.938	208.016	208.045

Table C.60: Scaled energy, mass, and proper separation for two equal sized holes, each with parallel angular momenta S/a_1^2 generated from an inversion symmetric extrinsic curvature obeying the isometry condition with a minus sign. The conformal separation is $\beta = 12$.

Appendix D: Numerical Solutions of the Two-Hole Hamiltonian Constraint in Čadež Coordinates

This appendix contains the most important details from the numerical solution of the two-hole Hamiltonian constraint described in Chapter 10. The difference equations for this approach were solved by Newton's method for systems of equations and each linearized equation for the iterative correction was solved directly by means of the LINPACK routines for factoring (DGBFA) and solving (DGBSL) general banded matrices. The solution for each configuration (except as noted) was obtained at three different mesh resolutions. The resolution of the mesh is parameterized by $\mathcal{I}^+$ as defined in (10.28). When computational memory requirements allowed, meshes defined by $\mathcal{I}^+ = \mathcal{I}^- = 6, 9, 12$ were used. The values of the angular discretization for these three meshes were, respectively, $\mathcal{S}^+ = \mathcal{S}^- = 16, 24, 32$. It was not always possible to use all three meshes because the number of mesh points in Region 3 (see Chapter 10) depends on the value of β. For $\beta < 6$ it was not feasable to use $\mathcal{I}^+ = 12$. For $\beta = 3$ it was not feasable to use $\mathcal{I}^+ = 9$ either. This is indicated in the tables by the notation N/A.

The 60 tables which follow can be considered as ten groups of six tables. Each group of six tables corresponds to the six cases described in Chapter 14. The ten groups of six tables represent ten values of the separation parameter $\beta = 3 \rightarrow 12$. Finally, each table lists results from the numerical computations for the scaled total energy E/a_1, the scaled minimal surface mass M/a_1, and the scaled proper separation L/a_1 as the linear or angular momentum parameter is varied.

The 60 tables presented below correspond directly to configurations for each of the tables in Appendix C. These can be directly compared to judge the accuracy of solutions found using Čadež coordinates. Note that for $\beta = 8$, all values for $\mathcal{I}^+ = 6$ are unreasonable. This occurs because the matrix used to construct the differencing scheme for the singular point (see (10.53)) is numerically ill-conditioned for this configuration. The difficulty can be eliminated by choosing a different radial discretization.

	E/a_1			M/a_1			L/a_1		
P/a_1	6	9	12	6	9	12	6	9	12
0.0	5.391	N/A	N/A	3.880	N/A	N/A	7.933	N/A	N/A
1.0	5.428	N/A	N/A	3.904	N/A	N/A	7.985	N/A	N/A
2.5	5.604	N/A	N/A	4.014	N/A	N/A	8.233	N/A	N/A
5.0	6.083	N/A	N/A	4.313	N/A	N/A	8.903	N/A	N/A
7.5	6.636	N/A	N/A	4.658	N/A	N/A	9.673	N/A	N/A
10.0	7.188	N/A	N/A	5.004	N/A	N/A	10.441	N/A	N/A
12.5	7.719	N/A	N/A	5.336	N/A	N/A	11.179	N/A	N/A
15.0	8.225	N/A	N/A	5.653	N/A	N/A	11.881	N/A	N/A
17.5	8.707	N/A	N/A	5.955	N/A	N/A	12.548	N/A	N/A

Table D.1: Scaled energy, mass, and proper separation for two equal sized holes, each with anti-parallel linear momenta P/a_1 generated from an inversion-symmetric extrinsic curvature obeying the isometry condition with a plus sign. The conformal separation is $\beta = 3$.

	E/a_1			M/a_1			L/a_1		
P/a_1	6	9	12	6	9	12	6	9	12
0.0	5.391	N/A	N/A	3.880	N/A	N/A	7.933	N/A	N/A
1.0	5.423	N/A	N/A	3.900	N/A	N/A	7.975	N/A	N/A
2.5	5.580	N/A	N/A	3.995	N/A	N/A	8.174	N/A	N/A
5.0	6.022	N/A	N/A	4.262	N/A	N/A	8.736	N/A	N/A
7.5	6.549	N/A	N/A	4.580	N/A	N/A	9.406	N/A	N/A
10.0	7.086	N/A	N/A	4.906	N/A	N/A	10.089	N/A	N/A
12.5	7.608	N/A	N/A	5.223	N/A	N/A	10.754	N/A	N/A
15.0	8.108	N/A	N/A	5.527	N/A	N/A	11.392	N/A	N/A
17.5	8.586	N/A	N/A	5.818	N/A	N/A	12.001	N/A	N/A

Table D.2: Scaled energy, mass, and proper separation for two equal sized holes, each with anti-parallel linear momenta P/a_1 generated from an inversion-symmetric extrinsic curvature obeying the isometry condition with a minus sign. The conformal separation is $\beta = 3$.

	E/a_1			M/a_1			L/a_1		
S/a_1^2	6	9	12	6	9	12	6	9	12
0.0	5.391	N/A	N/A	3.880	N/A	N/A	7.933	N/A	N/A
1.0	5.403	N/A	N/A	3.890	N/A	N/A	7.952	N/A	N/A
3.0	5.498	N/A	N/A	3.961	N/A	N/A	8.097	N/A	N/A
10.0	6.186	N/A	N/A	4.493	N/A	N/A	9.178	N/A	N/A
30.0	8.106	N/A	N/A	6.095	N/A	N/A	12.431	N/A	N/A
100.0	11.981	N/A	N/A	9.807	N/A	N/A	19.963	N/A	N/A
300.0	17.509	N/A	N/A	16.057	N/A	N/A	32.645	N/A	N/A
1000.0	26.599	N/A	N/A	28.393	N/A	N/A	57.668	N/A	N/A

Table D.3: Scaled energy, mass, and proper separation for two equal sized holes, each with anti-parallel angular momenta S/a_1^2 generated from an inversion-symmetric extrinsic curvature obeying the isometry condition with a minus sign. The conformal separation is $\beta = 3$.

P/a_1	E/a_1 6	9	12	M/a_1 6	9	12	L/a_1 6	9	12
0.0	5.391	N/A	N/A	3.880	N/A	N/A	7.933	N/A	N/A
1.0	5.917	N/A	N/A	4.005	N/A	N/A	8.188	N/A	N/A
2.5	8.048	N/A	N/A	4.472	N/A	N/A	9.140	N/A	N/A
5.0	12.849	N/A	N/A	5.367	N/A	N/A	10.966	N/A	N/A
7.5	18.083	N/A	N/A	6.191	N/A	N/A	12.646	N/A	N/A
10.0	23.436	N/A	N/A	6.933	N/A	N/A	14.159	N/A	N/A
12.5	28.801	N/A	N/A	7.608	N/A	N/A	15.536	N/A	N/A
15.0	34.114	N/A	N/A	8.230	N/A	N/A	16.807	N/A	N/A
17.5	39.327	N/A	N/A	8.810	N/A	N/A	17.990	N/A	N/A

Table D.4: Scaled energy, mass, and proper separation for two equal sized holes, each with parallel linear momenta P/a_1 generated from an inversion-symmetric extrinsic curvature obeying the isometry condition with a plus sign. The conformal separation is $\beta = 3$.

P/a_1	E/a_1 6	9	12	M/a_1 6	9	12	L/a_1 6	9	12
0.0	5.391	N/A	N/A	3.880	N/A	N/A	7.933	N/A	N/A
1.0	5.910	N/A	N/A	4.000	N/A	N/A	8.177	N/A	N/A
2.5	8.025	N/A	N/A	4.454	N/A	N/A	9.100	N/A	N/A
5.0	12.818	N/A	N/A	5.331	N/A	N/A	10.887	N/A	N/A
7.5	18.051	N/A	N/A	6.142	N/A	N/A	12.539	N/A	N/A
10.0	23.405	N/A	N/A	6.873	N/A	N/A	14.029	N/A	N/A
12.5	28.772	N/A	N/A	7.540	N/A	N/A	15.388	N/A	N/A
15.0	34.087	N/A	N/A	8.155	N/A	N/A	16.641	N/A	N/A
17.5	39.301	N/A	N/A	8.728	N/A	N/A	17.809	N/A	N/A

Table D.5: Scaled energy, mass, and proper separation for two equal sized holes, each with parallel linear momenta P/a_1 generated from an inversion-symmetric extrinsic curvature obeying the isometry condition with a minus sign. The conformal separation is $\beta = 3$.

S/a_1^2	E/a_1 6	9	12	M/a_1 6	9	12	L/a_1 6	9	12
0.0	5.391	N/A	N/A	3.880	N/A	N/A	7.933	N/A	N/A
1.0	5.411	N/A	N/A	3.894	N/A	N/A	7.960	N/A	N/A
3.0	5.560	N/A	N/A	3.990	N/A	N/A	8.157	N/A	N/A
10.0	6.590	N/A	N/A	4.662	N/A	N/A	9.524	N/A	N/A
30.0	9.423	N/A	N/A	6.545	N/A	N/A	13.357	N/A	N/A
100.0	15.746	N/A	N/A	10.826	N/A	N/A	22.079	N/A	N/A
300.0	26.281	N/A	N/A	18.047	N/A	N/A	36.797	N/A	N/A
1000.0	46.890	N/A	N/A	32.346	N/A	N/A	65.947	N/A	N/A

Table D.6: Scaled energy, mass, and proper separation for two equal sized holes, each with parallel angular momenta S/a_1^2 generated from an inversion-symmetric extrinsic curvature obeying the isometry condition with a minus sign. The conformal separation is $\beta = 3$.

	E/a_1			M/a_1			L/a_1		
P/a_1	6	9	12	6	9	12	6	9	12
0.0	5.189	5.270	N/A	3.440	3.512	N/A	11.827	12.241	N/A
1.0	5.251	5.331	N/A	3.474	3.545	N/A	11.953	12.363	N/A
2.5	5.533	5.605	N/A	3.628	3.695	N/A	12.522	12.917	N/A
5.0	6.222	6.283	N/A	4.005	4.068	N/A	13.911	14.289	N/A
7.5	6.954	7.010	N/A	4.405	4.467	N/A	15.382	15.755	N/A
10.0	7.654	7.707	N/A	4.789	4.850	N/A	16.787	17.163	N/A
12.5	8.311	8.364	N/A	5.149	5.212	N/A	18.105	18.487	N/A
15.0	8.928	8.980	N/A	5.488	5.552	N/A	19.341	19.732	N/A
17.5	9.509	9.562	N/A	5.807	5.873	N/A	20.506	20.906	N/A

Table D.7: Scaled energy, mass, and proper separation for two equal sized holes, each with anti-parallel linear momenta P/a_1 generated from an inversion-symmetric extrinsic curvature obeying the isometry condition with a plus sign. The conformal separation is $\beta = 4$.

	E/a_1			M/a_1			L/a_1		
P/a_1	6	9	12	6	9	12	6	9	12
0.0	5.189	5.270	N/A	3.440	3.512	N/A	11.827	12.241	N/A
1.0	5.245	5.324	N/A	3.469	3.541	N/A	11.931	12.344	N/A
2.5	5.502	5.574	N/A	3.605	3.674	N/A	12.412	12.818	N/A
5.0	6.155	6.216	N/A	3.949	4.015	N/A	13.635	14.037	N/A
7.5	6.867	6.921	N/A	4.326	4.391	N/A	14.968	15.378	N/A
10.0	7.557	7.607	N/A	4.693	4.757	N/A	16.262	16.684	N/A
12.5	8.210	8.257	N/A	5.039	5.105	N/A	17.485	17.922	N/A
15.0	8.824	8.870	N/A	5.366	5.434	N/A	18.638	19.091	N/A
17.5	9.404	9.449	N/A	5.676	5.745	N/A	19.728	20.197	N/A

Table D.8: Scaled energy, mass, and proper separation for two equal sized holes, each with anti-parallel linear momenta P/a_1 generated from an inversion-symmetric extrinsic curvature obeying the isometry condition with a minus sign. The conformal separation is $\beta = 4$.

	E/a_1			M/a_1			L/a_1		
S/a_1^2	6	9	12	6	9	12	6	9	12
0.0	5.189	5.270	N/A	3.440	3.512	N/A	11.827	12.241	N/A
1.0	5.208	5.289	N/A	3.452	3.525	N/A	11.869	12.283	N/A
3.0	5.348	5.424	N/A	3.544	3.614	N/A	12.175	12.587	N/A
10.0	6.253	6.312	N/A	4.159	4.224	N/A	14.224	14.652	N/A
30.0	8.493	8.537	N/A	5.817	5.888	N/A	19.746	20.285	N/A
100.0	12.819	12.857	N/A	9.513	9.612	N/A	32.054	32.889	N/A
300.0	18.927	18.963	N/A	15.684	15.836	N/A	52.604	53.952	N/A
1000.0	28.949	28.984	N/A	27.838	28.098	N/A	93.077	95.446	N/A

Table D.9: Scaled energy, mass, and proper separation for two equal sized holes, each with anti-parallel angular momenta S/a_1^2 generated from an inversion-symmetric extrinsic curvature obeying the isometry condition with a minus sign. The conformal separation is $\beta = 4$.

P/a_1	E/a_1 6	9	12	M/a_1 6	9	12	L/a_1 6	9	12
0.0	5.189	5.270	N/A	3.440	3.512	N/A	11.827	12.241	N/A
1.0	5.736	5.811	N/A	3.560	3.632	N/A	12.239	12.657	N/A
2.5	7.918	7.980	N/A	4.000	4.072	N/A	13.748	14.188	N/A
5.0	12.767	12.821	N/A	4.826	4.905	N/A	16.585	17.085	N/A
7.5	18.025	18.079	N/A	5.580	5.667	N/A	19.171	19.735	N/A
10.0	23.394	23.452	N/A	6.255	6.351	N/A	21.492	22.115	N/A
12.5	28.770	28.833	N/A	6.870	6.973	N/A	23.602	24.280	N/A
15.0	34.092	34.161	N/A	7.436	7.547	N/A	25.545	26.274	N/A
17.5	39.313	39.388	N/A	7.963	8.080	N/A	27.354	28.132	N/A

Table D.10: Scaled energy, mass, and proper separation for two equal sized holes, each with parallel linear momenta P/a_1 generated from an inversion-symmetric extrinsic curvature obeying the isometry condition with a plus sign. The conformal separation is $\beta = 4$.

P/a_1	E/a_1 6	9	12	M/a_1 6	9	12	L/a_1 6	9	12
0.0	5.189	5.270	N/A	3.440	3.512	N/A	11.827	12.241	N/A
1.0	5.727	5.802	N/A	3.554	3.626	N/A	12.217	12.635	N/A
2.5	7.891	7.953	N/A	3.978	4.051	N/A	13.665	14.106	N/A
5.0	12.731	12.785	N/A	4.785	4.865	N/A	16.420	16.924	N/A
7.5	17.989	18.043	N/A	5.524	5.613	N/A	18.948	19.515	N/A
10.0	23.359	23.417	N/A	6.189	6.286	N/A	21.221	21.848	N/A
12.5	28.738	28.800	N/A	6.794	6.898	N/A	23.290	23.973	N/A
15.0	34.062	34.129	N/A	7.352	7.463	N/A	25.197	25.932	N/A
17.5	39.284	39.358	N/A	7.871	7.989	N/A	26.973	27.757	N/A

Table D.11: Scaled energy, mass, and proper separation for two equal sized holes, each with parallel linear momenta P/a_1 generated from an inversion-symmetric extrinsic curvature obeying the isometry condition with a minus sign. The conformal separation is $\beta = 4$.

S/a_1^2	E/a_1 6	9	12	M/a_1 6	9	12	L/a_1 6	9	12
0.0	5.189	5.270	N/A	3.440	3.512	N/A	11.827	12.241	N/A
1.0	5.214	5.295	N/A	3.455	3.527	N/A	11.876	12.290	N/A
3.0	5.396	5.471	N/A	3.562	3.632	N/A	12.235	12.647	N/A
10.0	6.551	6.607	N/A	4.253	4.319	N/A	14.546	14.983	N/A
30.0	9.505	9.546	N/A	6.066	6.141	N/A	20.623	21.189	N/A
100.0	15.908	15.941	N/A	10.101	10.212	N/A	34.179	35.080	N/A
300.0	26.483	26.512	N/A	16.873	17.049	N/A	56.965	58.447	N/A
1000.0	47.114	47.143	N/A	30.269	30.577	N/A	102.072	104.712	N/A

Table D.12: Scaled energy, mass, and proper separation for two equal sized holes, each with parallel angular momenta S/a_1^2 generated from an inversion-symmetric extrinsic curvature obeying the isometry condition with a minus sign. The conformal separation is $\beta = 4$.

P/a_1	E/a_1 6	9	12	M/a_1 6	9	12	L/a_1 6	9	12
0.0	4.948	4.972	N/A	3.097	3.109	N/A	14.133	14.175	N/A
1.0	5.041	5.065	N/A	3.142	3.154	N/A	14.354	14.393	N/A
2.5	5.437	5.461	N/A	3.335	3.346	N/A	15.295	15.322	N/A
5.0	6.324	6.350	N/A	3.767	3.778	N/A	17.397	17.405	N/A
7.5	7.211	7.240	N/A	4.200	4.211	N/A	19.493	19.488	N/A
10.0	8.036	8.068	N/A	4.603	4.615	N/A	21.441	21.425	N/A
12.5	8.800	8.835	N/A	4.977	4.989	N/A	23.243	23.218	N/A
15.0	9.511	9.548	N/A	5.326	5.338	N/A	24.920	24.887	N/A
17.5	10.177	10.217	N/A	5.652	5.665	N/A	26.491	26.451	N/A

Table D.13: Scaled energy, mass, and proper separation for two equal sized holes, each with anti-parallel linear momenta P/a_1 generated from an inversion-symmetric extrinsic curvature obeying the isometry condition with a plus sign. The conformal separation is $\beta = 5$.

P/a_1	E/a_1 6	9	12	M/a_1 6	9	12	L/a_1 6	9	12
0.0	4.948	4.972	N/A	3.097	3.109	N/A	14.133	14.175	N/A
1.0	5.031	5.056	N/A	3.136	3.148	N/A	14.317	14.358	N/A
2.5	5.397	5.421	N/A	3.307	3.319	N/A	15.122	15.159	N/A
5.0	6.248	6.273	N/A	3.707	3.719	N/A	16.998	17.027	N/A
7.5	7.119	7.145	N/A	4.117	4.129	N/A	18.920	18.944	N/A
10.0	7.938	7.965	N/A	4.504	4.517	N/A	20.727	20.747	N/A
12.5	8.699	8.728	N/A	4.864	4.877	N/A	22.410	22.427	N/A
15.0	9.409	9.439	N/A	5.200	5.215	N/A	23.980	23.996	N/A
17.5	10.075	10.107	N/A	5.517	5.532	N/A	25.456	25.469	N/A

Table D.14: Scaled energy, mass, and proper separation for two equal sized holes, each with anti-parallel linear momenta P/a_1 generated from an inversion-symmetric extrinsic curvature obeying the isometry condition with a minus sign. The conformal separation is $\beta = 5$.

S/a_1^2	E/a_1 6	9	12	M/a_1 6	9	12	L/a_1 6	9	12
0.0	4.948	4.972	N/A	3.097	3.109	N/A	14.133	14.175	N/A
1.0	4.974	4.998	N/A	3.112	3.125	N/A	14.199	14.242	N/A
3.0	5.160	5.184	N/A	3.222	3.234	N/A	14.671	14.715	N/A
10.0	6.248	6.272	N/A	3.889	3.903	N/A	17.545	17.600	N/A
30.0	8.732	8.757	N/A	5.559	5.577	N/A	24.735	24.825	N/A
100.0	13.410	13.437	N/A	9.194	9.223	N/A	40.395	40.566	N/A
300.0	19.981	20.012	N/A	15.235	15.281	N/A	66.416	66.721	N/A
1000.0	30.756	30.794	N/A	27.118	27.200	N/A	117.609	118.179	N/A

Table D.15: Scaled energy, mass, and proper separation for two equal sized holes, each with anti-parallel angular momenta S/a_1^2 generated from an inversion-symmetric extrinsic curvature obeying the isometry condition with a minus sign. The conformal separation is $\beta = 5$.

P/a_1	E/a_1 6	9	12	M/a_1 6	9	12	L/a_1 6	9	12
0.0	4.948	4.972	N/A	3.097	3.109	N/A	14.133	14.175	N/A
1.0	5.518	5.542	N/A	3.214	3.227	N/A	14.670	14.712	N/A
2.5	7.755	7.778	N/A	3.636	3.650	N/A	16.593	16.634	N/A
5.0	12.659	12.680	N/A	4.412	4.428	N/A	20.131	20.176	N/A
7.5	17.952	17.970	N/A	5.113	5.131	N/A	23.327	23.377	N/A
10.0	23.349	23.363	N/A	5.740	5.759	N/A	26.184	26.239	N/A
12.5	28.752	28.760	N/A	6.309	6.329	N/A	28.778	28.836	N/A
15.0	34.099	34.101	N/A	6.832	6.854	N/A	31.164	31.226	N/A
17.5	39.345	39.339	N/A	7.319	7.343	N/A	33.384	33.450	N/A

Table D.16: Scaled energy, mass, and proper separation for two equal sized holes, each with parallel linear momenta P/a_1 generated from an inversion-symmetric extrinsic curvature obeying the isometry condition with a plus sign. The conformal separation is $\beta = 5$.

P/a_1	E/a_1 6	9	12	M/a_1 6	9	12	L/a_1 6	9	12
0.0	4.948	4.972	N/A	3.097	3.109	N/A	14.133	14.175	N/A
1.0	5.507	5.531	N/A	3.208	3.221	N/A	14.634	14.676	N/A
2.5	7.723	7.746	N/A	3.612	3.625	N/A	16.457	16.502	N/A
5.0	12.617	12.638	N/A	4.366	4.382	N/A	19.865	19.917	N/A
7.5	17.910	17.928	N/A	5.052	5.069	N/A	22.967	23.025	N/A
10.0	23.310	23.323	N/A	5.666	5.686	N/A	25.748	25.812	N/A
12.5	28.716	28.722	N/A	6.224	6.245	N/A	28.275	28.345	N/A
15.0	34.066	34.065	N/A	6.738	6.761	N/A	30.602	30.678	N/A
17.5	39.313	39.305	N/A	7.217	7.241	N/A	32.769	32.850	N/A

Table D.17: Scaled energy, mass, and proper separation for two equal sized holes, each with parallel linear momenta P/a_1 generated from an inversion-symmetric extrinsic curvature obeying the isometry condition with a minus sign. The conformal separation is $\beta = 5$.

S/a_1^2	E/a_1 6	9	12	M/a_1 6	9	12	L/a_1 6	9	12
0.0	4.948	4.972	N/A	3.097	3.109	N/A	14.133	14.175	N/A
1.0	4.979	5.003	N/A	3.114	3.126	N/A	14.206	14.248	N/A
3.0	5.196	5.220	N/A	3.233	3.245	N/A	14.720	14.764	N/A
10.0	6.475	6.499	N/A	3.944	3.958	N/A	17.797	17.853	N/A
30.0	9.538	9.562	N/A	5.707	5.726	N/A	25.444	25.535	N/A
100.0	16.011	16.038	N/A	9.561	9.592	N/A	42.226	42.395	N/A
300.0	26.612	26.643	N/A	16.004	16.053	N/A	70.346	70.643	N/A
1000.0	47.250	47.282	N/A	28.733	28.822	N/A	125.988	126.536	N/A

Table D.18: Scaled energy, mass, and proper separation for two equal sized holes, each with parallel angular momenta S/a_1^2 generated from an inversion-symmetric extrinsic curvature obeying the isometry condition with a minus sign. The conformal separation is $\beta = 5$.

P/a_1	E/a_1 6	9	12	M/a_1 6	9	12	L/a_1 6	9	12
0.0	4.786	4.787	4.790	2.888	2.876	2.876	16.069	15.832	15.792
1.0	4.908	4.911	4.915	2.943	2.931	2.931	16.392	16.153	16.111
2.5	5.407	5.418	5.423	3.165	3.155	3.155	17.706	17.455	17.406
5.0	6.458	6.481	6.489	3.634	3.625	3.625	20.463	20.182	20.121
7.5	7.472	7.503	7.514	4.086	4.078	4.078	23.117	22.803	22.730
10.0	8.401	8.440	8.452	4.501	4.494	4.494	25.546	25.201	25.118
12.5	9.255	9.299	9.313	4.883	4.876	4.876	27.775	27.402	27.310
15.0	10.045	10.094	10.110	5.238	5.230	5.231	29.840	29.441	29.340
17.5	10.784	10.837	10.854	5.569	5.562	5.562	31.770	31.345	31.237

Table D.19: Scaled energy, mass, and proper separation for two equal sized holes, each with anti-parallel linear momenta P/a_1 generated from an inversion-symmetric extrinsic curvature obeying the isometry condition with a plus sign. The conformal separation is $\beta = 6$.

P/a_1	E/a_1 6	9	12	M/a_1 6	9	12	L/a_1 6	9	12
0.0	4.786	4.787	4.790	2.888	2.876	2.876	16.069	15.832	15.792
1.0	4.897	4.899	4.903	2.936	2.924	2.924	16.339	16.102	16.061
2.5	5.361	5.370	5.375	3.134	3.124	3.124	17.470	17.230	17.187
5.0	6.378	6.397	6.404	3.569	3.562	3.563	19.947	19.693	19.643
7.5	7.379	7.405	7.414	4.000	3.994	3.994	22.390	22.116	22.059
10.0	8.303	8.335	8.345	4.398	4.393	4.394	24.650	24.355	24.292
12.5	9.156	9.192	9.203	4.766	4.761	4.763	26.735	26.420	26.351
15.0	9.946	9.987	9.999	5.109	5.104	5.105	28.672	28.338	28.264
17.5	10.686	10.730	10.743	5.429	5.425	5.426	30.485	30.133	30.054

Table D.20: Scaled energy, mass, and proper separation for two equal sized holes, each with anti-parallel linear momenta P/a_1 generated from an inversion-symmetric extrinsic curvature obeying the isometry condition with a minus sign. The conformal separation is $\beta = 6$.

S/a_1^2	E/a_1 6	9	12	M/a_1 6	9	12	L/a_1 6	9	12
0.0	4.786	4.787	4.790	2.888	2.876	2.876	16.069	15.832	15.792
1.0	4.818	4.820	4.823	2.906	2.894	2.894	16.159	15.922	15.882
3.0	5.041	5.046	5.050	3.028	3.018	3.018	16.780	16.547	16.508
10.0	6.264	6.280	6.286	3.726	3.720	3.722	20.339	20.102	20.064
30.0	8.929	8.958	8.966	5.396	5.395	5.397	28.863	28.581	28.541
100.0	13.888	13.930	13.940	8.989	8.992	8.997	47.205	46.806	46.760
300.0	20.844	20.902	20.915	14.942	14.951	14.959	77.607	77.006	76.949
1000.0	32.257	32.337	32.353	26.647	26.666	26.682	137.387	136.386	136.306

Table D.21: Scaled energy, mass, and proper separation for two equal sized holes, each with anti-parallel angular momenta S/a_1^2 generated from an inversion-symmetric extrinsic curvature obeying the isometry condition with a minus sign. The conformal separation is $\beta = 6$.

P/a_1	E/a_1 6	9	12	M/a_1 6	9	12	L/a_1 6	9	12
0.0	4.786	4.787	4.790	2.888	2.876	2.876	16.069	15.832	15.792
1.0	5.370	5.375	5.380	3.004	2.993	2.993	16.714	16.473	16.432
2.5	7.636	7.653	7.659	3.414	3.404	3.405	18.987	18.729	18.683
5.0	12.559	12.590	12.599	4.157	4.148	4.149	23.115	22.814	22.759
7.5	17.854	17.895	17.906	4.825	4.816	4.817	26.822	26.480	26.417
10.0	23.248	23.296	23.309	5.420	5.411	5.412	30.130	29.749	29.678
12.5	28.644	28.697	28.713	5.960	5.950	5.952	33.128	32.712	32.634
15.0	33.983	34.042	34.058	6.457	6.446	6.448	35.886	35.437	35.352
17.5	39.220	39.282	39.300	6.918	6.908	6.909	38.451	37.971	37.880

Table D.22: Scaled energy, mass, and proper separation for two equal sized holes, each with parallel linear momenta P/a_1 generated from an inversion-symmetric extrinsic curvature obeying the isometry condition with a plus sign. The conformal separation is $\beta = 6$.

P/a_1	E/a_1 6	9	12	M/a_1 6	9	12	L/a_1 6	9	12
0.0	4.786	4.787	4.790	2.888	2.876	2.876	16.069	15.832	15.792
1.0	5.357	5.362	5.366	2.997	2.986	2.986	16.662	16.423	16.383
2.5	7.600	7.616	7.622	3.387	3.377	3.378	18.797	18.545	18.502
5.0	12.513	12.542	12.551	4.107	4.098	4.099	22.746	22.459	22.409
7.5	17.809	17.847	17.858	4.758	4.749	4.751	26.322	25.999	25.942
10.0	23.206	23.251	23.264	5.340	5.331	5.333	29.523	29.166	29.103
12.5	28.605	28.656	28.670	5.868	5.860	5.861	32.430	32.041	31.973
15.0	33.948	34.003	34.018	6.355	6.346	6.348	35.106	34.688	34.614
17.5	39.188	39.246	39.262	6.807	6.798	6.800	37.597	37.151	37.073

Table D.23: Scaled energy, mass, and proper separation for two equal sized holes, each with parallel linear momenta P/a_1 generated from an inversion-symmetric extrinsic curvature obeying the isometry condition with a minus sign. The conformal separation is $\beta = 6$.

S/a_1^2	E/a_1 6	9	12	M/a_1 6	9	12	L/a_1 6	9	12
0.0	4.786	4.787	4.790	2.888	2.876	2.876	16.069	15.832	15.792
1.0	4.822	4.823	4.827	2.907	2.895	2.895	16.164	15.927	15.887
3.0	5.069	5.074	5.079	3.035	3.025	3.025	16.818	16.585	16.545
10.0	6.440	6.458	6.464	3.760	3.755	3.756	20.532	20.293	20.254
30.0	9.584	9.615	9.623	5.492	5.490	5.493	29.436	29.145	29.104
100.0	16.114	16.159	16.169	9.237	9.239	9.244	48.780	48.353	48.300
300.0	26.733	26.795	26.808	15.480	15.486	15.495	81.139	80.470	80.396
1000.0	47.353	47.438	47.455	27.806	27.821	27.837	145.168	144.011	143.891

Table D.24: Scaled energy, mass, and proper separation for two equal sized holes, each with parallel angular momenta S/a_1^2 generated from an inversion-symmetric extrinsic curvature obeying the isometry condition with a minus sign. The conformal separation is $\beta = 6$.

P/a_1	E/a_1 6	9	12	M/a_1 6	9	12	L/a_1 6	9	12
0.0	4.706	4.674	4.667	2.789	2.741	2.728	18.384	17.603	17.364
1.0	4.851	4.827	4.821	2.850	2.804	2.791	18.808	18.028	17.788
2.5	5.426	5.425	5.426	3.090	3.049	3.038	20.480	19.690	19.440
5.0	6.597	6.628	6.639	3.580	3.544	3.535	23.874	23.023	22.745
7.5	7.708	7.759	7.777	4.045	4.011	4.001	27.080	26.152	25.844
10.0	8.719	8.785	8.808	4.468	4.435	4.425	29.994	28.990	28.652
12.5	9.644	9.723	9.750	4.856	4.823	4.813	32.659	31.582	31.217
15.0	10.500	10.589	10.619	5.215	5.181	5.172	35.122	33.977	33.586
17.5	11.299	11.396	11.430	5.550	5.516	5.506	37.421	36.210	35.795

Table D.25: Scaled energy, mass, and proper separation for two equal sized holes, each with anti-parallel linear momenta P/a_1 generated from an inversion-symmetric extrinsic curvature obeying the isometry condition with a plus sign. The conformal separation is $\beta = 7$.

P/a_1	E/a_1 6	9	12	M/a_1 6	9	12	L/a_1 6	9	12
0.0	4.706	4.674	4.667	2.789	2.741	2.728	18.384	17.603	17.364
1.0	4.837	4.813	4.807	2.841	2.795	2.783	18.736	17.960	17.722
2.5	5.376	5.373	5.373	3.056	3.016	3.005	20.175	19.404	19.164
5.0	6.515	6.541	6.550	3.513	3.479	3.470	23.225	22.423	22.168
7.5	7.616	7.660	7.675	3.955	3.924	3.915	26.176	25.321	25.045
10.0	8.625	8.683	8.702	4.361	4.331	4.323	28.884	27.972	27.674
12.5	9.552	9.619	9.642	4.735	4.705	4.697	31.372	30.405	30.086
15.0	10.410	10.486	10.511	5.081	5.052	5.044	33.679	32.657	32.319
17.5	11.211	11.294	11.322	5.406	5.376	5.368	35.836	34.762	34.406

Table D.26: Scaled energy, mass, and proper separation for two equal sized holes, each with anti-parallel linear momenta P/a_1 generated from an inversion-symmetric extrinsic curvature obeying the isometry condition with a minus sign. The conformal separation is $\beta = 7$.

S/a_1^2	E/a_1 6	9	12	M/a_1 6	9	12	L/a_1 6	9	12
0.0	4.706	4.674	4.667	2.789	2.741	2.728	18.384	17.603	17.364
1.0	4.742	4.712	4.705	2.807	2.760	2.747	18.493	17.713	17.475
3.0	4.985	4.968	4.964	2.935	2.893	2.881	19.244	18.471	18.234
10.0	6.286	6.305	6.311	3.645	3.613	3.605	23.415	22.599	22.348
30.0	9.071	9.125	9.142	5.312	5.285	5.279	33.218	32.186	31.869
100.0	14.240	14.335	14.363	8.880	8.851	8.845	54.204	52.646	52.172
300.0	21.502	21.642	21.682	14.786	14.749	14.742	88.954	86.505	85.765
1000.0	33.435	33.639	33.696	26.395	26.341	26.331	157.271	153.063	151.799

Table D.27: Scaled energy, mass, and proper separation for two equal sized holes, each with anti-parallel angular momenta S/a_1^2 generated from an inversion-symmetric extrinsic curvature obeying the isometry condition with a minus sign. The conformal separation is $\beta = 7$.

P/a_1	E/a_1 6	9	12	M/a_1 6	9	12	L/a_1 6	9	12
0.0	4.706	4.674	4.667	2.789	2.741	2.728	18.384	17.603	17.364
1.0	5.291	5.272	5.268	2.902	2.856	2.844	19.128	18.340	18.098
2.5	7.558	7.566	7.574	3.301	3.258	3.247	21.745	20.908	20.648
5.0	12.482	12.509	12.531	4.022	3.980	3.969	26.482	25.518	25.215
7.5	17.782	17.806	17.842	4.669	4.624	4.613	30.734	29.640	29.295
10.0	23.186	23.195	23.243	5.246	5.198	5.186	34.525	33.312	32.927
12.5	28.595	28.583	28.643	5.768	5.718	5.705	37.961	36.637	36.217
15.0	33.949	33.912	33.983	6.249	6.196	6.182	41.122	39.695	39.241
17.5	39.203	39.137	39.219	6.696	6.641	6.626	44.061	42.538	42.052

Table D.28: Scaled energy, mass, and proper separation for two equal sized holes, each with parallel linear momenta P/a_1 generated from an inversion-symmetric extrinsic curvature obeying the isometry condition with a plus sign. The conformal separation is $\beta = 7$.

P/a_1	E/a_1 6	9	12	M/a_1 6	9	12	L/a_1 6	9	12
0.0	4.706	4.674	4.667	2.789	2.741	2.728	18.384	17.603	17.364
1.0	5.277	5.257	5.253	2.894	2.848	2.836	19.061	18.275	18.035
2.5	7.519	7.525	7.532	3.271	3.229	3.218	21.495	20.672	20.418
5.0	12.434	12.457	12.479	3.967	3.926	3.915	25.997	25.063	24.773
7.5	17.737	17.756	17.790	4.597	4.553	4.542	30.075	29.026	28.698
10.0	23.145	23.148	23.194	5.159	5.114	5.102	33.726	32.567	32.205
12.5	28.559	28.540	28.597	5.670	5.622	5.609	37.042	35.782	35.387
15.0	33.917	33.872	33.941	6.140	6.089	6.076	40.096	38.740	38.316
17.5	39.174	39.101	39.180	6.578	6.524	6.510	42.938	41.493	41.040

Table D.29: Scaled energy, mass, and proper separation for two equal sized holes, each with parallel linear momenta P/a_1 generated from an inversion-symmetric extrinsic curvature obeying the isometry condition with a minus sign. The conformal separation is $\beta = 7$.

S/a_1^2	E/a_1 6	9	12	M/a_1 6	9	12	L/a_1 6	9	12
0.0	4.706	4.674	4.667	2.789	2.741	2.728	18.384	17.603	17.364
1.0	4.744	4.715	4.708	2.808	2.761	2.748	18.497	17.717	17.479
3.0	5.007	4.990	4.987	2.940	2.897	2.886	19.273	18.500	18.263
10.0	6.425	6.445	6.452	3.668	3.636	3.628	23.570	22.748	22.495
30.0	9.611	9.670	9.687	5.379	5.351	5.344	33.701	32.649	32.326
100.0	16.163	16.267	16.297	9.060	9.028	9.021	55.615	53.996	53.501
300.0	26.772	26.923	26.968	15.188	15.145	15.136	92.258	89.658	88.869
1000.0	47.345	47.549	47.617	27.284	27.215	27.201	164.789	160.227	158.847

Table D.30: Scaled energy, mass, and proper separation for two equal sized holes, each with parallel angular momenta S/a_1^2 generated from an inversion-symmetric extrinsic curvature obeying the isometry condition with a minus sign. The conformal separation is $\beta = 7$.

P/a_1	E/a_1 6	9	12	M/a_1 6	9	12	L/a_1 6	9	12
0.0	9.740	4.407	4.524	12.155	2.434	2.563	248.286	15.837	17.803
1.0	9.746	4.627	4.717	12.160	2.513	2.635	248.380	16.347	18.313
2.5	9.776	5.421	5.440	12.184	2.797	2.905	248.869	18.208	20.222
5.0	9.881	6.883	6.822	12.269	3.326	3.422	250.570	21.689	23.880
7.5	10.047	8.197	8.087	12.404	3.805	3.899	253.268	24.853	27.243
10.0	10.264	9.365	9.222	12.580	4.234	4.327	256.796	27.687	30.268
12.5	10.522	10.421	10.253	12.788	4.623	4.718	260.979	30.260	33.021
15.0	10.812	11.390	11.202	13.021	4.981	5.078	265.653	32.628	35.558
17.5	11.124	12.290	12.084	13.272	5.315	5.413	270.682	34.831	37.921

Table D.31: Scaled energy, mass, and proper separation for two equal sized holes, each with anti-parallel linear momenta P/a_1 generated from an inversion-symmetric extrinsic curvature obeying the isometry condition with a plus sign. The conformal separation is $\beta = 8$.

P/a_1	E/a_1 6	9	12	M/a_1 6	9	12	L/a_1 6	9	12
0.0	9.740	4.407	4.524	12.155	2.434	2.563	248.286	15.837	17.803
1.0	9.746	4.608	4.700	12.159	2.505	2.626	248.370	16.300	18.245
2.5	9.774	5.355	5.380	12.181	2.767	2.872	248.804	18.030	19.957
5.0	9.873	6.773	6.724	12.257	3.269	3.360	250.321	21.332	23.354
7.5	10.030	8.066	7.975	12.379	3.729	3.816	252.739	24.361	26.527
10.0	10.238	9.222	9.103	12.539	4.143	4.230	255.922	27.083	29.400
12.5	10.487	10.270	10.130	12.729	4.520	4.607	259.721	29.559	32.023
15.0	10.767	11.233	11.076	12.944	4.868	4.956	263.997	31.841	34.444
17.5	11.070	12.129	11.957	13.177	5.191	5.281	268.628	33.965	36.702

Table D.32: Scaled energy, mass, and proper separation for two equal sized holes, each with anti-parallel linear momenta P/a_1 generated from an inversion-symmetric extrinsic curvature obeying the isometry condition with a minus sign. The conformal separation is $\beta = 8$.

S/a_1^2	E/a_1 6	9	12	M/a_1 6	9	12	L/a_1 6	9	12
0.0	9.740	4.407	4.524	12.155	2.434	2.563	248.286	15.837	17.803
1.0	9.741	4.460	4.570	12.156	2.459	2.585	248.300	15.976	17.936
3.0	9.745	4.803	4.873	12.161	2.620	2.732	248.412	16.873	18.824
10.0	9.792	6.378	6.352	12.225	3.395	3.483	249.659	21.224	23.354
30.0	10.149	9.460	9.346	12.715	5.075	5.159	259.244	30.704	33.490
100.0	12.142	15.035	14.820	15.541	8.594	8.696	314.451	50.652	54.939
300.0	16.575	22.811	22.487	22.335	14.391	14.533	446.800	83.584	90.383
1000.0	25.028	35.555	35.076	36.951	25.775	26.000	730.809	148.301	160.046

Table D.33: Scaled energy, mass, and proper separation for two equal sized holes, each with anti-parallel angular momenta S/a_1^2 generated from an inversion-symmetric extrinsic curvature obeying the isometry condition with a minus sign. The conformal separation is $\beta = 8$.

P/a_1	E/a_1 6	9	12	M/a_1 6	9	12	L/a_1 6	9	12
0.0	9.740	4.407	4.524	12.155	2.434	2.563	248.286	15.837	17.803
1.0	9.889	5.077	5.153	12.190	2.558	2.681	248.989	16.606	18.607
2.5	10.646	7.538	7.519	12.364	2.965	3.081	252.523	19.151	21.340
5.0	13.092	12.654	12.533	12.904	3.664	3.785	263.516	23.545	26.150
7.5	16.563	18.060	17.872	13.626	4.278	4.408	278.181	27.416	30.418
10.0	20.648	23.532	23.291	14.421	4.821	4.962	294.339	30.848	34.210
12.5	25.086	28.987	28.702	15.234	5.312	5.462	310.874	33.950	37.641
15.0	29.714	34.373	34.051	16.040	5.761	5.921	327.272	36.798	40.793
17.5	34.419	39.647	39.293	16.828	6.179	6.348	343.313	39.444	43.722

Table D.34: Scaled energy, mass, and proper separation for two equal sized holes, each with parallel linear momenta P/a_1 generated from an inversion-symmetric extrinsic curvature obeying the isometry condition with a plus sign. The conformal separation is $\beta = 8$.

P/a_1	E/a_1 6	9	12	M/a_1 6	9	12	L/a_1 6	9	12
0.0	9.740	4.407	4.524	12.155	2.434	2.563	248.286	15.837	17.803
1.0	9.889	5.057	5.135	12.189	2.549	2.672	248.977	16.558	18.540
2.5	10.644	7.483	7.471	12.360	2.938	3.052	252.457	18.994	21.103
5.0	13.086	12.577	12.471	12.894	3.616	3.731	263.298	23.268	25.707
7.5	16.553	17.977	17.809	13.607	4.214	4.338	277.788	27.057	29.827
10.0	20.637	23.445	23.230	14.394	4.745	4.877	293.779	30.422	33.498
12.5	25.076	28.898	28.644	15.200	5.225	5.366	310.162	33.466	36.825
15.0	29.704	34.284	33.995	16.000	5.666	5.815	326.422	36.263	39.885
17.5	34.410	39.559	39.239	16.782	6.075	6.233	342.337	38.863	42.730

Table D.35: Scaled energy, mass, and proper separation for two equal sized holes, each with parallel linear momenta P/a_1 generated from an inversion-symmetric extrinsic curvature obeying the isometry condition with a minus sign. The conformal separation is $\beta = 8$.

S/a_1^2	E/a_1 6	9	12	M/a_1 6	9	12	L/a_1 6	9	12
0.0	9.740	4.407	4.524	12.155	2.434	2.563	248.286	15.837	17.803
1.0	9.741	4.463	4.572	12.156	2.460	2.585	248.303	15.979	17.939
3.0	9.747	4.822	4.891	12.162	2.623	2.735	248.432	16.893	18.845
10.0	9.811	6.497	6.467	12.236	3.410	3.499	249.877	21.325	23.464
30.0	10.295	9.931	9.809	12.793	5.118	5.204	260.858	31.030	33.847
100.0	13.056	16.758	16.525	15.918	8.716	8.823	322.400	51.636	56.030
300.0	19.892	27.639	27.280	23.345	14.672	14.827	468.859	85.938	93.017
1000.0	35.541	48.551	48.008	39.423	26.407	26.665	786.576	153.742	166.179

Table D.36: Scaled energy, mass, and proper separation for two equal sized holes, each with parallel angular momenta S/a_1^2 generated from an inversion-symmetric extrinsic curvature obeying the isometry condition with a minus sign. The conformal separation is $\beta = 8$.

P/a_1	E/a_1 6	9	12	M/a_1 6	9	12	L/a_1 6	9	12
0.0	4.359	4.456	4.480	2.389	2.489	2.513	17.843	19.309	19.649
1.0	4.600	4.676	4.695	2.472	2.567	2.589	18.473	19.924	20.261
2.5	5.456	5.475	5.483	2.769	2.851	2.871	20.711	22.166	22.506
5.0	7.007	6.967	6.963	3.308	3.383	3.402	24.793	26.352	26.720
7.5	8.394	8.320	8.308	3.793	3.867	3.885	28.462	30.155	30.556
10.0	9.626	9.528	9.512	4.225	4.300	4.319	31.735	33.559	33.994
12.5	10.740	10.624	10.604	4.617	4.694	4.713	34.700	36.651	37.117
15.0	11.761	11.631	11.609	4.978	5.056	5.076	37.426	39.496	39.992
17.5	12.710	12.568	12.543	5.313	5.394	5.414	39.962	42.144	42.669

Table D.37: Scaled energy, mass, and proper separation for two equal sized holes, each with anti-parallel linear momenta P/a_1 generated from an inversion-symmetric extrinsic curvature obeying the isometry condition with a plus sign. The conformal separation is $\beta = 9$.

P/a_1	E/a_1 6	9	12	M/a_1 6	9	12	L/a_1 6	9	12
0.0	4.359	4.456	4.480	2.389	2.489	2.513	17.843	19.309	19.649
1.0	4.580	4.657	4.676	2.463	2.558	2.580	18.398	19.840	20.176
2.5	5.389	5.413	5.421	2.735	2.817	2.837	20.435	21.846	22.177
5.0	6.903	6.870	6.867	3.246	3.319	3.337	24.262	25.727	26.073
7.5	8.275	8.210	8.200	3.711	3.782	3.800	27.747	29.309	29.680
10.0	9.499	9.414	9.400	4.129	4.200	4.218	30.870	32.536	32.934
12.5	10.608	10.508	10.490	4.508	4.580	4.599	33.706	35.475	35.898
15.0	11.627	11.514	11.494	4.857	4.931	4.950	36.318	38.186	38.633
17.5	12.573	12.450	12.428	5.183	5.258	5.277	38.749	40.711	41.182

Table D.38: Scaled energy, mass, and proper separation for two equal sized holes, each with anti-parallel linear momenta P/a_1 generated from an inversion-symmetric extrinsic curvature obeying the isometry condition with a minus sign. The conformal separation is $\beta = 9$.

S/a_1^2	E/a_1 6	9	12	M/a_1 6	9	12	L/a_1 6	9	12
0.0	4.359	4.456	4.480	2.389	2.489	2.513	17.843	19.309	19.649
1.0	4.415	4.506	4.529	2.414	2.512	2.535	17.998	19.460	19.799
3.0	4.772	4.832	4.847	2.577	2.665	2.686	18.998	20.450	20.787
10.0	6.397	6.381	6.380	3.353	3.424	3.441	23.786	25.384	25.752
30.0	9.571	9.481	9.464	5.025	5.096	5.112	34.158	36.280	36.767
100.0	15.325	15.147	15.112	8.525	8.613	8.634	55.961	59.274	60.036
300.0	23.373	23.094	23.040	14.290	14.414	14.444	91.958	97.258	98.479
1000.0	36.581	36.161	36.078	25.608	25.807	25.857	162.708	171.916	174.041

Table D.39: Scaled energy, mass, and proper separation for two equal sized holes, each with anti-parallel angular momenta S/a_1^2 generated from an inversion-symmetric extrinsic curvature obeying the isometry condition with a minus sign. The conformal separation is $\beta = 9$.

P/a_1	E/a_1 6	9	12	M/a_1 6	9	12	L/a_1 6	9	12
0.0	4.359	4.456	4.480	2.389	2.489	2.513	17.843	19.309	19.649
1.0	5.029	5.092	5.109	2.511	2.607	2.629	18.719	20.197	20.539
2.5	7.486	7.471	7.475	2.913	3.003	3.024	21.612	23.192	23.556
5.0	12.599	12.490	12.486	3.602	3.694	3.716	26.596	28.438	28.860
7.5	18.009	17.827	17.824	4.206	4.304	4.328	30.983	33.085	33.564
10.0	23.489	23.242	23.245	4.740	4.846	4.871	34.869	37.210	37.744
12.5	28.956	28.648	28.659	5.222	5.335	5.362	38.382	40.942	41.526
15.0	34.357	33.990	34.012	5.665	5.785	5.814	41.606	44.370	45.000
17.5	39.647	39.227	39.259	6.075	6.202	6.233	44.602	47.557	48.229

Table D.40: Scaled energy, mass, and proper separation for two equal sized holes, each with parallel linear momenta P/a_1 generated from an inversion-symmetric extrinsic curvature obeying the isometry condition with a plus sign. The conformal separation is $\beta = 9$.

P/a_1	E/a_1 6	9	12	M/a_1 6	9	12	L/a_1 6	9	12
0.0	4.359	4.456	4.480	2.389	2.489	2.513	17.843	19.309	19.649
1.0	5.008	5.073	5.091	2.502	2.597	2.620	18.647	20.115	20.456
2.5	7.431	7.420	7.425	2.882	2.971	2.992	21.369	22.909	23.266
5.0	12.526	12.425	12.423	3.547	3.637	3.659	26.150	27.909	28.315
7.5	17.932	17.763	17.762	4.134	4.230	4.253	30.392	32.378	32.836
10.0	23.412	23.180	23.186	4.655	4.758	4.783	34.161	36.360	36.867
12.5	28.880	28.589	28.603	5.126	5.235	5.262	37.573	39.969	40.520
15.0	34.283	33.935	33.959	5.558	5.674	5.702	40.707	43.287	43.880
17.5	39.575	39.174	39.209	5.959	6.082	6.112	43.622	46.373	47.006

Table D.41: Scaled energy, mass, and proper separation for two equal sized holes, each with parallel linear momenta P/a_1 generated from an inversion-symmetric extrinsic curvature obeying the isometry condition with a minus sign. The conformal separation is $\beta = 9$.

S/a_1^2	E/a_1 6	9	12	M/a_1 6	9	12	L/a_1 6	9	12
0.0	4.359	4.456	4.480	2.389	2.489	2.513	17.843	19.309	19.649
1.0	4.417	4.508	4.530	2.415	2.513	2.536	18.001	19.462	19.801
3.0	4.787	4.846	4.862	2.579	2.667	2.688	19.014	20.467	20.804
10.0	6.494	6.476	6.474	3.364	3.435	3.452	23.868	25.472	25.841
30.0	9.971	9.875	9.857	5.058	5.129	5.146	34.441	36.582	37.074
100.0	16.848	16.654	16.616	8.619	8.710	8.733	56.872	60.250	61.027
300.0	27.761	27.452	27.393	14.511	14.645	14.678	94.239	99.709	100.970
1000.0	48.689	48.199	48.114	26.120	26.342	26.397	168.158	177.796	180.020

Table D.42: Scaled energy, mass, and proper separation for two equal sized holes, each with parallel angular momenta S/a_1^2 generated from an inversion-symmetric extrinsic curvature obeying the isometry condition with a minus sign. The conformal separation is $\beta = 9$.

P/a_1	E/a_1 6	9	12	M/a_1 6	9	12	L/a_1 6	9	12
0.0	4.350	4.410	4.427	2.378	2.438	2.454	19.956	20.794	21.011
1.0	4.605	4.652	4.666	2.464	2.520	2.535	20.673	21.499	21.712
2.5	5.504	5.520	5.526	2.765	2.815	2.829	23.206	24.025	24.236
5.0	7.129	7.112	7.111	3.311	3.357	3.370	27.794	28.666	28.891
7.5	8.580	8.545	8.540	3.800	3.846	3.858	31.908	32.852	33.095
10.0	9.871	9.824	9.816	4.236	4.282	4.296	35.574	36.590	36.852
12.5	11.038	10.981	10.972	4.631	4.678	4.692	38.896	39.980	40.260
15.0	12.109	12.045	12.034	4.994	5.043	5.057	41.949	43.098	43.395
17.5	13.103	13.033	13.021	5.331	5.382	5.397	44.787	45.999	46.312

Table D.43: Scaled energy, mass, and proper separation for two equal sized holes, each with anti-parallel linear momenta P/a_1 generated from an inversion-symmetric extrinsic curvature obeying the isometry condition with a plus sign. The conformal separation is $\beta = 10$.

P/a_1	E/a_1 6	9	12	M/a_1 6	9	12	L/a_1 6	9	12
0.0	4.350	4.410	4.427	2.378	2.438	2.454	19.956	20.794	21.011
1.0	4.584	4.632	4.646	2.454	2.510	2.525	20.581	21.404	21.616
2.5	5.437	5.455	5.461	2.730	2.779	2.793	22.868	23.669	23.876
5.0	7.028	7.014	7.013	3.246	3.291	3.304	27.150	27.978	28.192
7.5	8.469	8.437	8.432	3.715	3.760	3.772	31.043	31.926	32.154
10.0	9.754	9.712	9.704	4.136	4.181	4.194	34.532	35.472	35.716
12.5	10.919	10.868	10.859	4.517	4.564	4.577	37.700	38.697	38.956
15.0	11.988	11.931	11.921	4.869	4.916	4.930	40.617	41.669	41.943
17.5	12.982	12.920	12.908	5.196	5.245	5.259	43.331	44.437	44.724

Table D.44: Scaled energy, mass, and proper separation for two equal sized holes, each with anti-parallel linear momenta P/a_1 generated from an inversion-symmetric extrinsic curvature obeying the isometry condition with a minus sign. The conformal separation is $\beta = 10$.

S/a_1^2	E/a_1 6	9	12	M/a_1 6	9	12	L/a_1 6	9	12
0.0	4.350	4.410	4.427	2.378	2.438	2.454	19.956	20.794	21.011
1.0	4.406	4.463	4.480	2.404	2.462	2.478	20.126	20.961	21.176
3.0	4.768	4.807	4.818	2.566	2.618	2.633	21.218	22.045	22.258
10.0	6.416	6.410	6.411	3.341	3.384	3.395	26.444	27.351	27.582
30.0	9.646	9.598	9.588	5.010	5.053	5.064	37.755	38.963	39.272
100.0	15.527	15.428	15.406	8.503	8.557	8.572	61.532	63.426	63.914
300.0	23.781	23.622	23.587	14.258	14.335	14.357	100.800	103.835	104.620
1000.0	37.358	37.116	37.061	25.558	25.683	25.718	177.989	183.267	184.638

Table D.45: Scaled energy, mass, and proper separation for two equal sized holes, each with anti-parallel angular momenta S/a_1^2 generated from an inversion-symmetric extrinsic curvature obeying the isometry condition with a minus sign. The conformal separation is $\beta = 10$.

P/a_1	E/a_1 6	9	12	M/a_1 6	9	12	L/a_1 6	9	12
0.0	4.350	4.410	4.427	2.378	2.438	2.454	19.956	20.794	21.011
1.0	5.010	5.051	5.063	2.498	2.555	2.570	20.916	21.756	21.973
2.5	7.443	7.439	7.439	2.893	2.946	2.961	24.104	24.990	25.216
5.0	12.524	12.468	12.452	3.573	3.628	3.643	29.615	30.637	30.896
7.5	17.911	17.815	17.785	4.171	4.229	4.245	34.475	35.635	35.929
10.0	23.371	23.240	23.196	4.699	4.762	4.779	38.785	40.072	40.398
12.5	28.822	28.658	28.599	5.176	5.243	5.262	42.681	44.086	44.442
15.0	34.208	34.012	33.940	5.614	5.686	5.705	46.258	47.774	48.158
17.5	39.485	39.260	39.174	6.021	6.096	6.117	49.583	51.201	51.611

Table D.46: Scaled energy, mass, and proper separation for two equal sized holes, each with parallel linear momenta P/a_1 generated from an inversion-symmetric extrinsic curvature obeying the isometry condition with a plus sign. The conformal separation is $\beta = 10$.

P/a_1	E/a_1 6	9	12	M/a_1 6	9	12	L/a_1 6	9	12
0.0	4.350	4.410	4.427	2.378	2.438	2.454	19.956	20.794	21.011
1.0	4.989	5.031	5.043	2.488	2.545	2.560	20.827	21.664	21.880
2.5	7.387	7.386	7.386	2.861	2.914	2.928	23.801	24.670	24.894
5.0	12.454	12.402	12.386	3.515	3.569	3.585	29.057	30.042	30.294
7.5	17.840	17.750	17.720	4.095	4.153	4.169	33.735	34.842	35.125
10.0	23.302	23.178	23.135	4.609	4.671	4.689	37.896	39.120	39.432
12.5	28.755	28.599	28.541	5.075	5.141	5.159	41.664	42.996	43.336
15.0	34.144	33.957	33.885	5.502	5.572	5.592	45.128	46.561	46.926
17.5	39.424	39.208	39.123	5.899	5.973	5.993	48.349	49.876	50.266

Table D.47: Scaled energy, mass, and proper separation for two equal sized holes, each with parallel linear momenta P/a_1 generated from an inversion-symmetric extrinsic curvature obeying the isometry condition with a minus sign. The conformal separation is $\beta = 10$.

S/a_1^2	E/a_1 6	9	12	M/a_1 6	9	12	L/a_1 6	9	12
0.0	4.350	4.410	4.427	2.378	2.438	2.454	19.956	20.794	21.011
1.0	4.408	4.465	4.481	2.404	2.462	2.478	20.127	20.963	21.178
3.0	4.780	4.818	4.830	2.568	2.620	2.634	21.231	22.058	22.271
10.0	6.496	6.489	6.489	3.349	3.392	3.403	26.513	27.422	27.654
30.0	9.988	9.937	9.926	5.035	5.078	5.090	38.004	39.221	39.533
100.0	16.877	16.769	16.745	8.578	8.634	8.650	62.380	64.303	64.798
300.0	27.781	27.606	27.565	14.440	14.522	14.545	103.001	106.116	106.921
1000.0	48.654	48.373	48.304	25.987	26.124	26.163	183.403	188.889	190.310

Table D.48: Scaled energy, mass, and proper separation for two equal sized holes, each with parallel angular momenta S/a_1^2 generated from an inversion-symmetric extrinsic curvature obeying the isometry condition with a minus sign. The conformal separation is $\beta = 10$.

P/a_1	E/a_1 6	9	12	M/a_1 6	9	12	L/a_1 6	9	12
0.0	4.319	4.369	4.384	2.345	2.392	2.406	21.502	22.139	22.310
1.0	4.594	4.633	4.645	2.434	2.478	2.491	22.304	22.928	23.095
2.5	5.550	5.565	5.570	2.742	2.782	2.793	25.100	25.712	25.875
5.0	7.263	7.253	7.253	3.295	3.332	3.343	30.117	30.762	30.933
7.5	8.788	8.764	8.761	3.788	3.825	3.836	34.596	35.292	35.475
10.0	10.142	10.110	10.105	4.226	4.264	4.276	38.583	39.329	39.526
12.5	11.365	11.327	11.321	4.623	4.662	4.674	42.192	42.987	43.197
15.0	12.488	12.445	12.437	4.987	5.028	5.041	45.509	46.350	46.573
17.5	13.530	13.483	13.475	5.326	5.369	5.382	48.592	49.478	49.712

Table D.49: Scaled energy, mass, and proper separation for two equal sized holes, each with anti-parallel linear momenta P/a_1 generated from an inversion-symmetric extrinsic curvature obeying the isometry condition with a plus sign. The conformal separation is $\beta = 11$.

P/a_1	E/a_1 6	9	12	M/a_1 6	9	12	L/a_1 6	9	12
0.0	4.319	4.369	4.384	2.345	2.392	2.406	21.502	22.139	22.310
1.0	4.571	4.611	4.624	2.423	2.468	2.481	22.200	22.823	22.990
2.5	5.482	5.498	5.504	2.706	2.745	2.757	24.726	25.328	25.489
5.0	7.163	7.154	7.154	3.229	3.265	3.277	29.411	30.030	30.195
7.5	8.678	8.656	8.653	3.702	3.738	3.750	33.653	34.310	34.485
10.0	10.028	9.998	9.993	4.124	4.162	4.174	37.447	38.147	38.333
12.5	11.250	11.215	11.208	4.508	4.547	4.559	40.892	41.633	41.830
15.0	12.373	12.333	12.325	4.861	4.901	4.914	44.061	44.843	45.051
17.5	13.415	13.371	13.363	5.189	5.231	5.244	47.011	47.831	48.049

Talbe D50: Scaled energy, mass, and proper separation for two equal sized holes, each with anti-parallel linear momenta P/a_1 generated from an inversion-symmetric extrinsic curvature obeying the isometry condition with a minus sign. The conformal separation is $\beta = 11$.

S/a_1^2	E/a_1 6	9	12	M/a_1 6	9	12	L/a_1 6	9	12
0.0	4.319	4.369	4.384	2.345	2.392	2.406	21.502	22.139	22.310
1.0	4.378	4.425	4.439	2.371	2.417	2.430	21.686	22.320	22.490
3.0	4.753	4.785	4.795	2.536	2.577	2.589	22.866	23.489	23.656
10.0	6.442	6.439	6.440	3.314	3.348	3.358	28.439	29.119	29.299
30.0	9.742	9.707	9.699	4.981	5.015	5.025	40.436	41.343	41.584
100.0	15.765	15.689	15.672	8.465	8.509	8.522	65.636	67.059	67.441
300.0	24.237	24.115	24.086	14.205	14.267	14.286	107.259	109.539	110.155
1000.0	38.199	38.011	37.966	25.475	25.576	25.607	189.090	193.055	194.132

Table D.51: Scaled energy, mass, and proper separation for two equal sized holes, each with anti-parallel angular momenta S/a_1^2 generated from an inversion-symmetric extrinsic curvature obeying the isometry condition with a minus sign. The conformal separation is $\beta = 11$.

P/a_1	E/a_1 6	9	12	M/a_1 6	9	12	L/a_1 6	9	12
0.0	4.319	4.369	4.384	2.345	2.392	2.406	21.502	22.139	22.310
1.0	4.981	5.016	5.026	2.464	2.509	2.522	22.534	23.168	23.338
2.5	7.417	7.420	7.415	2.855	2.897	2.910	25.953	26.615	26.790
5.0	12.503	12.476	12.441	3.527	3.571	3.584	31.862	32.618	32.817
7.5	17.896	17.855	17.785	4.117	4.164	4.178	37.074	37.929	38.153
10.0	23.365	23.315	23.206	4.639	4.690	4.704	41.696	42.644	42.891
12.5	28.826	28.770	28.619	5.111	5.165	5.180	45.875	46.910	47.179
15.0	34.224	34.164	33.969	5.543	5.600	5.617	49.714	50.829	51.118
17.5	39.513	39.451	39.213	5.945	6.005	6.023	53.281	54.471	54.779

Table D.52: Scaled energy, mass, and proper separation for two equal sized holes, each with parallel linear momenta P/a_1 generated from an inversion-symmetric extrinsic curvature obeying the isometry condition with a plus sign. The conformal separation is $\beta = 11$.

P/a_1	E/a_1 6	9	12	M/a_1 6	9	12	L/a_1 6	9	12
0.0	4.319	4.369	4.384	2.345	2.392	2.406	21.502	22.139	22.310
1.0	4.959	4.995	5.004	2.453	2.498	2.512	22.434	23.067	23.236
2.5	7.359	7.365	7.359	2.821	2.864	2.876	25.614	26.266	26.440
5.0	12.431	12.408	12.373	3.467	3.511	3.524	31.239	31.973	32.167
7.5	17.825	17.787	17.717	4.040	4.086	4.100	36.247	37.071	37.288
10.0	23.297	23.250	23.142	4.547	4.598	4.612	40.705	41.614	41.852
12.5	28.761	28.709	28.559	5.006	5.060	5.076	44.742	45.731	45.990
15.0	34.162	34.107	33.913	5.428	5.485	5.502	48.454	49.518	49.795
17.5	39.454	39.398	39.161	5.819	5.880	5.897	51.906	53.040	53.335

Table D.53: Scaled energy, mass, and proper separation for two equal sized holes, each with parallel linear momenta P/a_1 generated from an inversion-symmetric extrinsic curvature obeying the isometry condition with a minus sign. The conformal separation is $\beta = 11$.

S/a_1^2	E/a_1 6	9	12	M/a_1 6	9	12	L/a_1 6	9	12
0.0	4.319	4.369	4.384	2.345	2.392	2.406	21.502	22.139	22.310
1.0	4.380	4.426	4.440	2.371	2.417	2.430	21.688	22.321	22.491
3.0	4.763	4.794	4.804	2.537	2.578	2.591	22.876	23.500	23.666
10.0	6.509	6.506	6.506	3.320	3.354	3.364	28.496	29.177	29.358
30.0	10.038	10.001	9.993	5.000	5.035	5.045	40.653	41.565	41.807
100.0	16.973	16.892	16.872	8.525	8.570	8.584	66.407	67.847	68.233
300.0	27.909	27.776	27.741	14.355	14.420	14.440	109.327	111.657	112.286
1000.0	48.795	48.589	48.514	25.836	25.945	25.978	194.313	198.413	199.523

Table D.54: Scaled energy, mass, and proper separation for two equal sized holes, each with parallel angular momenta S/a_1^2 generated from an inversion-symmetric extrinsic curvature obeying the isometry condition with a minus sign. The conformal separation is $\beta = 11$.

P/a_1	E/a_1 6	9	12	M/a_1 6	9	12	L/a_1 6	9	12
0.0	4.288	4.334	4.348	2.311	2.353	2.366	22.890	23.429	23.578
1.0	4.583	4.618	4.629	2.403	2.443	2.455	23.771	24.297	24.441
2.5	5.596	5.609	5.615	2.718	2.754	2.764	26.812	27.322	27.460
5.0	7.394	7.387	7.388	3.277	3.310	3.321	32.218	32.750	32.893
7.5	8.991	8.972	8.971	3.773	3.807	3.817	37.029	37.599	37.751
10.0	10.407	10.381	10.378	4.213	4.248	4.260	41.305	41.916	42.077
12.5	11.686	11.655	11.651	4.612	4.648	4.660	45.175	45.824	45.996
15.0	12.859	12.825	12.819	4.977	5.015	5.027	48.730	49.416	49.598
17.5	13.948	13.911	13.905	5.317	5.357	5.369	52.035	52.756	52.947

Table D.55: Scaled energy, mass, and proper separation for two equal sized holes, each with anti-parallel linear momenta P/a_1 generated from an inversion-symmetric extrinsic curvature obeying the isometry condition with a plus sign. The conformal separation is $\beta = 12$.

P/a_1	E/a_1 6	9	12	M/a_1 6	9	12	L/a_1 6	9	12
0.0	4.288	4.334	4.348	2.311	2.353	2.366	22.890	23.429	23.578
1.0	4.559	4.595	4.607	2.392	2.432	2.444	23.658	24.184	24.328
2.5	5.526	5.541	5.546	2.681	2.717	2.728	26.410	26.914	27.051
5.0	7.294	7.288	7.288	3.210	3.244	3.254	31.467	31.982	32.121
7.5	8.882	8.864	8.862	3.686	3.720	3.731	36.029	36.574	36.720
10.0	10.295	10.271	10.267	4.111	4.146	4.157	40.104	40.683	40.838
12.5	11.573	11.544	11.539	4.496	4.533	4.544	43.801	44.413	44.577
15.0	12.746	12.714	12.708	4.850	4.888	4.900	47.202	47.847	48.019
17.5	13.836	13.801	13.794	5.180	5.219	5.232	50.366	51.042	51.223

Table D.56: Scaled energy, mass, and proper separation for two equal sized holes, each with anti-parallel linear momenta P/a_1 generated from an inversion-symmetric extrinsic curvature obeying the isometry condition with a minus sign. The conformal separation is $\beta = 12$.

S/a_1^2	E/a_1 6	9	12	M/a_1 6	9	12	L/a_1 6	9	12
0.0	4.288	4.334	4.348	2.311	2.353	2.366	22.890	23.429	23.578
1.0	4.350	4.393	4.406	2.338	2.379	2.391	23.088	23.624	23.771
3.0	4.738	4.767	4.776	2.506	2.543	2.554	24.347	24.871	25.014
10.0	6.468	6.466	6.467	3.288	3.318	3.327	30.224	30.790	30.943
30.0	9.835	9.805	9.799	4.953	4.983	4.993	42.807	43.560	43.764
100.0	15.992	15.928	15.912	8.430	8.468	8.480	69.214	70.394	70.718
300.0	24.673	24.569	24.543	14.155	14.210	14.228	112.838	114.729	115.251
1000.0	39.003	38.842	38.801	25.397	25.487	25.516	198.621	201.905	202.820

Table D.57: Scaled energy, mass, and proper separation for two equal sized holes, each with anti-parallel angular momenta S/a_1^2 generated from an inversion-symmetric extrinsic curvature obeying the isometry condition with a minus sign. The conformal separation is $\beta = 12$.

P/a_1	E/a_1 6	9	12	M/a_1 6	9	12	L/a_1 6	9	12
0.0	4.288	4.334	4.348	2.311	2.353	2.366	22.890	23.429	23.578
1.0	4.953	4.985	4.994	2.430	2.470	2.482	23.987	24.522	24.668
2.5	7.395	7.399	7.393	2.818	2.856	2.868	27.614	28.166	28.314
5.0	12.484	12.463	12.427	3.484	3.523	3.535	33.875	34.500	34.666
7.5	17.879	17.845	17.772	4.068	4.109	4.122	39.397	40.101	40.287
10.0	23.350	23.309	23.193	4.584	4.629	4.643	44.296	45.075	45.280
12.5	28.813	28.766	28.606	5.050	5.098	5.113	48.726	49.574	49.797
15.0	34.212	34.163	33.956	5.477	5.529	5.544	52.795	53.709	53.948
17.5	39.503	39.453	39.199	5.874	5.929	5.945	56.577	57.552	57.806

Table D.58: Scaled energy, mass, and proper separation for two equal sized holes, each with parallel linear momenta P/a_1 generated from an inversion-symmetric extrinsic curvature obeying the isometry condition with a plus sign. The conformal separation is $\beta = 12$.

P/a_1	E/a_1 6	9	12	M/a_1 6	9	12	L/a_1 6	9	12
0.0	4.288	4.334	4.348	2.311	2.353	2.366	22.890	23.429	23.578
1.0	4.930	4.963	4.972	2.419	2.459	2.472	23.878	24.412	24.558
2.5	7.336	7.341	7.335	2.784	2.822	2.833	27.246	27.792	27.940
5.0	12.411	12.392	12.356	3.423	3.462	3.474	33.201	33.812	33.976
7.5	17.807	17.776	17.702	3.988	4.031	4.044	38.505	39.188	39.370
10.0	23.281	23.243	23.127	4.490	4.535	4.549	43.227	43.979	44.179
12.5	28.747	28.705	28.544	4.943	4.992	5.007	47.504	48.322	48.538
15.0	34.150	34.105	33.898	5.360	5.412	5.427	51.438	52.316	52.548
17.5	39.445	39.398	39.145	5.747	5.801	5.818	55.096	56.032	56.279

Table D.59: Scaled energy, mass, and proper separation for two equal sized holes, each with parallel linear momenta P/a_1 generated from an inversion-symmetric extrinsic curvature obeying the isometry condition with a minus sign. The conformal separation is $\beta = 12$.

S/a_1^2	E/a_1 6	9	12	M/a_1 6	9	12	L/a_1 6	9	12
0.0	4.288	4.334	4.348	2.311	2.353	2.366	22.890	23.429	23.578
1.0	4.351	4.394	4.407	2.338	2.379	2.391	23.089	23.625	23.772
3.0	4.746	4.775	4.784	2.507	2.543	2.555	24.355	24.879	25.022
10.0	6.524	6.523	6.523	3.293	3.323	3.332	30.272	30.839	30.992
30.0	10.094	10.063	10.056	4.968	4.999	5.008	42.995	43.751	43.956
100.0	17.080	17.012	16.994	8.479	8.518	8.531	69.913	71.106	71.432
300.0	28.057	27.944	27.912	14.280	14.338	14.356	114.775	116.701	117.232
1000.0	48.968	48.791	48.720	25.704	25.800	25.831	203.634	207.018	207.956

Table D.60: Scaled energy, mass, and proper separation for two equal sized holes, each with parallel angular momenta S/a_1^2 generated from an inversion-symmetric extrinsic curvature obeying the isometry condition with a minus sign. The conformal separation is $\beta = 12$.

References

Abrahams, A. M., [1990], Private Communication.

Abrahams, A. M., and Evans, C. R., [1988], "Reading off gravitational radiation waveforms in numerical relativity calculations: Mathching to linearized gravity," *Phys. Rev. D*, **37**, pp. 318–332.

Abrahams, A. M., and Evans, C. R., [1990], "Gauge invariant treatment of gravitational radiation near the source: Analysis and numerical simulations," submitted to *Phys. Rev. D.*

Adler, S. L., and Piran, T., [1984], "Relaxation methods for gauge field equilibrium equations," *Rev. Mod. Phys.*, **56**, pp. 1–40.

Allen, D. N. de G., [1954], *Relaxation Methods*, McGraw-Hill, New York.

Ames, W. F., [1977], *Numerical Methods for Partial Differential Equations*, Academic Press, New York.

Arnowitt, R., Desser, S., and Misner, C. W., [1962], "The dynamics of general relativity," in Witten [1962], pp. 227–265.

Bergman, S. and Schiffer, M., [1953], *Kernel Functions and Elliptic Differential Equations in Mathematical Physics*, Academic Press, New York.

Bernstein, D. H., and Hobill, D. W., [1990] Private Communication.

Bishop, N. T., [1982], "The closed trapped region and the apparent horizon of two Schwarzschild black holes," *Gen. Rel. and Grav.*, **14**, pp. 717–723.

Bishop, N. T., [1984], "The horizons of two Schwarzschild black holes," *Gen. Rel. and Grav.*, **16**, pp. 589–593.

Bishop, N. T., [1988], "The event horizons of two Schwarzschild black holes," *Gen. Rel. and Grav.*, **20**, pp. 573–581.

Bowen, J., [1979a], "General form for the longitudinal momentum of a spherically symmetric source," *Gen. Rel. and Grav.*, **11**, pp. 227–231.

Bowen, J., [1979b], *Initial Value Problem on Non-Euclidean Topologies*, Ph.D. dissertation, University of North Carolina–Chapel Hill.

Bowen, J., [1982], "General solutions for flat-space longitudinal momentum ," *Gen. Rel. and Grav.*, **14**, pp. 1183–1191.

Bowen, J., Rauber, J., and York, J. W., Jr., [1984], "Two black holes with axisymmetric parallel spins: Initial data," *Class. Quantum Grav.*, **1**, pp. 591–610.

Bowen, J. M., and York, J. W., Jr., [1980], "Time-asymmetric initial data for black holes and black-hole collisions," Phys. Rev. D, **21**, pp. 2047–2056.

Brandt, A., [1977], "Multi-level adaptive solutions to boundary-value problems," *Math. of Comp.*, **31**, pp. 333–390.

Brandt, A., [1982], "Guide to multigrid development," in Hackbusch and Trottenberg 1982, pp. 220–312.

Brill, D. R., and Lindquist, R. W., [1963], "Interaction energy in geometrostatics," *Phys. Rev.*, **131**, pp. 471–476.

Čadež, A.,[1971], *Colliding Black Holes*, Ph.D. dissertation, University of North Carolina–Chapel Hill.

Čadež, A.,[1974], "Apparent horizons in the two-black-hole problem," *Ann. Phys.*, **83**, pp. 449–457.

Cantor, M., and Kulkarni, A. D., [1982], "Physical distinctions between normalized solutions of the two-body problem of general relativity," *Phys. Rev. D*, **25**, pp. 2521–2526.

Centrella, J. M., [1986], *Dynamical Spacetimes and Numerical Relativity*, Cambridge University Press, London.

Choptuik, M. W., [1982], *A Study of Numerical Techniques for the Initial Value Problem of General Relativity*, Masters thesis, University of British Columbia.

Choptuik, M. W., and Unruh, W. G., [1986], "An introduction to the multi-grid method for numerical relativists," *Gen. Rel. and Grav.*, **18**, pp 813–843.

Choquet-Bruhat, Y., and York, J. W., Jr., [1980], "The Cauchy problem," in Held 1980, pp. 99–172.

Christodoulou, D., [1970], "Reversible and irreversible transformations in black-hole physics," *Phys. Rev. Letters*, **25**, pp. 1596–1597.

Cook, G. B., [1989], "The Multigrid Technique," in Evans, Finn, and Hobill 1989, pp. 222–229.

Cook, G. B., and York, J. W., Jr., [1990], "Apparent horizons for boosted or spinning black holes," *Phys. Rev. D*, **41**, pp. 1077–1085.

Damour, T., [1983], "Gravitational radiation and the motion of compact bodies," in Deruelle and Piran 1983, pp. 59–144.

Damour, T., [1987], "The problem of motion in Newtonian and Einsteinian gravity," in Hawking and Israel 1987, pp. 128–198.

Detweiler, S., [1989], "Kepler's third law in general relativity," in Evans, Finn, and Hobill 1989, pp. 43–56.

Detweiler, S., [1989], Private Communication.

Deruelle, N., and Piran, T., [1983], *Gravitational Radiation*, North-Holland Publishing Company, Amsterdam.

Einstein, A., and Rosen, N., [1935], "The particle problem in the general theory of relativity," *Phys. Rev.*, **48**, pp. 73–77.

Eppley, K., [1977], "Evolution of time-symmetric gravitational waves: Initial data and apparent horizons," *Phys. Rev. D*, **16**, pp. 1609–1614.

Evans, C. R., [1984], *A Method for Numerical Relativity: Simulation of Axisymmetric Gravitational Collapse and Gravitational Radiation Generation*, Ph.D. dissertation, University of Texas at Austin.

Evans, C. R., [1986a], "An approach for calculating axisymmetric gravitational collapse," in Centrella 1986, pp. 3–39.

Evans, C. R., [1986b], Unpublished work.

Evans, C. R., [1987], "Gravitational radiation from collisions of compact stars," in Ulmer 1987, pp. 152–156.

Evans, C. R., [1989], Private Communication.

Evans, C. R., Finn, L. S., and Hobill, D. W., [1989], *Frontiers in Numerical Relativity*, Cambridge University Press, London.

Ferrell, R. C., and Eardley, D. M., [1989], "Slowly moving maximally charged black holes," in Evans, Finn, and Hobill 1989, pp. 27–42.

Gibbons, G. W., [1972], "The time symmetric initial value problem for black holes," *Commun. Math. Phys.*, **27**, pp. 87–102.

Gibbons, G. W., and Schutz, B. F., [1972], "Limits on gravitational radiation from two gravitationally bound black holes," *Mon. Not. R. Astr. Soc.*, **159**, pp. 41P–45P.

Hackbusch, W., and Trottenberg, U., [1982], *Multigrid Methods*, Springer-Verlag, Berlin.

Hackbusch, W., [1985], *Multi-Grid Methods and Applications*, Springer-Verlag, Berlin.

Hahn, S., and Lindquist, R., [1964], "The two body problem in geometrodynamics," *Ann. Phys.*, **29**, pp. 304–331.

Hawking, S. W., [1971], "Gravitational radiation from colliding black holes," *Phys. Rev. Letters*, **26**, pp. 1344–1346.

Hawking, S. W., and Ellis, G. F. R., [1973], *The Large Scale Structure of Space-Time*, Cambridge University Press, London.

Hawking, S. W., and Israel, W., [1987], *300 Years of Gravitation*, Cambridge University Press, London.

Held, A., [1980], *General Relativity and Gravitation: One Hundred Years After the Birth of Albert Einstein*, Volume 1, Plenum Press, London.

Jaffe, J., [1975], "The gravitational spin-spin force," *Gen. Rel. and Grav.*, **6**, pp. 49–53.

Kulkarni, A. D., [1984], "Time-asymmetric initial data for the N black hole problem in general relativity," *J. Math. Phys.*, **25**, pp. 1028–1034.

Kulkarni, A. D., Shepley, L. C., and York, J. W., Jr., [1983], "Initial data for N black holes," *Phys. Lett.*, **96A**, pp. 228–230.

Lindquist, R. W., [1963], "Initial-value problems on Einstein-Rosen manifolds," *J. Math. Phys.*, **4**, pp. 938–950.

Mashoon, B., [1971], "Particles with spin in a gravitational field," *J. Math. Phys.*, **12**, pp. 1075–1077.

Matzner, R. and Shepley, L., [1982], *Spacetime and Geometry: The Alfred Schild Lectures*, University of Texas Press, Austin.

Misner, C. W., [1963], "The method of images in geometrostatics," *Ann. Phys.*, **24**, pp. 102–117.

Misner, C. W., Thorne, K. S., and Wheeler, J. A., [1973], *Gravitation*, W. H. Freeman and Company, New York.

Mitchell, A. R., and Griffiths, D. F., [1980], *The Finite Difference Method in Partial Differential Equations*, John Wiley and Sons, New York.

Moon, P., and Spencer, D. E., [1988], *Field Theory Handbook*, Springer-Verlag, Berlin.

Nakamura, T., Kojima, Y., and Oohara, K., [1984], "A method of determining apparent horizons in three-dimensional numerical relativity," *Phys. Lett.*, **106A**, pp. 235–238.

Nakamura, T., Kojima, Y., and Oohara, K., [1985], "Apparent horizons of time-symmetric initial value for three black holes," *Phys. Lett.*, **107A**, pp. 452–455.

Nakamura, T., and Oohara, K., [1989], "Methods in 3D numerical Relativity," in Evans, Finn, and Hobill 1989, pp. 254–280.

Ó Murchada, N., and York, J. W., Jr., [1973], "Existence and uniqueness of solutions of the Hamiltonian constraint of general relativity on compact manifolds," *J. Math. Phys.*, **14**, pp. 1551–1557.

Ó Murchada, N., and York, J. W., Jr., [1974a], "Initial-value problem of general relativity. I. General formulation and physical interpretation," *Phys. Rev. D*, **10**, pp. 428–436.

Ó Murchada, N., and York, J. W., Jr., [1974b], "Initial-value problem of general relativity. II. Stability of solution of the initial-value equations," *Phys. Rev. D*, **10**, pp. 437–446.

Ó Murchada, N., and York, J. W., Jr., [1974c], "Gravitational energy," *Phys. Rev. D*, **10**, pp. 2345–2357.

Ó Murchada, N., and York, J. W., Jr., [1976a], "Gravitational momentum," unpublished.

Ó Murchada, N., and York, J. W., Jr., [1976b], "Gravitational potentials: A constructive approach to general relativity," *Gen. Rel. and Grav.*, **7**, pp. 257–261.

Papagiannis, M. D., [1977], *Eighth Texas Symposium on Relativistic Astrophysics*, The New York Academy of Sciences, New York.

Piran, T., [1988], Private Communication.

Piran, T., [1989], Private Communication.

Press, W. H., Flannery, B. P., Teukolky, S. A., and Vetterling, W. T., [1988], *Numerical Recipes in C*, Cambridge University Press, London.

Rauber, J. D., [1985], *Initial Data for Black Hole Collisions*, Ph.D. dissertation, University of North Carolina–Chapel Hill.

Rauber, J. D., [1986], "Initial data for black hole collisions," in Centrella 1986, pp. 304–327.

Smarr, L. L., Čadež, A., DeWitt, W., Eppley, K., [1976], "Collision of two black holes: Theoretical framework," *Phys. Rev. D*, **14**, pp. 2443–2452.

Smarr, L. L., [1977], "Space-times generated by computers: black holes with gravitational radiation", in Papagiannis 1977, pp. 569–604.

Smarr, L. L., [1979], Sources of Gravitational Radiation, Cambridge University Press, London.

Smarr, L. L., and York, J. W., Jr., [1078a], "Radiation gauge in general relativity," *Phys. Rev. D*, **17**, pp. 1945–1956.

Smarr, L. L., and York, J. W., Jr., [1078b], "Kinematical conditions in the construction of space-time," *Phys. Rev. D*, **17**, pp. 2529–2551.

Thornburg, J., [1987], "Coordinates and boundary conditions for the general relativistic initial data problem," *Class. Quantum Grav.*, **4**, pp. 1119–11131.

Thorne, K. S., [1987], "Gravitational radiation," in Hawking and Israel 1987, pp. 330–458.

Tipler, F. J., [1980], *Essays in General Relativity*, Academic Press, New York.

Tomimatsu, A., [1989], "Gravitational field in a collision of two Schwarzschild black holes," Preprint.

Ulmer, M. P., [1987], *Proceedings of the 13th Texas Symposium on Relativistic Astrophysics*, World Scientific Publishing, Singapore.

Wald, R. M., [1972], "Gravitational spin interaction," *Phys. Rev. D*, **6**, pp. 406–413.

Wald, R. M., [1984], *General Relativity*, The University of Chicago Press, Chicago.

Weinberg, S., [1972], *Gravitation and Cosmology: Principles and Applications of the General Theory of Relativity*, Wiley and Sons, New York.

Witten, L., [1962], *Gravitation: An Introduction to Current Research*, John Wiley and Sons, New York.

York, J. W., Jr., [1971], "Gravitational degrees of freedom and the initial-value problem," *Phys. Rev. Letters*, **26**, pp. 1656–1658.

York, J. W., Jr., [1972], "Role of conformal three-geometry in the dynamics of gravitation," *Phys. Rev. Letters*, **28**, pp. 1082–1085.

York, J. W., Jr. [1973a], "Conformally invariant orthogonal decomposition of symmetric tensors on Riemannian manifolds and the initial-value problem of general relativity," *J. Math. Phys.*, **14**, pp. 456–464.

York, J. W., Jr. [1973b], "Initial-value problem and dynamics of general relativity," Lecture notes, Princeton University.

York, J. W., Jr. [1974], "Covariant decompositions of symmetric tensors in the theory of gravitation," *Ann. Inst. Henri Poincaré*, **21**, pp. 319–332.

York, J. W., Jr., [1979], "Kinematics and Dynamics of General Relativity," in Smarr 1979, pp. 83–126.

York, J. W., Jr., [1980], "Energy and momentum of the gravitational field," in Tipler, pp. 39–58.

York, J. W., Jr., [1984], "Initial data for N black holes," *Physica*, **124A**, pp. 629–637.

York, J. W., Jr., [1989], "Initial data for collisions of black holes and other gravitational miscellany," in Evans, Finn, and Hobill 1989, pp. 89–109.

York, J. W., Jr., and Piran, T., [1982], "The initial value problem and beyond," in Matzner and Shepley 1982, pp. 147–176.